Trellis coding with CPM for satellite-based land-mobile communications.

ABSTRACT OF FINAL REPORT

TECHNOLOGY GROUP

September 1989

PROJECT SUMMARY

This volume, prepared by Technology Group, contains the final report on the satellite-based mobile communications project. The research effort was based on the comprehensive study of a class of continuous-phase modulated (CPM) signals used in conjunction with trellis-coded modulation (TCM), interleaving/interlacing, and coherent/differential/noncoherent detection.

The general framework of our tasks was to provide a detailed analysis of a bandwidth-efficient coding and modulation, and select a candidate system which will be capable of transmitting 4800 bits/s over a channel with a 5-KHz bandwidth subject to Rician fading. In particular, we were expected to provide:

- A detailed analysis and design of a trellis-coded CPM transmission scheme with suboptimum detection, which could offer implementational simplicity and the provision for interleaving/deinterleaving to combat the fading effects.
- Development of software for the computation of power spectrum.
- Design and development of a Doppler frequency shift compensator.
- Design and development of a symbol timing recovery circuit.
- Extensive simulations to be used for system parameter optimization.
- Breadboard implementation of the transmission system.

As outlined in our initial Quarterly Report, the project was organized into a set of tasks and subtasks based on which, a comprehensive examination of all the issues was carried out. Accordingly, the following tasks were completed: extensive analysis and substantial simulations of partial response and full response CPM signals, generalized precoding, trellis codes, interleaving and interlacing, suboptimum detection schemes, theoretical performance bounds, and filters; development of a class of Doppler estimators; design of symbol synchronizer; extensive examinations the spectrum of the various CPM signals ; and, a comprehensive system optimization. Additionally, the hardware implementation of the final candidate system

has been undertaken[1]. In an effort to provide a detailed description of our work, a set of comprehensive and illustrative Quarterly Reports was produced and submitted.

Our study has demonstrated that the synergy between TCM, which improves error probability, and CPM signals, which provide constant envelope and low spectral occupancy, provides a satisfactory solution to the problem of transmitting on mobile satellite channels.

In principle, two implementations of this idea are feasible. The first one takes advantage of both the bandwidth efficiency *and* the power efficiency of CPM codes, by using a receiver which combines the trellis structure of TCM and that of CPM. In this situation, the complexity can grow very large and become quickly unmanageable, so that a suboptimum solution should be devised. Moreover, the introduction of an interleaver/deinterleaver pair, which is known to be beneficial fro transmission on fading channels, would not be allowed. To obviate the associated problems, we avoided maximum-likelihood decoding of the CPM signals, and instead, differentially demodulated the signals symbol-by-symbol. By doing this, the power efficiency of CPM is not exploited, however, its spectral properties are retained, and interleaving/deinterleaving is made possible.

This transmission scheme was extensively simulated under several conditions; full response and partial response formats, several frequency pulse shapes, with and without precoding, detection points, receiver filter shapes, TCM schemes, interleaving/deinterleaving sizes and depths, and various fading channel parameters were considered.

The results of our studies show that, after a careful selection of the system parameters, on fading channels differentially-detected CPM offers an error performance which is essentially the same as differentially coherent PSK. Now, since PSK does not use the bandwidth in a very efficient way, it has to be band-pass filtered to meet the requirements of closely-spaced mobile-radio channels. As a result, its envelope is no longer constant, and its performance would be degraded by power amplifiers operated at or near saturation for better power efficiency. On the other hand, CPM with the parameters chosen is bandwidth efficient, so that it does not require narrow filtering and consequently offers constant or near-constant envelope. Hence,

[1]Additional effort is required to finalize the hardware.

under the same mobile system configurations, the trellis coded CPM appears to offer a better performance than the filtered trellis coded 8DPSK.

ABSTRACT

1 Introduction and motivation of the work

In this Report we consider a satellite-based mobile communication scheme based on continuous-phase modulated (CPM) signals used in conjunction with trellis-coded modulation (TCM).

In satellite-based land mobile communication systems both bandwidth and power are limited resources. In fact, these systems employ frequency-division multiple access (FDMA) with a given channel spacing (say, 5 KHz), and the fraction of out-of-band power should be very small to prevent interferences to adjacent channels. On the other hand, the satellite distance from earth, its power limitations, and the need for low-cost (and hence low-gain) mobile antennas puts a serious limit on the power resources. Additionally, the fading environment of mobile communication further limits the power efficiency of the system.

In a bandwidth- and power-limited environment, a bandwidth- *and* power-efficient coding/modulation scheme must be used. Trellis coded modulation (TCM) offers an attractive scheme. It combines the choice of a higher-order modulation scheme with that of a convolutional code, while the receiver, instead of performing demodulation and decoding in two separate steps, combines the two operations into one. As a result, the reliability of a digital transmission system is increased without increasing the transmitted power nor the required bandwidth. By using TCM, simple schemes can be designed that achieve significant power gains (from 3 to 6 dB) without any bandwidth expansion.

Due to the strictly bandlimited environment created by the mobile satellite channel, the signals to be used in conjunction with trellis codes must be chosen carefully. Besides having excellent spectral characteristics, the signals used should have constant envelope if nonlinear amplifiers are used for better power efficiency. A class of bandwidth-efficient signals that satisfies both constraints is offered by continuous-phase modulated (CPM) signals, based on phase modulation where phase continuity is introduced to reduce the bandwidth occupancy.

The synergy between TCM, which improves error probability, and CPM signals, which provide constant envelope and low spectral occupancy, is expected to provide a satisfactory solution to the problem of transmitting on mobile satellite channels.

In principle, two implementations of this idea are feasible. The first one takes advantage of both the bandwidth efficiency *and* the power efficiency of CPM codes, by using a receiver which combines the trellis structure of TCM and that of CPM. In this situation, TCM and CPM can even be integrated in a single entity, but the number of states necessary for a trellis representation of these signals is given by the number of TCM states times the number of CPM states. As this number can grow very large, the complexity of the receiver may become quickly unmanageable, and a suboptimum solution should be devised. Moreover, the introduction of an interleaver/deinterleaver pair, which is well-known to introduce beneficial effects in digital transmission over channels affected by fading, would not be allowed without destroying the spectral properties of CPM.

We can trade a decrease in complexity for a decrease in power efficiency (but not in bandwidth efficiency) by giving up maximum-likelihood decoding of the CPM signals, which are instead demodulated symbol-by-symbol. By doing this, we still take advantage of the spectral properties of CPM, and the introduction of an interleaving/deinterleaver pair is now possible. This is an added attractive feature of this suboptimum solution, since it increases the protection of the transmitted signal from the effects of selective fading.

We have considered three solutions: *coherent, differentially-coherent,* and *non-coherent* symbol-by-symbol detection. Since differentially coherent detection appeared to us to be the most promising technique, our work was based on a CPM/TCM system based on this kind of detection. *This report describes our analysis, simulation, and implementation of differentially-coherent symbol-by-symbol detection of trellis-encoded continuous-phase modulated signals.*

2 Channel models, CPM, and TCM

Besides additive Gaussian noise, which is the standard environment for the analysis of coding schemes for the transmission of digital data or speech, there is a number of additional sources of performance degradation that must be taken into account to assess the merits of a proposed transmission scheme for mobile satellite channels. The most important among them are

- **Doppler shifts.** These are due to mobile vehicle motion. If differential detection is used, the information-bearing phase turns out to be shifted by an amount $2\pi f_d T_s$, where $1/T_s$ is the data symbol rate and f_d is the Doppler frequency shift, which for operation at L-band can be expected to be up to 200 Hz. At a rate of 2400 symbols per second the corresponding phase shift is 30°.

- **Fading and shadowing.** The transmitted radio signal reaches the receiver through different paths caused by reflections from obstacles, yielding a signal whose components, having different phases and amplitudes, may either reinforce or cancel each other. Shadowing is caused by the obstruction of radio waves by buildings, trees, and hills.

- **Adjacent channel interference.** The 5-KHz mobile channel used for transmission operates in a channelized environment. As a result, signals suffer from interference from signals occupying adjacent channels.

- **Channel nonlinearities.** Primarily because of the high-power amplifier in the transmitter, operated at or near saturation for better power efficiency, the channel is inherently nonlinear.

- **Finite interleaving depth.** In order to break up the error bursts caused by amplitudes fades of duration greater than symbol time, encoded symbols should be interleaved. Now, infinite interleaving provides a memoryless channel, but in practice the interleaving frame must be limited. In fact, for speech transmission the total coding/decoding delay must be kept below 60 ms in order not to cause perceptual annoyance. If the depth of interleaving cannot be larger than the maximum fade duration anticipated, this causes a performance degradation.

2.1 Continuous Phase Modulation (CPM)

A continuous-phase modulated signal is defined by

$$s(t, \mathbf{a}) = \sqrt{\frac{2E_s}{T_s}} \cos(2\pi f_0 t + \theta(t, \mathbf{a})) \tag{1}$$

where E_s is the symbol energy, T_s is the symbol time, and f_0 the carrier frequency. The transmitted information is contained in the phase

$$\theta(t, \mathbf{a}) = 2\pi h \sum_{n=-\infty}^{\infty} a_n q(t - nT_s) \tag{2}$$

with $q(t)$ the phase-shaping pulse given by

$$q(t) = \int_{-\infty}^{t} g(\tau) d\tau, \tag{3}$$

$g(t)$ is the frequency pulse with finite duration, i.e., $g(t)$ is nonzero only for $0 \leq t \leq LT_s$, L the pulse length. The value of L contributes to the taxonomy of CPM signals, namely:

- $L = 1$: Full-response signals
- $L > 1$: Partial-response signals.

It is common to assume

$$\int_{-\infty}^{\infty} g(\tau) d\tau = 1/2.$$

In (2),

$$\mathbf{a} = \cdots, a_{-2}, a_{-1}, a_0, a_1, \cdots$$

denotes the symbol sequence sent to the CPM modulator. The symbols a_n take values $\pm 1, \pm 3, \cdots, \pm(M-1)$, where $M = 2^m$, m a positive integer. The parameter h is called the *modulation index*.

2.2 Combining TCM With CPM

If CPM signals are combined with an external convolutional encoder, or equivalently they are used as the signal constellation to be used in a trellis-coded modulation (TCM) scheme, a further improvement can be obtained. This new scheme is obtained by observing that at the output of the trellis encoder we get a multilevel signal which in turn can be used as the input to the continuous-phase modulator. The design of the coding scheme and of the modulator scheme should be performed jointly in order to maximize the Euclidean distance resulting from the combination of the two.

To implement TCM/CPM, we may want to take advantage of both the bandwidth efficiency *and* the power efficiency of CPM codes. However, the complexity of the resulting optimum demodulator can grow very large, so that a suboptimum solution should be sought, which trades a decrease in complexity for a decrease in power efficiency (but not in bandwidth efficiency). *This is obtained by uncoupling the demodulation of CPM from decoding of TCM.*

To keep the demodulation problem separate from the decoding problem, we consider estimating the CPM phases symbol-by-symbol, and using these estimates to build up a metric for the TCM decoder. Then, we use an optimum (Viterbi) algorithm for decoding, the complexity of it being that of the TCM scheme only. This procedure obviously entails a loss of optimality, which is traded against a manageable receiver structure. However, as mentioned before, the spectral properties of CPM are preserved.

We have first analyzed *coherent* and *noncoherent* symbol-by-symbol demodulation of CPM signals. The result was that noncoherent demodulation entails a very large loss of optimality, while coherent demodulation, which offers a better performance, may still be too complex to implement. For these reasons, we decided to consider in more depth *differential detection,* which has a complexity comparable to noncoherent detection without its performance penalty.

2.3 Differential detection of CPM

The complex envelope of the received signal, say $\tilde{r}(t)$ is delayed by T_s seconds, transformed into its conjugate $\tilde{r}^*(t-T_s)$, and multiplied by itself.

Then the real and imaginary components of the signal $\tilde{r}(t)\tilde{r}^*(t-T_s)$ are sampled every T_s seconds. As a result, a discrete signal is obtained whose phase is

$$2\pi f_0 T_s + \Delta\theta_n + \eta_n$$

where $\Delta\theta_n$ represents the change over one symbol interval of the signal phase, and η_n represents the change in phase due to the noise. Under the assumption that $f_0 T_s$ is an integer number, estimate of this phase provides a noisy estimate of $\Delta\theta_n$, which is used to recover the information sequence.

For full-response CPM (the case of precoded partial response was also considered) we have

$$\Delta\theta_n = \pi h a_n,$$

so that the maximum value taken on by the phase shift is

$$|\Delta\theta|_{\max} = \pi h(M-1).$$

This quantity must be lower than π because the phases are observed modulo 2π. Thus, we must choose

$$h < \frac{1}{M-1}. \tag{4}$$

2.4 Doppler phase shift removal

Let us write the observed signal $r(t)$ in the form

$$r(t) = P(t)e^{j[2\pi f_d t + \theta(t,\mathbf{a}) + \nu(t)]}, \tag{5}$$

where $P(t)$ and $\nu(t)$ are the amplitude fluctuation and the phase fluctuation, respectively. They account for fading, noise, and intersymbol interference. f_d is the Doppler frequency shift.

For differential processing, the signal (5) is synchronously sampled at times $t_n = nT_s$, $n = 0, 1, \ldots$, and the following sequence is formed:

$$r_n = \frac{1}{2} r(t_n) r^*(t_{n-1}) = \rho_n e^{j[\phi_d + \Delta\theta_n + \eta_n]} \tag{6}$$

where $\phi_d = 2\pi f_d T_s$ is the Doppler phase shift,

$$\Delta\theta_n = \theta(t_n, \mathbf{a}) - \theta(t_{n-1}, \mathbf{a}) = \pi h a_n$$

represents the phase fluctuations due to the transmitted data, and $\eta_n = \nu(t_n) - \nu(t_{n-1})$. Finally,

$$\rho_n = \frac{1}{2} P(t_n) P(t_{n-1}).$$

(Perfect symbol synchronization is assumed.)

It is seen from (6) that the presence of a Doppler frequency shift causes the phase of the sequence r_n to be altered by a term ϕ_d, added to the information sequence $\Delta\theta_n$. This has to be removed prior to demodulation.

Two constraints are associated with the design of a Doppler compensation circuit for continuous-phase modulated signals with application to mobile satellite communications:

- Fast frequency acquisition is required. In fact, if data are transmitted in short bursts or packets, the acquisition time should not be a significant portion of the burst interval.
- Since multipath fading affects the propagation, the Doppler estimator must be insensitive to the signal amplitude fluctuations caused by fading.

As a consequence of the first requirement, we have consider open-loop estimation structures. Three estimators, that trade robustness to Doppler shifts for complexity, were proposed and their performance analyzed.

2.5 Symbol synchronization

The operation and performance of a symbol synchronizer suitable for our transmission scheme have been analyzed and simulated. The idea underlying the synchronizer scheme is the production of spectral lines in the CPM signal, as generated by passing it in a non-linear device. These spectral lines, or periodic-like contributions, provide a mechanism for extracting symbol timing. In fact, the spacing of the lines is $1/T_s$, where T_s is the symbol duration.

3 Simulation results and conclusions

The transmission scheme described here was extensively simulated under several conditions. Several frequency pulse shapes, receiver filter shapes, TCM schemes, interleaving/deinterleaving sizes and depths, and fading channels were considered. The results show that, for a careful selection of system parameters, *on fading channels differentially-detected CPM offers an error performance which is essentially the same as differentially coherent PSK. Now, since PSK does not use bandwidth in a very efficient way, it has to be band-pass filtered to meet the requirements of closely-spaced mobile-radio channelization. As a result, its envelope is not constant, and its performance would be degraded by power amplifiers operated at or near saturation for better power efficiency. On the other hand, CPM with the parameters chosen is bandwidth efficient, so that it does not require narrow filtering and consequently offers constant or near-constant envelope.*

4 Organization of this report

This Final Report is organized as follows. Chapter 1 provides the motivation for this work, as well as an overview of the channel model for which our system has been analyzed and designed. Chapter 2 reviews continuous-phase modulation, with emphasis on the spectral properties of continuously phase-modulated signals. Chapter 3 reviews trellis-coded modulation, and discusses the interactions between TCM and CPM, as well as the possible advantages resulting from it. Chapter 4 deals with suboptimum detection of trellis-encoded CPM. In particular, two extreme cases of suboptimum detection, viz., coherent and noncoherent, are analyzed. Differential detection of trellis-encoded CPM is the subject of Chapter 5. Chapters 6 and 7 describe the design and the analysis of two circuits that are needed for the proper operation of a differentially-detected, trellis-encoded CPM transmission system. In particular, Chapter 6 considers the effects of a Doppler frequency shift, and its removal. Chapter 7 considers a circuit for the recovery of the timing information from the received signal. Simulation results are included in Chapter 8, while Chapter 9 contains the conclusions drawn from the preceding body of work. Two appendices describe the sim-

ulation package written during the work and the hardware implementation of the transmitter and receiver[2].

[2]We observe here that this Final Report is not the result of a simple superposition of our Quarterly Reports. For legibility's sake, some discussions that are less relevant to our presentations, as well as a number of charts showing results of lesser importance, have been omitted, and the whole material has been reshuffled.

Trellis coding with CPM for satellite-based land-mobile communications.

FINAL REPORT

Technology Group

Contents

List of Figures

List of Tables

Chapter 1

Introduction

In this Report we consider a satellite-based mobile communication scheme based on continuous-phase modulated (CPM) signals used in conjunction with trellis-coded modulation (TCM).

In satellite-based land mobile communication systems both bandwidth and power are limited resources. In fact, these systems employ frequency-division multiple access (FDMA) with a given channel spacing (say, 5 KHz), and the fraction of out-of-band power should be very small to prevent interferences to adjacent channels. On the other hand, the satellite distance from earth, its power limitations, and the need for low-cost (and hence low-gain) mobile antennas put a serious limit on the power resources. Additionally, the fading environment of mobile communication further limits the power efficiency of the system.

In a bandwidth- and power-limited environment, a bandwidth- *and* power-efficient coding/modulation scheme must be used. Trellis coded modulation (TCM) offers an attractive scheme. It combines the choice of a higher-order modulation scheme with that of a convolutional code, while the receiver, instead of performing demodulation and decoding in two separate steps, combines the two operations into one. As a result, the reliability of a digital transmission system is increased without increasing the transmitted power nor the required bandwidth. By using TCM, simple schemes can be designed that achieve significant power gains (from 3 to 6 dB) without any bandwidth expansion (see, e.g., [60,80].)

Due to the strictly bandlimited environment created by the mobile satellite channel, the signals to be used in conjunction with trellis codes must be chosen carefully. Besides having excellent spectral characteristics, the signals used should have constant envelope if nonlinear amplifiers are used for

better power efficiency. A class of bandwidth-efficient signals that satisfies both constraints is offered by continuous-phase modulated (CPM) signals, based on phase modulation where phase continuity is introduced to reduce the bandwidth occupancy.

The synergy between TCM, which improves error probability, and CPM signals, which provide constant envelope and low spectral occupancy, is expected to provide a satisfactory solution to the problem of transmitting on mobile satellite channels.

In principle, two implementations of this idea are feasible. The first one takes advantage of both the bandwidth efficiency *and* the power efficiency of CPM codes, by using a receiver which combines the trellis structure of TCM and that of CPM. In this situation, TCM and CPM can be integrated in a single entity (see [51] and the references therein), but the number of states necessary for a trellis representation of these signals is given by the number of TCM states times the number of CPM states. As this number can grow very large, the complexity of the receiver may become quickly unmanageable, and a suboptimum solution should be devised. We can trade a decrease in complexity for a decrease in power efficiency (but not in bandwidth efficiency) by giving up maximum-likelihood decoding of the CPM signals, which are instead demodulated symbol-by-symbol. By doing this, the power efficiency of CPM codes is not exploited: we only take advantage of their spectral properties.

Hereafter we consider three solutions: coherent, differentially-coherent, and non-coherent symbol-by-symbol detection. Since differentially coherent detection appeared to us to be the most promising technique, most of this Report is devoted to a complete description of a CPM/TCM system based on this kind of detection.

1.1 The channel model

Besides additive Gaussian noise, which is the standard environment for the analysis of coding schemes for the transmission of digital data or speech, there is a number of additional sources of performance degradation that must be taken into account to assess the merits of a proposed transmission scheme for mobile satellite channels. The most important among them are [61,64]:

- **Doppler shifts.** They are due to mobile vehicle motion. If differential detection is used, the information-bearing phase turns out to be shifted

Velocity (MPH)	Frequency shift (Hz)	Phase shift (degrees)
30.0	67.04	10.06
60.0	134.08	20.11
90.0	201.13	30.17
120.0	268.17	40.22

Table 1.1: Doppler frequency and phase shifts.

by an amount $2\pi f_d T_s$, where $1/T_s$ is the data symbol rate and f_d is the Doppler frequency shift, which for operation at L-band can be expected to be up to 200 Hz. At a rate of 2400 symbols per second the corresponding phase shift is 30°. Table 1.1 shows some values of the Doppler shift obtained for various velocities, carrier frequency 1.5 GHz, and symbol interval $T_s = 1/2400$.

- **Fading and shadowing.** The transmitted radio signal reaches the receiver through different paths caused by reflections from obstacles, yielding a signal whose components, having different phases and amplitudes, may either reinforce or cancel each other. Shadowing is caused by the obstruction of radio waves by buildings, trees, and hills.

- **Adjacent channel interference.** The 5-KHz mobile channel used for transmission operates in a channelized environment. As a result, signals suffer from interference from signals occupying adjacent channels.

- **Channel nonlinearities.** Primarily because of the high-power amplifier in the transmitter, operated at or near saturation for better power efficiency, the channel is inherently nonlinear.

- **Finite interleaving depth.** In order to break up the error bursts caused by amplitudes fades of duration greater than symbol time, encoded symbols should be interleaved. Now, infinite interleaving provides a memoryless channel, but in practice the interleaving frame must be limited. In fact, for speech transmission the total coding/decoding delay must be kept below 60 ms in order not to cause perceptual annoyance. If the depth of interleaving cannot be larger than

the maximum fade duration anticipated, this causes a performance degradation.

Chapter 2

Continuous Phase Modulation (CPM)

In this Chapter we provide an overview of the basic features of continuous-phase modulated signals. Additional details can be found in [55,58].

A continuous-phase modulated signal is defined by

$$s(t, \mathbf{a}) = \sqrt{\frac{2E_s}{T_s}} \cos(2\pi f_0 t + \theta(t, \mathbf{a})) \tag{2.1}$$

where E_s is the symbol energy, T_s is the symbol time, and f_0 the carrier frequency. The transmitted information is contained in the phase

$$\theta(t, \mathbf{a}) = 2\pi h \sum_{n=-\infty}^{\infty} a_n q(t - nT_s) \tag{2.2}$$

with $q(t)$ the phase-shaping pulse given by

$$q(t) = \int_{-\infty}^{t} g(\tau) d\tau, \tag{2.3}$$

$g(t)$ is the frequency pulse with finite duration, i.e., $g(t)$ is nonzero only for $0 \leq t \leq LT_s$, L the pulse length. The value of L contributes to the taxonomy of CPM signals, namely:

- $L = 1$: Full-response signals
- $L > 1$: Partial-response signals.

It is common to assume

$$\int_{-\infty}^{\infty} g(\tau)d\tau = 1/2.$$

In (2.2),

$$\mathbf{a} = \cdots, a_{-2}, a_{-1}, a_0, a_1, \cdots$$

denotes the symbol sequence sent to the CPM modulator. The symbols a_n take values $\pm 1, \pm 3, \cdots, \pm(M-1)$, where $M = 2^m$, m a positive integer. The parameter h is called the *modulation index*, and we shall assume

$$h = \frac{2p}{q}$$

with p, q relatively prime integers. Notice that the change in the instantaneous frequency, i.e.,

$$f_o + \dot{\theta}(t, \mathbf{a})/2\pi$$

is proportional to the modulation index. The maximum phase change over a symbol interval is $\pi h(M-1)$.

When the duration of the frequency pulse $g(t)$ is greater than 1 (partial response CPM), the phase function $\theta(t, \mathbf{a})$ during the symbol interval may be written in the form

$$\theta(t, \mathbf{a}) = 2\pi h \sum_{j=n-L+1}^{n} a_j q(t - jT_s) + \theta_n, \quad nT_s \le t \le (n+1)T_s \tag{2.4}$$

where

$$\theta_n \equiv \pi h \sum_{j=-\infty}^{n-L} a_j \mod 2\pi. \tag{2.5}$$

It can be seen from (2.5) that θ_n can take q different values, namely

$$\theta_n \in \left\{0, \frac{2\pi p}{q}, \frac{4\pi p}{q}, \cdots, 2\pi\frac{(q-1)p}{q}\right\}. \tag{2.6}$$

Thus, we can say that the phase function during any given interval depends on the actual transmitted symbol a_n and on the state of the modulator, defined as the value taken by the vector

$$(a_{n-1}, a_{n-2}, \cdots, a_{n-L+1}, \theta_n) \tag{2.7}$$

For each state there are M signal trajectories, and the total number of distinct signal paths over any T_s-second interval is qM^L. The total number

of states is qM^{L-1}. As a special case, for full-response signaling there are Mq signal paths, and q states: this reduction in the number of paths and states, and hence in the complexity of the modulator-demodulator pair, is traded off for an inferior spectrum.

2.1 Optimum detection of CPM Signals

Optimum (maximum-likelihood sequence) estimation of CPM signals involves maximization of the probability density function for the observed signal conditioned on the symbol sequence **a**. Under the assumption that the only disturbance affecting the received signal is an additive white Gaussian noise process $n(t)$, i.e., that $r(t) = s(t) + n(t)$, optimum detection is equivalent to maximizing the quantity

$$J(\mathbf{a}) = \int_{-\infty}^{\infty} r(t)s(t,a)dt.$$

If we define

$$J_n(\mathbf{a}) = \int_{-\infty}^{(n+1)T_s} r(t)s(t,\mathbf{a})dt, \tag{2.8}$$

we can write

$$J_n(\mathbf{a}) = J_{n-1}(\mathbf{a}) + Z_n(\mathbf{a}), \tag{2.9}$$

where

$$Z_n(\mathbf{a}) = \int_{nT_s}^{(n+1)T_s} r(t)\cos[2\pi f_0 t + \theta(t,\mathbf{a})]dt, \tag{2.10}$$

called the *branch metric*, is the correlation between the received signal and a reconstructed version of the transmitted signal over the n-th symbol interval. By using (2.8)-(2.10) it is possible to compute $J(\mathbf{a})$ recursively. The Viterbi algorithm chooses the sequence **a** that maximizes $J_n(\mathbf{a})$.

Because of (2.4) we can also write

$$Z_n(\mathbf{a},\theta_n) = \int_{nT_s}^{(n+1)T_s} r(t)\cos[2\pi f_0 t + \theta(t,\mathbf{a}_n) + \theta_n]dt, \tag{2.11}$$

where

$$\theta(t,\mathbf{a}_n) = 2\pi h \sum_{j=n-L+1}^{n} a_j q(t - jT_s).$$

The receiver computes $Z_n(\mathbf{a}_n,\theta_n)$ for all M^L possible sequences

$$\mathbf{a}_n = (a_n, \cdots, a_{n-L+1})$$

and all q possible θ_n. This shows that Z_n can take on qM^L possible values. The computation of these values requires feeding the observed signal $r(t)$ into a bank of qM^L matched filters which correlate the received signal over one symbol interval.

A maximum-likelihood detector provides a bit error probability that for high signal-to-noise ratios can be roughly approximated by

$$P_b(e) \approx \frac{1}{2}\text{erfc}\left(\frac{d_{\text{free}}}{2\sqrt{2N_0}}\right), \tag{2.12}$$

where d^2_{free} is the minimum integral-squared difference between any two signals corresponding to phase trajectories that are merged till a certain time, then split and remerged at an arbitrary time later.

2.2 Computation of Power Spectrum

We consider here the evaluation of the power spectral density of CPM signals. The method used is based on a technique developed by Aulin and Sundberg [56], and computing the spectrum by Fourier transformation of the autocorrelation function of the modulated signal.

The essence of the method is the following. First, the CPM signal is multiplied by its shifted version and its expectation is taken to obtain the autocorrelation. As the CPM signal process is not wide-sense stationary (but rather cyclostationary), a time-averaged version of the autocorrelation function is determined, then its Fourier transform is taken to get the power density spectrum.

First, let us rewrite (2.1) in a complex form as follows:

$$s(t, \mathbf{a}) = \sqrt{2P}\mathcal{R}\{e^{j(2\pi f_0 t + \theta(t,\mathbf{a}))}\}, \tag{2.13}$$

where $P = E_s/T_s$ is the average signal power, and $\mathcal{R}$ denotes "real part". The other symbols are the same as in (2.1). We assume here, for simplicity, that the data symbols are independent: this assumption is not consistent with our model if trellis-encoded CPM is considered, but we assume that the effect of TCM on the power spectrum is negligible.

Let M denote time average (over the interval $(0, T_s)$), and E denote expectation with respect to the random variables a_n representing the transmitted data. The (stationary) autocorrelation function of the CPM signal is then, under the assumption $f_0 T_s \gg 1$,

$$\begin{aligned} r(\tau) &= \text{ME}\{s(t+\tau, \mathbf{a})s^*(t, \mathbf{a})\} \\ &= P\mathcal{R}\{R(\tau)e^{j2\pi f_0 \tau}\}. \end{aligned}$$

Here,

$$\begin{aligned} R(\tau) &= \mathrm{ME}\{e^{j[\theta(t+\tau,\mathbf{a})-\theta(t,\mathbf{a})]}\} \\ &= \mathrm{ME}\{e^{j[2\pi h\sum_i a_i[q(t+\tau-iT_s)-q(t-iT_s)]}\} \\ &= \mathrm{M}\prod_i \mathrm{E}\{e^{j2\pi h a_i[q(t+\tau-iT_s)-q(t-iT_s)]}\}. \end{aligned}$$

Now,

$$\mathrm{E}\{e^{j2\pi h a_i[q(t+\tau-iT_s)-q(t-iT_s)]}\}$$
$$= \frac{1}{M}\sum_{k=-M/2}^{M/2-1} e^{j2\pi h(2k+1)[q(t+\tau-iT_s)-q(t-iT_s)]}.$$

Moreover, noting that $q(t) = 1/2$ for $t \geq LT_s$, and $q(t) = 0$ for $t < 0$, and letting

$$\tau = \tau' + mT_s, \quad 0 \leq \tau' < T_s, \quad m = 0, 1, 2, \ldots,$$

it can be shown that

$$\begin{aligned} R(\tau) &= R(\tau' + mT_s) \\ &= \frac{1}{T_s}\int_0^{T_s}\prod_{i=1-L}^{m+1}\left\{\frac{1}{M}\sum_{k=-M/2}^{M/2-1} e^{j2\pi h(2k+1)[q(t+\tau'-(i-m)T_s)-q(t-iT_s)]}dt\right\} \end{aligned}$$

so that the power spectrum takes the expression

$$\mathcal{G}(f) = 2\mathcal{R}\left\{\int_0^{LT_s} R(\tau)e^{-j2\pi f\tau}d\tau + \frac{e^{-j2\pi fLT_s}}{1-C_a e^{-j2\pi fT_s}}\int_0^{T_s} R(\tau+LT_s)e^{-j2\pi f\tau}d\tau\right\} \tag{2.14}$$

where

$$C_a = \frac{1}{M}\sum_{k=-M/2}^{M/2-1} e^{j\pi hk}. \tag{2.15}$$

To compute $R(\tau)$ effectively and accurately, we subdivide the integration interval $(0, T_s)$ into n subintervals, and use a 5-point Gaussian quadrature formula to compute the integral over each subinterval. The number n will be chosen to be large enough so as the limitation in accuracy comes from computational roundoff errors rather than from numerical approximations. After computing the autocorrelation function, the fast-Fourier transform algorithm is used to obtain the power density spectrum.

Power density spectra, in the form of fractional out-of-band power (in dB) were calculated for several different pulse shapes. The results for four

of them (namely, LREC, LRC, HCS, and CRC for $L = 1, 2, 3$, and 4) are shown in the next figures. Specifically, Fig. 2.1 shows the expressions for the frequency pulses in the four cases considered here. Fig. 2.2 shows the corresponding expressions for phase pulses. Frequency pulses and phase pulses are tabulated in Fig. 2.3 and Fig 2.4, respectively. Figs 2.5 to 2.12 show the fractional out-of-band powers.

LREC	0	$t \le 0$
	$\frac{t}{2LT}$	$0 \le t \le LT$
	$\frac{1}{2}$	$t \ge LT$
LRC	0	$t \le 0$
	$\frac{1}{2LT} - \frac{1}{4\pi}\sin\frac{2\pi t}{LT}$	$0 \le t \le LT$
	$\frac{1}{2}$	$t \ge LT$
HCS	0	$t \le 0$
	$\frac{1}{4} - \frac{1}{4}\cos\frac{\pi t}{LT}$	$0 \le t \le LT$
	$\frac{1}{2}$	$t \ge LT$
CRC	0	$t \le 0$
	$\frac{1}{LT}\left(\frac{t^2}{LT} - \frac{LT}{8\pi^2}\cos\frac{4\pi t}{LT} - \frac{LT}{8\pi^2}\right)$	$0 \le t \le \frac{LT}{2}$
	$\frac{1}{2} + \frac{1}{LT}\left(2t - \frac{t^2}{LT} - \frac{LT}{8\pi^2}\cos\frac{4\pi t}{LT} - \frac{LT}{8\pi^2}\right)$	$\frac{LT}{2} \le t \le LT$
	$\frac{1}{2}$	$t \ge LT$

Table A.2 q(t) for LREC, LRC, HCS, and CRC

Figure 2.2: Phase pulse $q(t)$ for LREC, LRC, HCS, and CRC.

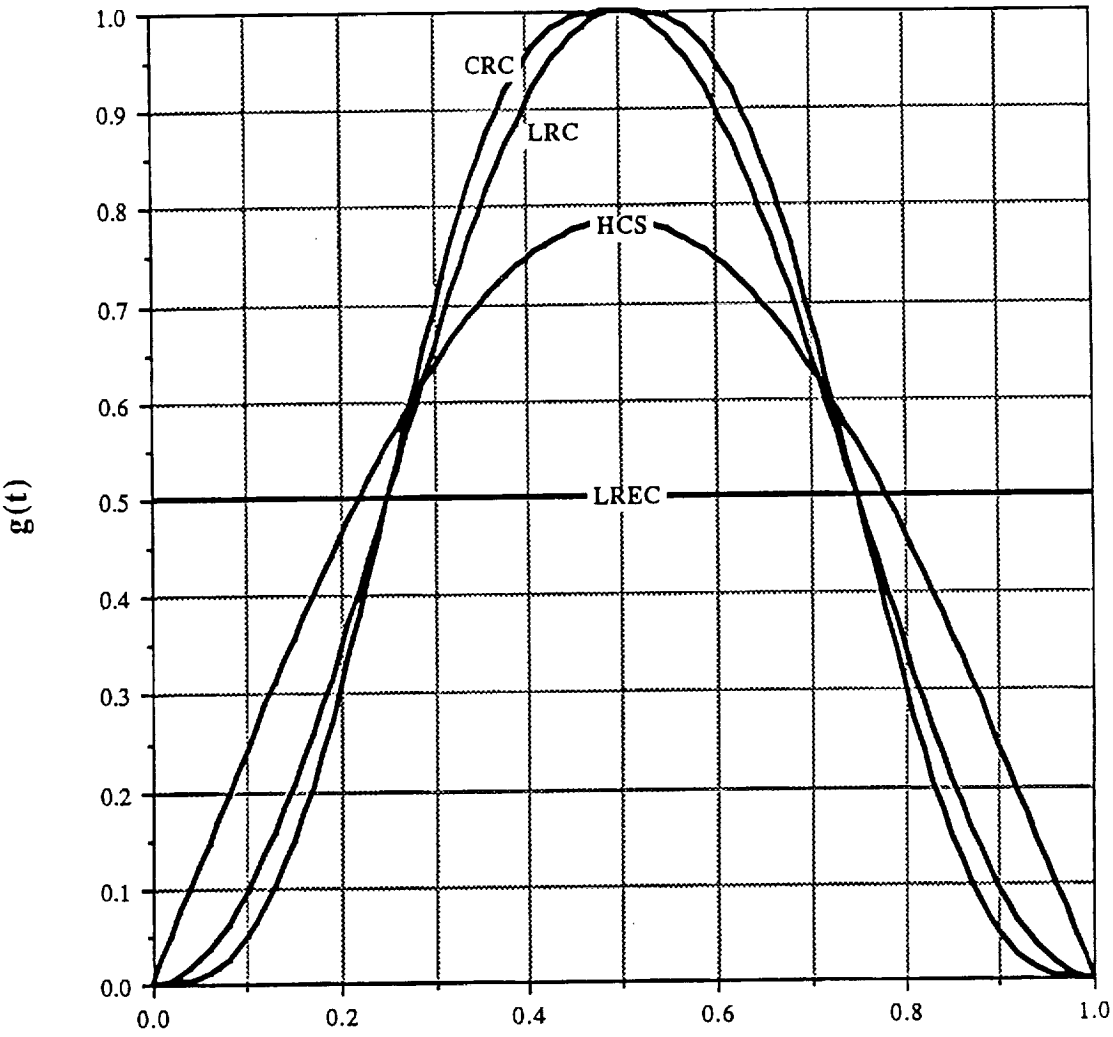

Figure 2.3: Frequency pulse $g(t)$ for LREC, LRC, HCS, and CRC.

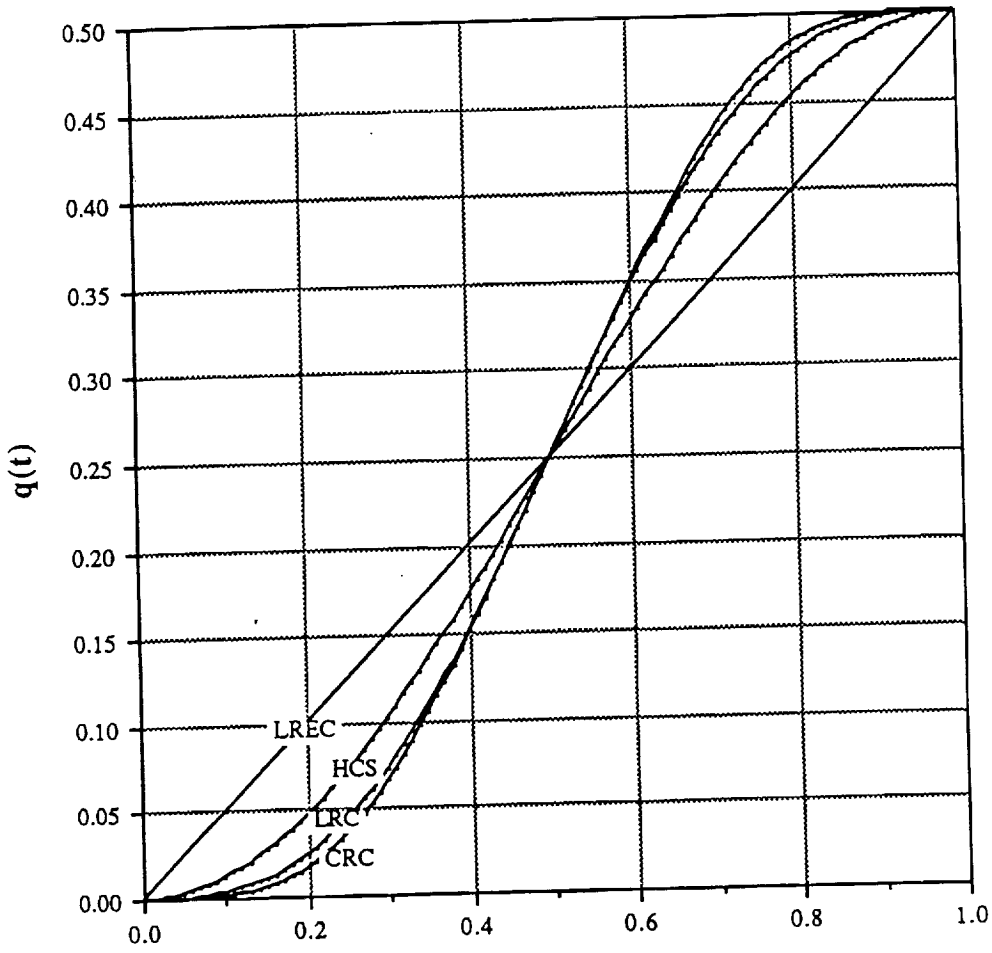

Figure 2.4: Phase pulse $g(t)$ for LREC, LRC, HCS, and CRC.

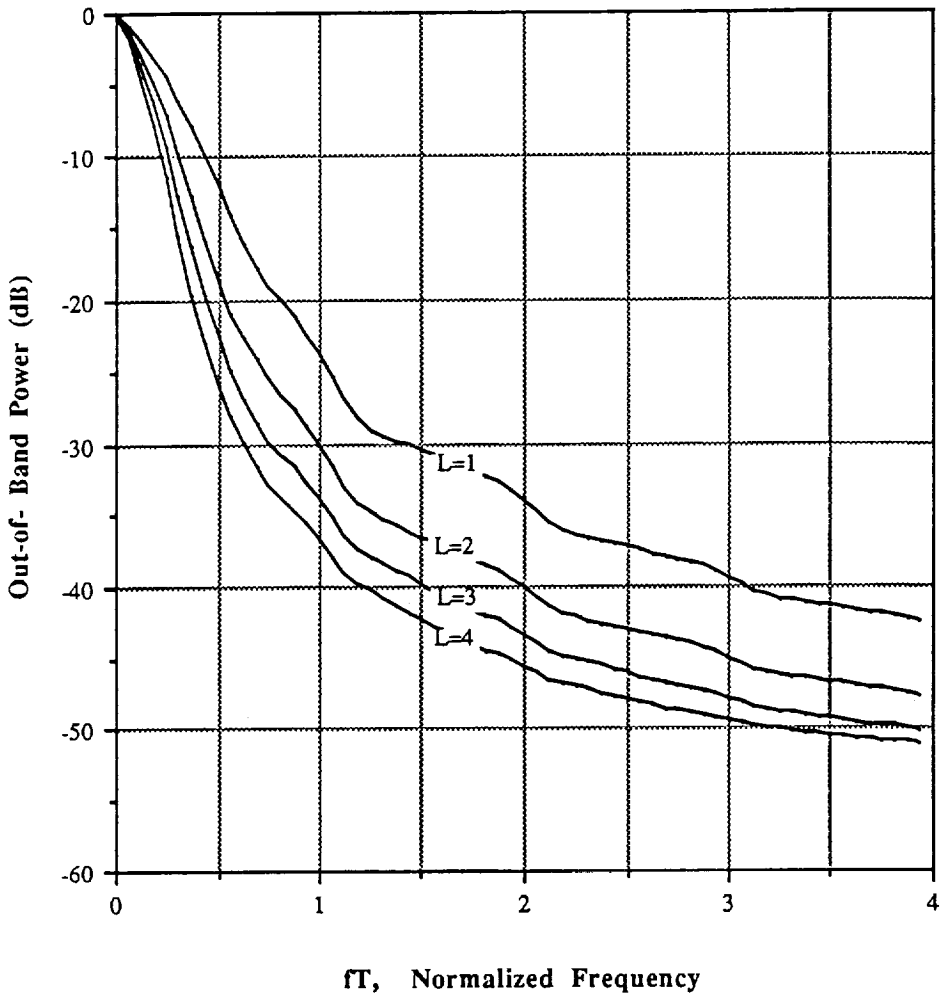

Figure 2.5: Fractional out-of-band power (in dB) of octonary CPM signals with modulation index $h = 1/8$ for LREC pulse shape, $L = 1, 2, 3, 4$.

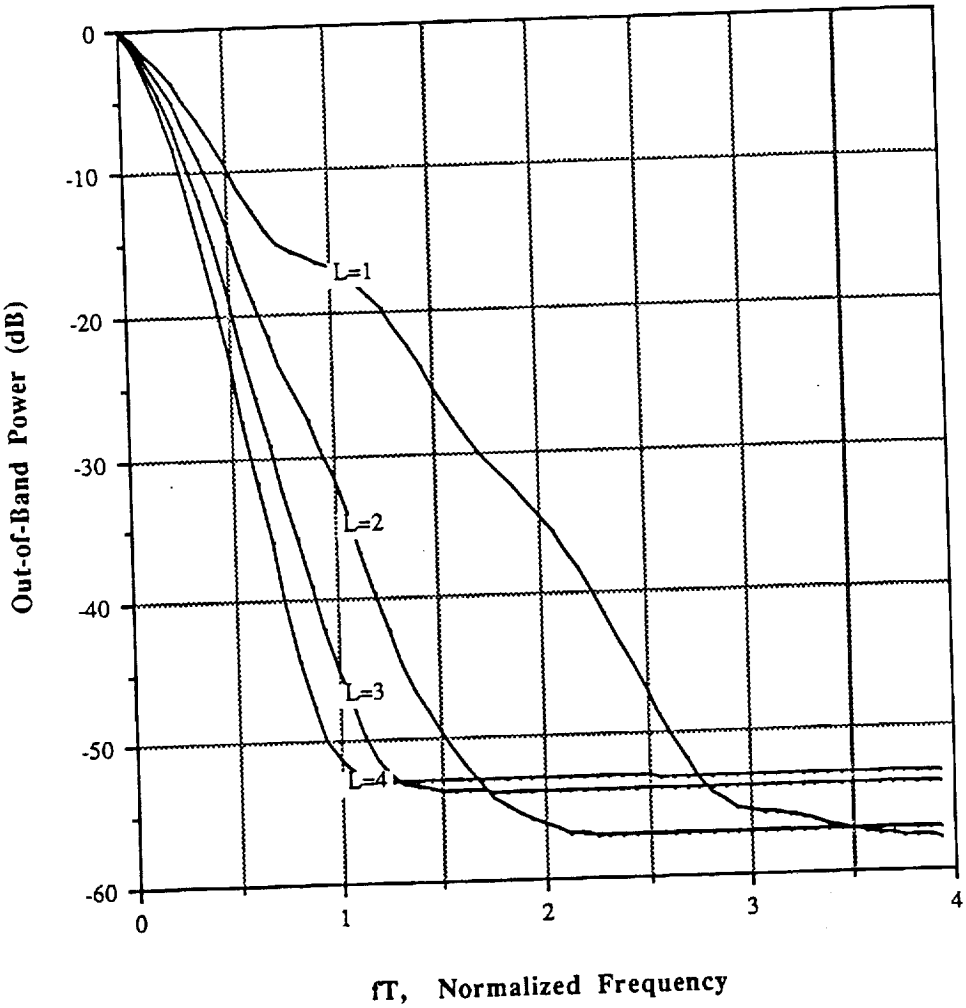

Figure 2.6: Fractional out-of-band power (in dB) of octonary CPM signals with modulation index $h = 1/8$ for LRC pulse shape, $L = 1, 2, 3, 4$.

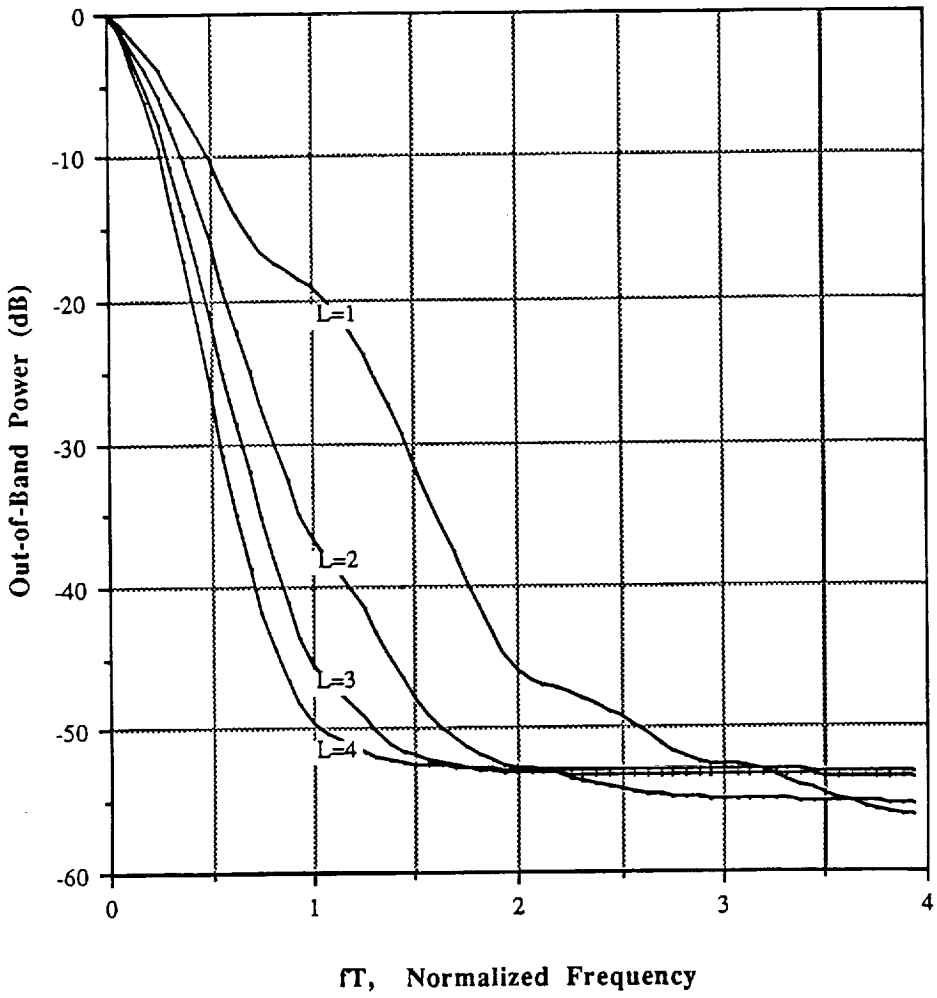

Figure 2.7: Fractional out-of-band power (in dB) of octonary CPM signals with modulation index $h = 1/8$ for HCS pulse shape, $L = 1, 2, 3, 4$.

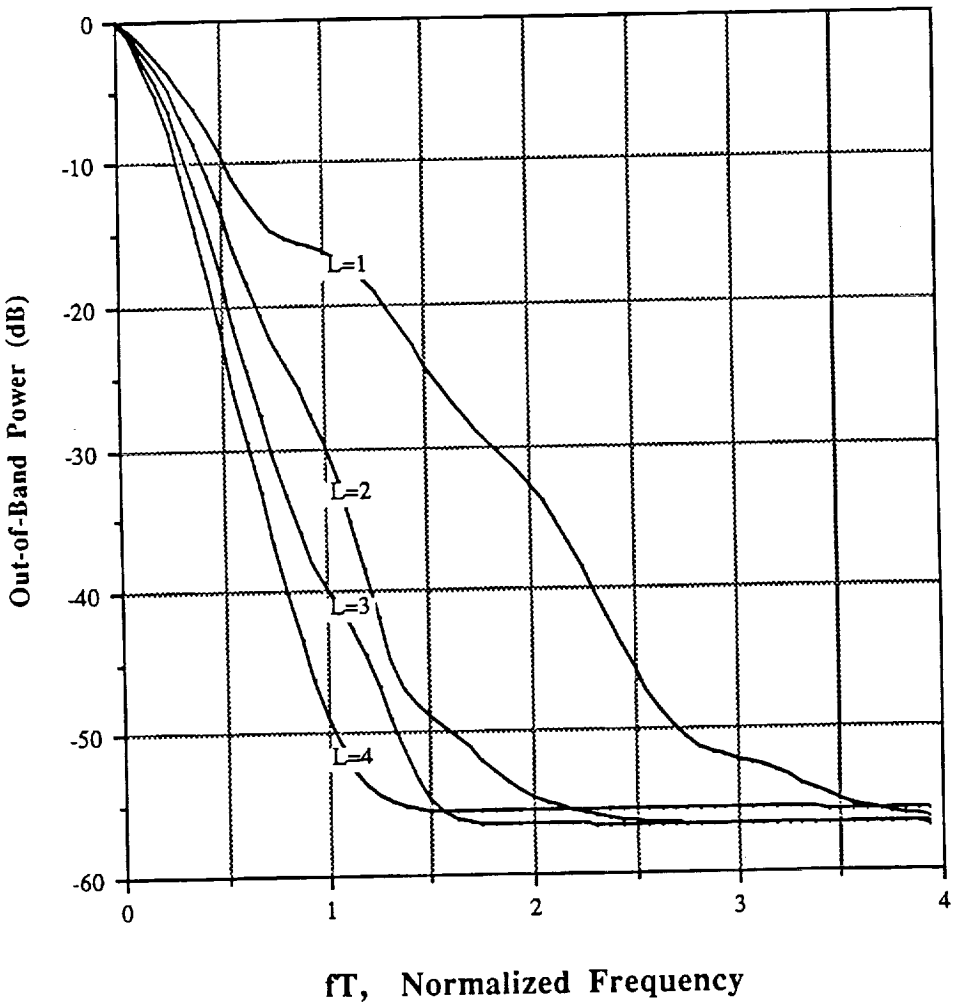

Figure 2.8: Fractional out-of-band power (in dB) of octonary CPM signals with modulation index $h = 1/8$ for CRC pulse shape, $L = 1, 2, 3, 4$.

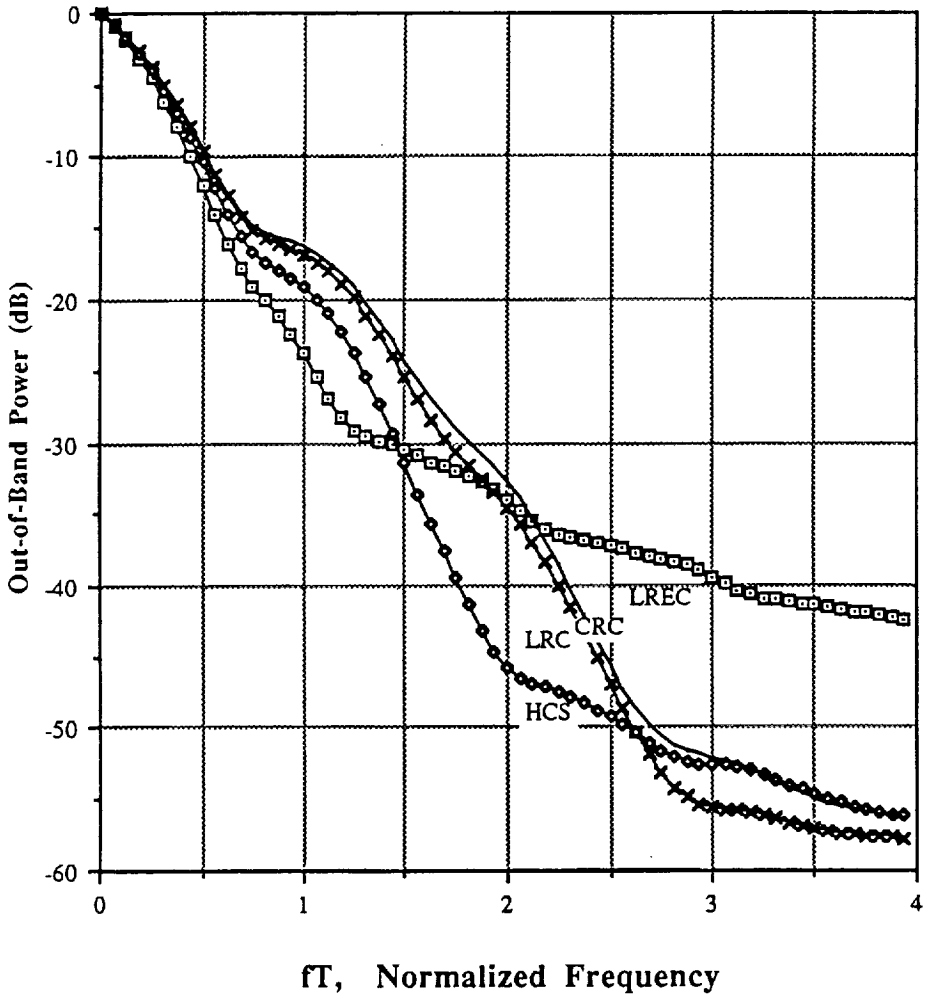

Figure 2.9: Comparison of fractional out-of-band power (in dB) of octonary CPM signals with modulation index $h = 1/8$ for different pulse shapes, $L = 1$.

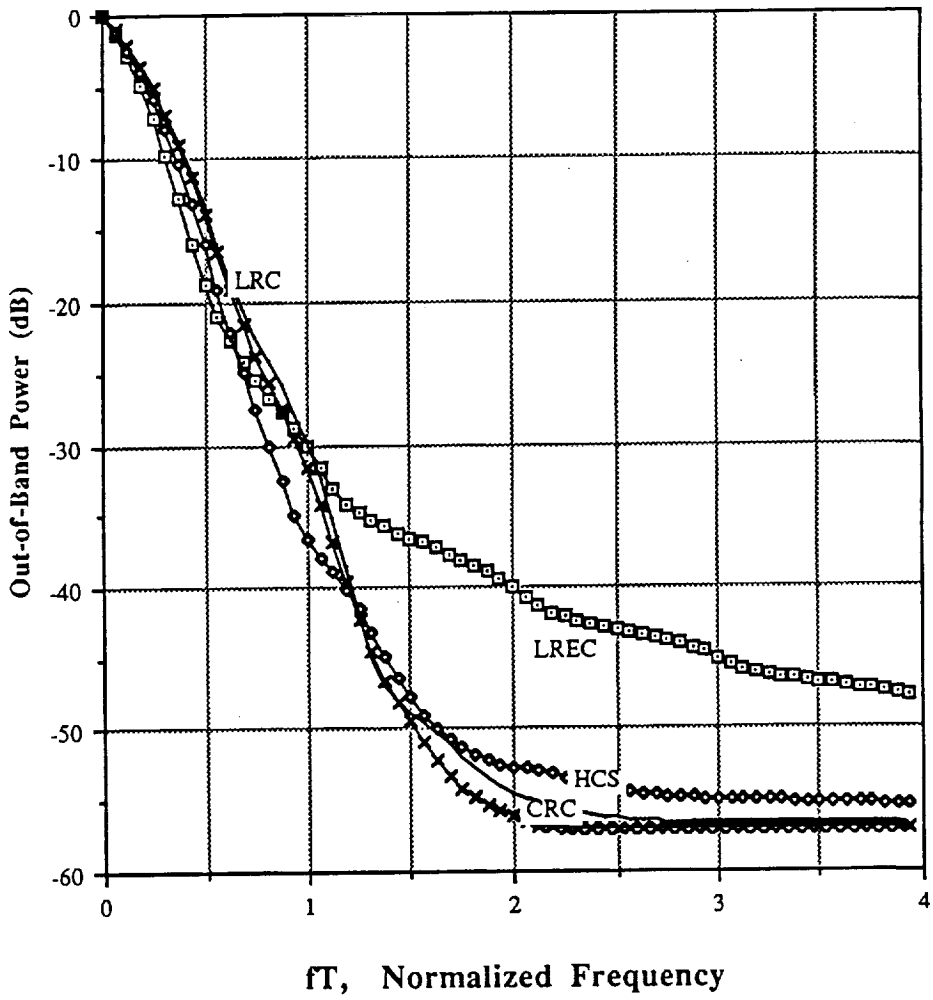

Figure 2.10: Comparison of fractional out-of-band power (in dB) of octonary CPM signals with modulation index $h = 1/8$ for different pulse shapes, $L = 2$.

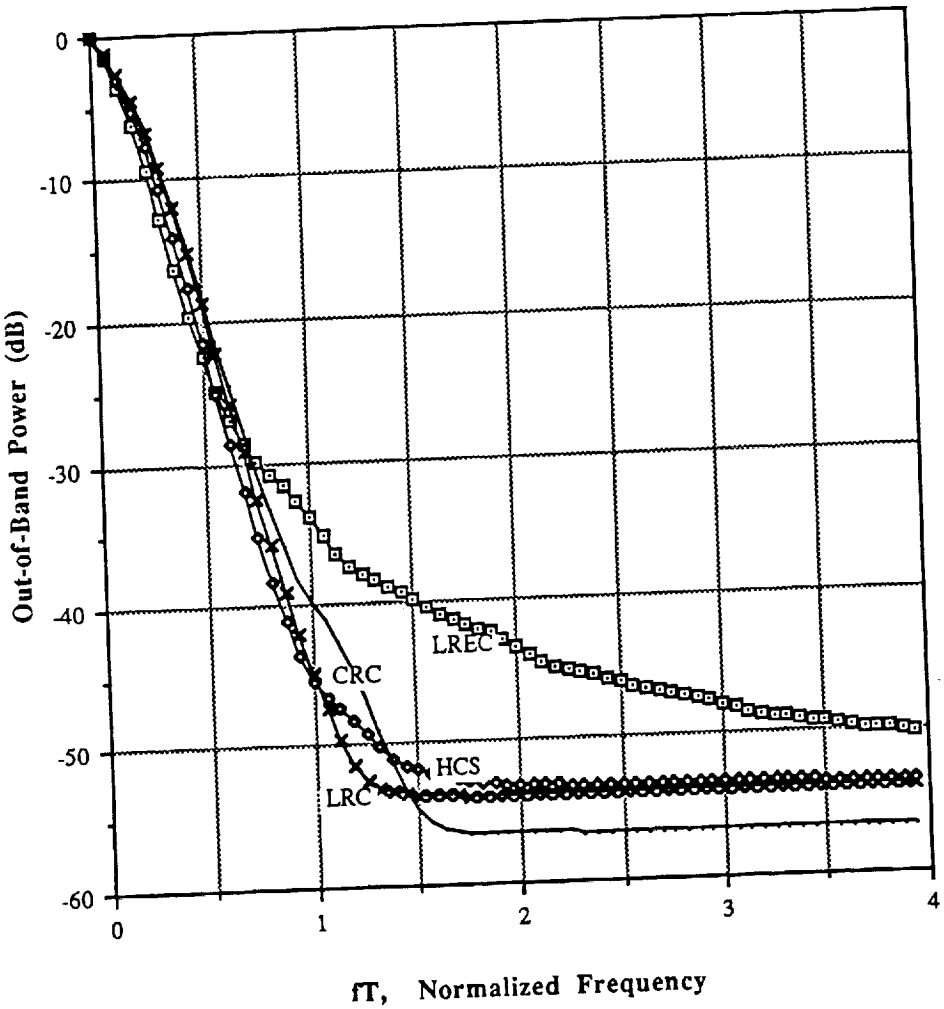

Figure 2.11: Comparison of fractional out-of-band power (in dB) of octonary CPM signals with modulation index $h = 1/8$ for different pulse shapes, $L = 3$.

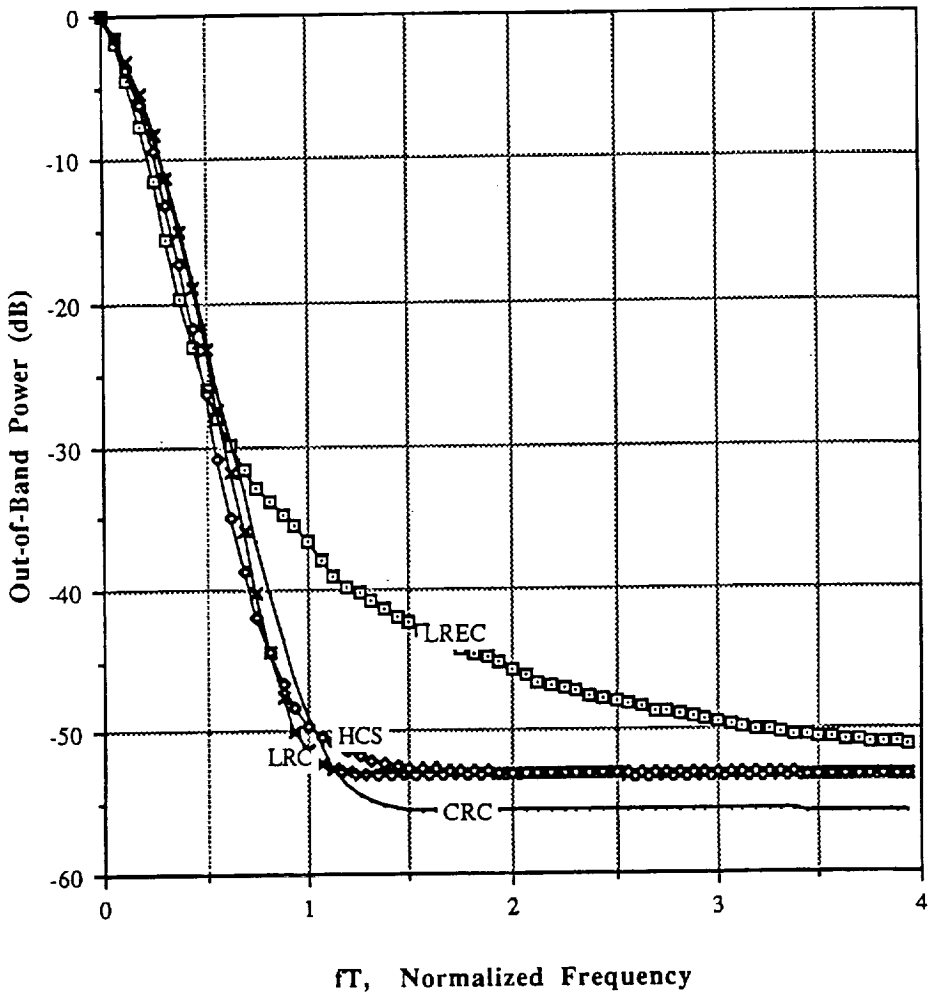

Figure 2.12: Comparison of fractional out-of-band power (in dB) of octonary CPM signals with modulation index $h = 1/8$ for different pulse shapes, $L = 4$.

Chapter 3

Trellis Coded Modulation (TCM)

In this Chapter, we present a review of the main features of trellis-coded modulation (TCM) as used for digital data communication with the purpose of gaining noise immunity over uncoded transmission without altering the data rate.

For the purpose of this discussion, we shall assume a discrete-time, continuous-amplitude model for the transmission of data on the additive white Gaussian noise channel. In this communication model, the messages to be delivered to the user are represented by vectors in an N-dimensional Euclidean space $\mathbf{R}^N$, called the *signal space*. When the vector $\mathbf{x}$ is transmitted, the received signal is represented by the vector

$$\mathbf{z} = \mathbf{x} + \mathbf{y},$$

where $\mathbf{y}$ is a noise vector whose components are independent Gaussian random variables with mean zero and the same variance $N_0/2$. The vector $\mathbf{x}$ is chosen from a set Ω consisting of M signal vectors and which will be referred to as the *signal constellation*. The average square length

$$\mathcal{E} = \frac{1}{M} \sum_{\mathbf{x} \in \Omega} |\mathbf{x}|^2$$

will be referred to as the average signal *energy*.

Consider now the transmission of a sequence $\{\mathbf{x}_i\}_{i=0}^{K-1}$ of K signal vectors, where the subscript i denotes discrete time. The receiver which minimizes the average error probability over the sequence operates as follows.

It first observes the received sequence $\mathbf{Z}_0, \ldots, \mathbf{Z}_{K-1}$, then it decides that $\mathbf{X}_0, \ldots, \mathbf{X}_{K-1}$ was transmitted if the squared Euclidean distance

$$d^2 = \sum_{i=0}^{K-1} |\mathbf{Z}_i - \mathbf{x}_i|^2 \tag{3.1}$$

is minimized for $\mathbf{x}_i = \mathbf{X}_i$, $i = 0, \ldots, K-1$. In words, the sequence $\mathbf{X}_0, \ldots, \mathbf{X}_{K-1}$ is closest to the received sequence than any other allowable signal vector sequence. The resulting sequence error probability, as well as the symbol error probability, are upper bounded, at least for high signal-to-noise ratios, by a decreasing function of the ratio $d^2_{\min}/N_0$, where $d^2_{\min}$ is the minimum squared Euclidean distance between two allowable signal vector sequences.

Uncoded Transmission

An important special case occurs when the signal vectors form an *independent* sequence. In this case, the allowable vector sequences are all the elements of Ω^K, and hence d^2 is minimized by minimizing separately the individual terms of (3.1), i.e., $|\mathbf{Z}_i - \mathbf{x}_i|^2$ for $\mathbf{x}_i \in \Omega$ and $i = 0, \ldots, K-1$. The performance of this "symbol-by-symbol receiver" will then depend on the minimum distance

$$d^2_{\min} = \min_{\mathbf{x}' \neq \mathbf{x}''} |\mathbf{x}' - \mathbf{x}''|^2$$

as $\mathbf{x}', \mathbf{x}''$ run through Ω. In fact, the symbol error probability is upper bounded (and for high signal-to-noise ratios well approximated) by

$$P(e) \leq \frac{M-1}{2} \operatorname{erfc}\left(\frac{d_{\min}}{2\sqrt{N_0}}\right) \tag{3.2}$$

(see, e.g., [58, page 152]).

With this model, the problem of designing an efficient communication system is that of choosing a set of vector signals such that the minimum distance between any two of them is a maximum, once the quantities M, N, and $\mathcal{E}$ are given. It is convenient to define two quantities that are useful in comparing different constellations, namely their *information rate* (measured in bits/dimension):

$$R = \frac{\log M}{N}, \tag{3.3}$$

and their *normalized squared minimum distance*

$$\delta^2 = \frac{d_{\min}^2}{\mathcal{E}} \log M. \tag{3.4}$$

The first parameter is also referred to as the "bandwidth efficiency", because it represents the ratio between the number of information bits carried by a single signal in the constellation and the number of dimensions, which is roughly proportional to the transmission bandwidth. The second parameter can be referred to as the "energy efficiency" of the signal constellation: in fact, observe that the upper bound (3.2) can be rewritten in the form

$$P(e) \leq \frac{M-1}{2} \operatorname{erfc}\left(\frac{\delta}{2}\sqrt{\frac{\mathcal{E}_b}{N_0}}\right), \tag{3.5}$$

where

$$\mathcal{E}_b = \frac{\mathcal{E}}{\log M}$$

represents the average energy per bit. It is seen from (3.5) that the same $P(e)$ can be achieved with a a smaller signal-to-noise ratio $\mathcal{E}_b/N_0$ if δ is larger.

3.1 The Concept of TCM

TCM is a *coded* system: this means that it tries to achieve an improvement of system performance by introducing a redundancy, i.e., an interdependency between signal vectors. This is equivalent to restricting the transmitted sequences to a subset of Ω^K. Now, if we do this, the transmission rate will also be reduced. To avoid this unwanted reduction, we may choose to increase the size of Ω. For example, if we change Ω into $\Omega' \supset \Omega$, and M into $M' > M$, and we select M^K sequences as a subset of Ω'^K, we can have sequences which are less tightly packed, and hence increase the minimum distance between them. In conclusion, we get a minimum distance d_{free} between two possible sequences which turns out to be greater than the minimum distance $d_{\min}$ between signals in Ω, the constellation from which they were drawn. Use of maximum-likelihood sequence detection will yield a "coding gain" $d_{\text{free}}^2/d_{\min}^2$, less the additional power necessary for signaling using the alphabet Ω' instead of Ω. We define the *energy gain* of a TCM scheme as

$$\gamma = \frac{d_{\text{free}}^2/\mathcal{E}'}{d_{\min}^2/\mathcal{E}},$$

where $\mathcal{E}$ and $\mathcal{E}'$ denote the average energies spent to transmit with uncoded and coded transmission, respectively.

The introduction of interdependencies between signals as a way of introducing the wanted redundancy into the sequence set is one of the basic ideas underlying trellis-coded modulation. (Another one is *set partitioning*, which will be described later).

We assume that the signal $\mathbf{x}_n$, transmitted at discrete time n, depends not only on the source symbol a_n transmitted at the same time instant (as it would be with memoryless modulation), but also on a finite number of previous source symbols:

$$\mathbf{x}_n = f(a_n, a_{n-1}, \cdots, a_{n-L}). \tag{3.6}$$

By defining

$$\sigma_n = (a_{n-1}, \cdots, a_{n-L}) \tag{3.7}$$

as the *state* of the encoder at time n, we can rewrite (3.6) in the more compact form

$$\mathbf{x}_n = f(a_n, \sigma_n) \tag{3.8}$$

$$\sigma_{n+1} = g(a_n, \sigma_n). \tag{3.9}$$

The last two equations can be interpreted as follows. The function $f(\cdot,\cdot)$ describes the fact that each channel signal depends not only on the corresponding source symbol but also on the parameter σ_n. In other words, at any time instant the transmitted signal is chosen from a constellation which is selected by the value of σ_n. The function $g(\cdot,\cdot)$ describes the *memory part* of the encoder and shows the evolution of the modulator states (see Fig. 3.1). Here we shall assume that the functions f and g are time-invariant, although it is possible to consider time-varying TCM schemes as well.

3.1.1 Trellis Representation

For a graphical representation of the functions f and g it is convenient to use a *trellis*. The values that can be taken by σ_n, the encoder state at time n, are the *nodes* of the trellis. With each source symbol we associate a branch which stems from each modulator state at time n, and reaches the encoder state at time $n+1$. The branch is labeled by the corresponding value of f. The trellis structure is determined by the function g, while f describes how channel signals are associated with each branch along the trellis.

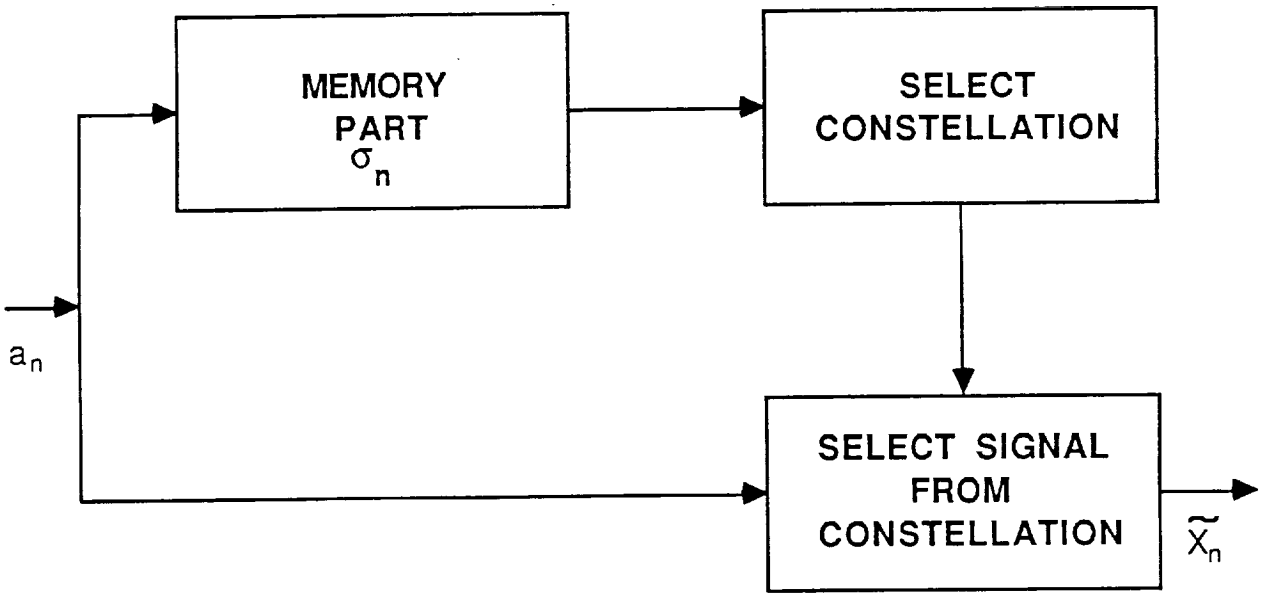

Figure 3.1: A general model for TCM

If the source symbols are M-ary, each node must have M branches stemming from it (one per source symbol). This implies that in some cases two or more branches connect the same pair of nodes: when this occurs, we say that *parallel transitions* take place.

Fig.3.2 shows an example of this representation. It is assumed that the encoder has four states, the source emits binary symbols, and a constellation with four signals 0,1,2,3 is used. The distance properties of a TCM scheme can be studied through its trellis diagram.

3.2 Some Examples of TCM Schemes

Here we describe a few examples of TCM schemes based on their trellis diagrams. We first consider the transmission of quaternary source symbols, i.e., 2 bits per symbol. With uncoded transmission a channel constellation with $M = 4$ would be adequate. We shall examine TCM schemes with $M' = 8$.

Let us assume M-ary coherent PSK transmission. With $M = 4$ we get

$$\frac{d^2_{\min}}{\mathcal{E}} = 2,$$

a figure which will be used as a reference to compute the coding gain of PSK-based TCM. We use TCM schemes based on two quaternary constellations $\{0, 2, 4, 6\}$ and $\{1, 3, 5, 7\}$ shown in Fig. 3.3. We have

$$\mathcal{E}' = \frac{d'^2}{4 \sin^2 \frac{\pi}{8}}.$$

Consider first a scheme with two states as shown in Fig. 3.4. If the encoder is in state S_1, constellation $\{0, 2, 4, 6\}$ is used. If it is in state S_2, constellation $\{1, 3, 5, 7\}$ is used instead. (Notice the presence of parallel transitions).

Let us compute the free distance of this scheme. This can be done by choosing the smallest between the distance among signals associated with parallel transitions, and the distance associated with a pair of paths in the trellis that originate from a common node and merge into a single node at a later time. The pair of paths giving the free distance is shown in Fig. 3.4, and we have, by denoting $d(i, j)$ the Euclidean distance between signals i and j:

$$\frac{d^2_{\text{free}}}{\mathcal{E}'} = \frac{1}{\mathcal{E}'}[d^2(0, 2) + d^2(0, 1)] = 2 + 4 \sin^2 \frac{\pi}{8} = 2.586.$$

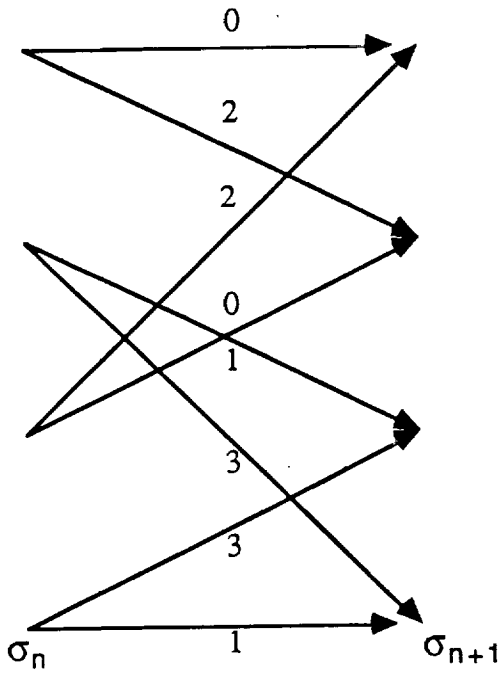

Figure 3.2: An example of trellis describing a TCM scheme with four states and four signals used to transmit from a binary source.

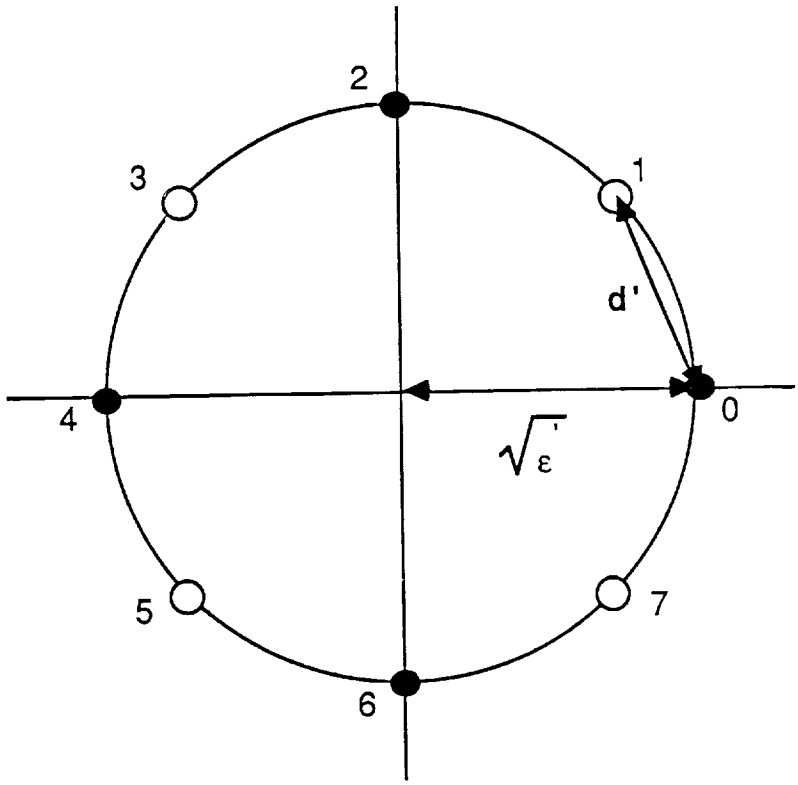

Figure 3.3: Two quaternary constellations used in a TCM scheme are $\{0, 2, 4, 6\}$ and $\{1, 3, 5, 7\}$.

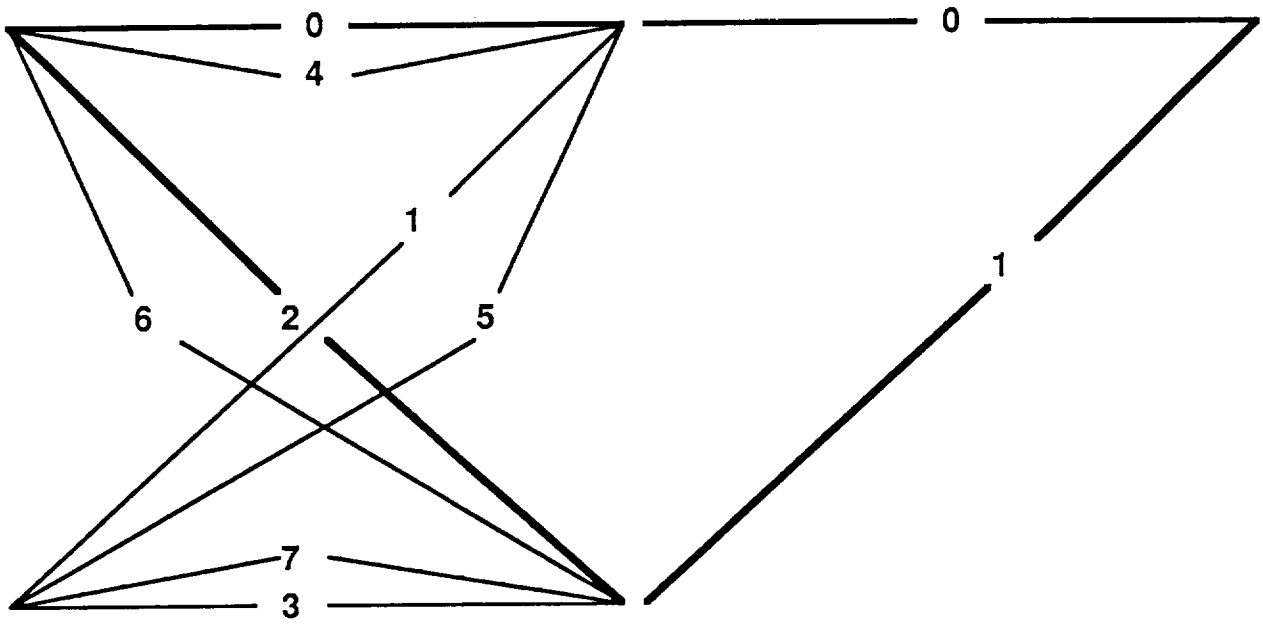

Figure 3.4: A TCM scheme based on a 2-state trellis, $M = 4$, and $M' = 8$

Hence, we get a coding gain

$$\gamma = \frac{2.586}{2} = 1.293 \Rightarrow 1.1 \text{ dB}.$$

Let us now use a TCM scheme with a more complex structure to increase the coding gain. With the same constellation of Fig. 3.3, take a trellis with 4 states as in Fig. 3.5. We associate the constellation $\{0, 2, 4, 6\}$ to states S_1 and S_3, and $\{1, 3, 5, 7\}$ to S_2 and S_4. The pair of paths giving d_{free} has length 1 (a parallel transition) and is shown in Fig. 3.5. We get

$$\frac{d^2_{\text{free}}}{\mathcal{E}'} = d^2(0, 4) = 4,$$

and hence

$$\gamma = \frac{4}{2} = 2 \Rightarrow 3 \text{ dB}.$$

A further step can be taken by choosing a trellis with 8 states as shown in Fig. 3.6. For simplicity, the four symbols associated with each node are used as node labels. The pair of paths leading to d_{free} is also shown and yields

$$\frac{d^2_{\text{free}}}{\mathcal{E}'} = \frac{1}{\mathcal{E}'}[d^2(0, 6) + d^2(0, 7) + d^2(0, 6)] = 2 + 4\sin^2\frac{\pi}{8} + 2 = 4.586,$$

and hence

$$\gamma = \frac{4.856}{2} = 2.293 \Rightarrow 3.6 \text{ dB}.$$

Consider now the transmission of 3 bits per symbol and AM-PM schemes. The octonary constellation

$$\{0, 2, 5, 7, 9, 10, 13, 15\}$$

of Fig. 3.7 will be used as a reference uncoded scheme. It yields

$$\frac{d^2_{\text{min}}}{\mathcal{E}} = 0.8.$$

A TCM scheme with 8 states and based on this alphabet is shown in Fig. 3.8. The subconstellations used are

$$\{0, 2, 5, 7, 9, 10, 13, 15\}$$

and

$$\{1, 3, 4, 6, 9, 11, 12, 14\}.$$

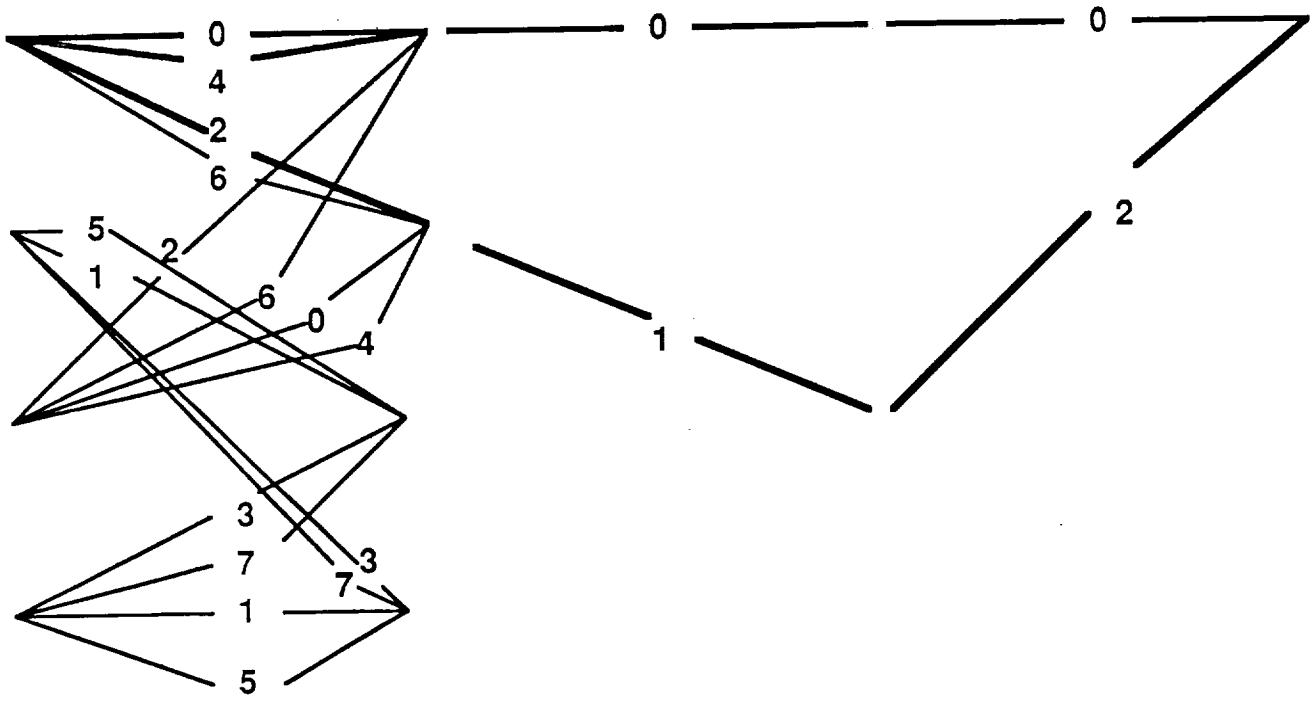

Figure 3.5: A TCM scheme based on a 4-state trellis, $M = 4$, and $M' = 8$

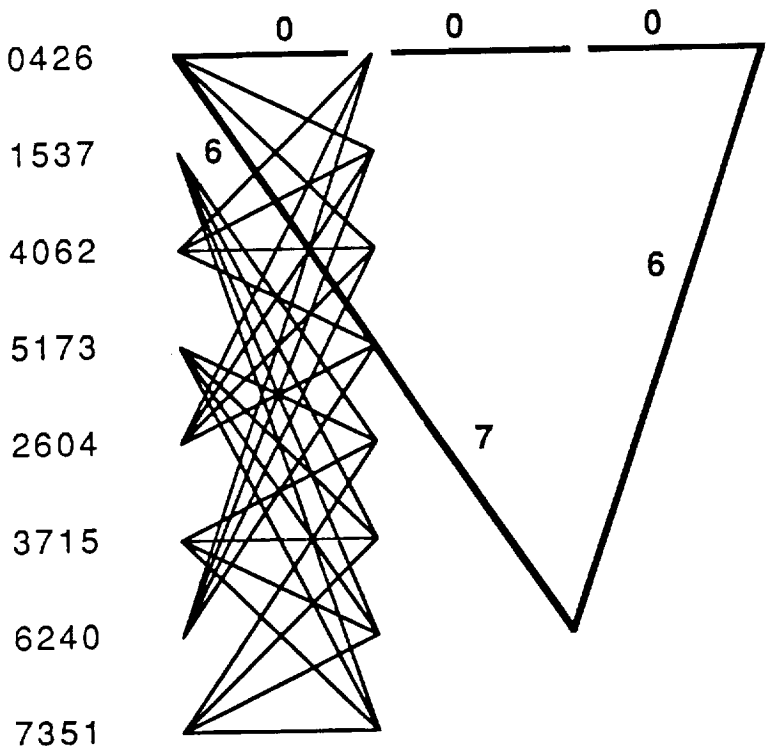

Figure 3.6: A TCM scheme based on an 8-state trellis, $M = 4$, and $M' = 8$

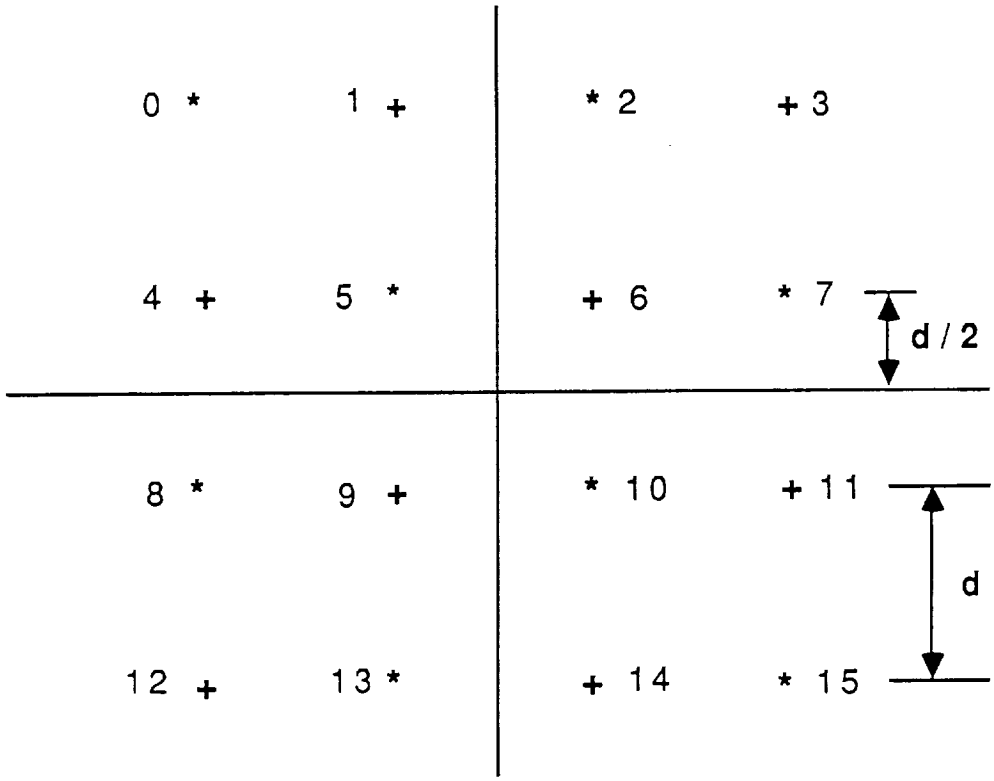

Figure 3.7: Two octonary AM-PM constellations.

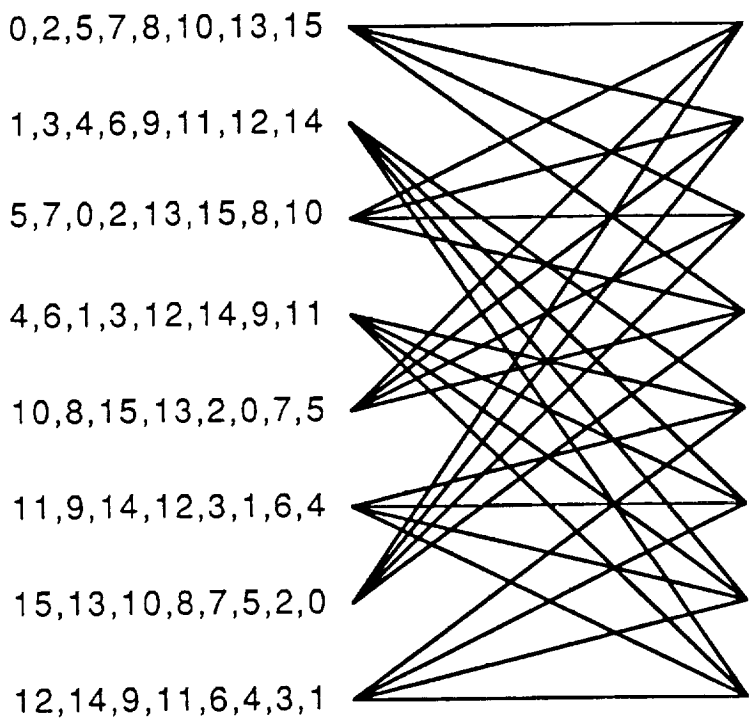

Figure 3.8: A TCM scheme based on an 8-state trellis and AM-PM constellations, with $M = 8$ and $M' = 16$

We get

$$\mathcal{E}' = 2.5\, d'^2.$$

We get

$$\begin{aligned}\frac{d^2_{\text{free}}}{\mathcal{E}'} &= \frac{1}{\mathcal{E}'}[d^2(10,13) + d^2(0,1) + d^2(0,5)] \\ &= \frac{1}{\mathcal{E}'}[0.8\mathcal{E}' + 0.4\mathcal{E}' + 0.8\mathcal{E}'] \\ &= 2\end{aligned}$$

and hence

$$\gamma = \frac{2}{0.8} = 2.5 \Rightarrow\ 3.98 \text{ dB}.$$

Set Partitioning

Consider the determination of d_{free}. This is the distance between the signals associated with a pair of paths that originate from an initial split, and, after L time instants, merge into a single node as shown in Fig. 3.9. Assume first that the free distance is determined by parallel transitions, i.e., $L = 1$. If A denotes the set of signals associated with a given node, then d_{free} equals the minimum distance among signals in A.

Consider then $L > 1$. With A, B, C, D denoting subset of signals associated with each branch, and $d(X, Y)$ denoting the minimum Euclidean distance between one signal in X and one in Y, d^2_{free} will have the expression

$$d^2_{\text{free}} = d^2(A, B) + \cdots + d^2(C, D).$$

This implies that, in a good code, the subsets assigned to the same originating state or to the same terminating state ("adjacent transitions") must have the largest possible distance. To implement these rules, the technique suggested by Ungerboeck [80] and called *set partitioning* is the following. Set partitioning has been described as "the key that cracked the problem of constructing efficient coded modulation techniques for band-limited channels."

The M'-ary constellation is successively partitioned into $2, 4, 8, \ldots$, subsets with size $M'/2, M'/4, M'/8, \ldots$, having progressively larger minimum distances $d^{(1)}_{\text{min}}, d^{(2)}_{\text{min}}, d^{(3)}_{\text{min}}, \ldots$ (see Fig.3.10). Then,

1. Parallel transitions are assigned members of the same partition.

2. Adjacent transitions are assigned members of the next larger partition.

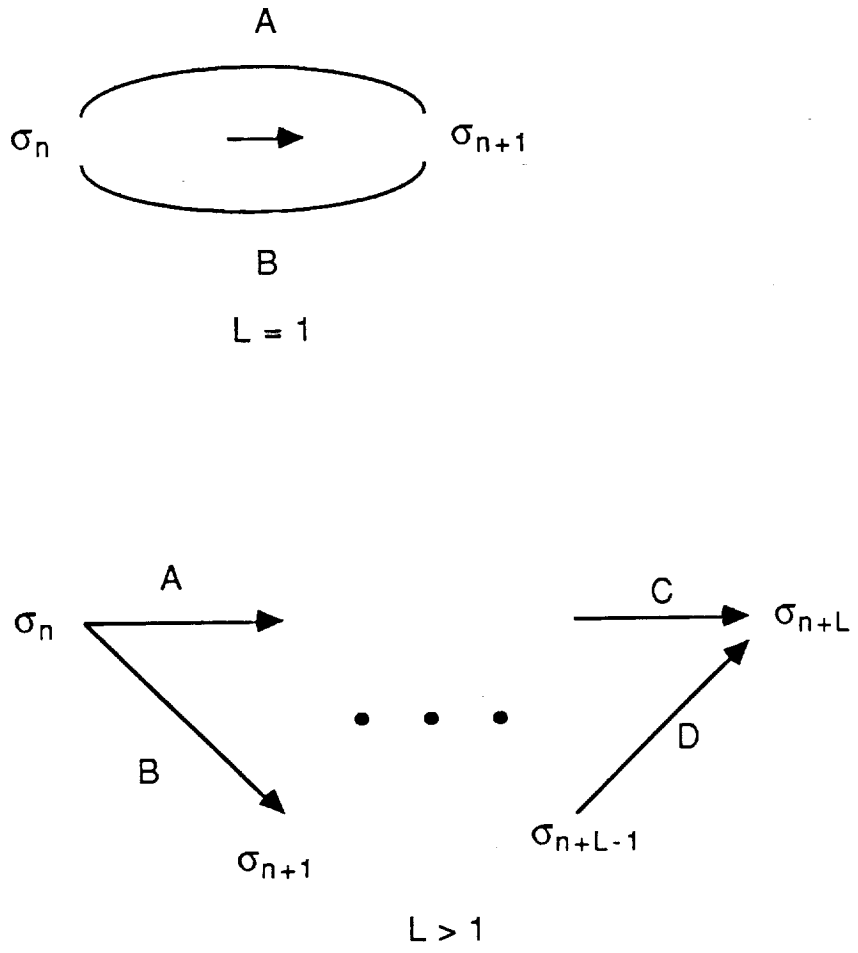

Figure 3.9: A pair of splitting and remerging paths for $L = 1$ (parallel transitions) and $L > 1$.

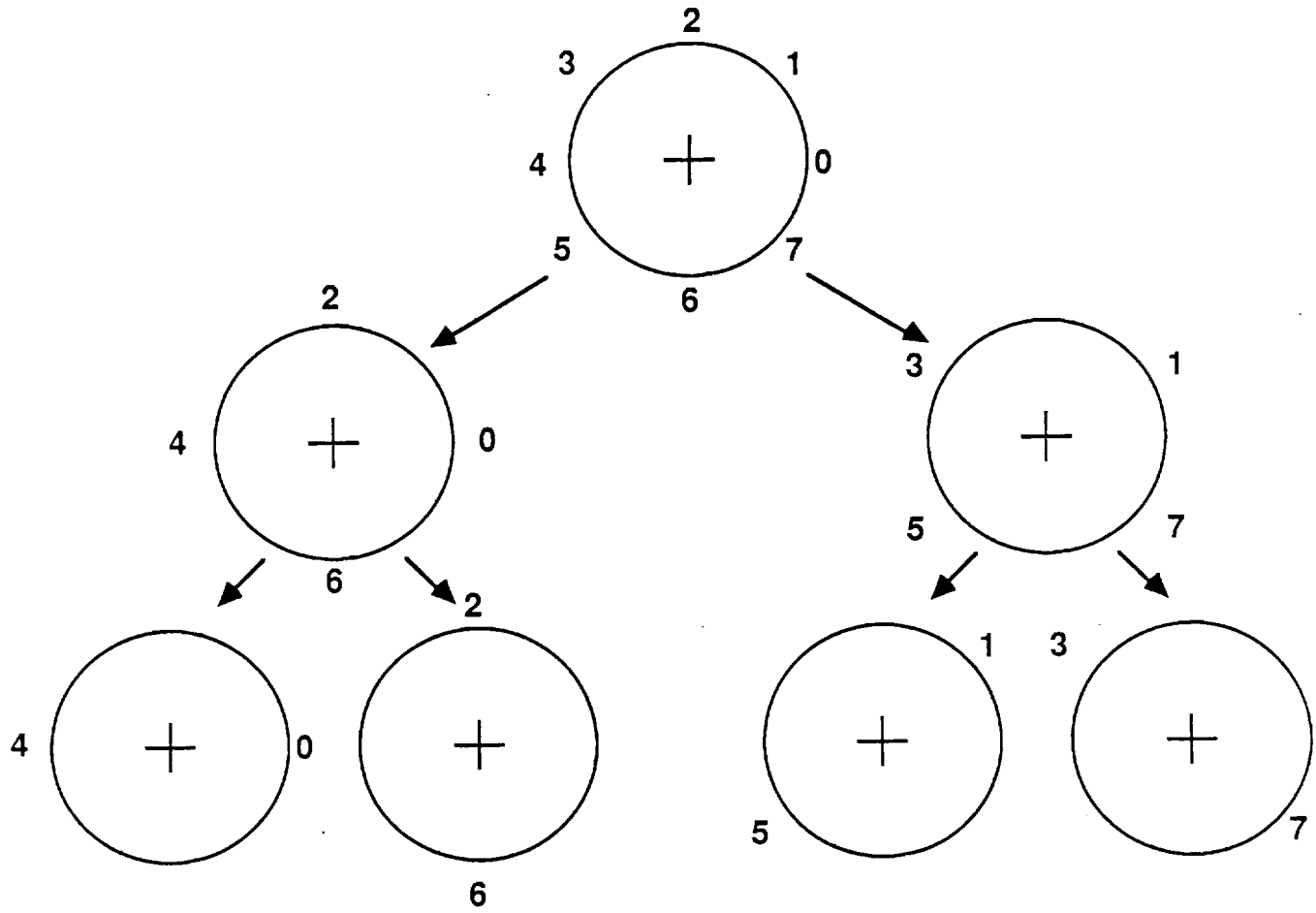

Figure 3.10: Set partition of an 8-PSK constellation.

3.3 Combining TCM With CPM

If CPM signals are combined with an external convolutional encoder, or equivalently they are used as the signal constellation to be used in a TCM scheme, a further improvement can be obtained. This new scheme is obtained by observing that at the output of the trellis encoder we get a multilevel signal which in turn can be used as the input to the continuous-phase modulator. The design of the coding scheme and of the modulator scheme should be performed jointly in order to maximize the Euclidean distance resulting from the combination of the two. As observed in [76], to maximize the Euclidean distance of the coding/modulation scheme, the trellis encoder should reduce the connectivity of its trellis in such a way that:

- The Euclidean distance between signals leaving the same state is maximized.
- The Euclidean distance merging into the same state is maximized.

To implement TCM/CPM, we may want to take advantage of both the bandwidth efficiency *and* the power efficiency of CPM codes. In this case, the receiver combines the trellis structure of TCM with that of CPM, and TCM and CPM can be integrated in a single entity (see [51] and the references therein). The number of states necessary for a trellis representation of these signals, and hence for their demodulation, is the product of the number of states needed by TCM and the number of states needed by CPM. Since this number can grow very large, a suboptimum solution should be sought, which trades a decrease in complexity for a decrease in power efficiency (but not in bandwidth efficiency). This is obtained by using a differential demodulator or a discriminator instead of a coherent receiver.

Chapter 4

Coherent vs. noncoherent CPM detection

To keep the demodulation problem separate from the decoding problem, we consider estimating the CPM phases symbol-by-symbol, and using these estimates to build up a metric for the decoder. Provided that the number of decoder states is finite and the metric chosen is additive, we can use a Viterbi algorithm for demodulation, the number of states being that related to the TCM scheme only. This procedure obviously entails a loss of optimality, which is traded against a manageable receiver structure. However, as mentioned before, the spectral properties of CPM are preserved.

In this Chapter we consider *coherent* and *noncoherent* symbol-by-symbol demodulation of CPM signals. Coherence can be achieved by taking advantage of the synchronization properties of CPM [38,62], although, as observed in [57,52], as the spectrum of the transmitted signal becomes narrower, the problem of finding the exact phase of the carrier increases. To avoid the problem of finding the phase of the carrier, one viable solution is the use of noncoherent detection.

Suboptimum coherent and noncoherent detection of CPM (in the special case of CPFSK) was considered in [48] for uncoded transmission. In this Chapter, consideration of suboptimum schemes involves the derivation of a *metric* to be used with the Viterbi decoder for TCM. Thus, the appropriate performance measure in our case is the cutoff rate R_0 [47] of the channel generated by CPM in conjunction with its detection scheme. The use of R_0 to demonstrate the efficiency of a coding scheme in the case of a fading channel, typical of mobile satellite and terrestrial mobile radio applications,

was advocated in [45].

The organization of this chapter is the following. We first summarize our signal and channel model. Symbol-by-symbol *coherent* detection of CPM is first examined, then *incoherent* detection is covered in Section 4. The Appendix reviews the basic steps involved in the computation of R_0 for fading channels.

4.1 Signal and channel models

The communication scheme considered in this section is shown in Fig. 4.1. The source data

$$\mathbf{u} = u_0, u_1, \cdots$$

are first sent into an encoder component, whose output is the symbol sequence

$$\mathbf{a} = a_0, a_1, \cdots$$

The encoder includes a conventional linear convolutional encoder with rate $m/(m+1)$, followed by an M-ary mapper. The convolutionally encoded output sequence consists of binary data symbols. The output of the mapper is the sequence $\mathbf{a}$ of M-ary symbols, generated according to some specific mapping rule. We assume that M is a power of 2, and that the symbols a_n take values $\pm 1, \pm 3, \cdots, \pm(M-1)$.

The coded sequence $\mathbf{a}$ is first interleaved (by using a block or convolutional interleaver [41, pp. 347-349]), to produce $\mathbf{a}'$. This new sequence is then sent to the continuous-phase modulator, which outputs a signal whose complex envelope is

$$s(t, \mathbf{a}', \phi_0) = \sqrt{\frac{2E_s}{T_s}} \exp j[\theta(t, \mathbf{a}') + \phi_0] \tag{4.1}$$

where ϕ_0 is the carrier phase, E_s is the signal energy per symbol, and T_s is the symbol time. The energy per bit is $E_b = E_s/\log_2 M$. The transmitted information is contained in the phase

$$\theta(t, \mathbf{a}') = 2\pi h \sum_{k=0}^{\kappa-1} a'_k q(t - kT_s) \tag{4.2}$$

with $q(t)$ the phase-shaping pulse given by $q(t) = \int_0^t g(\tau)d\tau$, and $g(t)$ is the frequency pulse with finite duration, i.e., $g(t)$ is nonzero only for $0 \leq t \leq$

LT_s, L the pulse length. The parameter h is called the *modulation index*, and we assume it to take on a rational value. The maximum phase change over a symbol interval is $\pi h(M-1)$.

A CPM scheme is defined by selecting the values of M, h, and the frequency pulse shape. Some of the most popular pulse shapes are LREC (for $L=1$ often referred to as Continuous-Phase Frequency Shift Keying, or CPFSK), Tamed Frequency Modulation (TFM), Raised Cosine (LRC), Half Cycle Sine (HSC), Convolved Raised Cosine (LCRC), Gaussian Minimum Shift Keying (GMSK), Spectrally Raised Cosine (LSRC). (For further details, see [55,58].) In this Chapter we consider Full Response (i.e., $L=1$) CPM.

In our analysis, we assume that the channel includes multipath reflections in addition to Gaussian noise. Thus, if $r(t)$ and $\nu(t)$ denote the signal observed at the channel output and a complex Gaussian noise process, respectively, we have

$$r(t) = \rho(t)s(t, \mathbf{a}', \phi_0) + \nu(t)$$

where it is assumed that $r(t)$ is observed during the time interval $(0, \kappa T_s)$, and $\rho(t)$ represents the (normalized) random fading amplitude. The probability density function of $\rho(t)$ depends on the model chosen for the fading process: we have

$$p(\rho) = 2\rho e^{-\rho^2}, \quad \rho \geq 0$$

for the *Rayleigh model*,

$$p(\rho) = 2\rho(1+K)e^{-K-\rho^2(1+K)}I_0(2\rho\sqrt{K(1+K)}), \quad \rho \geq 0$$

for the *Rician model*. In the latter expression, K denotes the ratio of power in the line-of-sight component to that in the diffuse or noncoherent component, and $I_0(\cdot)$ the modified Bessel function of order 0. Note that $\mathrm{E}[|\rho|^2] = 1$ for the Rayleigh and (unshadowed) Rician model. Note also that the Rayleigh fading model is the limiting case of the Rician model when $K = 0$.

4.1.1 Computation of R_0

Here we summarize the relevant steps in the derivation of the cutoff rate R_0 of the memoryless channel generated by CPM in conjunction with an interleaver/deinterleaver pair. Consider the transmitted codeword $\mathbf{x}_N$ with block length N. Let us assume that decoding is based on the observation of

the received N-tuple $\mathbf{r}_N$ and on the use of the additive metric

$$\mathbf{m}(\mathbf{r}_N, \mathbf{x}_N) = \sum_{i=1}^{N} m(r_i, x_i), \tag{4.3}$$

where r_i, x_i are the components of $\mathbf{r}_N$, $\mathbf{x}_N$, respectively. The decoding rule is then: choose $\hat{\mathbf{x}}_N$ if

$$\mathbf{m}(\mathbf{r}_N, \hat{\mathbf{x}}_N) = \max_{\mathbf{x}_N} \mathbf{m}(\mathbf{r}_N, \mathbf{x}_N).$$

In this situation, the pairwise error probability, i.e., the probability that $\hat{\mathbf{x}}_N \neq \mathbf{x}_N$ have a larger metric than the transmitted $\mathbf{x}_N$, can be bounded from above by using Chernoff bound. Under our assumption that the channel is memoryless, we have

$$\begin{aligned} P[\mathbf{x}_N \to \hat{\mathbf{x}}_N] &\leq \mathbf{E}\left\{ e^{\lambda \sum_{i=1}^{N} [m(r_i,\hat{x}) - m(r_i,x_i)]} \middle| \mathbf{x}_N \right\} \\ &= \prod_{i=1}^{N} \mathbf{E}\left\{ e^{\lambda [m(r_i,\hat{x}_i) - m(r_i,x_i)]} \middle| x_i \right\}. \end{aligned}$$

Now, define the quantity D_λ as follows:

$$e^{-D_\lambda(x,\hat{x})} = \mathbf{E}\left\{ e^{\lambda [m(r,\hat{x}) - m(r,x)]} \middle| x \right\}, \tag{4.4}$$

so that

$$P[\mathbf{x}_N \to \hat{\mathbf{x}}_N] \leq \prod_{i=1}^{N} e^{-D_\lambda(x_i,\hat{x}_i)}.$$

Next, apply a random coding argument. With the assumption that the code alphabet consists of M distinct signals, randomly select the $2N$ signals forming $\mathbf{x}_N$ and $\hat{\mathbf{x}}_N$, where each signal is independently selected with uniform probability. The *average* pairwise error bound is then

$$\begin{aligned} \overline{P[\mathbf{x}_N \to \hat{\mathbf{x}}_N]} &\leq \overline{\prod_{i=1}^{N} e^{-D_\lambda(x_i,\hat{x}_i)}} \\ &= \prod_{i=1}^{N} \overline{e^{-D_\lambda(x_i,\hat{x}_i)}} \\ &= \left[\overline{e^{-D_\lambda(x,\hat{x})}} \right]^N \\ &= 2^{-R_0(\lambda)N} \end{aligned}$$

where we have defined

$$R_0(\lambda) = -\log_2 \overline{e^{-D_\lambda(x,\hat{x})}}, \tag{4.5}$$

and the random coding average has the explicit expression

$$\overline{e^{-D_\lambda(x,\hat{x})}} = \frac{1}{M^2} \sum_x \sum_{\hat{x}} e^{-D_\lambda(x,\hat{x})}. \tag{4.6}$$

The value of λ should be chosen in order to minimize the Chernoff bound, i.e., to maximize $R_0(\lambda)$. If this is not feasible, a suboptimum bound will be obtained.

Fading channel

With a channel affected only by additive complex white Gaussian noise n with two-sided power spectral density $2N_0$) and fading (represented by a random variable ρ), if perfect state information is assumed we may use the metric

$$m(r, x) = - \| r - \rho x \|^2,$$

where $r = \rho x + n$. In this case, by observing that for a complex Gaussian random variable n with mean zero, variance $2N_0$ and independent real and imaginary parts we have

$$\mathbf{E}[e^{\alpha n}] = e^{|\alpha|^2 N_0/2},$$

a simple calculation shows that, by choosing for λ its optimum value $1/4N_0$,

$$e^{-D_{1/4N_0}(x,\hat{x})} = \mathbf{E}\left\{ e^{-\frac{1}{8N_0}\rho^2 \|x-\hat{x}\|^2} \right\},$$

where the expectation is taken with respect to the random variable ρ representing the fading effect. We get the expression

$$R_0 = -\log_2 \left\{ \frac{1}{M^2} \sum_x \sum_{\hat{x}} \mathbf{E}\left[e^{-\frac{1}{8N_0}\rho^2 \|x-\hat{x}\|^2} \right] \right\}. \tag{4.7}$$

4.2 Suboptimum coherent detection

The detection problem is as follows. The optimum (maximum likelihood sequence) detector must find the sequence of source symbols **u** which is

mapped into the sequence $\mathbf{a}'$ that maximizes the likelihood function

$$\begin{aligned}\Lambda[r(t)|\mathbf{a}', \rho(t), \phi_0] &= \exp\left\{-\frac{1}{N_0}\int_0^{\kappa T_s} |r(t) - \rho(t)s(t, \mathbf{a}', \phi_0)|^2 dt\right\} \\ &= \exp\left\{-\frac{1}{N_0} \parallel r(t) - \rho(t)s(t, \mathbf{a}', \phi_0) \parallel^2 dt\right\}.\end{aligned}$$

Now, let us divide the total observation interval into κ subintervals of duration T_s seconds each. Then we can write

$$\parallel r(t) - \rho(t)s(t, \mathbf{a}', \phi_0) \parallel^2 = \sum_{k=0}^{\kappa-1} \parallel r_k - \rho_k s(a'_k, \phi_k, \phi_0) \parallel^2 .$$

The time dependence has been omitted for simplicity, r_k and ρ_k denote $r(t)$ and $\rho(t)$ in the interval $(kT_s, (k+1)T_s)$, and, in the same time interval,

$$s(a'_k, \phi_k, \phi_0) = \sqrt{\frac{2E_s}{T_s}} \exp j[2\pi h a'_k q(t - kT_s) + \phi_k + \phi_0], \qquad (4.8)$$

where

$$\phi_k = \pi h \sum_{n=0}^{k-1} a'_n, \quad k = 1, \ldots, \kappa, \qquad (4.9)$$

is the value of the phase accumulated up to the k-th time interval. The latter is also called the "phase state" of the CPM signal.

If we assume that the receiver achieves perfect coherence, the value of ϕ_0 is known, and hence, without loss of generality, we shall assign it the value 0 and exclude it from consideration as well as from our notations. Disregard, for a moment, the interleaver/deinterleaver pair. In this situation, optimum coherent detection of the received sequence would be obtained by using in the TCM detector the additive metric

$$m[r(t), s(t, \mathbf{a}')] = \sum_{k=0}^{\kappa-1} \parallel r_k - \rho_k s(a'_k, \phi_k) \parallel^2 .$$

In the Viterbi-algorithm parlance this corresponds to associating the branch metric $\parallel r_k - \rho_k s(a'_k, \phi_k) \parallel^2$ with the trellis branches corresponding to the transmitted symbol a'_k. Now, it is apparent that the metric values depend on ϕ_k as well, i.e., on the state of the CPM modulator when the signal $s(a'_k, \phi_k)$ was transmitted. To take this fact into account, we should expand the TCM trellis. Let us denote by S_{TCM} the number of TCM states and

by S_{CPM} the number of CPM states. The latter is equal to the number of distinct values (mod 2π) of the accumulated phases, i.e., if $h = p/q$ is the modulation index, with p and q relatively prime integers, equal to either q (if p is even) or $2q$ (if p is odd) [58, p. 169]. Then every state in the original TCM trellis must be transformed into S_{CPM} states, one for each value of ϕ_k. The resulting "product trellis" has $S_{\mathrm{TCM}}S_{\mathrm{CPM}}$ states, and this is the number that determines the computational complexity of the "single-approach" Viterbi algorithm.

To avoid this state growth and to be able to perform interleaving/de-interleaving (which is feasible only if we separate the operations of CPM demodulator and TCM decoder), we should get rid of the term ϕ_k, possibly by using non-coherent or differential detection (see, e.g., [36]). Here we consider a coherent scheme, based on the following idea. The CPM signal is sent to an optimum coherent detector, based on the Viterbi algorithm and which outputs only the sequence of states, i.e., the values of the sequence ϕ_k. These phases are then removed from the received signal, which turns out to be, in the interval $(kT_s, (k+1)T_s)$,

$$r(t) = \sqrt{\frac{2E_s}{T_s}} \exp ja'_k q(t - kT_s) + \nu(t).$$

After deinterleaving, the original order of the sequence **a** is restored, and hence the metrics $\| r_k - \rho_k s(a_k) \|^2$ can be sent to the TCM decoder. To be able to analyze this receiver, we shall make the simplifying assumption that the sequence of states ϕ_k is delivered to the TCM decoder without errors.[1]

With this receiver structure, we generate (see Fig. 4.1) an equivalent discrete-time, discrete-input, continuous-output channel, whose inputs are the TCM encoded symbols a_n and whose output is a sequence of quantities used to compute the metrics to be associated with the symbols a_n. This channel should resemble a memoryless channel (due to the ideal interleaving/deinterleaving process) perturbed by additive noise and independent fading. Notice that with this transmission scheme the design of the TCM scheme is simplified, because we may take advantage of the wide set of results available on the design of TCM schemes for these channels [44].

[1]This assumption is similar to the standard assumption usually accepted in the study of coherent detection systems, i.e., that the carrier phase recovery system operates with zero error. In both cases this is not realistic, since it implies an infinite signal-to-noise ratio, and hence zero error probability. Consequently, the results that follow should be interpreted as *bounds* to the performance of any real-life system.

4.2.1 Computation of R_0

Given a transmission channel to be used for coding, a suitable one-parameter characterization of its coding capabilities is provided by the cutoff rate R_0 created by the modulation system [47]. In fact, although no formal proof is available, it is widely believed that R_0 is the rate beyond which it becomes very expensive to communicate reliably over a channel.

The computation of R_0 is described in the Appendix. For the AWGN channel without fading, (4.7) specializes to

$$R_0 = 2\log_2 M - \log_2 \left[M + \sum_{i=1}^{M} \sum_{\substack{j=1 \\ j \neq i}}^{M} e^{-\| s(2i-M-1) - s(2j-M-1) \|^2 / 8N_0} \right]. \quad (4.10)$$

where in our case

$$\begin{aligned} \| s(2i-M-1) - s(2j-M-1) \|^2 &= \frac{2E_s}{T_s} \int_0^{T_s} \| e^{j2\pi h(2i-M-1)q(t)} - e^{j2\pi h(2j-M-1)q(t)} \|^2 \, dt \\ &= \frac{2E_s}{T_s} \left[2T_s - 2\int_0^{T_s} \cos 4\pi h(i-j) q(t) dt \right]. \end{aligned}$$

For example, in CPFSK we have

$$q(t) = \frac{t}{2T_s},$$

and hence

$$\| s(2i-1) - s(2j-1) \|^2 = 4E_s \left[1 - \frac{\sin 2\pi h(i-j)}{2\pi h(i-j)} \right].$$

The 1RC phase pulse is defined as

$$q(t) = \frac{t}{2T_s} - \frac{1}{4\pi} \sin 2\pi \frac{t}{T_s},$$

and the distances $\| s(2i-1) - s(2j-1) \|$ can be evaluated by numerical integration. The corresponding values of R_0 are plotted, along with R_0 for coherent PSK, in Fig. 4.2 for $M = 8$ and in Fig. 4.3 for $M = 16$. It is noticed that for low values of the modulation index h (i.e., small spectrum occupancy) PSK has a larger R_0, due to its better distance properties (which are traded for the better spectral properties of CPM).

When fading is present and perfect state information [64] is available, (4.7) becomes

$$R_0 = 2\log_2 M - \log_2 \left(M + \sum_{i=1}^{M} \sum_{\substack{j=1 \\ j\neq i}}^{M} \mathbf{E}_\rho \left\{ e^{-\rho^2 \| s(2i-1) - s(2j-1) \|^2 / 8N_0} \right\} \right). \tag{4.11}$$

Now, by using the results of [64], we obtain, for a Rician channel,

$$\mathbf{E}[\exp -\rho^2 \beta_{ij}] = \frac{1+K}{1+K+\beta_{ij}} \exp - \frac{\beta_{ij} K}{1+K+\beta_{ij}}, \tag{4.12}$$

while for a Rayleigh channel

$$\mathbf{E}[\exp -\rho^2 \beta_{ij}] = \frac{1}{1+\beta_{ij}}. \tag{4.13}$$

By substituting

$$\beta_{ij} = \frac{1}{8N_0} \| s(2i-1) - s(2j-1) \|^2 \tag{4.14}$$

in (4.11), we get the desired expression for R_0. The corresponding values of R_0 are plotted in Fig. 4.4 for $M = 8$ and Fig. 4.5 for $M = 16$.

Fig. 4.6 shows the effect over R_0 of the selection of the modulation index h. If trellis-coded modulation, based on an $m/(m+1)$ convolutional code, $m = \log_2 M - 1$, is to be used in conjunction with M-ary CPM, we are interested in the signal-to-noise ratio necessary to achieve a value of R_0 equal to $\log_2 M - 1$, the actual number of information bits carried by each T_s-second signal. This value is plotted versus h for octonary CPFSK. It is seen that the lowest values of E_b/N_0, and hence the most power-efficient coding channel, is generated for higher values of h. This fact can be explained by observing that higher modulation indices correspond to larger phase fluctuations in the transmitted waveforms, which means that the waveforms are more easily distinguishable. On the other hand, larger values of h imply a broader power density spectrum, so that the trade-off is between spectrum occupancy and power efficiency. This is illustrated in Fig. 4.7, which shows the out-of-band power of 1RC-CPM as a function of the modulation index. It may also be observed that for large h the power efficiency of CPFSK can be greater than that of PSK.

Figure 4.8 shows, for $M = 8$ and $h = 1/4$, a comparison between R_0 associated with optimum and suboptimum coherent detection of CPFSK. It is seen that for $R_0 = 2$ suboptimum detection causes a loss in signal-to-noise ratio of about 2 dB.

4.3 Suboptimum noncoherent detection

As noted before, to avoid the state growth caused by optimum detection and in order to be able to perform interleaving/deinterleaving, we must get rid of the term $\phi_k + \phi_0$ appearing in (4.8). Here we do this by considering *noncoherent* symbol-by-symbol demodulation of CPM signals.

4.3.1 Computation of R_0

Let us define the quantities

$$\lambda_i = \int_{iT_s}^{(i+1)T_s} r(t)s^*(t, a_i')dt \tag{4.15}$$

and

$$\hat{\lambda}_i = \int_{iT_s}^{(i+1)T_s} r(t)s^*(t, \hat{a}_i')dt. \tag{4.16}$$

These quantities, for given values of the fading variable and of the transmitted symbol a_i', are complex-valued Gaussian random variables. Since we assuming perfect interleaving, the sequence $\{\lambda_i\}$ is an independent, identically distributed sequence.

We assume here the following noncoherent detection rule: choose the symbol sequence $\{\hat{a}_i'\}$ if

$$\sum_i |\hat{\lambda}_i|^2 = \max \sum_i |\lambda_i|^2, \tag{4.17}$$

where the maximum is taken over all the possible sequences $\{a_i\}$.

The pairwise error probability $P[\mathbf{a}' \to \hat{\mathbf{a}}']$ that the detector chooses $\hat{\mathbf{a}}' \neq \mathbf{a}'$ when it is known that either $\hat{\mathbf{a}}'$ or $\mathbf{a}'$ was transmitted may be upper bounded by using the Chernoff bound:

$$P[\mathbf{a}' \to \hat{\mathbf{a}}'|\rho\ ] \leq \min_\xi \mathbf{E}\left\{\exp(-\xi[\sum_i |\lambda_i|^2 - \sum_i |\hat{\lambda}_i|^2])|\rho\ , \mathbf{a}'\right\} \tag{4.18}$$

$$= \min_\xi \prod_i \mathbf{E}\left\{\exp(-\xi[|\lambda_i|^2 - |\hat{\lambda}_i|^2])|\rho_i, a_i'\right\} \tag{4.19}$$

$$= \min_\xi \prod_i \mathbf{E}\left\{e^{\xi\gamma_i}|\rho_i, \gamma_i\right\}, \tag{4.20}$$

where ξ is the Chernoff bound parameter (to be optimized to get the tightest possible bound) and

$$\gamma_i = |\hat{\lambda}_i|^2 - |\lambda_i|^2. \tag{4.21}$$

The actual computation of the Chernoff bound requires the calculation of the expectation $\mathbf{E}$ over γ_i, i.e., over the pair of complex random variables $\hat{\lambda}_i, \lambda_i$. Let $\mathbf{z}_i$ denote the following Gaussian random vector:

$$\mathbf{z}_i = [\hat{\lambda}_i, \lambda_i],$$

so that we can write

$$\gamma_i = |\hat{\lambda}_i|^2 - |\lambda_i|^2 = \hat{\lambda}_i \hat{\lambda}_i^* - \lambda_i \lambda_i^* = \mathbf{z}_i^* \mathbf{A} \mathbf{z}_i^T \tag{4.22}$$

where

$$\mathbf{A} = \begin{bmatrix} 1 & 0 \\ 0 & -1 \end{bmatrix},$$

and the superscript T denote transpose. Thus, the computation of the Chernoff bound is based on the evaluation of an average of the form

$$\mathbf{E}\left\{\exp \xi \mathbf{z}^* \mathbf{A} \mathbf{z}^T | \rho, a'\right\} = \int \exp \xi \mathbf{z}^* \mathbf{A} \mathbf{z}^T f_{\mathbf{z}}(\mathbf{z}|\rho, a') d\mathbf{z} \tag{4.23}$$

where $f_{\mathbf{z}}(\mathbf{z}|\rho, a')$ denotes the conditional Gaussian probability density function

$$f_{\mathbf{z}}(\mathbf{z}|\rho, a') = \frac{1}{(2\pi)^2 |\mathbf{Q}|} \exp\{-\frac{1}{2}[\mathbf{z} - \bar{\mathbf{z}}]^* \mathbf{Q}^{-1} [\mathbf{z} - \bar{\mathbf{z}}]^T\} \tag{4.24}$$

with $\mathbf{Q}$ the conditional covariance matrix

$$\mathbf{Q} = \frac{1}{2}\mathbf{E}\left[\exp\left\{[\mathbf{z} - \bar{\mathbf{z}}]^* [\mathbf{z} - \bar{\mathbf{z}}]^T\right\} | \rho, a\right] \tag{4.25}$$

and $\bar{\mathbf{z}} = \mathbf{E}[\mathbf{z}|\rho, a']$. Explicitly, we must compute the integral

$$\frac{1}{(2\pi)^2 |\mathbf{Q}|} \int \exp\{\xi \mathbf{z}^* \mathbf{A} \mathbf{z}^T - \frac{1}{2}[\mathbf{z} - \bar{\mathbf{z}}]^* \mathbf{Q}^{-1} [\mathbf{z} - \bar{\mathbf{z}}]^T\} d\mathbf{z}. \tag{4.26}$$

After a certain amount of algebra, we find

$$\mathbf{E}\left\{\exp[\xi \mathbf{z}^* \mathbf{A} \mathbf{z}^T] | \rho, a'\right\} = \frac{|\mathbf{H}|}{|\mathbf{Q}|} e^{\mathbf{B}}, \tag{4.27}$$

where

$$\mathbf{B} = -\frac{1}{2} \bar{\mathbf{z}}^* \mathbf{Q}^{-1} [\mathbf{I} - (\mathbf{I} - 2\xi \mathbf{Q} \mathbf{A})^{-1}] \bar{\mathbf{z}}^T \tag{4.28}$$

and

$$\frac{|\mathbf{H}|}{|\mathbf{Q}|} = \frac{1}{|\mathbf{I} - 2\xi \mathbf{Q} \mathbf{A}|}, \tag{4.29}$$

so that, in conclusion,

$$P[\mathbf{a}' \to \hat{\mathbf{a}}'|\rho\ ] \leq \min_{\xi} \prod_i \frac{\exp\{-\frac{1}{2}\bar{\mathbf{z}}_i^* \mathbf{Q}_i^{-1}[\mathbf{I} - (\mathbf{I} - 2\xi\mathbf{A})^{-1}]\}\bar{\mathbf{z}}_i^T}{|\mathbf{I} - 2\xi\mathbf{Q}_i\mathbf{A}|}. \tag{4.30}$$

We now determine the entries of the covariance matrix $\mathbf{Q}_i$. Under the assumption that the noise is white and complex with power spectral density $2N_0$ we obtain

$$\mathbf{Q}_i = 2N_0E_s \begin{bmatrix} 1 & \Delta_i \\ \Delta_i^* & 1 \end{bmatrix} \tag{4.31}$$

where we define

$$\Delta_i = \frac{1}{T_s}\int_{iT_s}^{(i+1)T_s} \exp[j2\pi h(a_i' - \hat{a}_i')q(t - iT_s)]dt \tag{4.32}$$

and E_s is the average signal energy in a T_s-second interval.

We also have

$$\bar{\mathbf{z}}_i = 2\rho_i E_s[\Delta_i\ ,\ 1], \tag{4.33}$$

and

$$\begin{aligned} |\mathbf{I} - 2\xi\mathbf{Q}_i\mathbf{A}| &= \det \begin{bmatrix} 1-\lambda & \Delta_i\lambda \\ -\Delta_i^*\lambda & 1+\lambda \end{bmatrix} \\ &= 1 - \lambda^2\mu_i \end{aligned}$$

where

$$\lambda = 4\xi N_0 E_s$$

and

$$\mu_i = 1 - |\Delta_i|^2.$$

After some further lengthy but straightforward computations, we finally obtain

$$P[\mathbf{a}' \to \hat{\mathbf{a}}'|\ \rho\ ] \leq \min_{\lambda} \prod_i \frac{1}{1-\lambda^2\mu_i} \exp[-\frac{E_s}{N_0}\frac{\rho_i^2(\lambda - \lambda^2)\mu_i}{1-\lambda^2\mu_i}]. \tag{4.34}$$

It can be easily proved that, under the constraint

$$0 < \lambda < 1,$$

the exponent of the right-hand side of (4.34) is always negative, as it should be to provide a meaningful bound.

By using a result in [64], we observe that, for a Rician channel,

$$\mathbf{E}[\exp -\rho^2\beta] = \frac{1+K}{1+K+\beta}\exp -\frac{\beta K}{1+K+\beta},$$

while for a Rayleigh channel, as $K = 0$,

$$\mathbf{E}[\exp -\rho^2\beta] = \frac{1}{1+\beta}.$$

Thus, by substituting

$$\beta = \frac{E_s}{N_0}\frac{(\lambda-\lambda^2)\mu_i}{1-\lambda^2\mu_i}$$

in (4.34), we obtain, for any $\lambda \in (0,1)$,

$$P[\mathbf{a}' \to \hat{\mathbf{a}}'] \leq \prod_i \frac{1+K}{(1-\lambda^2\mu_i)(1+K)+\frac{E_s}{N_0}(\lambda-\lambda^2)\mu_i} \exp\left\{-\frac{\frac{E_s}{N_0}(\lambda-\lambda^2)\mu_i K}{(1-\lambda^2\mu_i)(1+K)+\frac{E_s}{N_0}(\lambda-\lambda^2)\mu_i}\right\}$$

for Rician fading, while for Rayleigh fading we find

$$P[\mathbf{a}' \to \hat{\mathbf{a}}'] \leq \prod_i \frac{1}{(1-\lambda^2\mu_i)+\frac{E_s}{N_0}(\lambda-\lambda^2)\mu_i}. \tag{4.35}$$

The corresponding values of R_0 are plotted in Fig. 4.9 to 4.12, where λ was chosen equal to 0.5, a value which was found optimum or near optimum in most cases. Fig. 4.13 shows the effect over R_0 of the selection of the modulation index h. The signal-to-noise ratio necessary to achieve a value of R_0 equal to $\log_2 M - 1$ is plotted versus h for octonary CPFSK. As for coherent detection, the lowest values of E_b/N_0, and hence the most power-efficient coding channel, correspond to higher values of h.

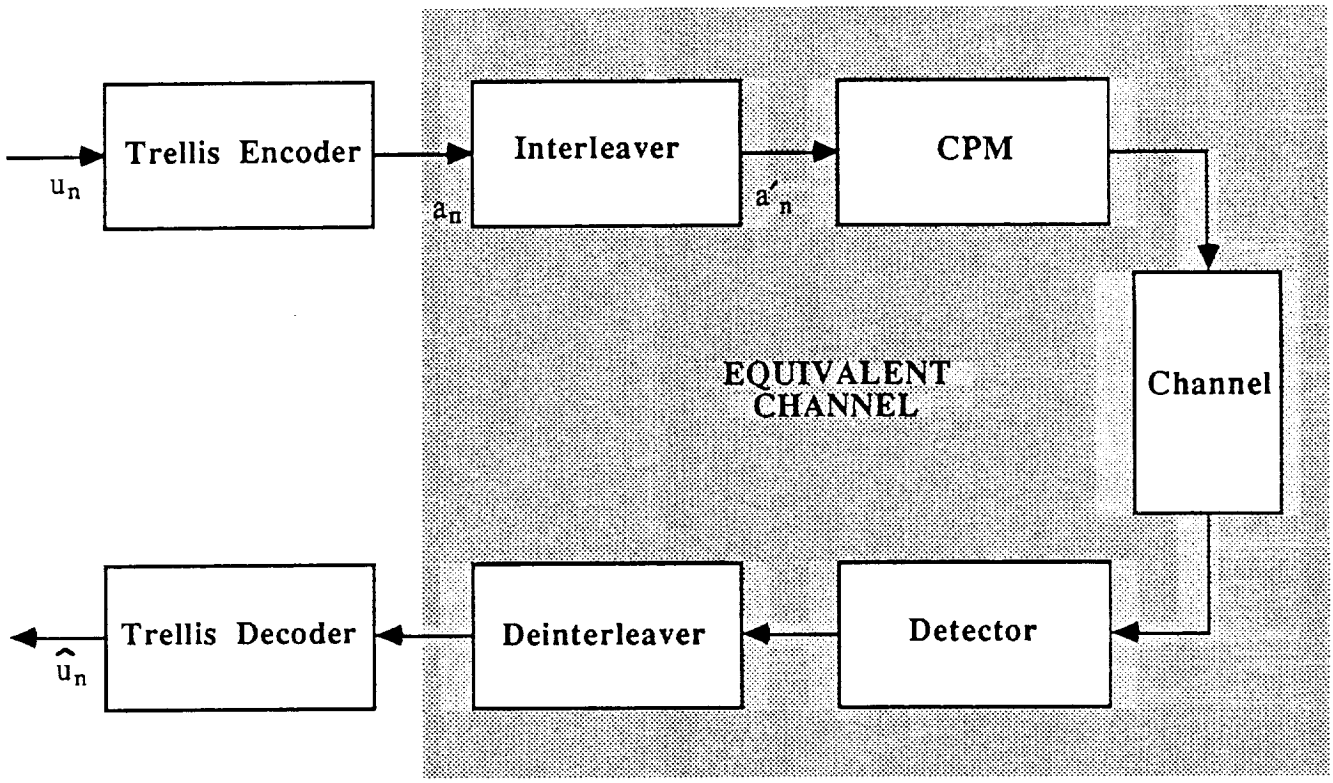

Figure 4.1: Block diagram of the transmission system.

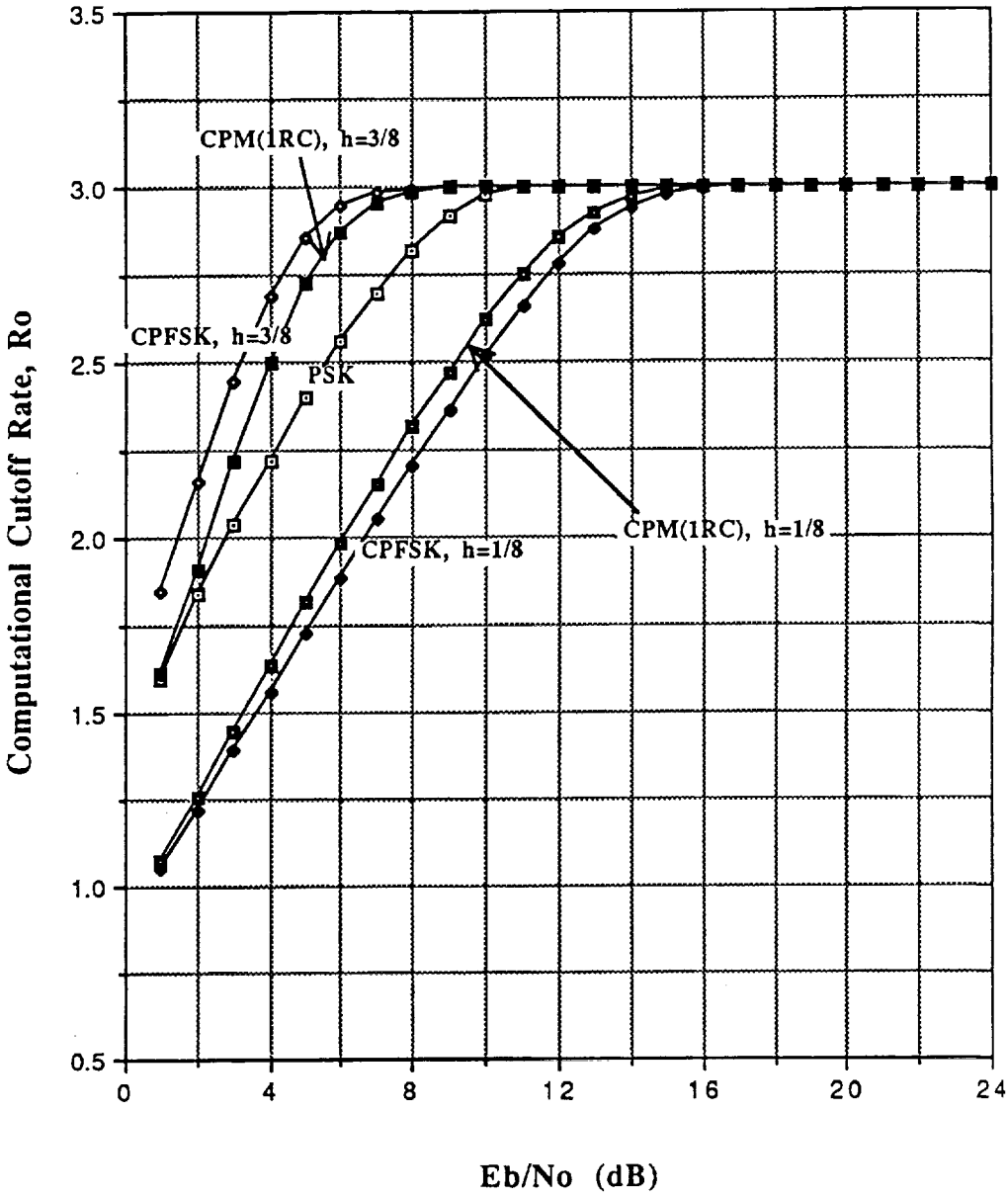

Figure 4.2: Comparison of cutoff rate R_0 of coherent octonary PSK, 1RC-CPM and CPFSK with coherent, symbol-by-symbol detection and additive, white Gaussian noise channel.

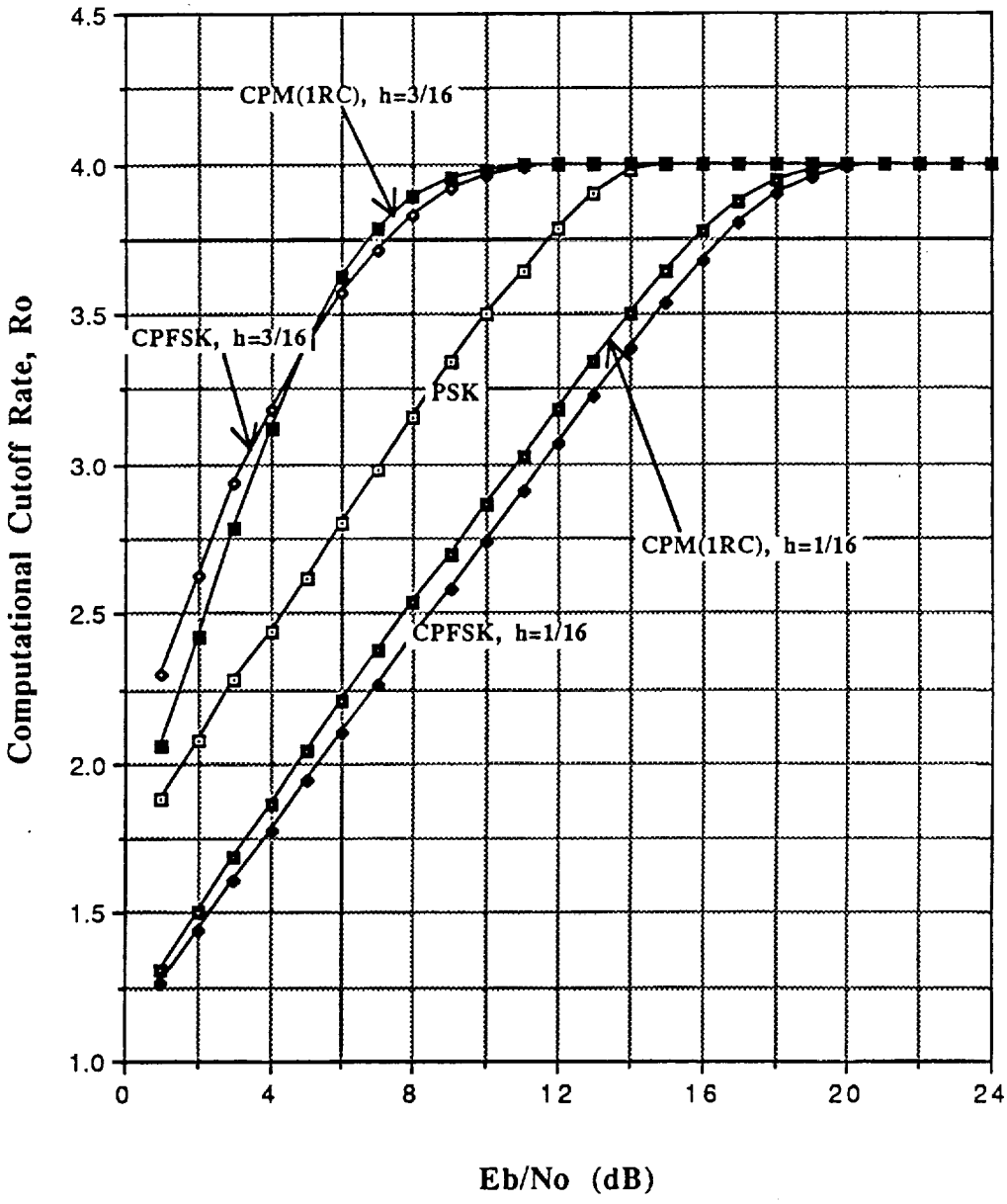

Figure 4.3: Comparison of cutoff rate R_0 of coherent 16-ary PSK, 1RC-CPM and CPFSK with coherent, symbol-by-symbol detection and additive, white Gaussian noise channel.

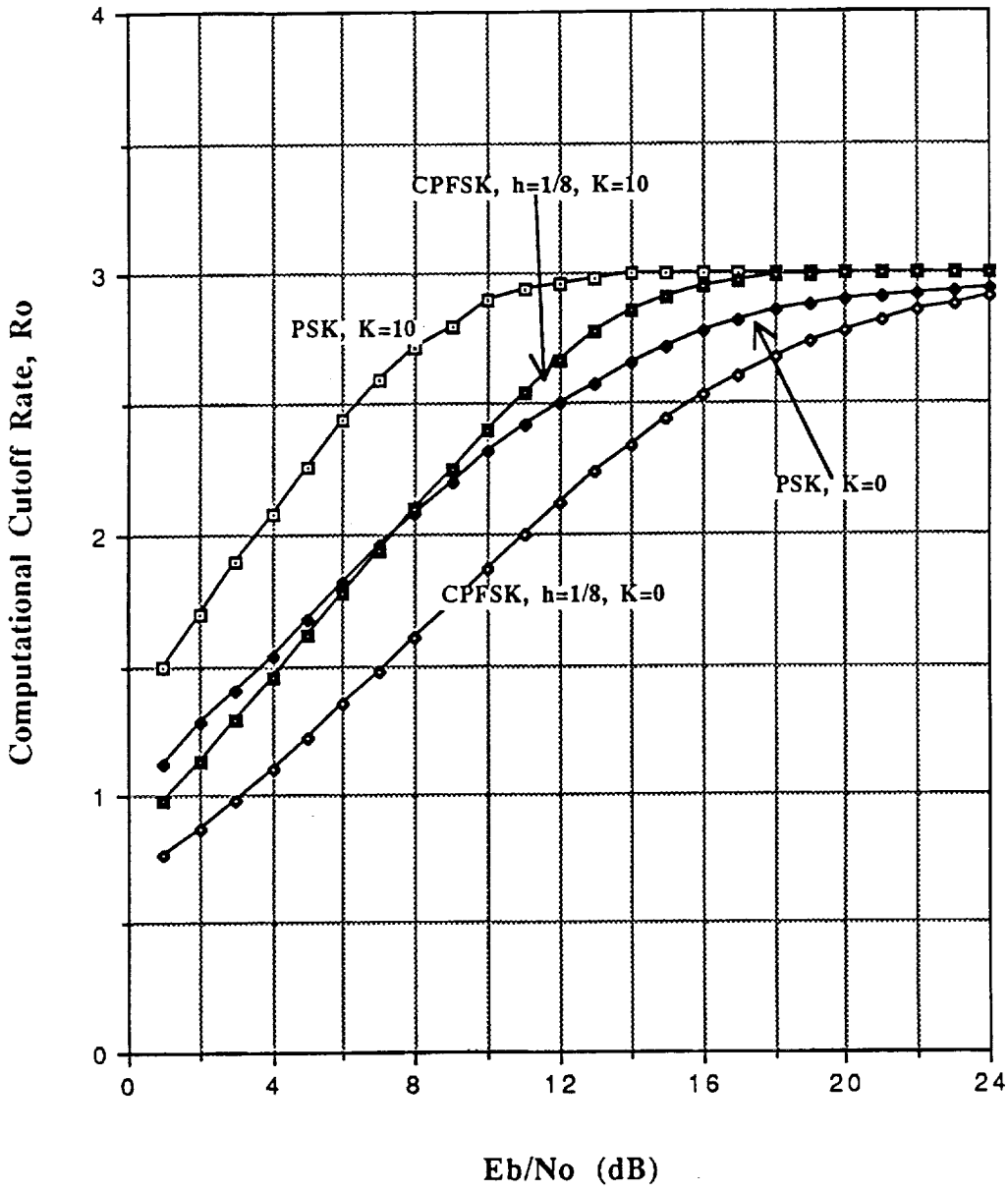

Figure 4.4: Comparison of cutoff rate R_0 of octonary coherent PSK, 1RC-CPM and CPFSK with coherent, symbol-by-symbol detection and Rice/Rayleigh fading channel.

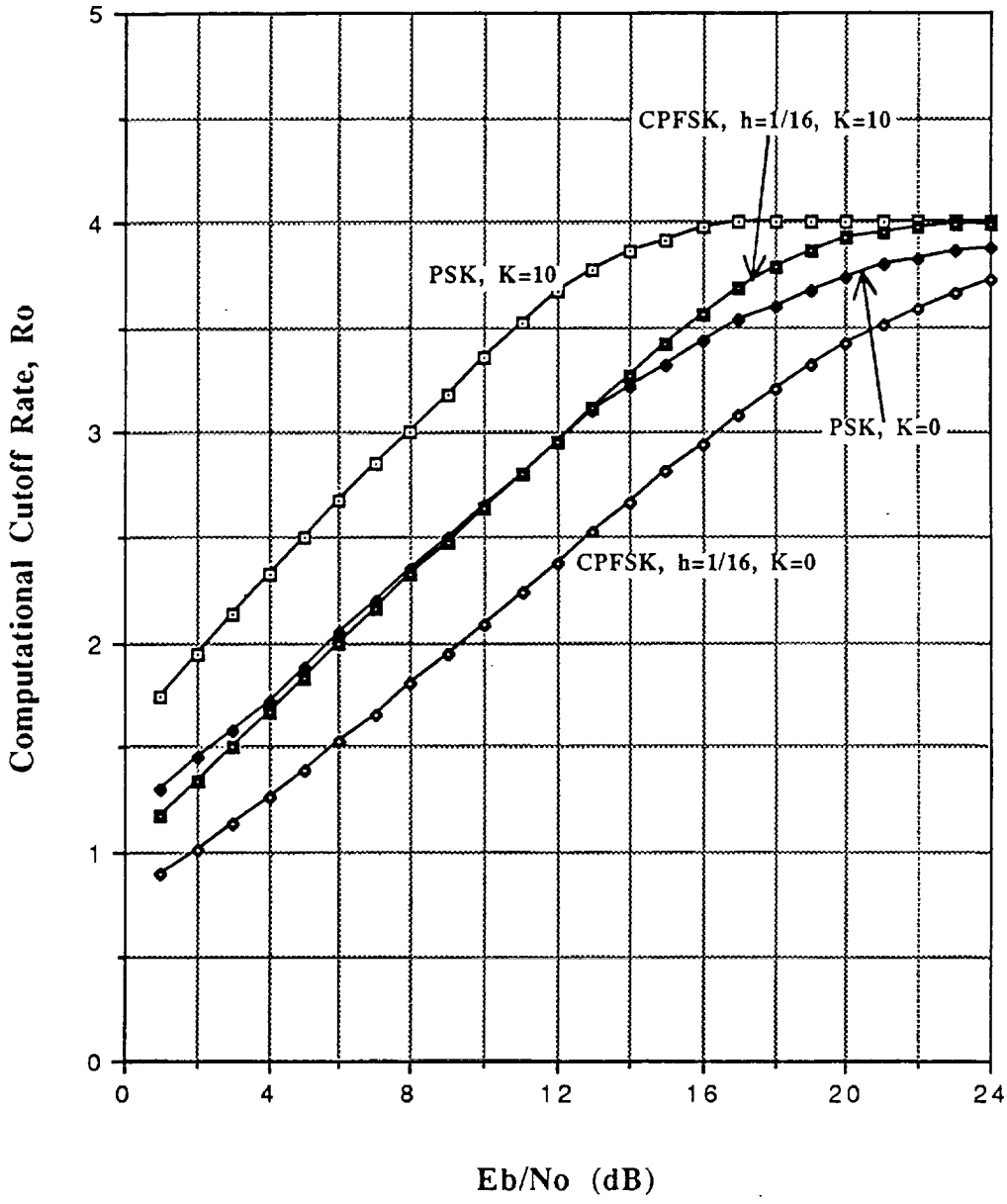

Figure 4.5: Comparison of cutoff rate R_0 of 16-ary coherent PSK, 1RC-CPM and CPFSK with coherent, symbol-by-symbol detection and Rice/Rayleigh fading channel.

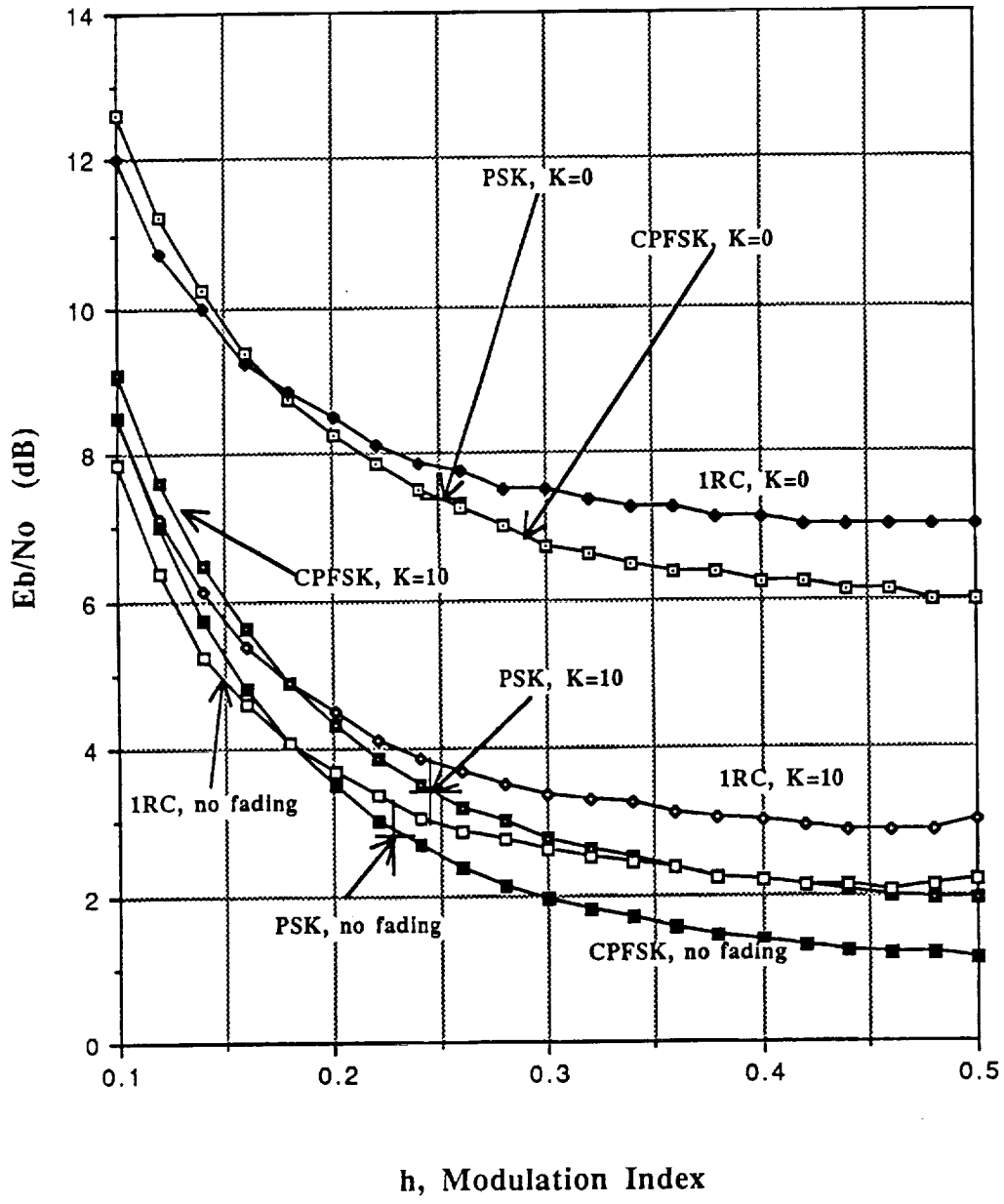

Figure 4.6: E_b/N_0 for $R_0 = 2$ bits/symbol with octonary CPFSK versus the modulation index h. + denote the points at which CPM starts outperforming PSK.

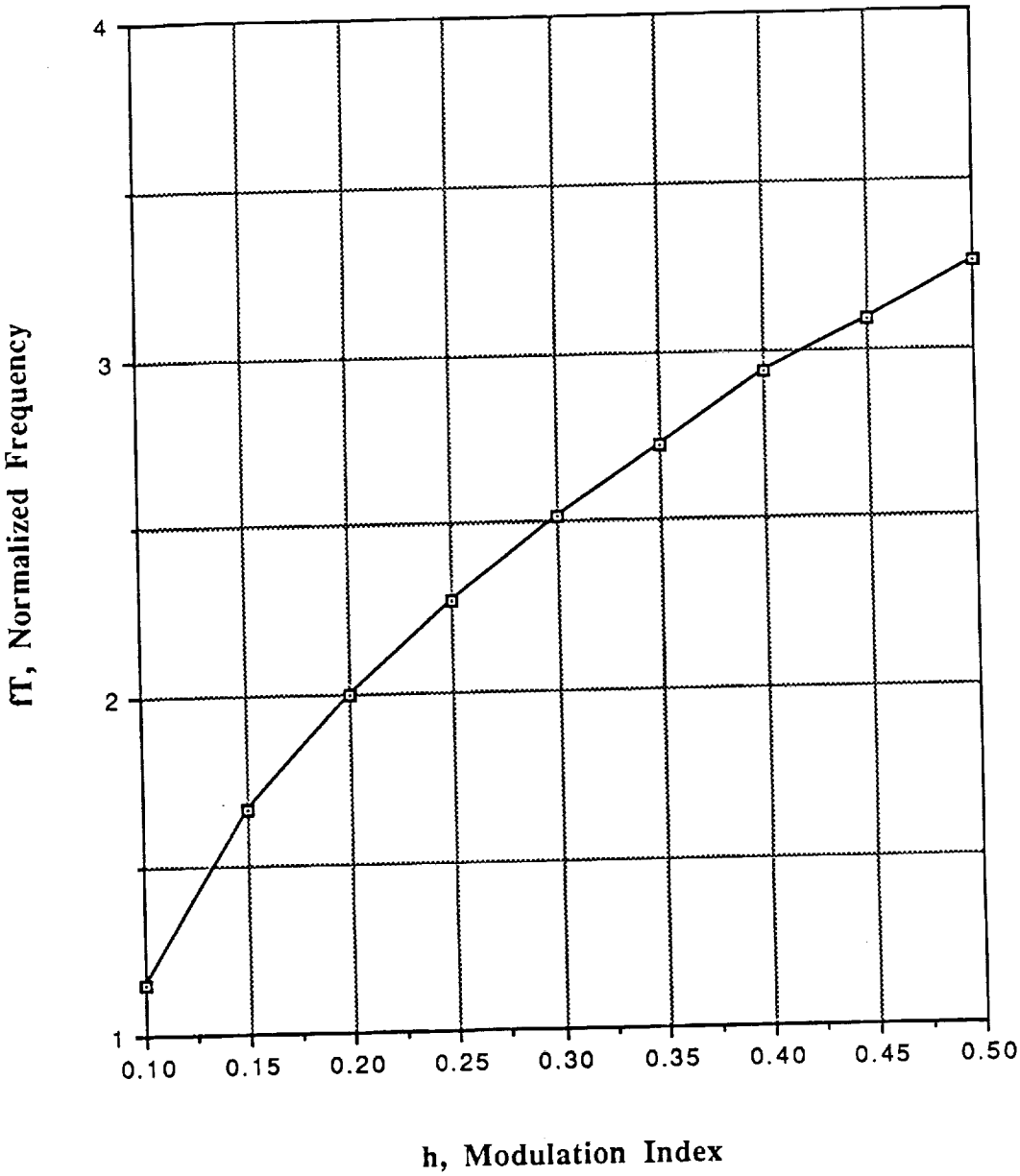

Figure 4.7: Out-of-band power for 1RC CPM. The ordinate is the bandwidth containing the 99.9% of the signal power.

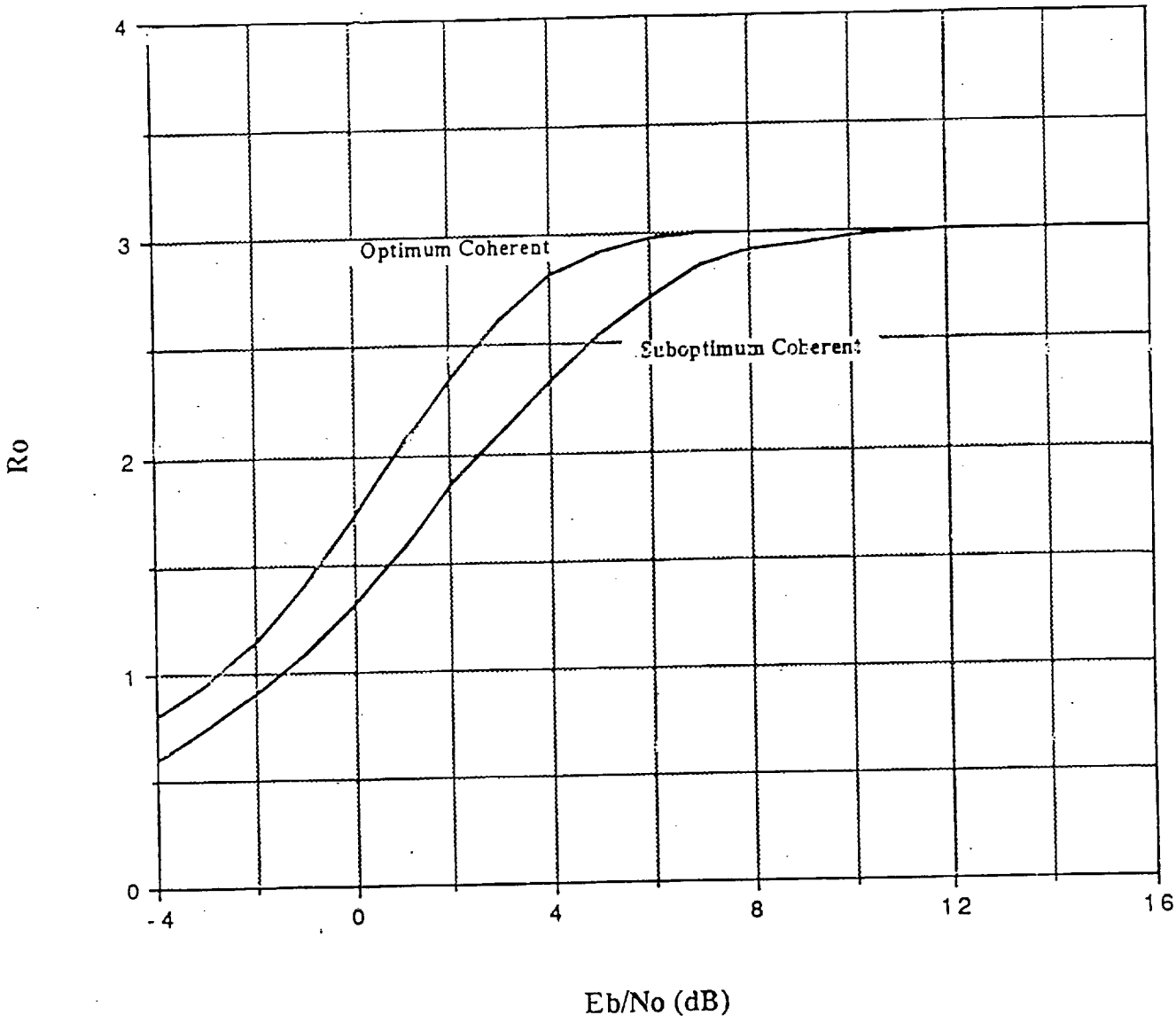

Figure 4.8: Comparison of R_0 for optimum and suboptimum coherent detection of octonary CPFSK with $h = 1/4$.

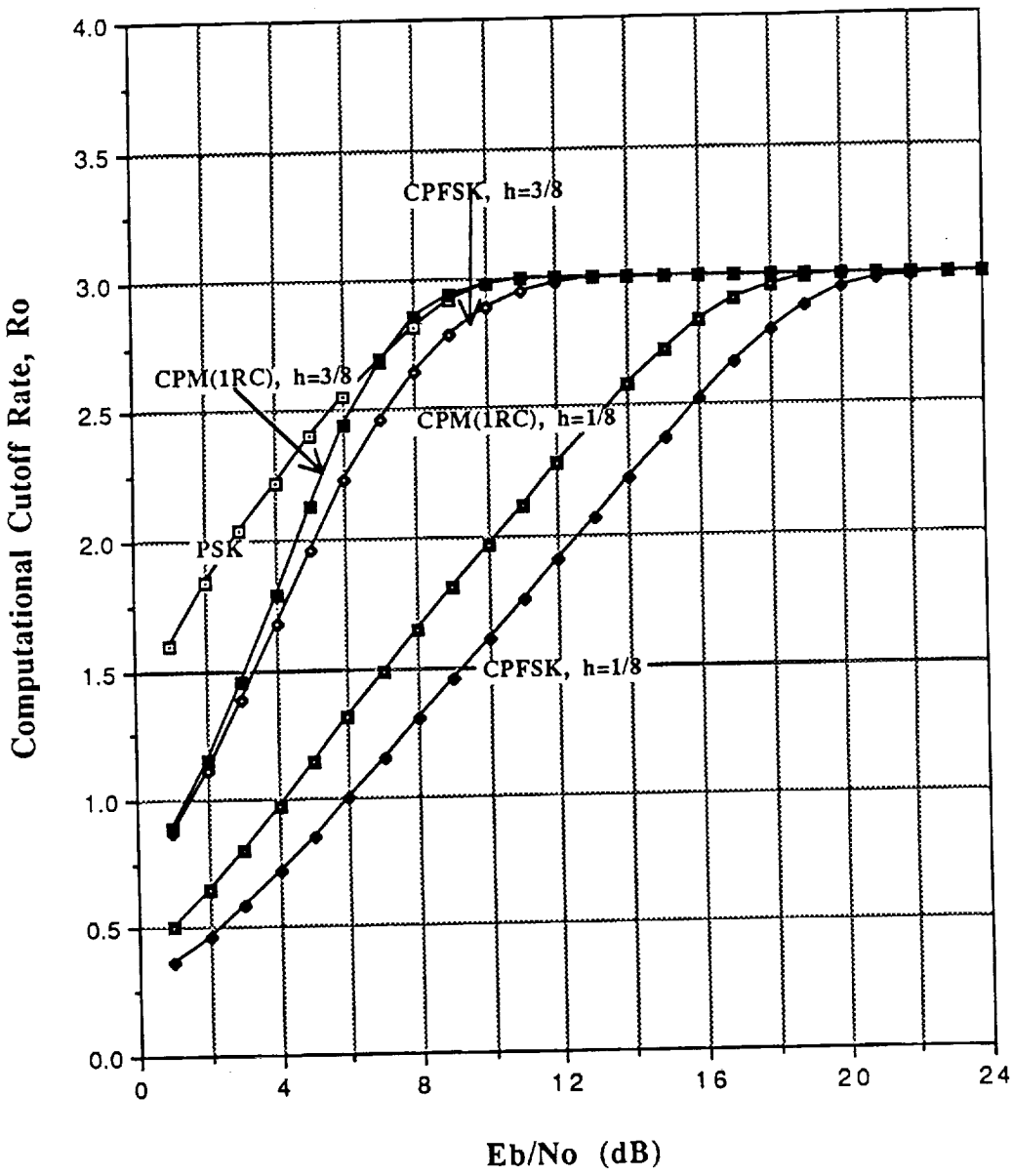

Figure 4.9: Comparison of cutoff rate R_0 of 1RC-CPM and CPFSK with noncoherent symbol-by-symbol detection and of coherent PSK over additive, white Gaussian noise channel. ($M = 8$).

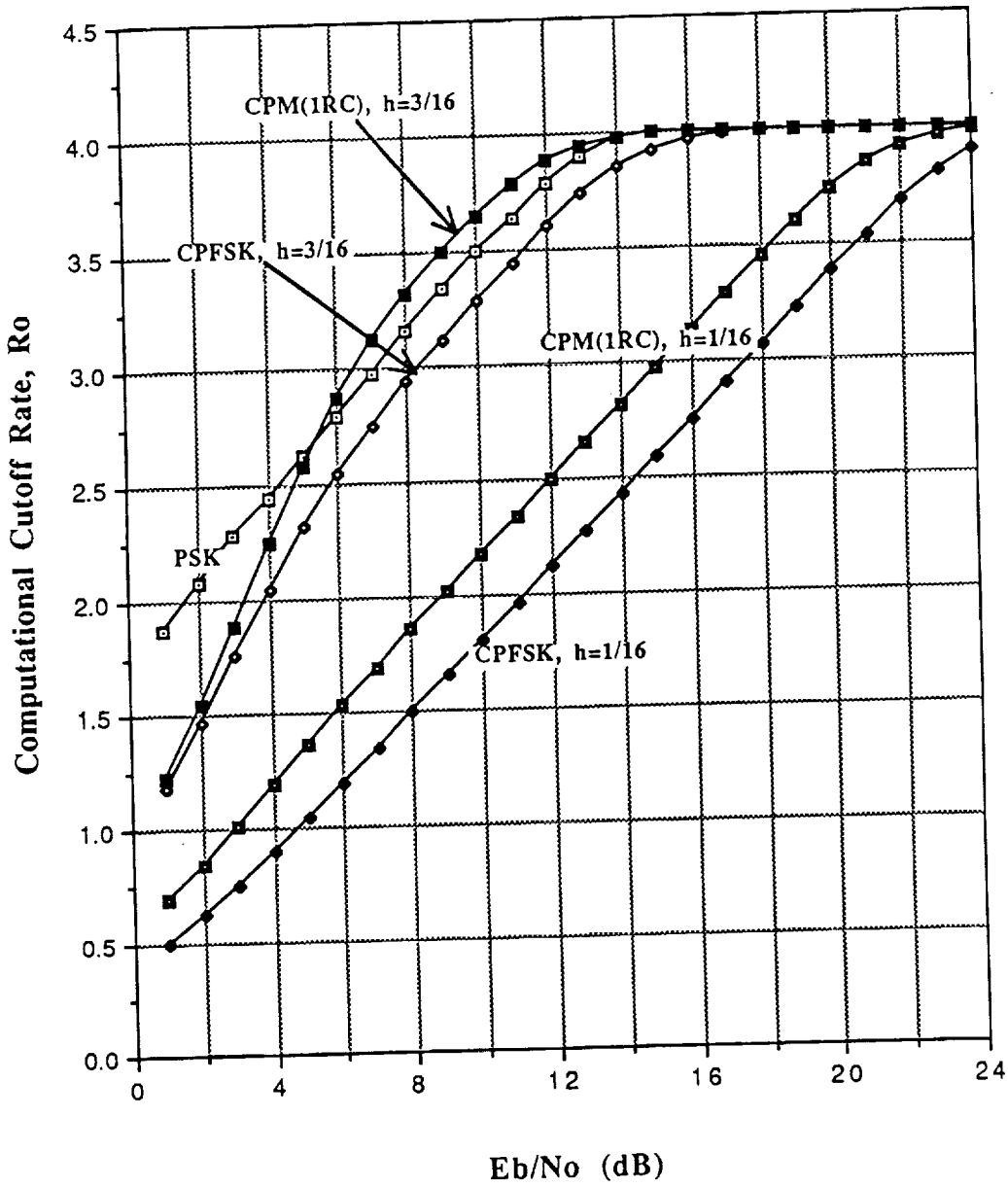

Figure 4.10: Comparison of cutoff rate R_0 of 1RC-CPM and CPFSK with noncoherent symbol-by-symbol detection and of coherent PSK over additive, white Gaussian noise channel. ($M = 16$).

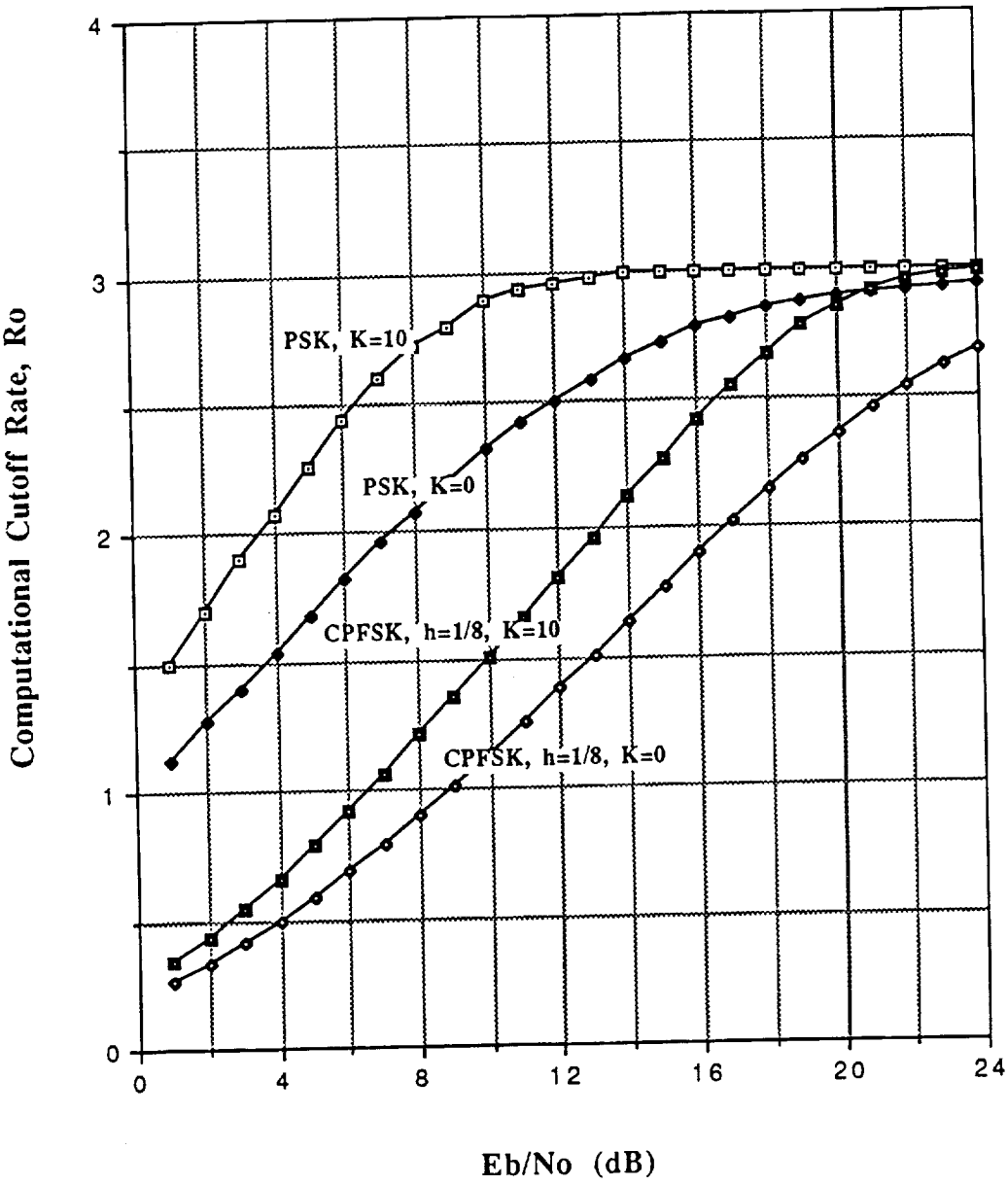

Figure 4.11: Comparison of cutoff rate R_0 of 1RC-CPM and CPFSK with noncoherent symbol-by-symbol detection and of coherent PSK over Rice/Rayleigh fading channel. ($M = 8$).

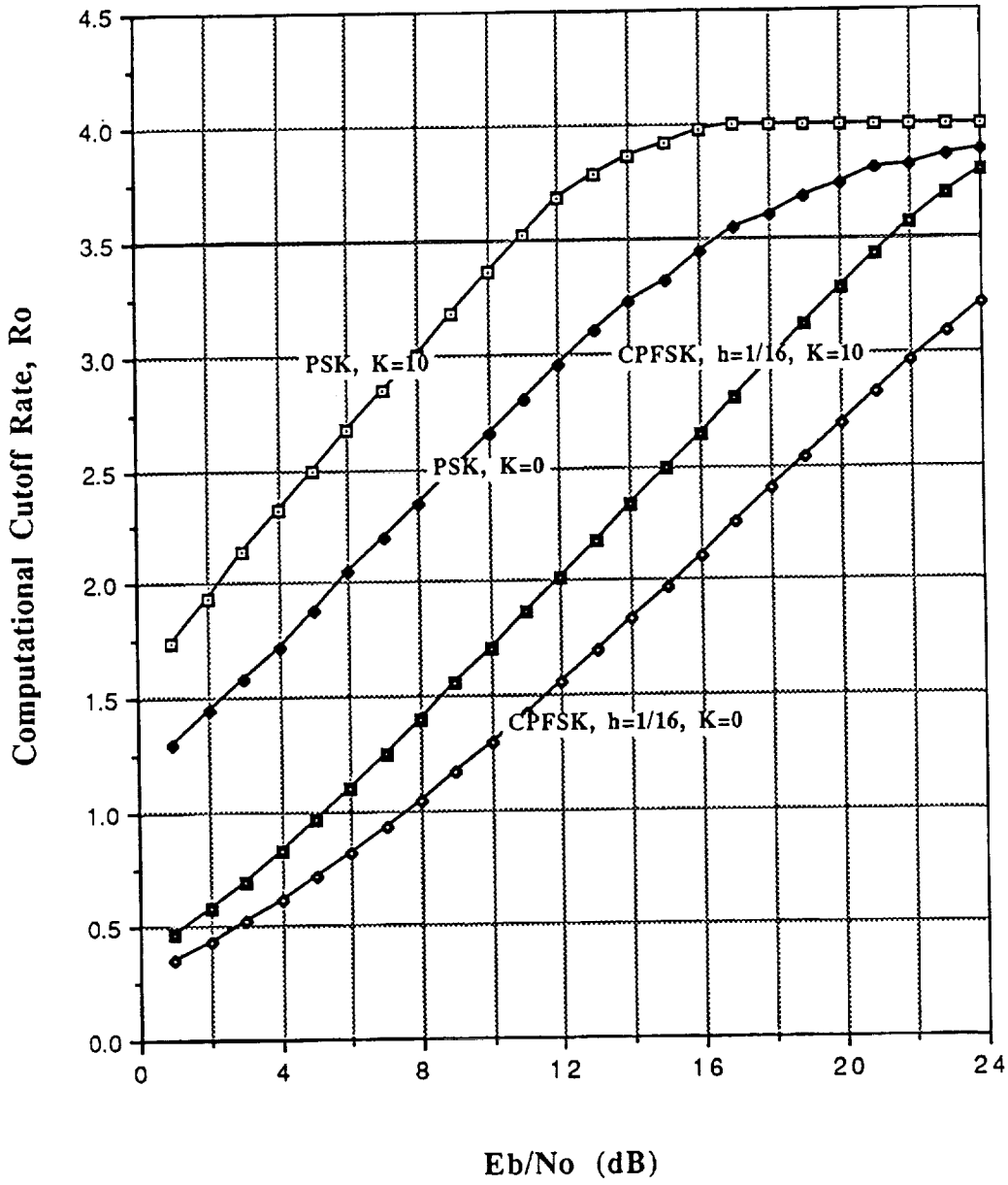

Figure 4.12: Comparison of cutoff rate R_0 of 1RC-CPM and CPFSK with noncoherent symbol-by-symbol detection and of coherent PSK over Rice/Rayleigh fading channel. ($M = 16$).

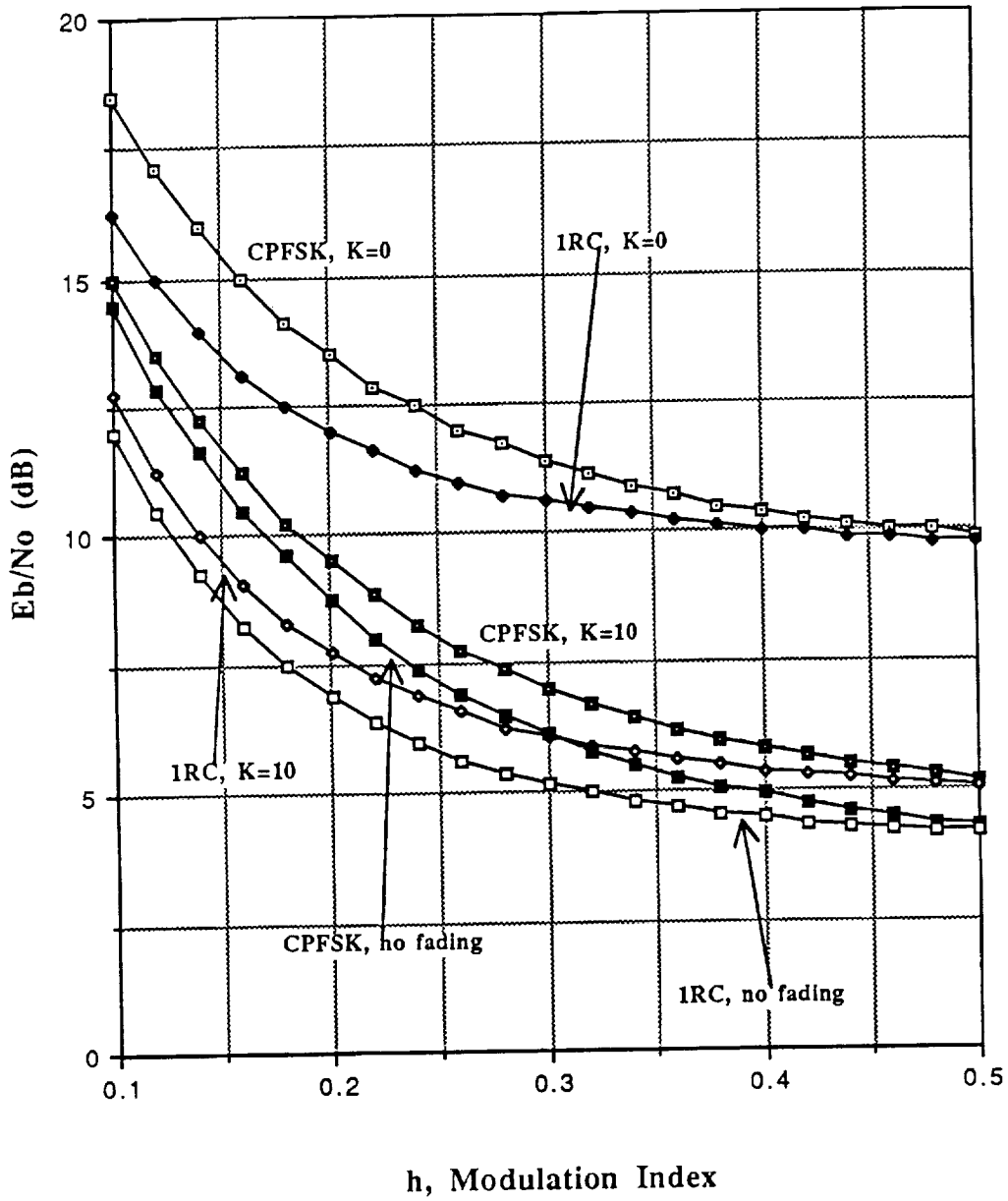

Figure 4.13: E_b/N_0 for $R_0 = 2$ bits/symbol with octonary, noncoherent CPFSK versus the modulation index h.

Chapter 5

Differential CPM

In this Chapter we describe symbol-by-symbol differential detection of CPM. Further, we consider precoding of differentially-detected CPM. The material that follows is adapted from [35].

The complex envelope of the received signal, say $\tilde{r}(t)$ is delayed by T_s seconds, transformed into its conjugate $\tilde{r}^*(t-T_s)$, and multiplied by itself. Then the real and imaginary components of the signal $\tilde{r}(t)\tilde{r}^*(t-T_s)$ are sampled every T_s seconds. As a result, a discrete signal is obtained whose phase is

$$2\pi f_0 T_s + \Delta\theta_n + \eta_n$$

where $\Delta\theta_n$ represents the change over one symbol interval of the signal phase, and η_n represents the change in phase due to the noise. Under the assumption that $f_0 T_s$ is an integer number, estimate of this phase provides a noisy estimate of $\Delta\theta_n$, which is used to recover the information sequence.

For full-response CPM (the case of precoded partial response will be considered later) we have

$$\Delta\theta_n = \pi h a_n,$$

so that the maximum value taken on by the phase shift is

$$|\Delta\theta|_{\max} = \pi h(M-1).$$

This quantity must be lower than π because the phases are observed modulo 2π. Thus, we must choose

$$h < \frac{1}{M-1}. \tag{5.1}$$

5.1 Precoding differential CPM

A form of precoding is developed for use in the channel, to allow symbol-by-symbol detection even for partial-response signalling, in which the frequency pulse duration is longer than one symbol time. This precoding undoes, before it is done, the correlation among symbols introduced by the modulator and the differential detector. The precoding is based on a modulo-M operation. Precoding is not needed for full-response CPM when the minimal modulation index is desired; for a larger modulation index or for partial-response signalling, it is needed.

Our description of the precoder will be based on the CPM modulator model developed by Rimoldi [34]. The source output (see Fig. 5.1 is a sequence $\mathbf{u}$ of independent, equally likely, M-ary symbols u_n. The first element in the transmitter is the precoder, the output of which is the sequence $\mathbf{u}'$ of M-ary symbols u'_n. This sequence is input to the continuous-phase modulator. The output of the modulator is an RF signal with information-carrying phase $\psi(t)$. The receiver consists of a differential detector and a baseband signal processor (BSP). The next element is a phase detector, with output $\Delta\psi(t)$ + noise, modulo 2π, where $\Delta\psi(t) = \psi(t) - \psi(t - T_s)$. This output is sampled every T_s to yield the sequence $\Delta\psi_n$ + noise, modulo 2π. This is input to the BSP, which outputs the sequence of soft-decision estimates of the u_n.

We write the CPM signal phase in the form

$$\exp\{j[2\pi f_1 t + \psi(t, \mathbf{u}')]\}.$$

In particular, following the notation of [34], we define the "tilted phase" ψ by

$$\psi((\tau + n)T_s, \mathbf{u}') = 2\pi h \sum_{i=0}^{n-L} u'_i + 4\pi h \sum_{i=0}^{L-1} u'_{n-i}\, q((\tau + i)T_s) + W(\tau T_s)$$

for $0 \le \tau \le 1$. Here W is a time function dependent on h, M, and q. The frequency f_1 is lower than the signal's center frequency by $h(M-1)/2T_s$.

The differential detector outputs noisy samples of the differential phase. Let us suppose that the sampling epoch is $\tau_s T_s$. Without loss of generality,

$$\tau_s \in (0, 1].$$

We define the samples q_i of q by

$$q_i = q((\tau_s + i)T_s) \quad \text{for } i = 0, 1, \ldots, L-1$$

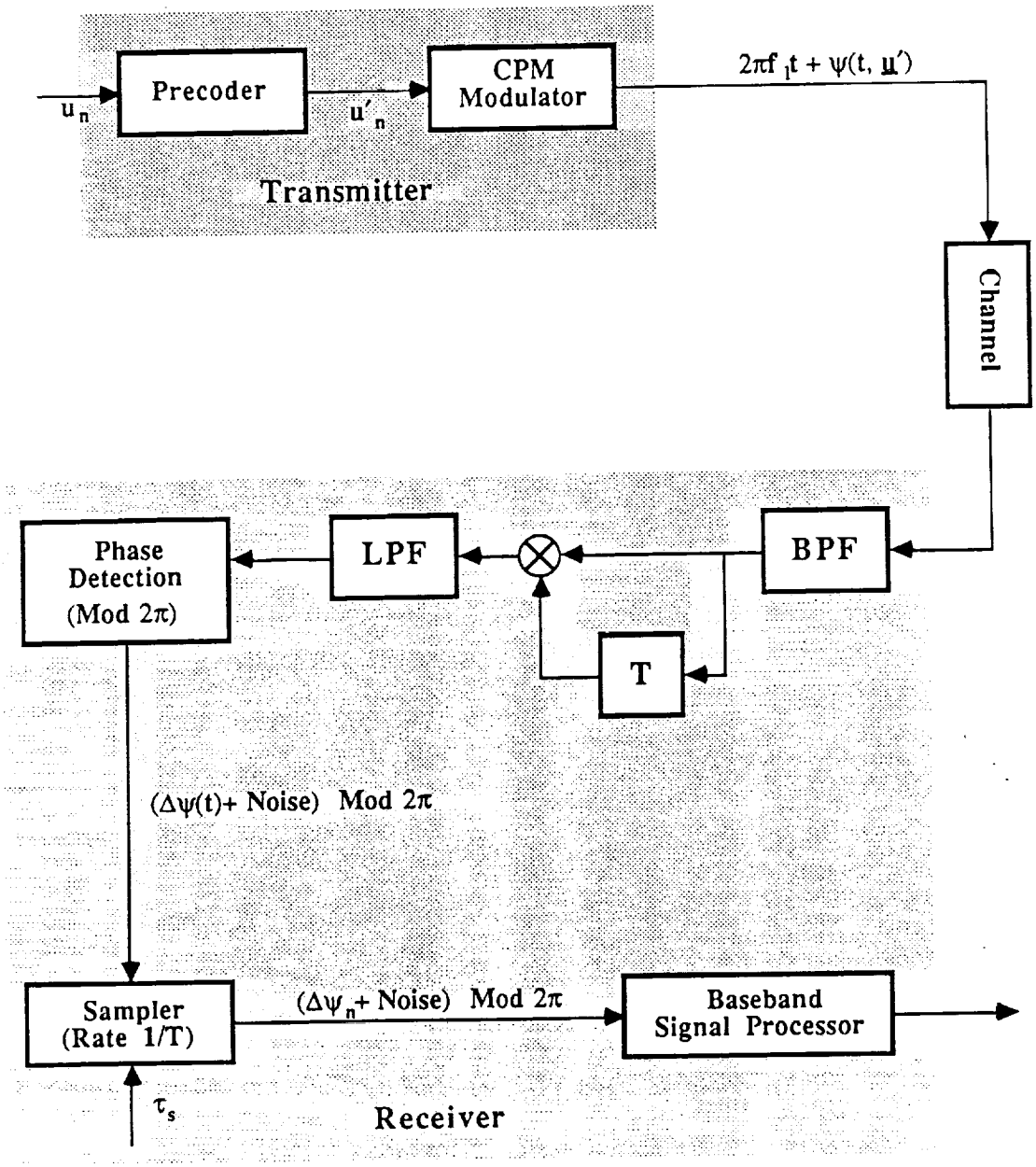

Figure 5.1: Block diagram of differential CPM detection.

while requiring that

$$q_0 > 0.$$

The phase ψ_n at the n-th sampling time is

$$\begin{aligned} \psi_n &= \psi((\tau_s + n)T_s, \mathbf{u}') \\ &= 2\pi h \sum_{i=0}^{n-L} u'_i + 4\pi h \sum_{i=0}^{L-1} u'_{n-i}\, q_i + W(\tau_s T_s) \quad \text{for } n \geq 0 \end{aligned} \tag{5.2}$$

The n-th sampled, differential phase $\Delta\psi_n$ is then

$$\begin{aligned} \Delta\psi_n &= \psi_n - \psi_{n-1} \\ &= 2\pi h\,[u'_n\, 2q_0 + \sum_{i=1}^{L-1} u'_{n-1}(2q_i - 2q_{i-1}) + u'_{n-L}(2 \times \frac{1}{2} - 2q_{L-1})] \end{aligned}$$

for $n \geq 1$. For the case of full-response CPM (i.e. $L = 1$), we may choose $\tau_s = 1$ so $q_0 = 1/2$. Then

$$\Delta\psi_n = 2\pi h\, u'_n. \tag{5.3}$$

Now we are in a position to see what a precoder can do for us. If precoding is not used in the transmitter, so that $\mathbf{u}'$ is the channel input sequence, then the receiver has to try to remove the effects of $u'_{n-1}, \ldots, u'_{n-L}$ from $\Delta\psi_n$, the better to detect u'_n. (This is "opening the eye" of the signal.) It is better to remove the effects of nearby symbols in the transmitter, where the symbols are known without error [32]. To that effect, let us presume that $\mathbf{u}'$ is the symbol sequence out of a precoder and that $\mathbf{u}$ is the M-ary symbol sequence input to the precoder and thus to the channel. We want $\Delta\psi_n$ to be closely related to u_n only. We have to assume now that all the q_i's are rational. Then

$$\Delta\psi_n = \frac{2\pi h}{Q} \sum_{i=0}^{L} u'_{n-i}\, d_i \tag{5.4}$$

where

$$\begin{aligned} d_0 &= Q \times 2q_0 \\ d_i &= Q \times (2q_i - q_{i-1}) \quad \text{for } i = 1, \ldots, L-1 \\ d_L &= Q \times (2 \times \frac{1}{2} - 2q_{L-1}) \end{aligned}$$

and Q is the smallest positive integer such that all the d_i's are integers. In analogy with the coherent reception case [32], we want a precoder that makes

$$u_n = R_M\,(\sum_{i=0}^{L} u'_{n-i}\,d_i)$$

where R_x is the modulo-x function. Then we shall have

$$u_n = R_M(\kappa\,\Delta\psi_n), \tag{5.5}$$

where

$$\kappa = \frac{Q}{2\pi h}.$$

The precoder has to perform the operation

$$u'_n = R_M\,[d_0^{-1}\,(u_n - \sum_{i=1}^{L} u'_{n-i}\,d_i)].$$

It is required that d_0 and M be relatively prime. In the case where $L = 1$ and $\tau_s = 1$, there is no need for a precoder, so $u_n = u'_n$. We can think that $Q = 1$. $\Delta\psi_n$ and u_n are simply related by

$$u_n = \kappa\,\Delta\psi_n \tag{5.6}$$

The spectrum of the CPM signal is the same with or without precoding, since the u'_n's are equally likely and independent when the u_n's are [33].

5.2 Computation of R_0

In this section we consider the computation of the parameter R_0 for the channel created by CPM modulation with precoding and differential detection. The results obtained from this computation will allow us to choose the parameters for the combination of CPM with trellis-coded modulation.

We now make two assumptions which allow us to calculate R_0. The baseband signal processor (BSP) input (see Fig. 5.1) is $R_{2\pi}(\Delta\psi_n + \text{noise})$. The first assumption is that the BSP output V_n is simply given by

$$V_n = R_M[\kappa R_{2\pi}(\Delta\psi_n + \text{noise})] \quad \in [0, M).$$

The second assumption is that

$$Q/h = AM \tag{5.7}$$

for some positive integer A. The first assumption then takes the form

$$V_n = R_M[\kappa(\Delta\psi_n + \text{ noise})].$$

Thus, whether precoding is used or not, the following simple relationship between the channel input U_n and output V_n can be derived:

$$V_n = R_M\,[U_n + \kappa(\text{noise})] \tag{5.8}$$

The noise term in the differential detector output, which is the BSP input, is

$$\text{noise} = \mu_n - \mu_{n-1}, \tag{5.9}$$

where μ_n is the error in the N-th noisy phase. It turns out that R_0 for the channel can be calculated once the probability density function of μ_n is known. The pdf of μ_n is

$$p_\mu(\alpha) = \frac{1}{2\pi}\exp(-\gamma)\{1 + 2\sqrt{\pi\gamma}\cos(\alpha)[1 - \mathcal{Q}(\sqrt{2\gamma}\cos\alpha)]\exp(\gamma\cos^2\alpha)\} \tag{5.10}$$

for $0 \le \alpha < 2\pi$, where

$$\mathcal{Q}(x) = \frac{1}{\sqrt{2\pi}}\int_x^\infty \exp(-t^2/2)dt.$$

We can now calculate the cutoff rate R_0 for our channel. We derive a discrete-input memoryless channel equivalent to our channel in terms of R_0, then we present numerical results. From Equations (5.8) and (5.9) we know that successive channel outputs V_{n-1} and V_n are given by

$$\begin{aligned} V_{n-1} &= R_M\,[u_{n-1} + \kappa(\mu_{n-1} - \mu_{n-2})] \\ V_n &= R_M\,[u_n + \kappa(\mu_n - \mu_{n-1})]. \end{aligned} \tag{5.11}$$

This does not represent a memoryless channel. While the channel input symbols u_{n-1} and u_n are independent, the noise terms $\mu_{n-1} - \mu_{n-2}$ and $\mu_n - \mu_{n-1}$ are not.

Here we construct a discrete-input memoryless channel, for which R_0 can be calculated. In constructing the memoryless channel, let us define a new sequence of continuous-valued random variables Y_n by

$$Y_n = R_M(V_n + \cdots + V_1 + V_0) \quad \in [0, M) \quad \text{for } n \ge 1 \tag{5.12}$$

The receiver must observe V_0 defined by

$$V_0 = R_M\,[\kappa(\psi_0 + \mu_0)].$$

Given V_0, for each N the set $\{Y_1, \ldots, Y_N\}$ of random variables can be calculated from the set $\{V_1, \ldots, V_N\}$ of random variables, and vice versa. We can show that the new channel is memoryless. We find that

$$Y_n = R_M(\sum_{i=1}^{n-1} u_i + \kappa\psi_0 + \kappa\mu_n) \tag{5.13}$$

from which we can show that the Y_n's are independent. The fact that the distribution of Y_n depends only on the value of X_n follows from the relation

$$Y_n = R_M(X_n + \kappa\psi_0 + \kappa\mu_n),$$

where the receiver must know $R_M(\kappa\psi_0)$. (The latter point means that there must be phase synchronism at time zero, which can be obtained along with symbol synchronism by the transmission of a training sequence before the data.)

R_0 is given by

$$R_0 = -\log_2 \left[\frac{1}{M^2} \int_0^M dy \sum_{k=0}^{M-1} \sum_{i=0}^{M-1} \sqrt{p(y|k)p(y|i)} \right] \tag{5.14}$$

where p denotes the conditional probability density function for Y_1 given X_1. For a given SNR, R_0 is determined solely by A and M.

Figure 5.2 shows how R_0 varies with A and SNR, for $M = 2$ and $A = 1, 2, 3, 4, 8$. From this plot (and similar plots that have been obtained for $M = 3, 4, 8$, and 16, we find thet for R_0 in the mid-range, having $A = 2$ instead of $A = 1$ represents a 4.5-5 dB loss in SNR. Similarly, having $A = 3$ instead of $A = 2$ represents a 3-3.5 dB loss. Figure 5.3 shows how R_0 varies with M and SNR, for $A = 1$, $M = 2, 3, 4, 8, 16$.

5.3 Selection of channel parameters

In this section we will look at how one makes a good selection of the channel parameters, which are as follows:

1. the modulation index h;
2. the phase pulse q;
3. the scaled sampling epoch τ_s, a positive time no greater than 1 (the actual sampling epoch being $\tau_s T_s$).

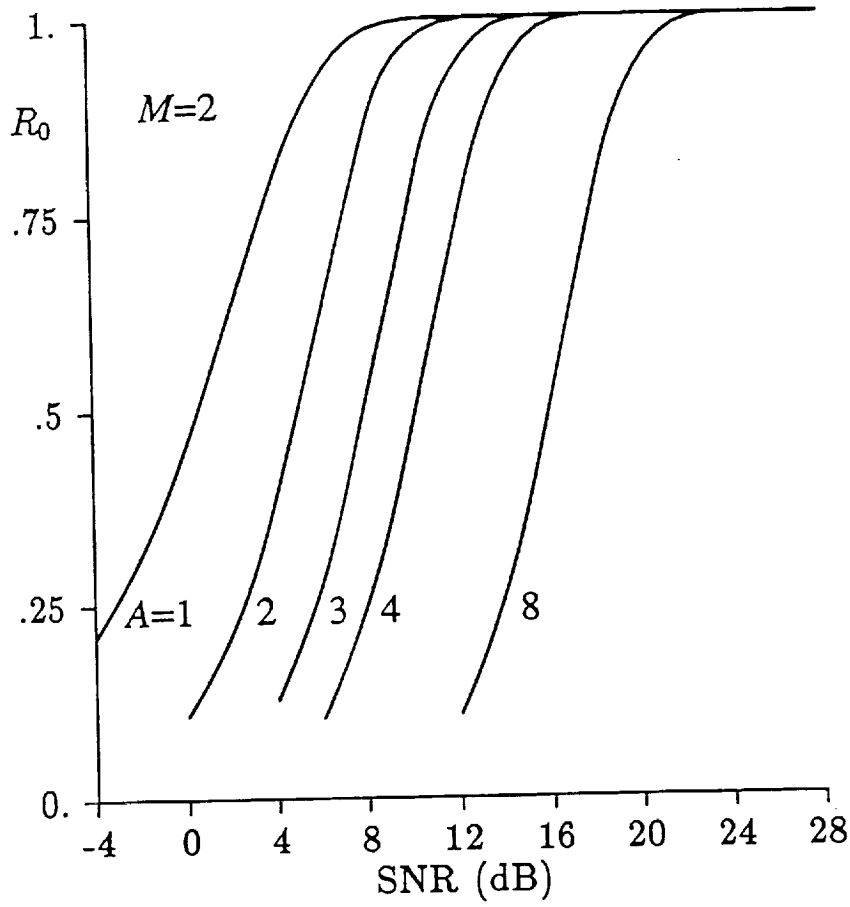

Figure 5.2: R_0 as a Function of A and SNR, for $M = 2$

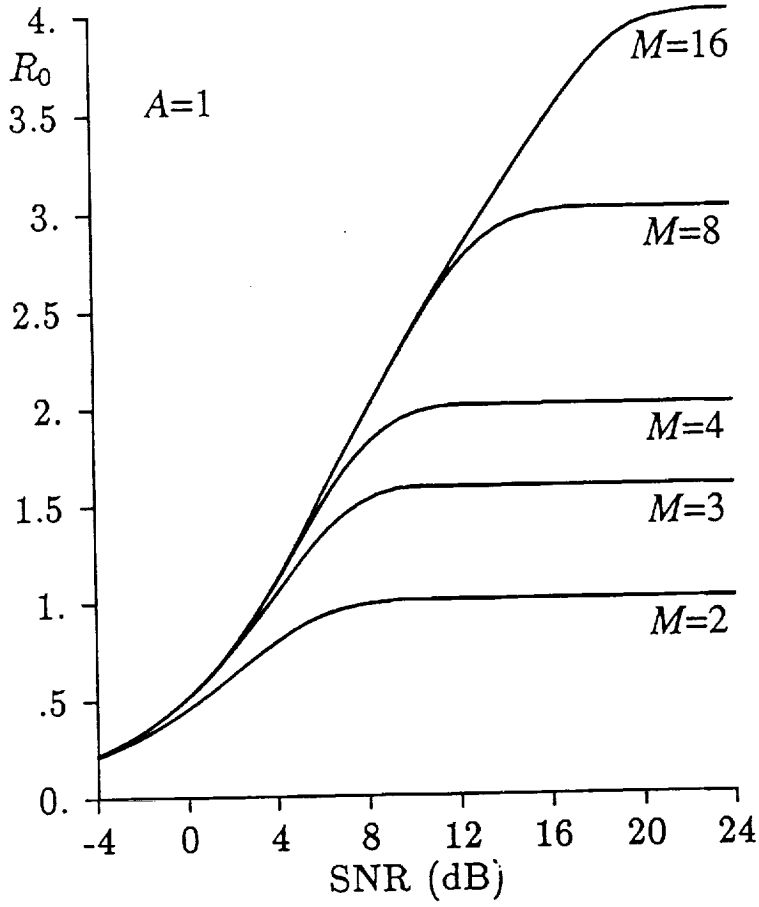

Figure 5.3: R_0 as a Function of A and SNR, for $M = 3$

Here we will give examples of the good selection of channel parameters. The families of pulse to be treated are named, as is common usage, by the frequency pulse and not the phase pulse. The families will be treated in order of increasing smoothness, which corresponds to the signal spectrum having a wider mainlobe and faster roll-off at frequencies far from the carrier frequency.

The highest quality channel ($A = 1$) can be obtained with a frequency pulse of duration LT if $h = L/M$ and L is as follows: for the rectangular (LREC) pulse, L is any integer; for the triangular (LTRI), L is any integer; for the raised cosine (LRC), $L = 1$ or 2; for the convolved-raised-cosine (LCRC), $L = 1$ or 2. The second highest quality channel ($A = 2$) can be obtained with h half the size. In general, larger h means wider spectrum, so we have listed only the smallest h in each case. For a given L, different h's are provided by different r's. In general, larger L means narrower spectrum, but larger L calls for larger h to maintain the channel quality, so it needs to be investigated which L provides the best spectrum.

Chapter 6

Doppler phase shift removal

In this Chapter we consider the effect of a Doppler frequency shift over differentially-detected CPM signals, and we derive a circuit that makes it possible to estimate and to remove the corresponding phase shift.

Let us write the observed signal $r(t)$ in the form

$$r(t) = P(t)e^{j[2\pi f_d t + \theta(t,\mathbf{a}) + \nu(t)]}, \tag{6.1}$$

where $P(t)$ and $\nu(t)$ are the amplitude fluctuation and the phase fluctuation, respectively. They account for fading, noise, and intersymbol interference. f_d is the Doppler frequency shift.

For differential processing, the signal (6.1) is synchronously sampled at times

$$t_n = nT_s, \quad n = 0, 1, \ldots,$$

and the following sequence is formed:

$$r_n = \frac{1}{2} r(t_n) r^*(t_{n-1}) = \rho_n e^{j[\phi_d + \Delta\theta_n + \eta_n]} \tag{6.2}$$

where

$$\phi_d = 2\pi f_d T_s$$

is the Doppler phase shift,

$$\Delta\theta_n = \theta(t_n, \mathbf{a}) - \theta(t_{n-1}, \mathbf{a}) = \pi h a_n$$

represents the phase fluctuations due to the transmitted data, and

$$\eta_n = \nu(t_n) - \nu(t_{n-1}).$$

Finally,

$$\rho_n = \frac{1}{2} P(t_n) P(t_{n-1}).$$

(Perfect symbol synchronization is assumed.)

It is seen from (6.2) that the presence of a Doppler frequency shift causes the phase of the sequence r_n to be altered by a term ϕ_d, added to the information sequence $\Delta\theta_n$. This has to be removed prior to demodulation.

6.1 Estimation schemes

Two constraints are associated with the design of a Doppler compensation circuit for continuous-phase modulated signals with application to mobile satellite communications:

- Fast frequency acquisition is required. In fact, if data are transmitted in short bursts or packets, the acquisition time should not be a significant portion of the burst interval.
- Since multipath fading affects the propagation, the Doppler estimator must be insensitive to the signal amplitude fluctuations caused by fading.

As a consequence of the first requirement, we consider open-loop estimation structures, as first suggested (for different systems) in [82,78,29].

The class of methods we propose to estimate the Doppler phase shift ϕ_d is based on the following considerations. Consider a random variable Θ, observed mod $2\pi/A$ and taking values $\theta \in (-\pi/A, \pi/A)$. Let $f(e^{jA\theta})$ be its probability density function. We assume that $f(\cdot)$ is a symmetric function, so that

$$\mathbf{E}[e^{jA\Theta}] = \int_{-2\pi/A}^{2\pi/A} e^{jA\theta} f(e^{jA\theta}) d\theta$$

is a *real* quantity. Now the problem is the following. Assume that we observe K (say) values of $\Psi = \Theta + \phi$, where ϕ is a constant, and we want to estimate ϕ based on these observations. The probability density of $\Theta + \phi$ is obtained by shifting (mod $2\pi/A$) the original function $f(\theta)$, so that we get

$$\begin{aligned} \mathbf{E}[e^{jA\Psi}] &= \int_{-2\pi/A}^{2\pi/A} e^{jA\psi} f(e^{jA(\psi-\phi)}) d\psi \\ &= e^{jA\phi} \mathbf{E}[e^{jA\Theta}]. \end{aligned}$$

Thus, under our symmetry assumption, ϕ can be obtained from the phase of $\mathbf{E}[e^{jA\Psi}]$, which in turn can be estimated as

$$\mathbf{E}[e^{jA\Psi}] \cong \frac{1}{K}\sum_{k=1}^{K} e^{jA\psi_k} \tag{6.3}$$

where ψ_k, $k = 1, \ldots, K$, denote the observed values of Ψ.

Observation of eq. (6.2) shows that the phase of the received samples includes a noise term η_n, which we shall assume to have a symmetric probability density function, and a data term $\Delta\theta_n$, which takes on values

$$\pm\pi h, \pm 3\pi h, \ldots, \pm(M-1)\pi h \pmod{2\pi}.$$

Since $h = J/M$, the probability density function of the above phase turns out to be periodic with period $2\pi h$, and in the interval $(-\pi, \pi)$ it has copies centered at $i\pi h$, $i = \pm 1, \pm 3, \ldots, \pm(M-1)$.

From the theory presented before we see that the estimate of the Doppler shift ϕ_d can be based on the phase of the quantity

$$\frac{1}{K}\sum_{k=1}^{K} z_n,$$

where

$$z_n = F(\rho_n)e^{jM(\phi_d+\Delta\theta_n+\eta_n)}, \tag{6.4}$$

and the positive function $F(\cdot)$ is arbitrary. Thus, the estimator of the Doppler phase shift becomes, if $\mathbf{E}[e^{jA\Theta}]$ is a *positive* quantity,

$$\hat{\phi} = \frac{1}{M}\tan^{-1}\frac{\frac{1}{K}\sum_{n=0}^{K-1} F(\rho_n)\sin M(\phi_d+\Delta\theta_n+\eta_n)}{\frac{1}{K}\sum_{n=0}^{K-1} F(\rho_n)\cos M(\phi_d+\Delta\theta_n+\eta_n)}. \tag{6.5}$$

In words, (6.4) is equivalent to performing a transformation from rectangular to polar coordinates on each complex sample r_n. Next, we perform two transformations on its amplitude and phase. Finally, we perform a polar-to-rectangular transformation on the result. As observed in [82], in a practical implementation the nonlinearity becomes a read-only memory transforming a quantized complex number into another quantized complex number.

The choice of the function F should take into account the presence of fading. In fact, samples heavily affected by fading should be given a lower weight in the time averages which form the estimate $\hat{\phi}$. In our simulations, we have always assumed $F(\rho_n) = \rho_n$, which is perhaps the simplest choice to

decrease the influence of the samples whose amplitude is lowered by fading effects.

For future reference, observe that (6.5) can be rewritten in the form

$$\hat{\phi} = \frac{1}{M} \tan^{-1} \frac{A_C \sin M\phi_d + A_S \cos M\phi_d}{A_S \cos M\phi_d - A_C \sin M\phi_d}, \tag{6.6}$$

where

$$\begin{aligned} A_C &= \frac{1}{K} \sum_{n=0}^{K-1} F(\rho_n) \cos M(\Delta\theta_n + \eta_n) \\ A_S &= \frac{1}{K} \sum_{n=0}^{K-1} F(\rho_n) \sin M(\Delta\theta_n + \eta_n) \end{aligned}$$

The trigonometric identity

$$\tan^{-1} \frac{B \sin\psi + A \cos\psi}{B \cos\psi - A \sin\psi} = \psi + \tan^{-1} \frac{A}{B}, \tag{6.7}$$

in conjunction with (6.6), provides an expression for the estimation error:

$$\hat{\phi} - \phi_d = \frac{1}{M} \tan^{-1} \frac{A_S}{A_C}. \tag{6.8}$$

6.1.1 Estimator A

The first estimator we consider is based on eq.(6.5), with $F(\rho_n) = \rho_n$.

6.1.2 Estimator B

We consider here an estimator structure whose aim is to broaden the range of Doppler phases that can be tracked.

Assume that the received signal is sampled *twice* per signaling interval, namely, at time instants $(n + a)T_s$ and $(n + b)T_s$, $n = 0, 1, \ldots$, where $0 \leq a < b \leq 1$. If one sample is multiplied by the conjugate of the other one, we get a sequence of quantities whose phases have the form

$$\phi_n = (b - a)\phi_d + 2\pi h a_n \mathcal{A}(a, b) + \eta_n,$$

where $\mathcal{A}(a, b) < \frac{1}{2}$ denotes the area of the frequency pulse used for CPM between times aT_s and bT_s. (Note that η_n has now a meaning different from

before). The presence of the factor $b-a$ in the Doppler phase term causes an increase in the estimator variance: in fact, we have

$$\hat{\phi} - \phi_d = \frac{1}{(b-a)M} \tan^{-1} \frac{A_S}{A_C}$$

instead of (6.8). Under the rough assumption that the term $\tan^{-1} \frac{A_S}{A_C}$ remains the same, the estimation error increases by a factor $1/(b-a)$. This, in turn, increases by a factor of approximately $1/(b-a)^2$ the value of the sample size K necessary to achieve a given estimator variance.

As a consequence of this estimator structure, the probability density function of the phase ϕ_n turns out to be periodic with period $4\pi h\mathcal{A}(a,b)$, a quantity less than $2\pi h$. To avoid ambiguities in the estimation procedure, we must have: $|(b-a)\phi_d| < \pi h\mathcal{A}(a,b)$. Thus, with respect to Estimator A, we get a broader range of Doppler phases that can be estimated if the ratio $\rho = 2\mathcal{A}(a,b)/b-a$ is greater than 1.

6.1.3 Estimator C

This estimator further extends the range of Doppler frequencies that can be tracked.

The basic idea underlying Estimator C is that in one symbol interval the phase variation due to the Doppler frequency shift is linear, while that due to data modulation depends on the shape of the phase pulse, and hence can be made nonlinear. Thus, it exploits the nonlinearity of the phase pulse by performing two differential detections based on four samples within each symbol interval. Details about it can be found in [36].

6.2 Simulation results

We now describe some results arising from computer simulation of Doppler frequency shift estimators A,B, and C. We assume an octonary, full-response CPM with modulation index $h = 1/8$ and 1RC frequency pulse, i.e.,

$$g(t) = \frac{1}{2T_s}(1 - \cos\frac{2\pi t}{T_s}).$$

In Estimator B, $a = 0.1$ and $b = 0.9$, so that

$$\mathcal{A}(a,b) = \frac{2}{5} + \frac{\sqrt{5-\sqrt{5}}}{\sqrt{32}\pi} = 0.4935,$$

and

$$\rho = \frac{2\mathcal{A}}{b-a} = 1.234.$$

The comparisons are made in terms of the variance of the Doppler frequency estimation error. For all the estimators, 4095 symbol intervals were simulated. For Estimators A and B, a window of K intervals was used to compute $\hat{\phi}$, and hence $\hat{f}_d$. This window was slided by one symbol interval at the time to generate a set of estimates. The estimate of σ^2 was then obtained by averaging the squared estimation error over $4095 - K$ runs. (Notice that with this procedure the estimates become less and less accurate as K increases). For Estimator C, the time-average was evaluated by using a one-pole Butterworth filter whose output was sampled at time KT_s.

In Figs. 6.1 to 6.6 the variance of the Doppler frequency estimation error is plotted vs. K for several values of signal-to-noise ratio. Figs. 6.7 to 6.9 compare the error variances of estimators A,B, and C for three values of signal-to-noise ratio.

6.3 Conclusions

Three estimators of Doppler frequency shift in CPM signals were proposed, and their performance evaluated by simulation. Their structure is based on differential detection, which makes them attractive for use in a differentially coherent receiver (although in principle they can be used in conjunction with any other CPM detection scheme).

These estimators are in order of increasing complexity. Increased complexity is made necessary to remove ambiguities in the estimate when the Doppler frequency shift is high. Moreover, at least for high signal-to-noise ratios, a wider range of trackable Doppler frequencies causes a substantial increase in the variance of the estimation error.

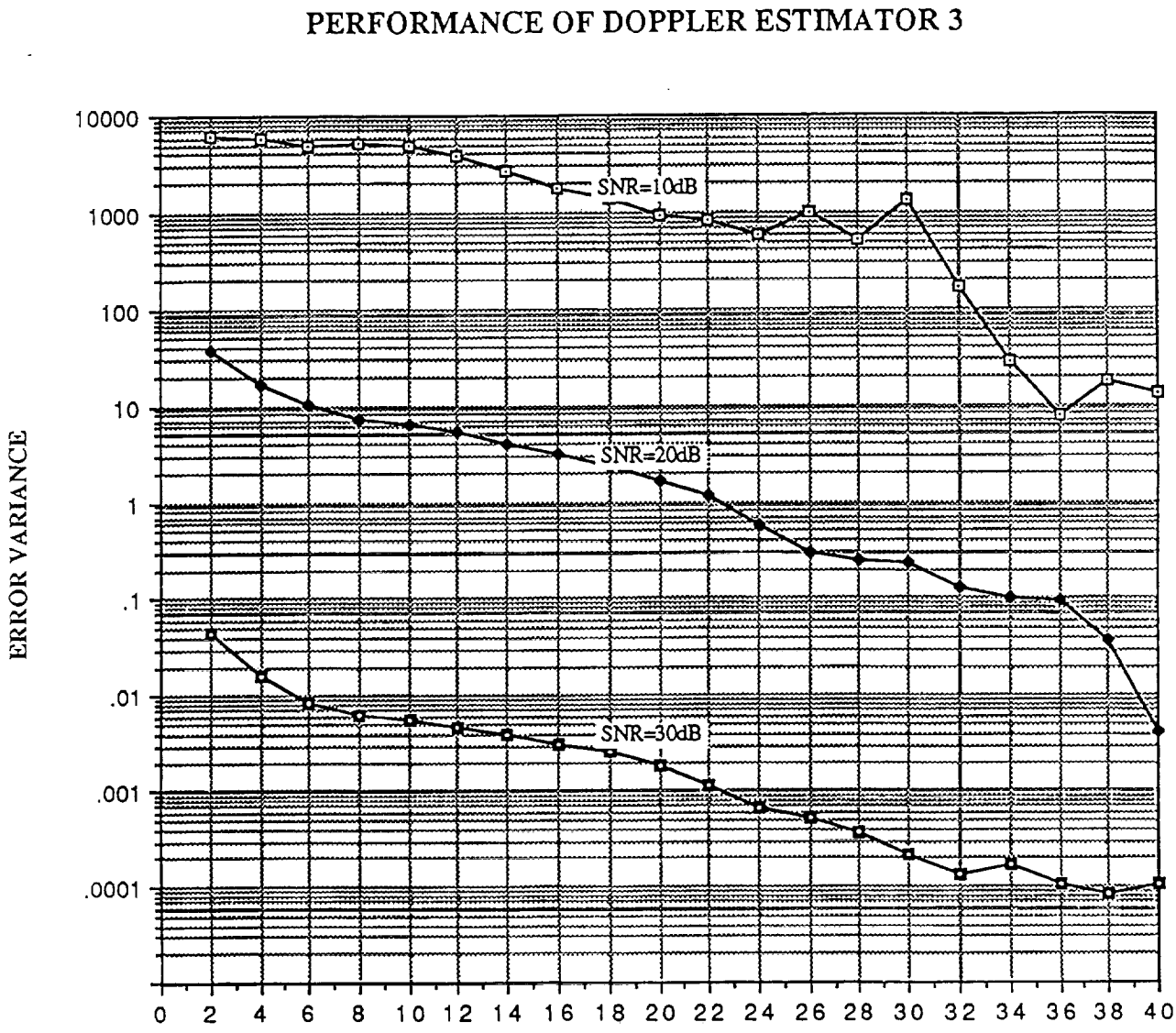

Figure 6.1: Estimator A. Variance of the Doppler frequency estimation error in the presence of AWGN and data modulation, $f_d = 0$ Hz, vs. the number K of samples averaged (abscissa label is $K/100$).

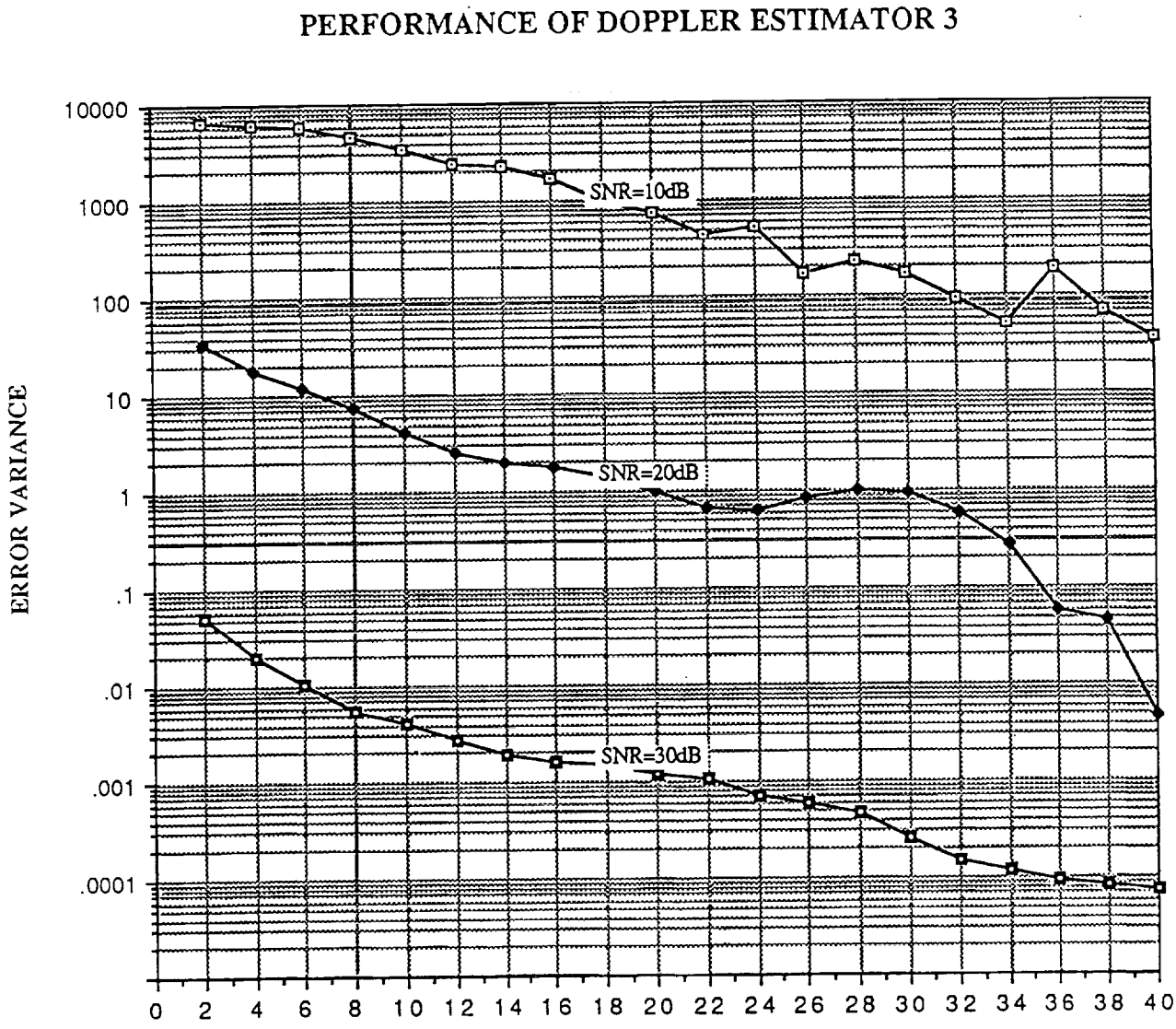

Figure 6.2: Estimator A. Variance of the Doppler frequency estimation error in the presence of AWGN and data modulation, $f_d = 134$ Hz, vs. the number K of samples averaged (abscissa label is $K/100$).

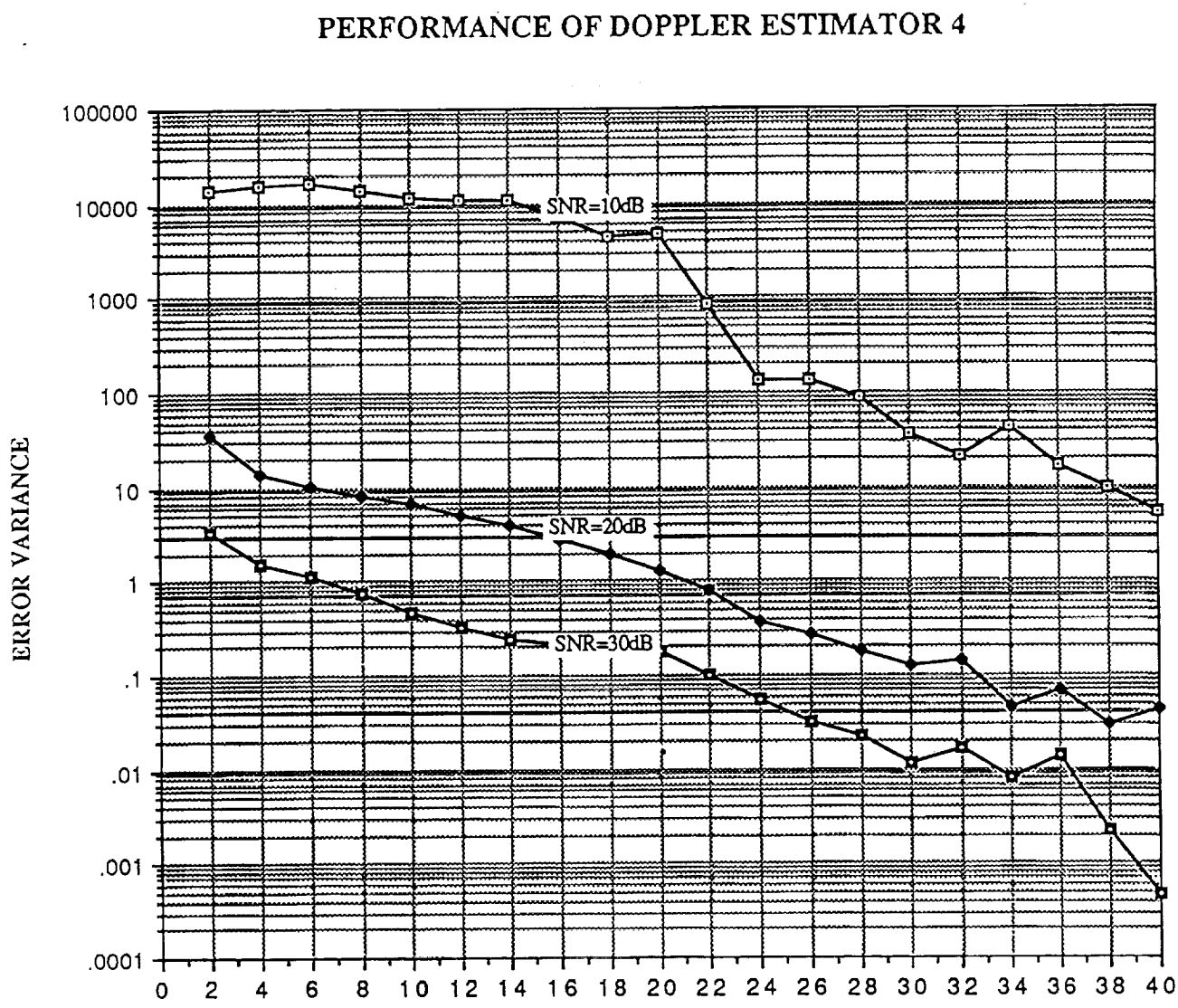

Figure 6.3: Estimator B. Variance of the Doppler frequency estimation error in the presence of AWGN and data modulation, $f_d = 0$ Hz, vs. the number K of samples averaged (abscissa label is $K/100$).

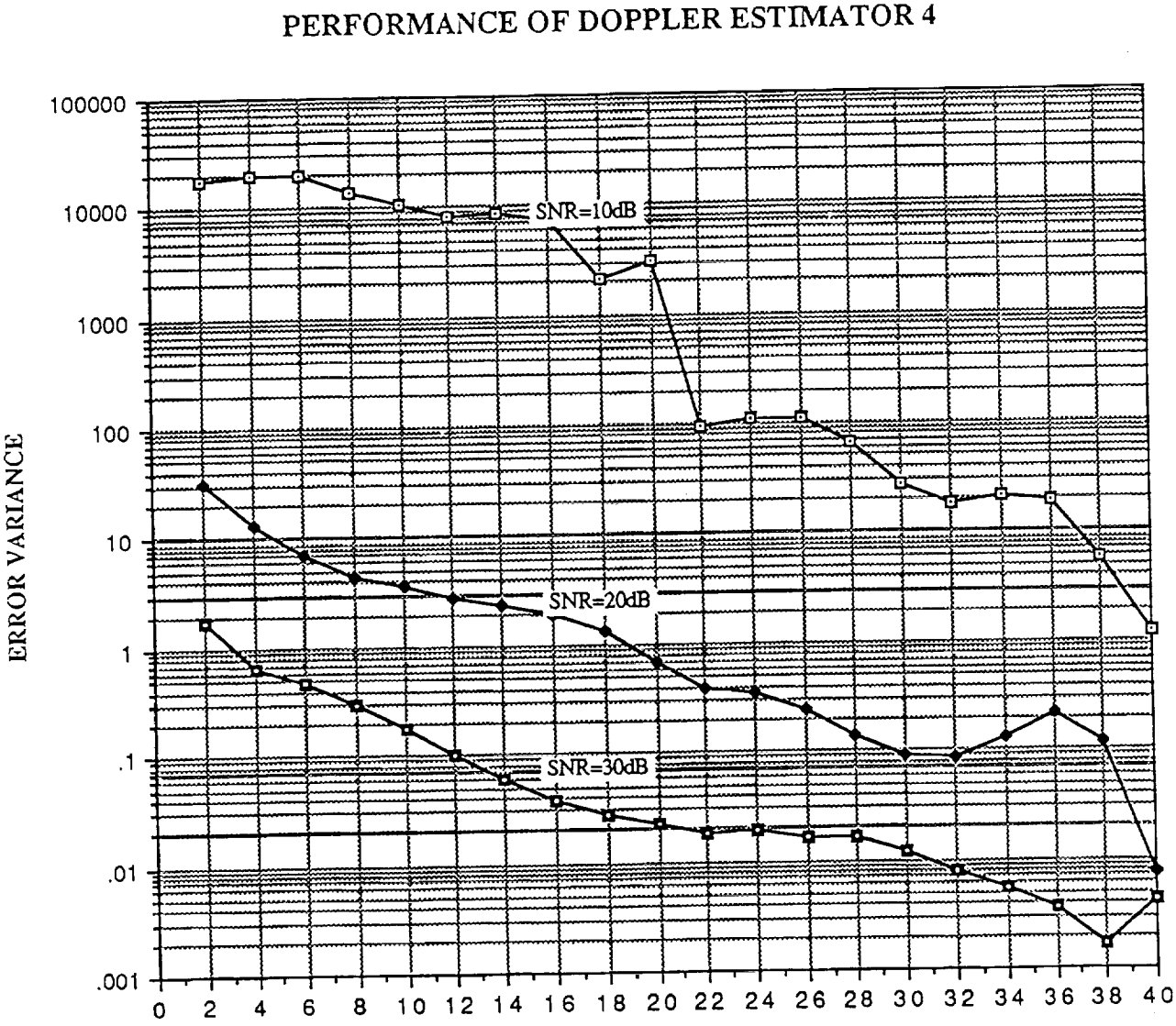

Figure 6.4: Estimator B. Variance of the Doppler frequency estimation error in the presence of AWGN and data modulation, $f_d = 134$ Hz, vs. the number K of samples averaged (abscissa label is $K/100$).

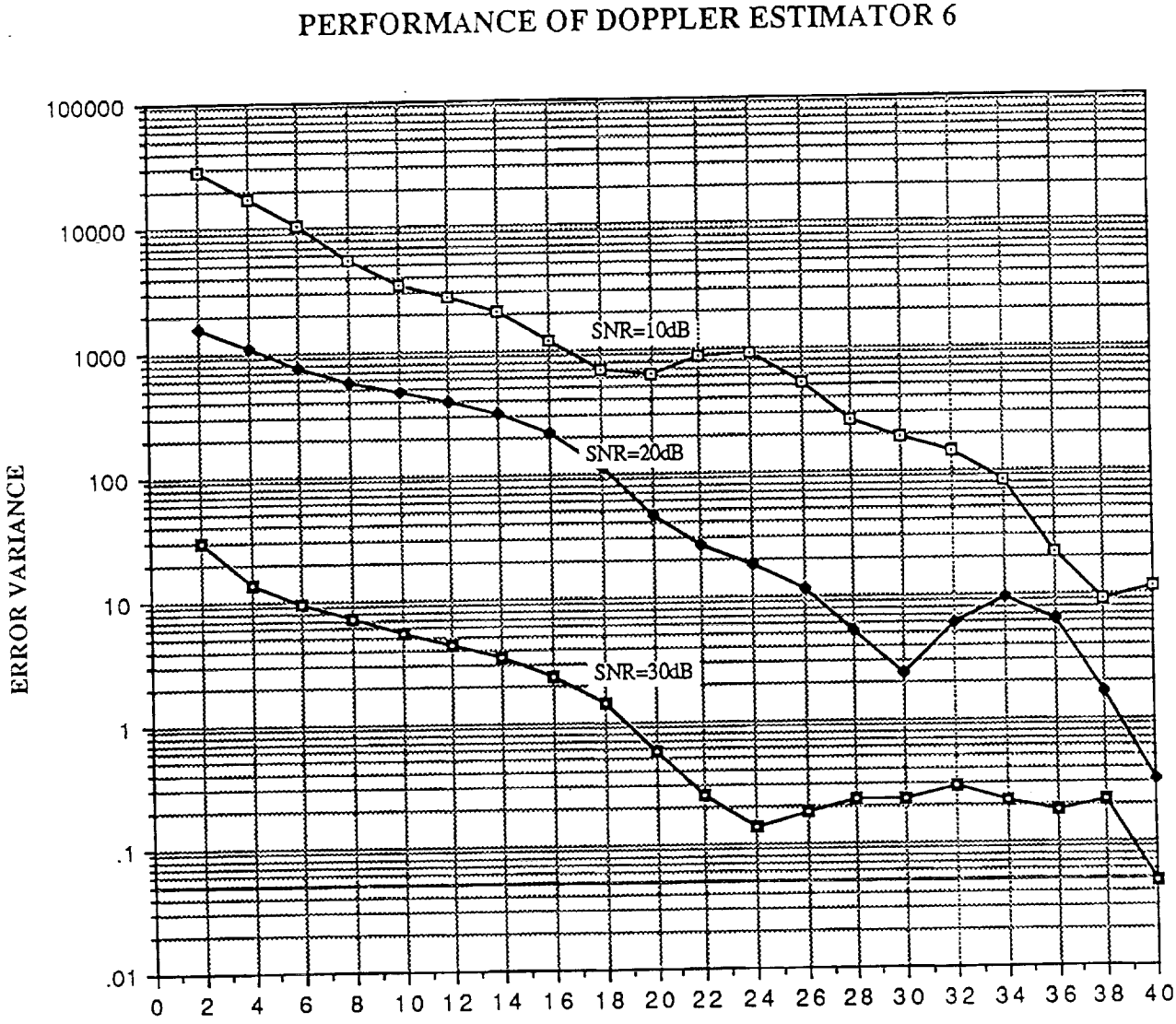

Figure 6.5: Estimator C. Variance of the Doppler frequency estimation error in the presence of AWGN and data modulation, $f_d = 0$ Hz, vs. the number K of samples averaged (abscissa label is $K/100$).

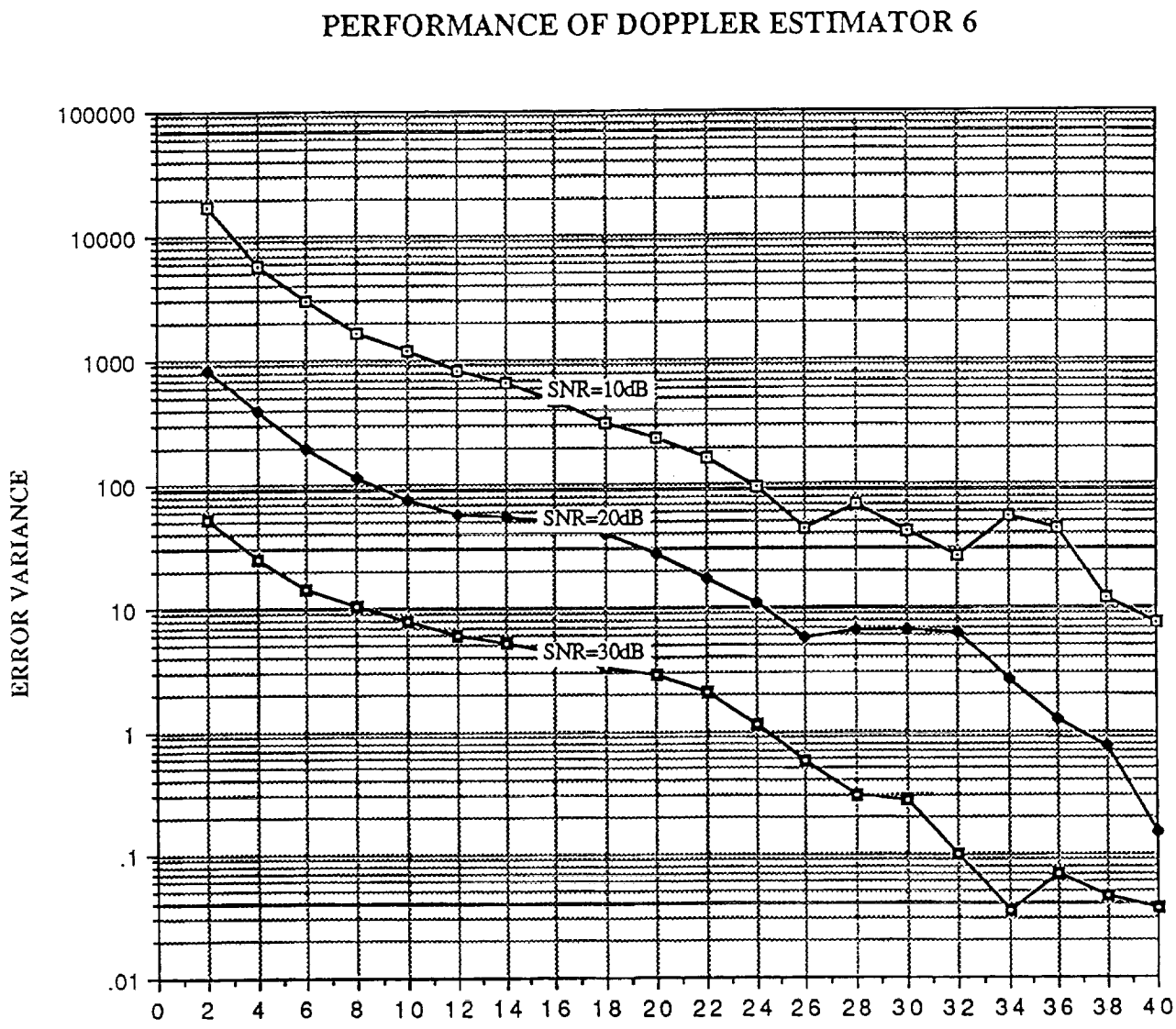

Figure 6.6: Estimator C. Variance of the Doppler frequency estimation error in the presence of AWGN and data modulation, $f_d = 134$ Hz, vs. the number K of samples averaged (abscissa label is $K/100$).

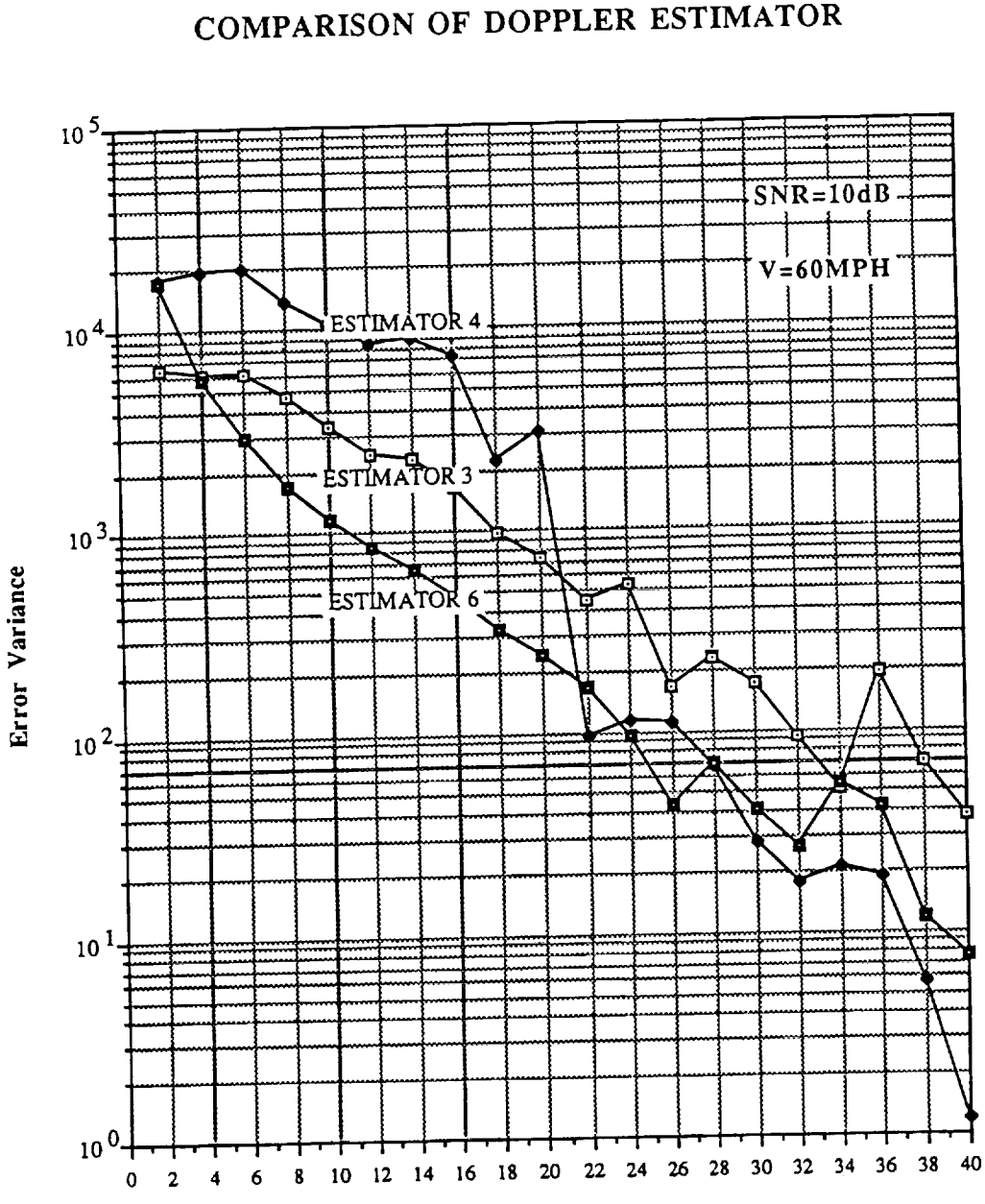

Figure 6.7: Variance of the Doppler frequency estimation error in the presence of AWGN and data modulation, SNR=10 dB, f_d = 134 Hz, vs. the number K of samples averaged (abscissa label is $K/100$).

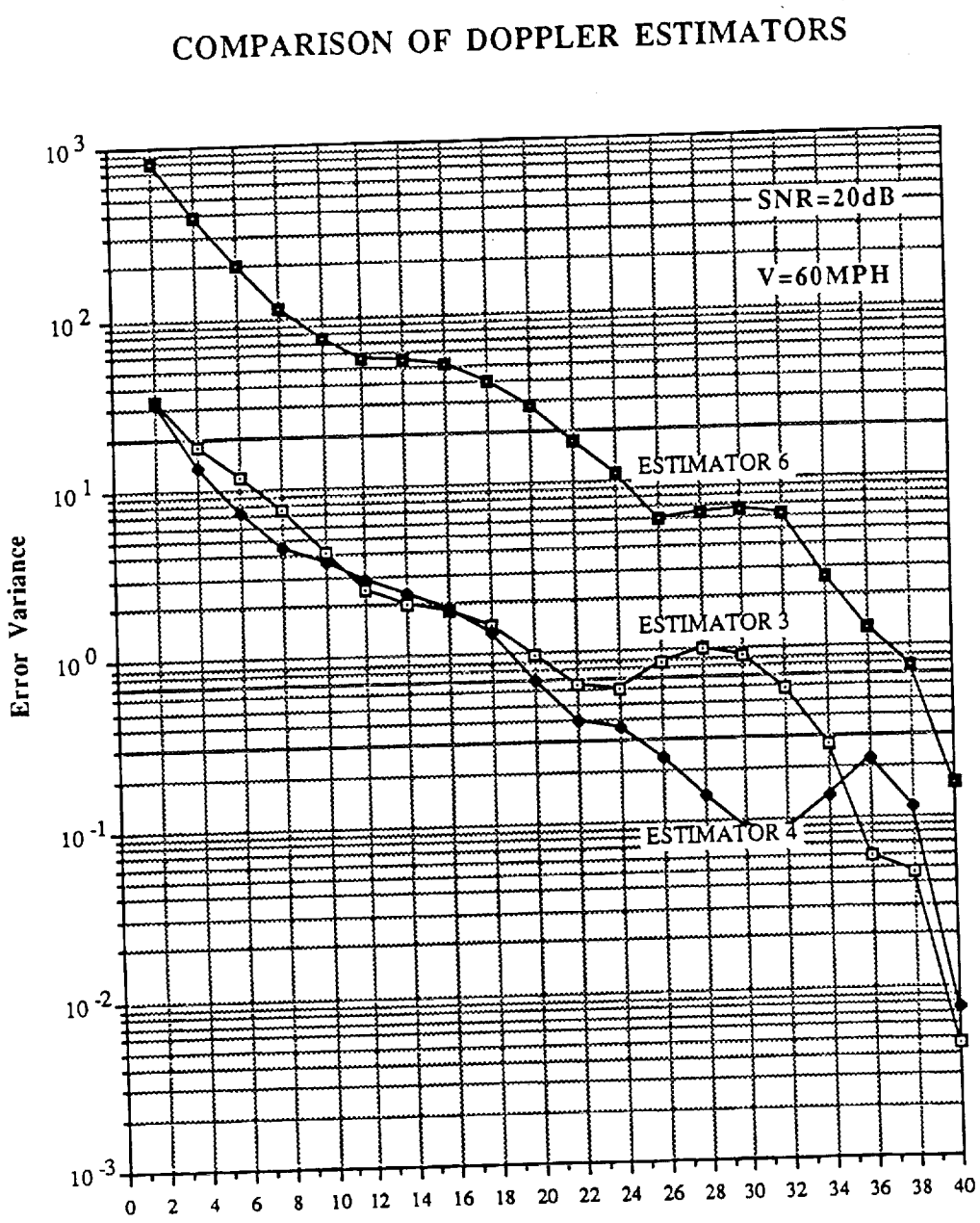

Figure 6.8: Variance of the Doppler frequency estimation error in the presence of AWGN and data modulation, SNR=20 dB, $f_d = 134$ Hz, vs. the number K of samples averaged (abscissa label is $K/100$).

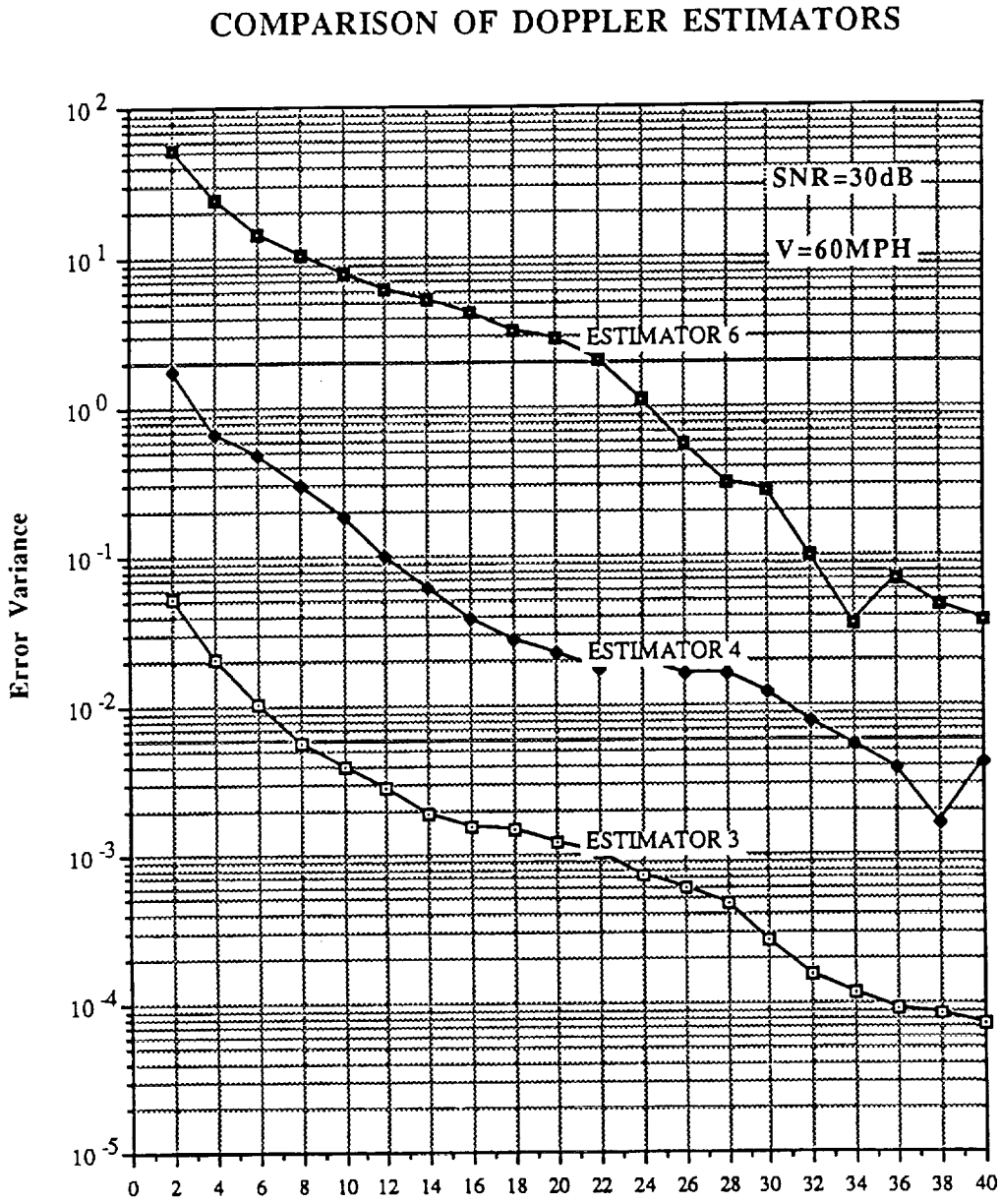

Figure 6.9: Variance of the Doppler frequency estimation error in the presence of AWGN and data modulation, SNR=30 dB, f_d = 134 Hz, vs. the number K of samples averaged (abscissa label is $K/100$).

Chapter 7

Timing recovery circuit

This Chapter presents analysis and simulation of a circuit designed to recover the symbol timing from a CPM signal. This circuit is based on the inherent self-synchronizing capabilities of CPM, and in particular on the property that, when raised to a suitable power, a CPM signal with rational modulation index will exhibit a power spectral density with *spectral lines* spaced by the clock frequency.

After the relevant mathematical analysis, we describe the simulation procedure. Simulation results are presented and interpreted, with the aim of obtaining design guidelines. The conclusion is that, with a proper choice of the filters and of the CPM pulse shapes, this circuit can actually solve the problem of recovering the symbol timing in our system with a high enough accuracy.

7.1 Generalities on symbol synchronization

In this section we show the basic operation of the synchronizer. Later on, we shall expand on this analysis to illustrate how to modify the synchronizer to allow it to work in the presence of fading and Doppler frequency shift. The original design was suggested in [3], which presented the system as a general method for recovering symbol timing and carrier wave phase and frequency in a CPM system. For our purposes, the system was simplified to recover only the symbol timing. Fig. 7.1 shows the elements of the system, with typical filter bandwidths for an 8-ary CPM system, when $R_s = 2400$, $h = 1/8$, and in the absence of Doppler shift.

The analysis in this section is the basis for a computer simulation of the

system. The graphs in this chapter were obtained from simulation, using the above mentioned parameters and a pulse shape of 1-REC. Later, simulation will be used to calculate the variance of the symbol timing jitter in the presence of Rician fading, Doppler shift, and Gaussian noise.

The motivation behind the system stems from the fact that a CPM signal with an integer valued modulation index h contains spectral lines [2], which can be extracted to produce the symbol timing information. When Doppler shift is present, the lines shift in frequency, but, since they all shift the same amount, the timing information is not lost. This will become more clear as the analysis progresses. The underlying principle of the system is based on two standard trigonometric identities:

$$\cos^2 x = \frac{1}{2} + \frac{1}{2}\cos 2x \tag{7.1}$$

$$\cos x \cos y = \frac{1}{2}\cos(x+y) + \frac{1}{2}\cos(x-y) \tag{7.2}$$

These two identities suggest that, given a CPM signal with modulation index, $h = 1/\gamma$, we can change it into a CPM signal with $h = 1$ by raising the signal to the γ^{th} power. This is illustrated below, with a simple cosine function with argument θ:

$$\cos^2 \theta = \frac{1}{2} + \frac{1}{2}\cos 2\theta \tag{7.3}$$

$$\cos^3 \theta = \frac{3}{4}\cos\theta + \frac{1}{4}\cos 3\theta \tag{7.4}$$

$$\cos^4 \theta = \frac{3}{8} + \frac{1}{2}\cos 2\theta + \frac{1}{8}\cos 4\theta \tag{7.5}$$

So, if we pass a CPM signal with $h = 1/\gamma$ through a γ-power device, the value of θ in the above equations is $2\pi f_0 t + \phi(t, \bar{\alpha})$. The output from the device contains several cosine terms, including one with argument $\gamma 2\pi f_0 t + \gamma\phi(t, \bar{\alpha})$. Now, since the original $\phi(t, \bar{\alpha})$ is calculated using h as the modulation index, the "new" $\phi(t, \bar{\alpha})$ is essentially the same as the original one, except that the "new" h is equal to γ times the original h, or $h_{new} = \gamma h_{original} = 1$. In [2] it is shown that an integer-h CPM system contains spectral lines, and the "new" CPM signal, with $h = 1$, is in that category.

7.1.1 Basic Synchronizer

Figure 7.1 is the block diagram of the basic synchronizer. The operation is straightforward. First, BPF1 passes the received signal, while limiting

the amount of noise. Next, the CPM signal is passed through a γ-power device, which changes it to integer-h CPM. Now, the only term in the power expansion that is useful is the highest frequency term (γf_0), so BPF2 selects the zone of frequencies near γf_0. Next, filters NBF1 and NBF2 each select a spectral line, one located at $\gamma f_0 + nR_s/2$ and one at $\gamma f_0 - nR_s/2$, which appear in the newly formed integer-h CPM. The two selected lines are then multiplied together to form sum and difference frequencies. The difference frequency is then selected by LBPF, yielding a sinusoid of frequency nR_s. The frequency of the recovered sinusoid is then divided by n, yielding a signal with frequency R_s, the symbol rate.

7.1.2 Low-Pass Equivalent Signals

In order to simulate the system described in Fig. 7.1, low-pass equivalent signals representing the *complex envelopes* of the bandpass signals were used throughout the simulation. (This is also a possible means of actual hardware implementation.) The advantage of using low-pass equivalents instead of their bandpass counterparts is that a lower sampling rate could be used, without any loss of information. This keeps simulation run times to a minimum. For this reason, the frequency spectrum plots shown in this chapter are for the complex envelopes of each signal. The spectrum of the actual bandpass signals are derived by shifting the spectrum of the complex envelope up in frequency, such that the dc (zero-frequency) component is located at the reference frequency of each plot, and each plot, being symmetrical, is reflected across its own reference frequency.

Although the analysis below is general enough to include the effects of Doppler shift, noise, and fading, the spectra illustrated in this chapter were calculated without adding any of these parameters, in order to illustrate the basic principles of the system without any complications. The effects of those parameters on symbol timing recovery will be included later.

7.2 System Analysis

7.2.1 Signal Definitions

We begin the analysis by referring to the definition of the CPM signal. The spectrum of this signal (point "A" on Fig. 7.1) is shown in Fig. 7.2. This plot is the spectrum of the complex envelope of the signal, whichs is referenced to f_c, the carrier frequency of the CPM signal. This spectrum

was calculated using the computer simulation to provide a time-domain representation of the signal, and then taking the discrete Fourier transform of the data points. The sampling frequency of the simulation was $f_s = 16R_s$. BPF1 was designed to have a bandwidth sufficiently wide to pass the CPM signal undistorted, and to allow for a given amount of Doppler shift, while limiting noise. Therefore, the spectrum at point "B" is identical to the spectrum at point "A", except that the noise power at "B" is reduced. A theoretical power spectrum is shown in Fig. 7.3, which was calculated using a technique described in [9] and presented in greater detail in what follows. In Fig. 7.3, the frequency range is normalized to the symbol rate, R_s, but the plot is otherwise in agreement with the simulated results. Notice that the magnitudes of the two power spectra are different, but that the relative magnitudes are essentially the same. There are two reasons for the difference in *absolute* magnitude. First, the theoretical graph is normalized to the symbol rate, so the magnitude is scaled to the normalization factor. Second, the simulation results were calculated using a discrete Fourier transform, so the resulting power level depends on the block-length N. Notice that the main lobe of the signal is fairly narrow, with a low-pass-equivalent 3 dB bandwidth of about $R_s/4$ (the actual band-pass signal has twice this bandwidth, or $R_s/2$).

At the output of BPF1, we have the undistorted CPM signal with Doppler shift, Δf, plus bandpass Gaussian noise, $n(t)$ (In this section Δf and $n(t)$ are both set to 0, but they are included for completeness.) We let the signal power be P. Thus

$$\begin{aligned} y(t) &= \sqrt{2P}\cos\left(2\pi(f_0+\Delta f)t + \phi(t,\bar{\alpha})\right) + n(t) && (7.6)\\ &= I(t)\cos 2\pi f_0 t - Q(t)\sin 2\pi f_0 t && (7.7)\end{aligned}$$

where

$$I(t) = \sqrt{2P}\cos\left(2\pi\Delta f t + \phi(t,\bar{\alpha})\right) + n_c(t) \quad (7.8)$$

$$Q(t) = \sqrt{2P}\sin\left(2\pi\Delta f t + \phi(t,\bar{\alpha})\right) + n_s(t) \quad (7.9)$$

and $n_c(t)$ and $n_s(t)$ are the in-phase and quadrature-phase noise components, respectively. In polar form:

$$y(t) = R(t)\cos\left(2\pi f_0 t + \theta(t)\right) \quad (7.10)$$

where

$$R(t) = \sqrt{I^2(t) + Q^2(t)} \quad (7.11)$$

$$\theta(t) = \tan^{-1}\frac{Q(t)}{I(t)} \quad (7.12)$$

7.2.2 γ-Power Device Operation

At the output of the γ-power device, the signal enters BPF2, which serves as a zonal filter, allowing components in the vicinity of γf_0 to pass through it. The signal in the vicinity of γf_0 is:

$$\begin{aligned} y^\gamma(t) &= [R^\gamma(t)\cos^\gamma(2\pi f_0 t + \theta(t))]_{\gamma f_0} \\ &= k[R^\gamma(t)\cos(\gamma\theta(t))\cos 2\pi\gamma f_0 t - R^\gamma(t)\sin(\gamma\theta(t))\sin 2\pi\gamma f_0 t] \\ &= I_\gamma(t)\cos 2\pi\gamma f_0 t - Q_\gamma(t)\sin 2\pi\gamma f_0 t \\ &= \mathrm{Re}[R^\gamma(t)e^{j\gamma\theta(t)}e^{j2\pi\gamma f_0 t}] \end{aligned} \tag{7.13}$$

where k is a constant, and equation (7.13) is a bandpass signal with complex envelope (referenced to γf_0):

$$U(t) = R^\gamma(t)e^{j\gamma\theta(t)} \tag{7.14}$$

Without noise, and with $h = 1/\gamma$,

$$\gamma\theta(t) = \gamma\phi(t,\bar{\alpha}) = \gamma(2\pi\frac{1}{\gamma})\sum_{i=-\infty}^{\infty}\alpha_i q(t-iT_s) = 2\pi\sum_{i=-\infty}^{\infty}\alpha_i q(t-iT_s) \tag{7.15}$$

which corresponds to *integer-valued h* CPM, having spectral lines located at odd integral multiples of $R_s/2$, as shown in [2]. The spectrum at point "C" is shown in Fig. 7.4, which is the low-pass equivalent spectrum referenced to f_0. The actual bandpass signal has 8 spectral lines centered about f_0. The spectral lines are very striking in that plot, confirming the results in [2].

7.2.3 Filters NBF1 and NBF2

Next, we need to select certain spectral lines using bandpass filters NBF1 and NBF2. The choice is somewhat arbitrary. In fact, any narrow filter should work (without Doppler shift). Since the signal is defined as a low-pass signal, the bandpass filters must also be described in terms of their low-pass equivalents, with in-phase and quadrature-phase impulse response components of each filter.

We will analyze the case for NBF1; the analysis for NBF2 is identical, except for several obvious substitutions. Starting with the signal entering the filter, we realize that it is a low-pass signal referenced to γf_0. NBF1 has a center frequency of $(\gamma f_0 + nR_s/2)$, which means it can be described

by a low-pass filter, referenced to its center frequency. It has an impulse response:

$$h(t) = \mathrm{Re}[\tilde{h}(t)e^{j2\pi(\gamma f_0 + \frac{n}{2}R_s)t}] \tag{7.16}$$

where

$$\tilde{h}(t) = h_c(t) + jh_s(t) \tag{7.17}$$

and $h_c(t)$ and $h_s(t)$ are the in-phase and quadrature-phase impulse responses of the filter. Rewriting the bandpass signal, $x(t)$, entering NBF1 as:

$$\begin{aligned} x(t) &= \mathrm{Re}[\tilde{x}(t)e^{j2\pi\gamma f_0 t}] && (7.18)\\ &= \mathrm{Re}[\tilde{x}(t)e^{-j2\pi\frac{n}{2}R_s t}e^{j2\pi(\gamma f_0 + \frac{n}{2}R_s)t}] && (7.19)\\ &= \hat{x}_c(t)\cos 2\pi(\gamma f_0 + \frac{n}{2}R_s)t - \hat{x}_s(t)\sin 2\pi(\gamma f_0 + \frac{n}{2}R_s)t && (7.20) \end{aligned}$$

where

$$\tilde{x}(t) = x_c(t) + jx_s(t) \tag{7.21}$$

$$\begin{aligned} \hat{x}_c(t) &= \mathrm{Re}[\tilde{x}(t)e^{-j2\pi\frac{n}{2}R_s t}]\\ &= x_c(t)\cos(2\pi\frac{n}{2}R_s t) + x_s(t)\sin(2\pi\frac{n}{2}R_s t) \end{aligned}$$

$$\begin{aligned} \hat{x}_s(t) &= \mathrm{Im}[\tilde{x}(t)e^{-j2\pi\frac{n}{2}R_s t}]\\ &= -x_c(t)\sin(2\pi\frac{n}{2}R_s t) + x_s(t)\cos(2\pi\frac{n}{2}R_s t) \end{aligned}$$

where $x_c(t)$ and $x_s(t)$ are the in-phase and quadrature components of the low-pass equivalent of $x(t)$.

Now, with this new signal referenced to the same center frequency as NBF1, we use the equivalent low-pass filtering technique described in [10] and diagramed in Fig. 7.5. The digital filters used were designed using *Atlanta Signal Processors Digital Filter Design Package Version 1.02.* With symmetrical bandpass filters referenced to their center frequencies, only the in-phase component, $h_c(t)$, of the impulse response is needed, since the quadrature-phase component, $h_s(t)$, is exactly zero. Therefore, Fig. 7.5 simplifies to Fig. 7.6. A similar analysis holds for NBF2, with $x(t)$ being re-referenced to $(\gamma f_0 - nR_s/2)$. Thus, we produce $y_1(t)$, the filtered version of $x(t)$ through NBF1, and $y_2(t)$, the filtered version of $x(t)$ through NBF2. The power spectrum at point "D" is shown in Fig. 7.7, and at point "E" in Fig. 7.8 using $n = 1$. In Fig. 7.7. These two figures are plotted slightly differently from the others. They include both the positive and the negative

frequencies of the spectra, since the spectra are not symmetrical about their center frequencies, and it is important to show what is occurring on each side of the center frequency. In Fig. 7.7, the center frequency is $(\gamma f_0 + 1/2T_s)$. Notice that there are 3 additional spectral lines that are higher in frequency than the selected line, and 4 lines lower in frequency. Although the presence of these additional spectral lines is visually apparent in the graphs, they are attenuated about 55 dB from the spectral line of interest, due to the attenuation of the narrow-band filters. Since they are greatly attenuated, they actually have little effect in the spectrum. In Fig. 7.8, the center frequency is $(\gamma f_0 - 1/2T_s)$. In that graph, there are 4 spectral lines in the positive frequency direction, and 3 lines in the negative direction. The difference between the two plots is related to the spectral line that we are recovering; the first one has 3 lines above it, and the second one has 4. But in either case, the additional lines are greatly attenuated, so as to be insignificant.

In Figs. 7.7 and 7.8, there are basically two discrete frequency signals (one at $\gamma f_0 + 1/2T_s$, and one at $\gamma f_0 - 1/2T_s$) plus some continuum, due to the randomness of the data stream and any additive noise in the signal. (If the data stream were periodic and there were no additive noise, there would not be any continuum.) At point "D", the signal is a sinusoid of frequency $(\gamma f_0 + nR_s/2)$. At point "E", it has a frequency of $(\gamma f_0 - nR_s/2)$. When the two are multiplied together, they produce a signal that has the sum and difference of the two frequencies. The resultant waveform contains three types of components: line $\times$ line (the desired components), line $\times$ continuum, and continuum $\times$ continuum. Obviously, the first component is what we need to produce our final results, while the effects of the additional components must be minimized.

7.2.4 Multiplier and LBPF

Next, we multiply these two bandpass signals together, and keep them in low-pass terms, referenced to a common center frequency. We have the two signals, $y_1(t)$, which is referenced to $(\gamma f_0 + nR_s/2)$, and $y_2(t)$, which is referenced to $(\gamma f_0 - nR_s/2)$. Writing them as bandpass signals, we have:

$$y_1(t) = y_{c_1}(t)\cos 2\pi(\gamma f_0 + \frac{n}{2}R_s)t - y_{s_1}(t)\sin 2\pi(\gamma f_0 + \frac{n}{2}R_s)t \qquad (7.22)$$

$$y_2(t) = y_{c_2}(t)\cos 2\pi(\gamma f_0 - \frac{n}{2}R_s)t - y_{s_2}(t)\sin 2\pi(\gamma f_0 - \frac{n}{2}R_s)t \qquad (7.23)$$

Multiplying them together yields

$$\begin{aligned} y_1(t)y_2(t) &= \frac{y_{c_1}(t)y_{c_2}(t)}{2}[\cos 2\pi 2\gamma f_0 t + \cos 2\pi n R_s t] \\ &\quad -\frac{y_{c_1}(t)y_{s_2}(t)}{2}[\sin 2\pi 2\gamma f_0 t - \sin 2\pi n R_s t] \\ &\quad -\frac{y_{c_2}(t)y_{s_1}(t)}{2}[\sin 2\pi n R_s t + \sin 2\pi 2\gamma f_0 t] \\ &\quad +\frac{y_{s_1}(t)y_{s_2}(t)}{2}[\cos 2\pi n R_s t - \cos 2\pi 2\gamma f_0 t] \end{aligned} \tag{7.24}$$

which contains frequency components around $2\gamma f_0$ and nR_s. This suggests that we can now recover either the carrier frequency (by high-pass filtering and dividing by 2γ), or the symbol timing information (clock rate). To recover the symbol timing, we select the components around nR_s. In the vicinity of nR_s:

$$\begin{aligned} z(t) = y_1(t)y_2(t) &= \frac{1}{2}(y_{c_1}(t)y_{c_2}(t) + y_{s_1}(t)y_{s_2}(t))\cos 2\pi n R_s t \\ &\quad -\frac{1}{2}(y_{c_2}(t)y_{s_1}(t) - y_{s_2}(t)y_{c_1}(t))\sin 2\pi n R_s t \end{aligned} \tag{7.25}$$

So, the low-pass equivalent signal referenced to nR_s is:

$$z(t) = \mathrm{Re}[\tilde{z}(t)e^{j2\pi n R_s t}] \tag{7.26}$$

with

$$\tilde{z}(t) = z_c(t) + jz_s(t) \tag{7.27}$$

and

$$z_c(t) = \frac{1}{2}(y_{c_1}(t)y_{c_2}(t) + y_{s_1}(t)y_{s_2}(t)) \tag{7.28}$$

$$z_s(t) = \frac{1}{2}(y_{c_2}(t)y_{s_1}(t) - y_{s_2}(t)y_{c_1}(t)) \tag{7.29}$$

The spectrum of this recovered signal is shown in Fig. 7.9, representing the signal at point "F". In the simulation we have let $n = 1$, so the spectrum in the figure is referenced to $nR_s = R_s$, the symbol rate. This signal is then filtered by LBPF in a similar way as in NBF1 and NBF2. Now, we have a signal $T(t)$, which is the filtered version of $z(t)$, with an in-phase component, $T_c(t)$, and a quadrature-phase component $T_s(t)$. $T(t)$ will become the symbol timing signal, $T_{sym}(t)$. The bandpass signal after LBPF is now:

$$T(t) = \mathrm{Re}[(T_c^2(t) + T_s^2(t))^{1/2} e^{j(2\pi n R_s t + \phi(t))}] \tag{7.30}$$

where

$$\phi(t) = \arctan\left(\frac{T_s(t)}{T_c(t)}\right) \tag{7.31}$$

7.2.5 Symbol Timing Recovery

In order to recover the symbol timing signal, the hardware would count zero crossings of this bandpass signal, and then divide the frequency by n. For simulation purposes, we form the signal

$$T_{sym}(t) = \cos\frac{1}{n}[2\pi n R_s t + \phi(t)] \tag{7.32}$$

which is a sinusoid of frequency $2\pi R_s$, and phase, $\phi(t)/n$, that varies slightly with time, otherwise known as phase jitter. Ideally, $\phi(t)/n$ would be constant at a value proportional to the time delay between when the signal is transmitted and when it is received. This allows the system to track the CPM signal, given varying delay times. Of course, in practice, the phase is not constant, due to the noise, fading, and signal dependent jitter. Therefore, a suitable performance measure is the variance of $\phi(t)$, which is a measure of how $\phi(t)$ varies with time. The spectrum of the recovered signal is shown in Fig. 7.10, representing the signal at point "G". Since this is the signal of interest, we have chosen to plot the spectrum of the actual bandpass signal, rather than the spectrum of the complex envelope of the signal. Therefore, the line at $R_s = 2400$ contains the symbol timing information (frequency and phase). The phase of this recovered signal is shown in Fig. 7.11. The variance of the recovered phase in the figure is 1.3×10^{-6}, which is quite small. A more detailed discussion on interpreting the phase-jitter variance is included later.

7.2.6 Fading Description

In order to simulate the fading effects on the CPM signal, a Rician fading model was used. The complex fading envelope has an in-phase and quadrature-phase component given by:

$$F_c(t) = A + w_c(t) \tag{7.33}$$

$$F_s(t) = w_s(t), \tag{7.34}$$

where A is the direct component, and $w_c(t)$ and $w_s(t)$ combine to give the scattered component of the signal. The ratio $P_{direct}/P_{scattered}$ is called K,

where

$$K = \frac{A^2/2}{\sigma_{scat}^2} \tag{7.35}$$

and σ_{scat}^2 is the power in the scattered component. The scattered component of the signal is calculated by first generating two independent sequences of white Gaussian variables, each with a variance σ_i^2. The two sequences are then filtered by a low-pass filter, yielding a variance (coming out of the filter) of σ_{scat}^2, which is equal to the power in the scattered component of the noise. The bandwidth of this filter is chosen to equal the *Doppler spread*, B_d, of the channel [17]. The reciprocal of B_d is approximately equal to the *coherence time* of the channel, which is a measure of how fast the envelope of the fading signal changes. A large coherence time means that the fading signal is slow to change, and that the bandwidth, B_d, is fairly narrow. In our simulation, we used a slow-fading approximation, which means $B_d \ll R_s$ (in our case, $B_d \approx 100$ Hz), and the fading variable was updated only once every symbol time, so it stayed constant from symbol to symbol. The relationship between the input variance and output variance of a Gaussian random process going through a linear, shift-invariant filter is:

$$\sigma_0^2 = \frac{B}{f_s/2}\sigma_i^2 \tag{7.36}$$

where f_s is the sampling frequency, and B is the one-sided noise-equivalent bandwidth of the low-pass filter (100 Hz in our case). Therefore, σ_{scat}^2 is given by:

$$\sigma_{scat}^2 = \frac{B}{f_s/2}\sigma_i^2 \tag{7.37}$$

Combining (7.35) and (7.37), we find that σ_i^2 is given by

$$\sigma_i^2 = \frac{A^2 f_s}{4KB} \tag{7.38}$$

Once the fading envelope is generated, the original CPM signal is multiplied by the fading envelope to produce:

$$\begin{aligned} I_{fade}(t) &= \mathrm{Re}\{(I(t) + jQ(t))(F_c(t) + jF_s(t))\} \\ &= I(t)F_c(t) - Q(t)F_s(t) \end{aligned} \tag{7.39}$$

$$\begin{aligned} Q_{fade}(t) &= \mathrm{Im}\{(I(t) + jQ(t))(F_c(t) + jF_s(t))\} \\ &= I(t)F_s(t) + Q(t)F_c(t) \end{aligned} \tag{7.40}$$

7.2.7 Noise Description

Finally, in order to add bandpass noise to the signal, we use a low-pass equivalent noise signal. We must first determine a relationship between σ_i^2, the input variance of the Gaussian noise source, and E_b/N_0, the bit energy per noise power density ratio. For a bandpass filter with bandwidth $2B$, we know the following:

$$\frac{S}{N} = \frac{P}{N_0 2B} = \frac{E_b R_b}{N_0 2B} = \frac{R_b}{2B}\left(\frac{E_b}{N_0}\right) \tag{7.41}$$

Therefore,

$$N = \frac{P2B}{R_b(E_b/N_0)} = \sigma_0^2 \tag{7.42}$$

Setting equation (7.36) equal to (7.42) gives:

$$\sigma_i^2 = \frac{P f_s}{R_b(E_b/N_0)} \tag{7.43}$$

Therefore, in order to simulate a given E_b/N_0, we generate two independent sequences of white Gaussian variables with variance σ_i^2, defined by equation (7.43). Then, we filter those sequences through BPF1, using the technique in Fig. 7.6, and the resulting σ_0^2 produces the desired E_b/N_0, when the noise is added to the signal. A plot of the noise spectrum is shown in Fig. 7.12, for $E_b/N_0 = 10$ dB, with a low-pass equivalent bandwidth of 2500 Hz for BPF1. The sidelobes in the noise spectrum are a result of using an elliptic filter design for BPF1, since the noise spectrum is essentially the frequency response of BPF1.

The nex Section will address the additional problems encountered when the CPM signal gets faded, noise is added, and Doppler frequency shift is introduced.

7.3 Application to Mobile Environment

The basic synchronizer system described in the last section was designed for a non-mobile (stationary), non-fading environment. However, in a mobile environment there are additional problems that must be taken into account, in order to ensure that the synchronizer will work.

7.3.1 Time Delay

The basic problem that must be solved in any environment is to recover the phase of R_s, which is proportional to the time delay between the point when the CPM signal gets transmitted and when it is received. In the mobile environment, accurate phase recovery is important because of the unknown distance (hence unknown delay time) between the vehicle and the satellite. As an example, a time delay that is an integer multiple of $T_s/4$ would yield a recovered phase, ϕ, equal to $2\pi/4 = \pi/2$. Because of the extreme importance in recovering this exact phase, *the synchronizer must be able to unambiguously track the symbol timing over the range 0 to T_s, and over any time delay.*

Notice that the last block of Fig. 7.1 is a divide-by-n function. The analysis in the last section suggests the reason why the divide-by-n is needed. Basically, the frequency of the recovered signal entering the divide-by-n block is n times the symbol rate (nR_s). Because the *phase* of the signal gets divided by n as well as the *frequency*, a value of n that is anything other than 1 will produce an n-fold ambiguity in the recovered phase of the signal. Take, for example, the case when $n = 3$. Assume the true phase of the CPM signal is $2\pi/3$. When multiplied by 3, it becomes 2π, and after the divide-by-n, it becomes $2\pi/3$. Next assume the true phase is $4\pi/3$. When multiplied by 3, it becomes 4π, which is indistinguishable from 2π. When passed through the divide-by-n, it becomes $2\pi/3$, which is obviously incorrect. Similarly, a CPM signal with a true phase of 2π becomes $2\pi/3$ at the output of the synchronizer. Clearly, this produces an ambiguity in the recovered phase. The result of this ambiguity is the inability to track the recovered phase for varying signal delays.

There are several approaches to resolving this ambiguity problem. One approach is to recover *two* pairs of spectral lines, such as the $n = 5$ and the $n = 7$ lines. That will produce two phases, $\phi_5(t)$ and $\phi_7(t)$, which may be different from one another:

$$\phi_5(t) = \beta_5(t) + e_5\frac{2\pi}{5} \tag{7.44}$$

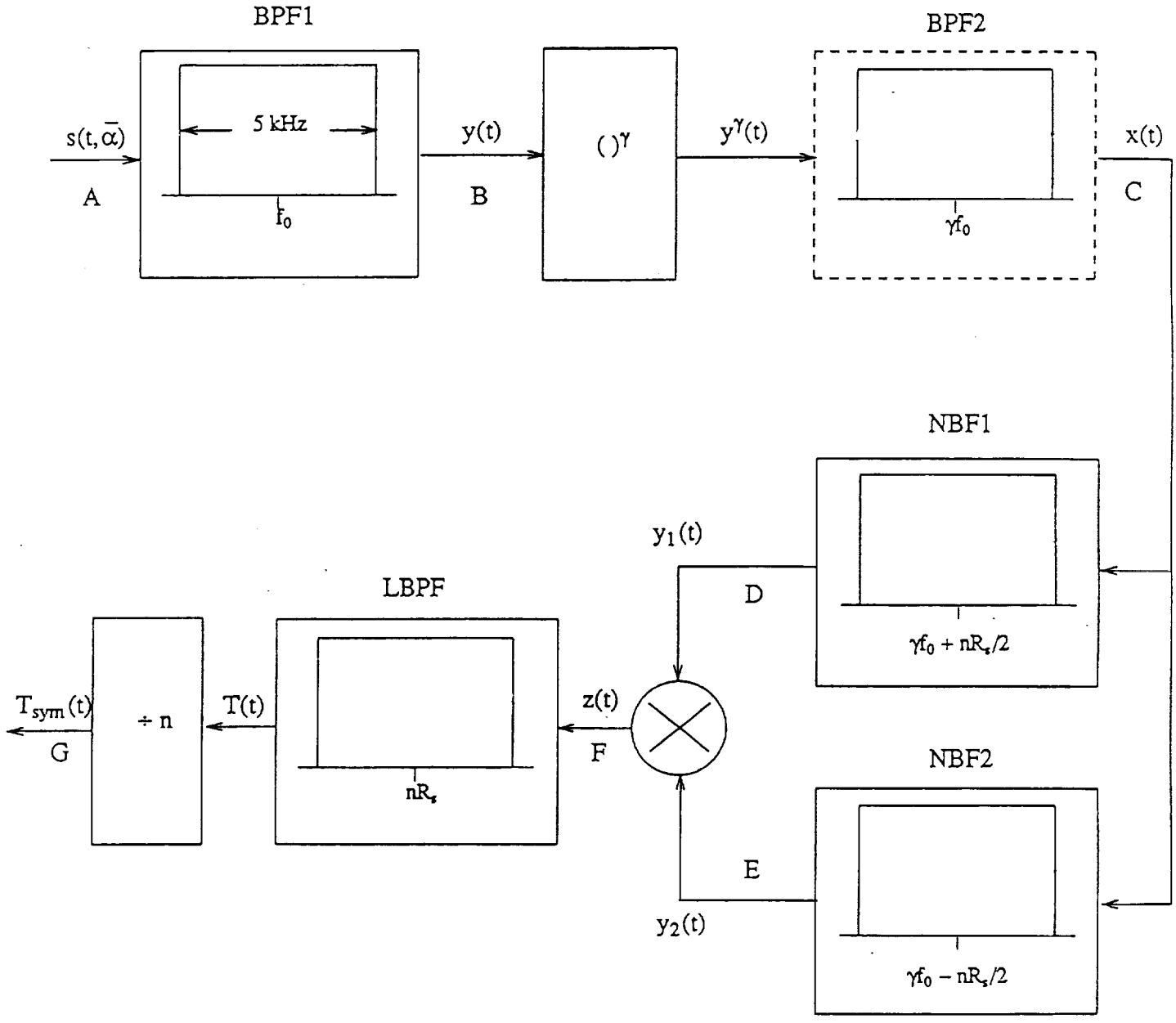

Figure 7.1: Symbol Synchronizer Block Diagram

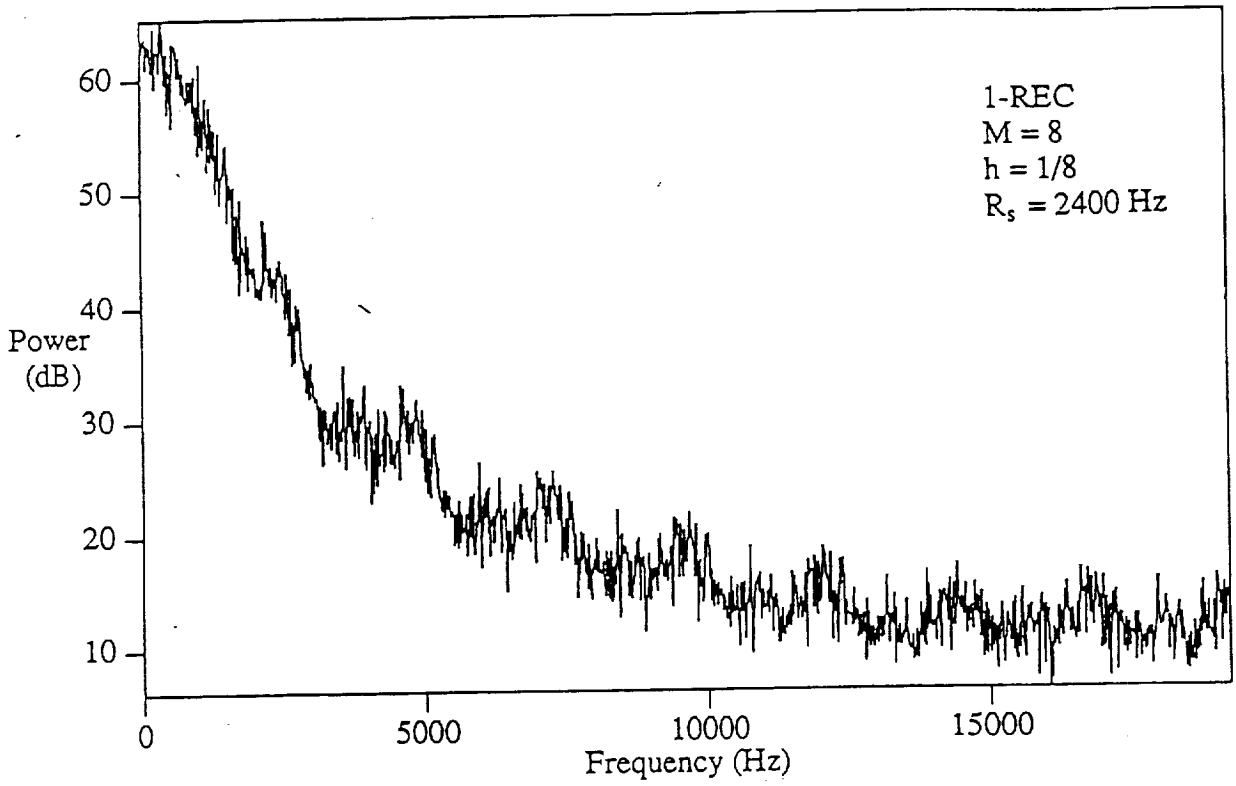

Figure 7.2: CPM spectrum (Point "A")

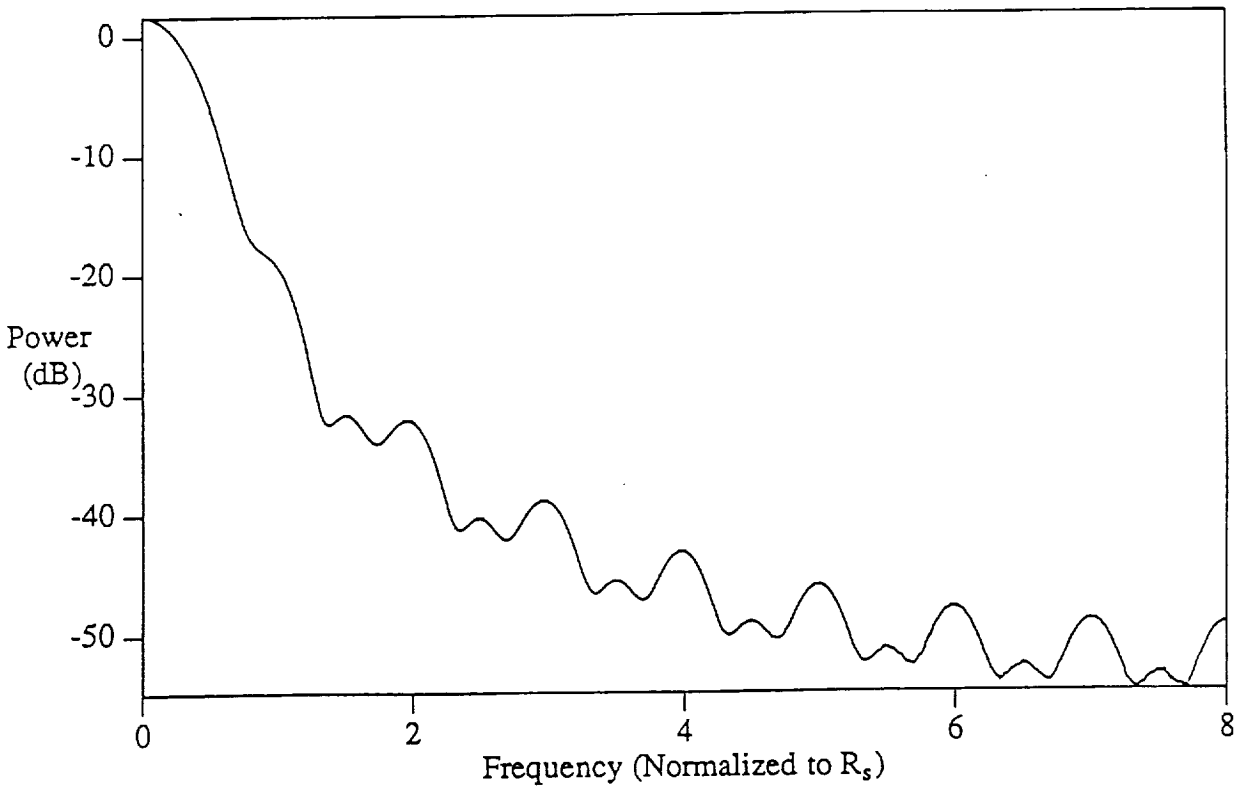

Figure 7.3: Theoretical CPM Spectrum (1-REC, $M = 8$, $h = 1/8$)

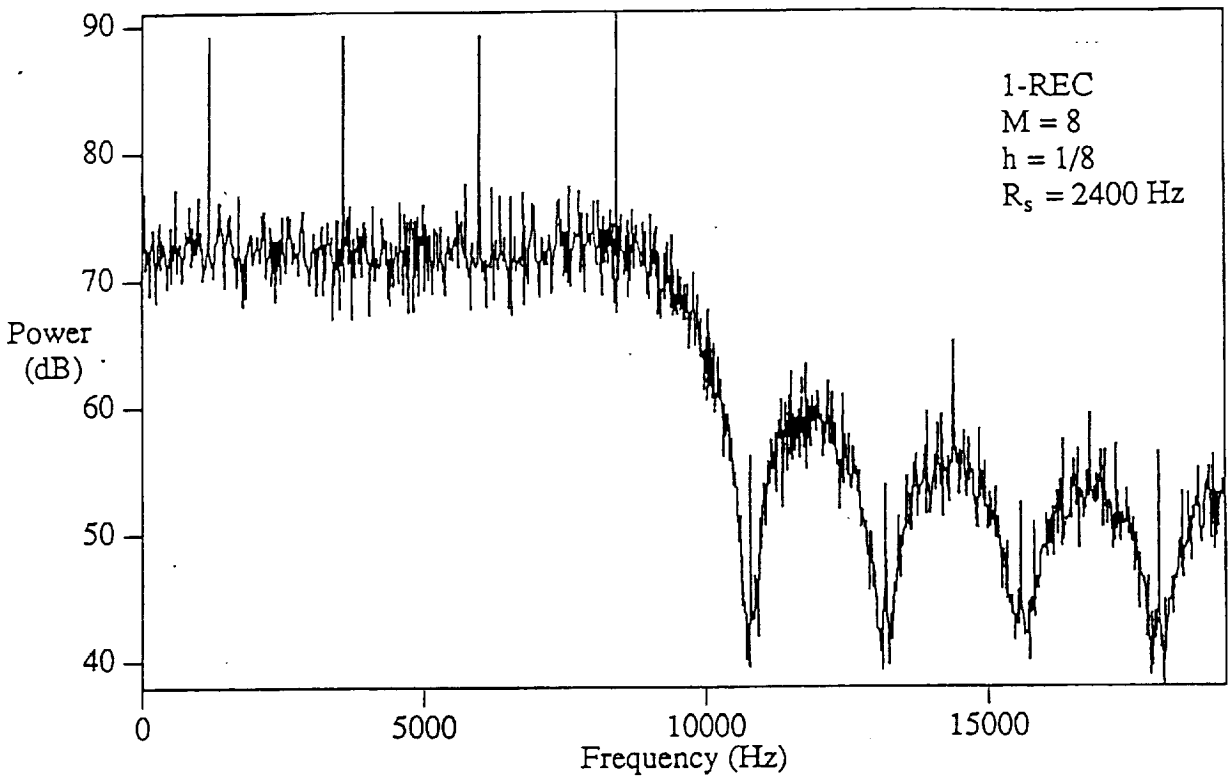

Figure 7.4: CPM Spectrum (Point "C")

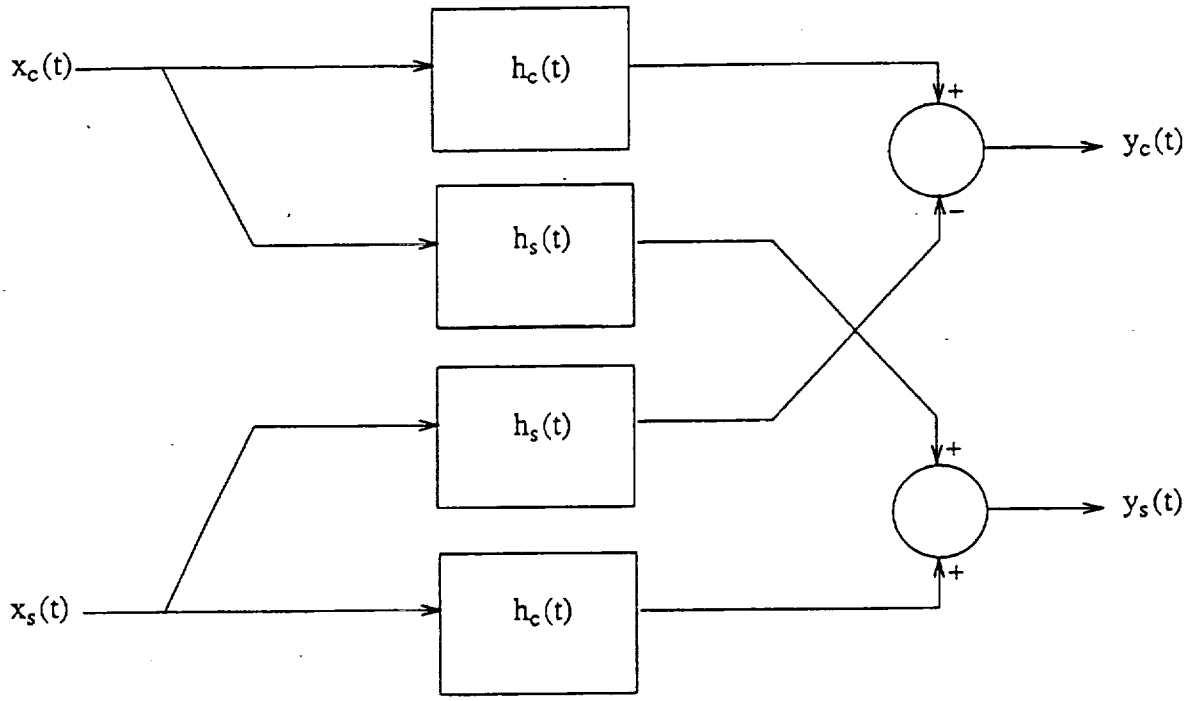

Figure 7.5: Low-Pass Equivalent Filtering Technique

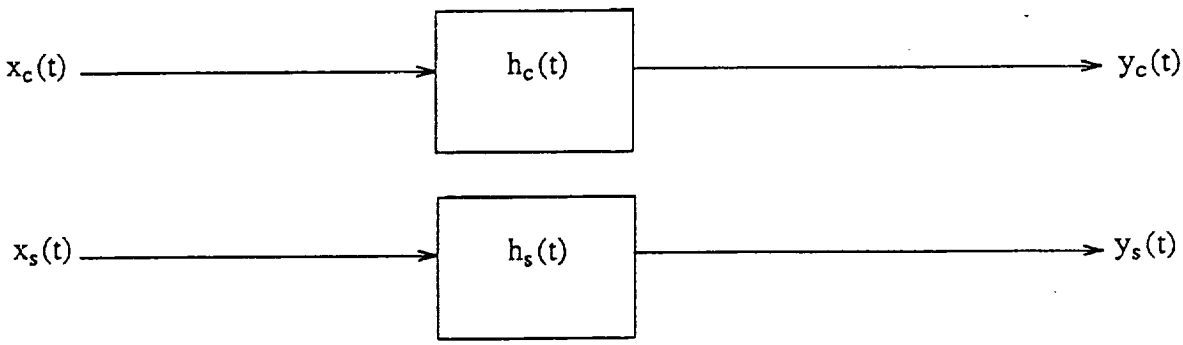

Figure 7.6: Simplified Low-Pass Equivalent Filtering Technique

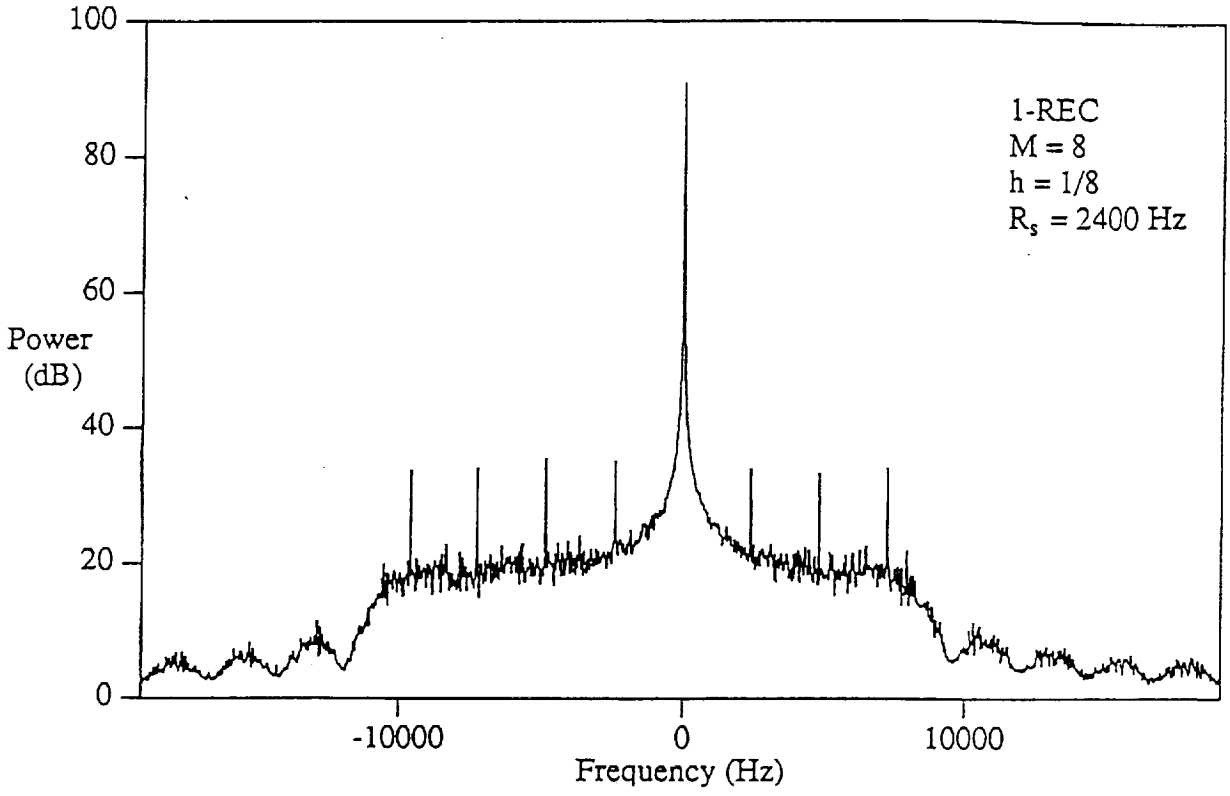

Figure 7.7: CPM Spectrum (Point "D")

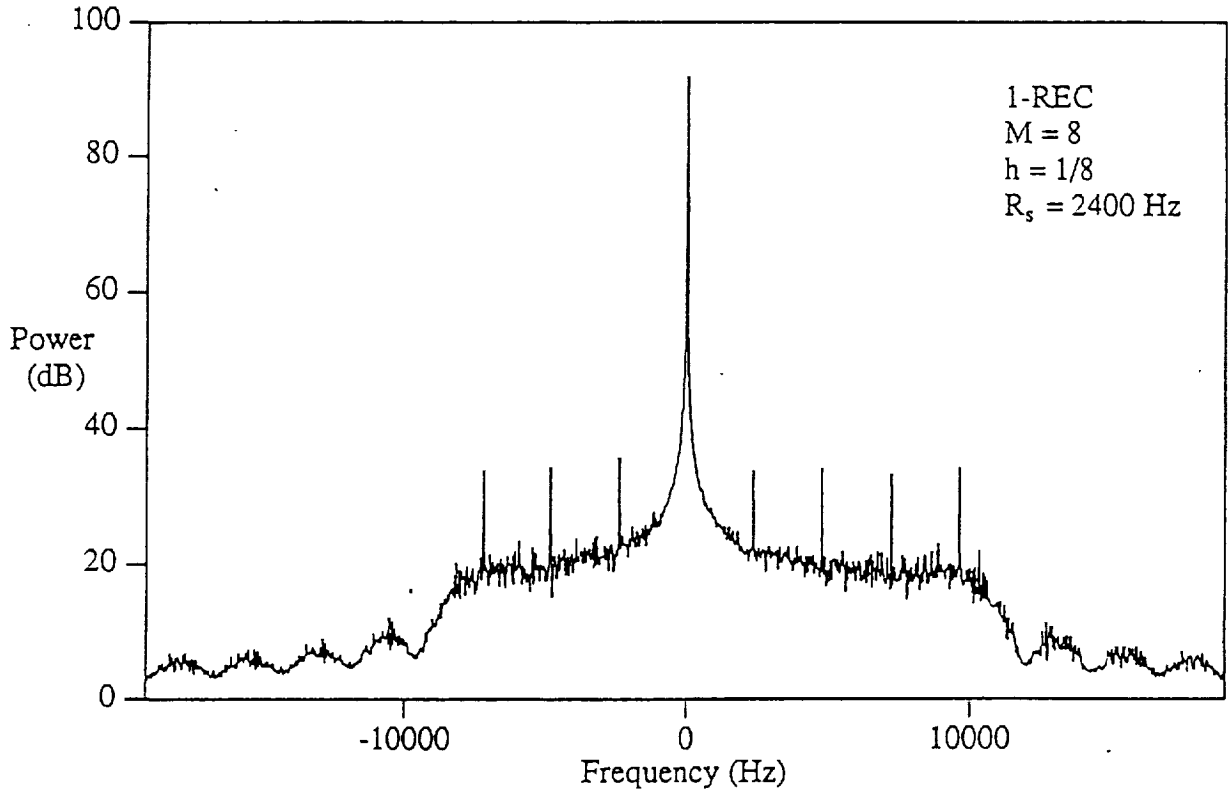

Figure 7.8: CPM Spectrum (Point "E")

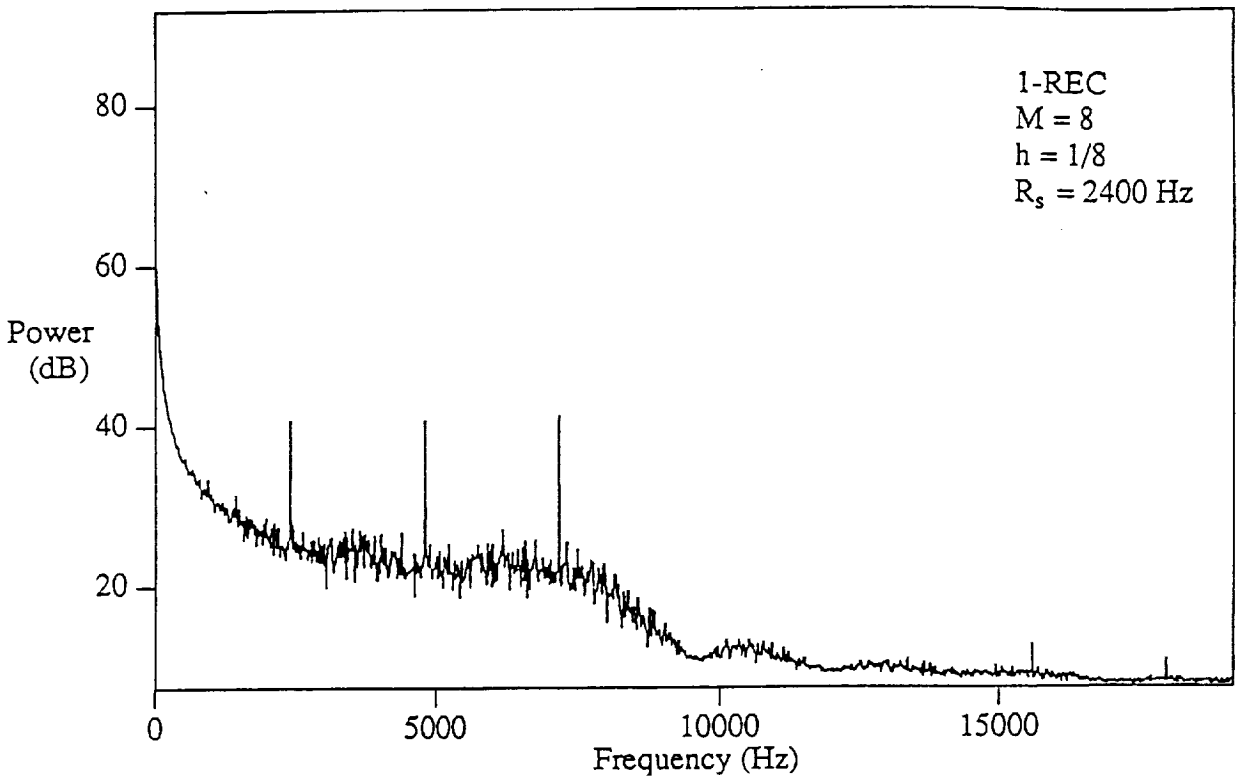

Figure 7.9: CPM Spectrum (Point "F")

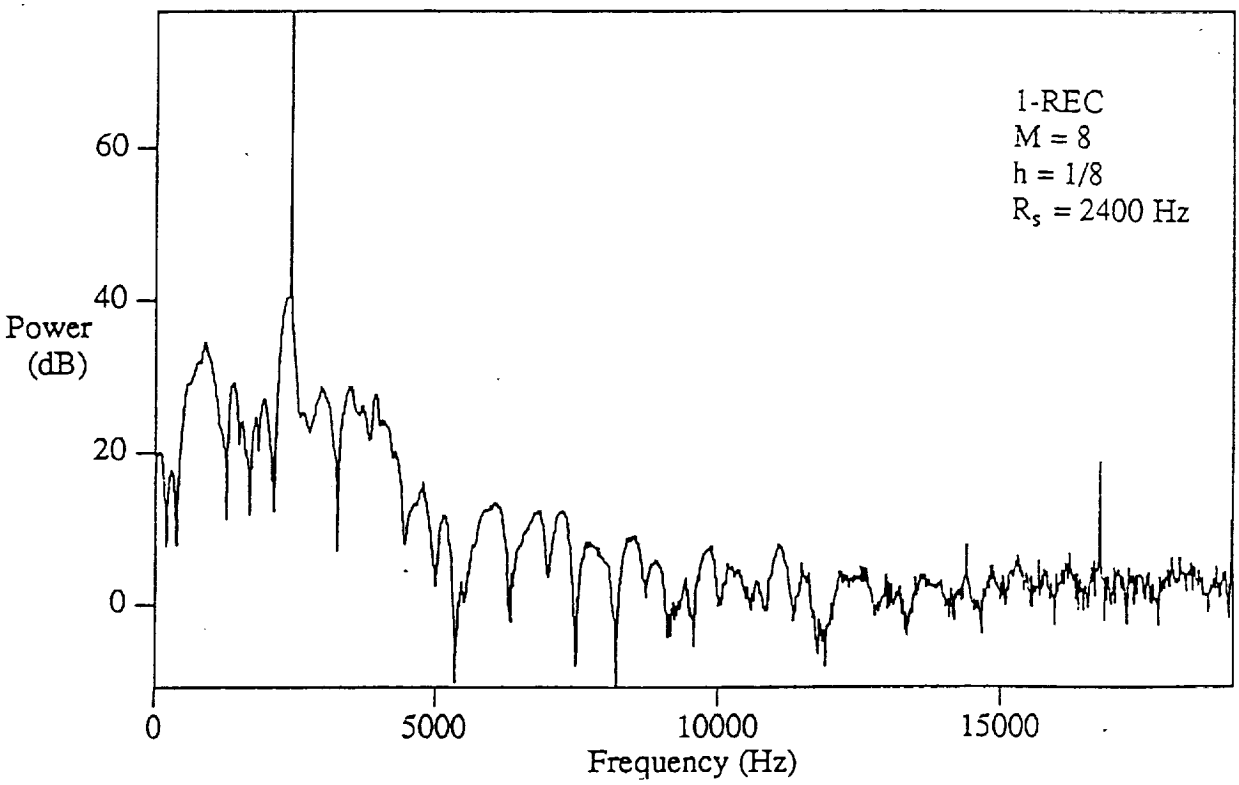

Figure 7.10: CPM Spectrum (Point "G")

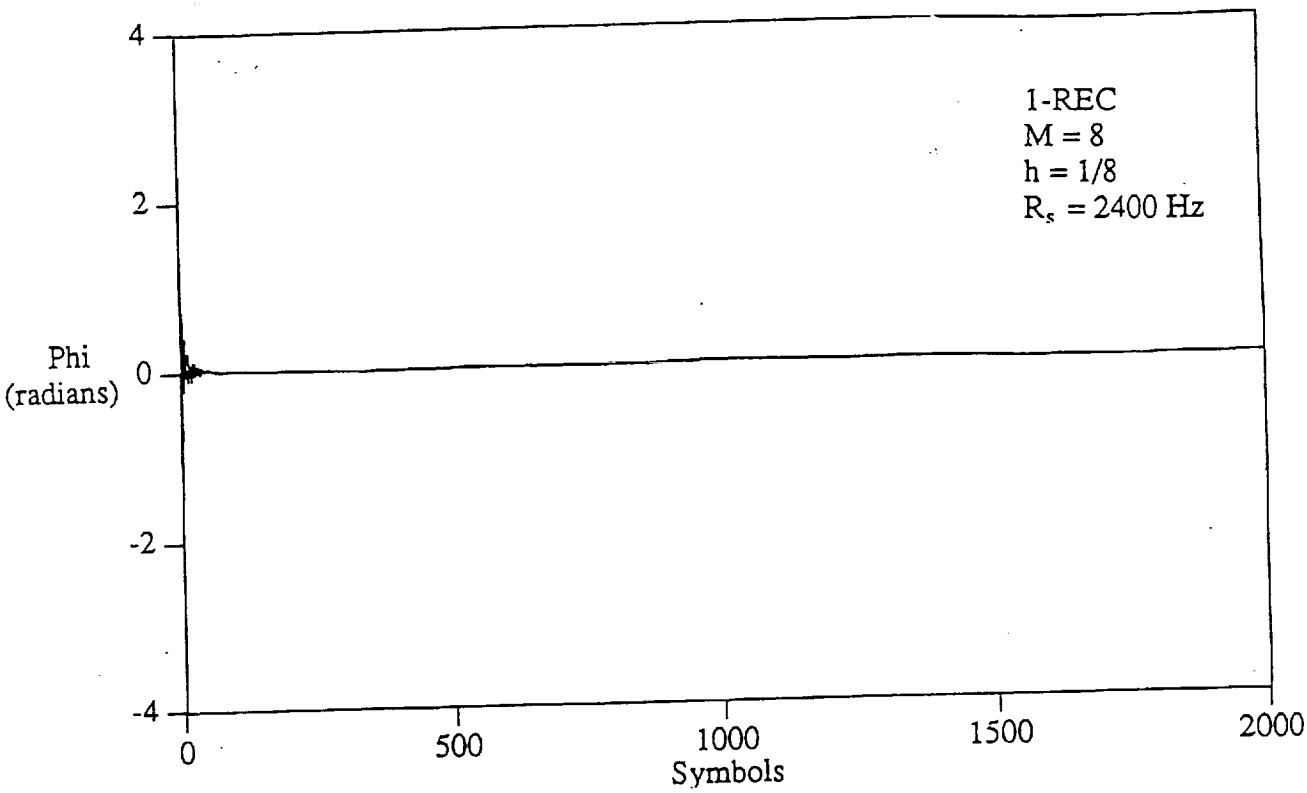

Figure 7.11: Recovered phase (No Doppler shift, no fading, 1-REC pulse shape, $M = 8$, $h = 1/8$, $n = 1$)

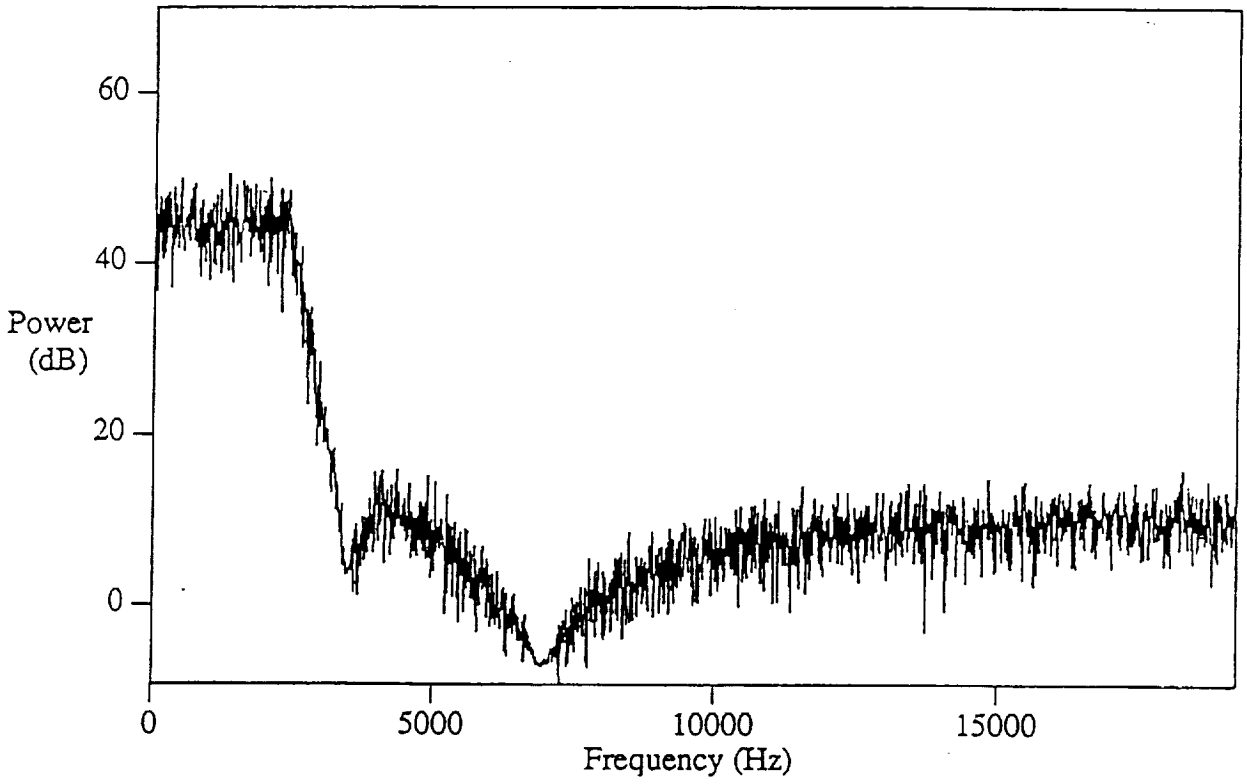

Figure 7.12: Typical noise spectrum

$$\phi_7(t) = \beta_7(t) + e_7\frac{2\pi}{7}. \tag{7.45}$$

The inherent ambiguity may be resolved by finding the smallest integer values of e_5 and e_7 in the range $(0 \leq e_5 \leq 5;\ 0 \leq e_7 \leq 7)$ such that

$$\phi_5(t) \cong \phi_7(t) \tag{7.46}$$

Aside from the fact that there would still be the possibility of an error in the recovered phase, this technique is inherently complicated and time consuming. A better technique, in the sense that it is simpler and less prone to errors, is to avoid the ambiguity issue completely, by choosing $n = 1$.

The selection of $n = 1$ can cause difficulty in the recovery process. In [4], it is stated that the value of n which produces the least phase jitter is $n = M - 1$, where M is the alphabet size. If $M > 2$, then the best value of n is greater than 1. However, in resolving the ambiguity issue, we have already chosen $n = 1$. Therefore, we must be careful, when we select a pulse shape, to choose one that will produce as small a phase jitter as possible, given that we are using the $n = 1$ spectral line. This means we need a pulse shape with a strong spectral line at $n = 1$. Next section includes the results that support our preference for 1-RC.

7.3.2 γ-power device effects

The system considered contains a component that magnifies some of the disturbances (noise, fading, Doppler) that occur in a mobile-satellite environment. The component is the γ-power device, which raises the CPM signal to the γ power. Breaking the action into magnitude and phase relations, it raises the *magnitude* to the γ power, and multiplies the *phase* by γ. Therefore, disturbances that affect the amplitude of the CPM signal are exponentially-magnified, while distortions that affect the phase of the CPM signal are linearly-magnified.

The negative effects of the γ-power device are especially noticeable on the Doppler shift and the fading of the CPM signal. First, the device multiplies the received Doppler shift by γ, making Doppler uncertainty γ times larger than originally anticipated. The two filters (NBF1 and NBF2) must be chosen to have adequate bandwidth in order to accommodate the maximum possible Doppler shift of the CPM wave. The maximum possible Doppler shift depends on the vehicle speed, relative to the satellite. It is calculated as follows:

$$\Delta f_{max} = f_0\frac{v_{max}}{c} \tag{7.47}$$

where f_0 is the carrier frequency, v_{max} is the maximum vehicle speed, and c is the speed of light. As stated earlier, the γ-power device produces an *apparent* Doppler shift (as seen by NBF1 and NBF2) equal to $\gamma\Delta f$. Therefore, NBF1 and NBF2 must be wide enough to account for the maximum apparent Doppler shift, $\gamma\Delta f_{max}$. In Fig. 7.13, the system parameters are listed. From those parameters and equation (7.47), we calculate $\Delta f_{max} = 138$ Hz, and $\gamma\Delta f_{max} = 1104$ Hz. Therefore, NBF1 and NBF2 must allow for a frequency shift of ± 1104 Hz, so they must have bandwidths of at least 2208 Hz. On Fig. 7.17 they have bandwidths of 3200 Hz, which is more than enough to allow for the Doppler shift, and narrow enough to reject the higher order sinusoids that appear at spacings of R_s above the $n = 1$ line.

Since NBF1 and NBF2 must be quite wide, their memory is reduced considerably, and they are more susceptible to noise. This effect can be viewed as follows. Every time a symbol of $\{+1\}$ is transmitted, the instantaneous CPM frequency (the derivative of the phase) is in the center of NBF1, so the filter gets excited. The filter then begins to resonate at its center frequency, with the filter output decaying exponentially after the data symbol ends. The filter continues to decay until it gets excited again, by another $\{+1\}$ symbol transmission. Similarly, NBF2 gets excited when a symbol of $\{-1\}$ is transmitted, and decays between $\{-1\}$ symbol transmissions. The decay can be described by a time constant of the form $1/2\pi B$, so a wide filter has a short time constant, and decays quicker than a narrow filter. Once the filters are completely decayed, the phase information they contain is no longer useful, so the recovered phase tends to drift randomly between 0 and 2π. In order to limit these effects, we can narrow the post-detection filter, so that it has a long time constant, and retains the phase information longer.

Viewing the action of the filters in the frequency domain, we can visualize the CPM signal as a random process that contains spectral lines and continuum. Filters NBF1 and NBF2 select the appropriate spectral lines, while allowing some amount of continuum to pass through. This continuum is then a source of noise, in the sense that it is an undesirable signal. If the filters are narrow, the signal that passes through them is predominately sinusoidal, but if the filters are wide, more noise passes through. The amount of spectral line power relative to continuum at the center frequency of filter NBF1 is then related to the frequency of $\{+1\}$ symbol transmissions, pulse shape, M, and h. Similarly, the power of the spectral line at the center of filter NBF2 is related to the frequency of $\{-1\}$ symbol transmissions. The final filter, from this viewpoint, limits the amount of noise that passes to the synchronization signal.

The other *mobile*-related effect that is magnified by the presence of the γ-power device is the dynamically-changing fading. First, the magnitude of the fading is raised to the γ power, causing a large dynamic range expansion. Second, the fading-induced phase distortions are multiplied by γ, increasing the swing of the phase. Figure 4.3 is the spectrum of the CPM signal after the γ-power device for a 1-RC pulse shape, when noise (10 dB SNR) and fading (K = 10 dB) are added to the CPM signal. Notice the asymmetry of the spectrum; most importantly, where we used to see *only* spectral lines, we now see that the lines are modulated by the fading. Therefore, when we recover the synchronization signal, we get a sinusoid that is phase-modulated by the fading channel. Therefore, the recovered phase contains a lot of jitter. Figure 4.4 shows the recovered phase under the above mentioned conditions. It has an initial transient, which seems strange, coming out of such a narrow filter. However, the initial transient can be explained by the fact that the final filter is slow to respond to an input signal, so its output is slow to increase in *magnitude*. In the complex plane, that corresponds to an output which is near the origin. Being near the origin, the phase can easily move from one quadrant to another, causing large swings, until the output magnitude increases. Once the magnitude of the filter output builds, its output phase is more stable. Although the mean value of the phase is correct (0 radians), the variance is quite large, so the tracking is not very good. Shortly, we will describe a device that limits these effects.

Finally, the non-linearity increases the effects of noise in the original CPM signal by producing additional cross-terms between the noise and the desired signal. This tends to degrade the performance of the system. Once again, a narrow post-detection filter will limit these effects, and will be discussed in the next section.

7.3.3 Doppler Shift

As mentioned in the previous section, Doppler shift is an important factor in a *mobile* environment, especially when it is time-varying, due to the change in the relative motion between the vehicle and the satellite. However, since Doppler shift affects all of the spectral lines equally, the timing information is not lost. In other words, when the two Doppler-shifted spectral lines are multiplied together and the symbol timing is recovered, the shift is self-canceling.

Because filters NBF1 and NBF2 must be wide, however, to allow the CPM signal to shift by Δf_{max}, they decay quickly, after being excited.

$R_s = 2400$ Hz
$T_s = 1/2400$ sec
$h = 1/8$
$\gamma = 8$
$M = 8$
$g(t) =$ 1-RC
$\alpha_i \in \{\pm 1, \pm 3, \pm 5, \pm 7\}$
$f_0 = 1.5$ GHz
$v_{max} = 100$ km/hr

Figure 7.13: System Parameters

Therefore, the recovered phase is prone to drifting, because the memory in the filters is relatively short, and once the filters are completely decayed, the phase they produce is no longer reliable. This problem was overcome by using a very narrow final post-detection filter, which limits the excursions in the recovered phase that pass through the relatively wide NBF1 and NBF2.

7.3.4 Reducing fading effects

Basically, the fading is caused by reflections and blockages of the CPM signal due to obstructions in the signal path (i.e. buildings). Also, because the signal path keeps changing as the vehicle moves, the received composite signal changes over time. This makes it difficult to maintain a lock on the received signal. A step that greatly reduces the fading effects is to insert a *hard limiter* at the front end of the synchronizer. This device maintains a constant signal *amplitude*, but it produces additional frequencies at multiples of the carrier, while keeping the original signal intact. The additional frequencies must then be filtered out through BPF1. The hard-limiter thus limits the effect of fading to only phase-shifting of the received signal, rather than phase *and* magnitude distortion. In effect, it restores the constant-envelope characteristic of the CPM wave, leaving residual phase modulation.

7.3.5 System Parameters

The parameters that were used in the simulation, described both in the analog and digital domain, are shown in Fig. 7.13.

Parameter	Analog	Digital
Sampling Frequency	$f_s = 38.4$ kHz	$f_s = 16$
Symbol Time	$T_s = 1/2400$ sec	$T_s = 1$
Doppler Shift	$\Delta f_{max} = 138$ Hz	$\Delta f_{max} = 0.0579$
NBF1 Bandwidth	3200 Hz	4/3
NBF2 Bandwidth	3200 Hz	4/3
LBPF Bandwidth	50 Hz	1/48
BPF1 Bandwidth	5000 Hz	50/24

Figure 7.14: Simulation Parameters

The modified block diagram of the synchronizer is shown in Fig. 7.17. Most notably, it contains the added hard limiter, the narrow post-detection filter, and eliminates the divide-by-n, because n is always 1. In the simulation, the addition of the hard limiter was handled very simply. The polar form of the received CPM signal is:

$$y(t) = R(t)\cos[2\pi f_0 t + \theta(t)]. \tag{7.48}$$

The limiter simply keeps the magnitude of this signal constant, setting $R(t)$ equal to 1. Therefore, (7.48) simplifies to

$$y(t) = \cos[2\pi f_0 t + \theta(t)]. \tag{7.49}$$

The next section will present the results obtained in simulations of the complete modified system, as shown in Fig. 7.17.

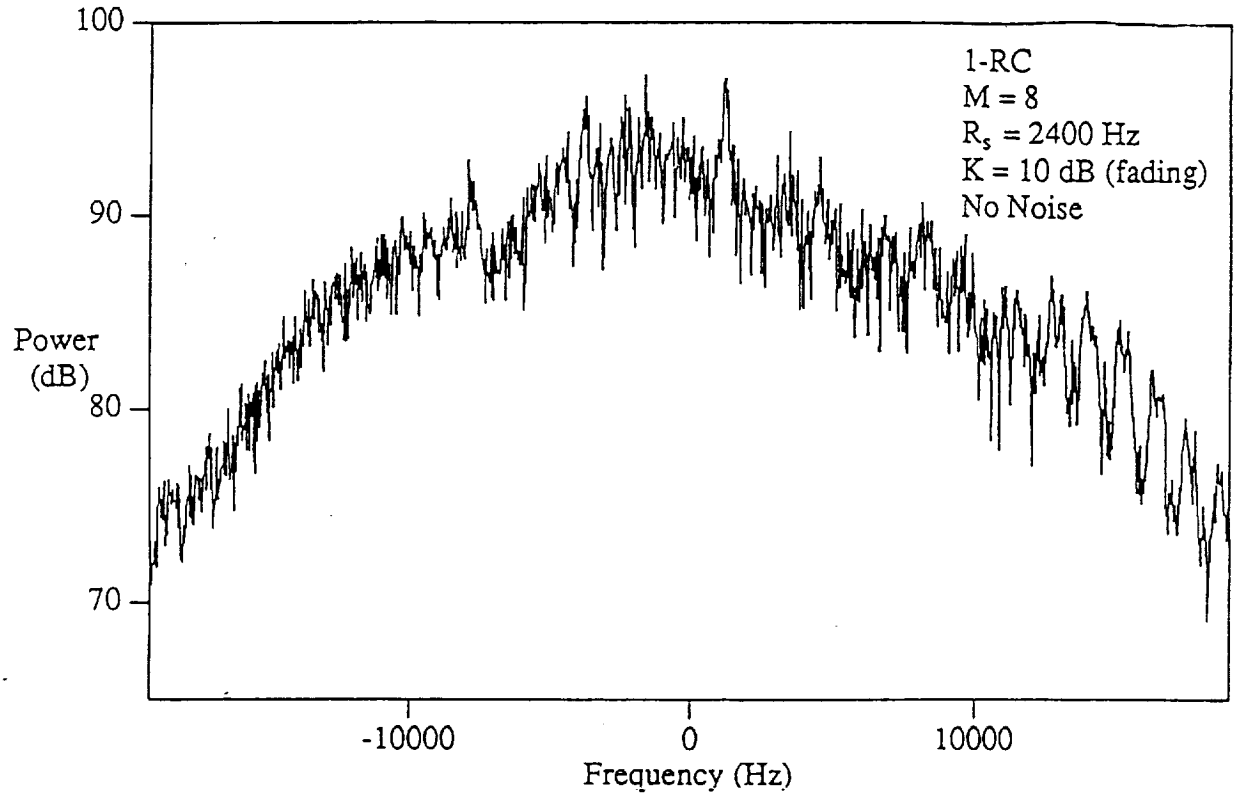

Figure 7.15: CPM Spectrum with Fading ($h = 1$, 1-RC, $M = 8$)

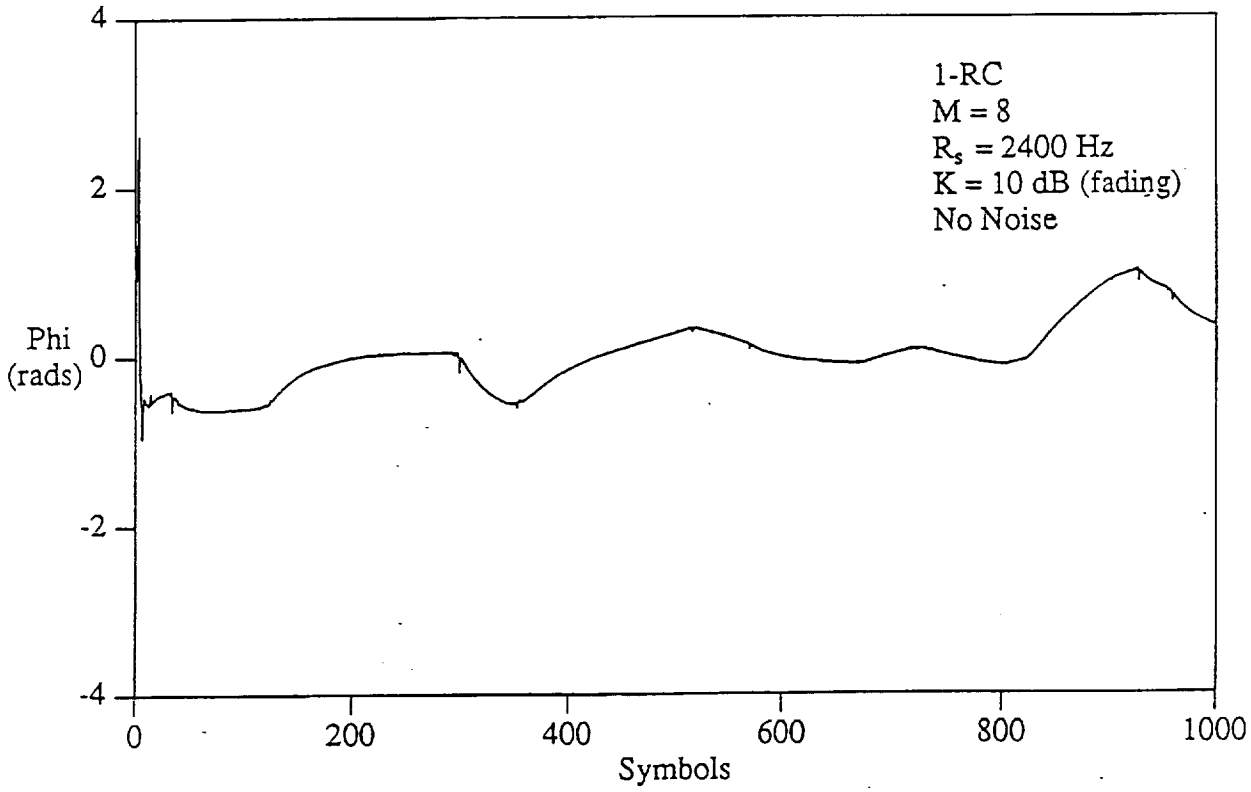

Figure 7.16: Recovered Phase with 1-RC Pulse Shape, without Limiter

7.4 Results and Conclusions

In [4] an analysis was presented that calculated the timing jitter of the recovered symbol timing, using the block diagram in Fig. 7.1. The main assumption in the analysis was that the spectrum of the integer-h CPM (after the γ-power device) consisted of a spectral line in the presence of a continuum, and that the continuum was *constant* near the spectral line. Therefore, the analysis calculated the magnitude of the spectral line, and the value of the continuum at the frequency of the spectral line. Then it showed how to calculate the timing jitter from those two values. The above assumption is very good, provided that the bandwidths of NBF1 and NBF2 are small, compared to the symbol rate. Some results are tabulated in Fig. 7.18 using a bandwidth of $2.0/T_s$ for BPF1, and a bandwidth of $0.005/T_b$ for NBF1 and NBF2. Note that the jitter variance is normalized to $(2\pi)^2\text{rad}^2$, which means that when we calculate the standard deviation of the phase jitter, by taking the square root of the variance, we should interpret the units as being fractions of a symbol time.

7.4.1 Performance Criteria

With that interpretation of phase jitter in mind, we need to establish an acceptable level of jitter, in order to judge the performance of the synchronizer. Ultimately, we are concerned with a method of producing reliable communication using this digital system, so we need a low bit-error rate. The relationship between error rate and phase jitter takes the form:

$$P_e(\Delta t) = \int P(e|\Delta t) f(\Delta t) d\Delta t \tag{7.50}$$

where Δt represents the error in the timing, and $f(\Delta t)$ is the probability distribution of Δt. A higher phase-jitter variance yields a higher timing-jitter variance, which means that (7.50) will produce a higher bit-error rate. Generally, a phase jitter corresponding to about 5% of a symbol time is considered good, and 10% of a symbol time is acceptable. Therefore, our goal is to keep the timing jitter below 10%, which means that the normalized phase jitter should be below $(0.1)^2 = 0.01$.

For narrow filters (NBF1 and NBF2), the final post-detection filter need only serve as a zonal filter, allowing frequencies in the vicinity of R_s to pass. Therefore its bandwidth is of little concern. Fig. 7.19 presents the results when those filters are much wider. These results were calculated

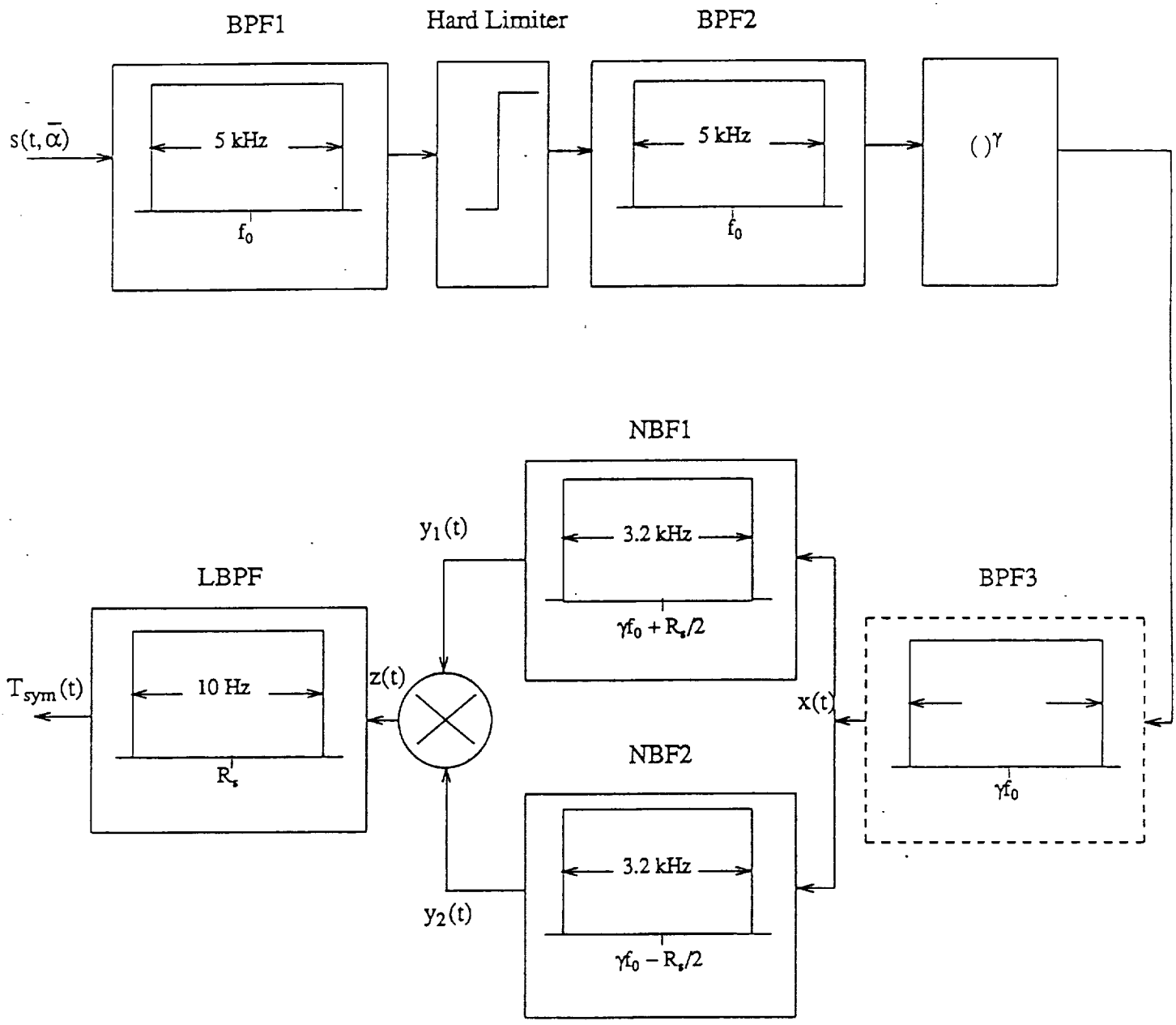

pag. 58, Report # 5

Figure 7.17: Modified Symbol Synchronizer

Pulse Shape	E_b/N_0 (dB)	Normalized Variance
1-REC	0	unreliable
	10	1.0
	20	4.5×10^{-3}
	30	3.1×10^{-4}
	40	2.9×10^{-5}
	50	2.7×10^{-6}
1-RC	0	unreliable
	10	8.8×10^{-2}
	20	3.3×10^{-4}
	30	2.1×10^{-5}
	40	2.0×10^{-6}
	50	1.8×10^{-7}

Figure 7.18: Analytical Results (NBF1 and NBF2 bandwidth = $0.005/T_b$) ($M = 8$, $h = 1/8$, $n = 1$)

using bandwidths of $2.0/T_s$ for BPF1, and a bandwidth of $0.5/T_b$ for NBF1 and NBF2.

Notice that, for very large bandwidths of NBF1 and NBF2, the calculated jitter variance is unreliable because it falls out of the range 0 to 1, corresponding to phase jitter in the range 0 to 2π. The reason for that behavior is that the original assumptions which supported that particular analysis fall apart (i.e., the assumption that the continuum is constant near the spectral line). In this situation, the final post-detection filter serves a far more important role, and must be narrowed considerably.

7.4.2 Pulse shape selection

Even with a narrow post-detection filter, the system did not perform reliably with some choices of pulse shape, even without noise or fading! An example is with the 1-REC pulse shape. A typical graph of the recovered phase in this situation is shown in Fig. 7.21 without noise or fading. In this situation the phase drifts slowly from $-\pi$ to π, without any sign of stabilizing. Even though it seems like there are sudden phase discontinuities at several points in the graph, these discontinuities are just shifts between $-\pi$ and π, which really are not shifts at all; they occur due to the definition of the arctangent

Pulse Shape	E_b/N_0 (dB)	Normalized Variance
1-REC	0	unreliable
	10	unreliable
	20	4.5×10^{-1}
	30	3.1×10^{-2}
	40	2.9×10^{-3}
	50	2.7×10^{-4}
1-RC	0	unreliable
	10	unreliable
	20	3.3×10^{-2}
	30	2.1×10^{-3}
	40	2.0×10^{-4}
	50	1.8×10^{-5}

Figure 7.19: Analytical Results (NBF1 and NBF2 bandwidth = $0.500/T_b$) ($M = 8$, $h = 1/8$, $n = 1$)

function. When the drifting phase gets close to one of the extremes and crosses over into the next quadrant in the x-y plane, the arctangent function redefines the signal to fit the new quadrant. In any case, the behavior of this waveform is unacceptable.

The reason for the unacceptable behavior is due to the spectrum of the integer-h CPM signal, given the 1-REC pulse. We will see, in the next section, an analysis that calculates the spectrum, but basically it shows that the power in the spectral line at $n = 1$ is not strong enough to track reliably, given that the wide filters pass a large amount of continuum. If the filters were narrow, then there would be no problem with the REC waveform, but because they are wide, they pass a lot of power that is not at the frequency of the spectral line of interest. Therefore, we need to select a pulse that has a high power in the $n = 1$ spectral line.

Power Spectrum Calculated

In [9] Aulin and Sundberg present a method for calculating the spectrum of a CPM signal. First, they derived an exact expression for the autocorrelation

function of the CPM signal:

$$R(\tau) = R(\tau' + mT_s) \tag{7.51}$$

$$= \frac{1}{T_s}\int_0^{T_s} \prod_{n=1-L}^{m+1} \{ \sum_{k=-(M-1)}^{M-1} p_k e^{j2\pi hk[q(t+\tau'-(n-m)T_s)-q(t-nT_s)]} \} dt \tag{7.52}$$

over the interval:

$$0 \leq \tau < (L+1)T_s \tag{7.53}$$

where p_k is the probability of the k^{th} symbol occurring. Note that the time difference τ has been written as:

$$\tau = \tau' + mT_s;\ 0 \leq \tau' < 1,\ m = 0, 1, \ldots \tag{7.54}$$

The power spectrum is then the Fourier transform of the autocorrelation function:

$$S(f) = 2\mathrm{Re}\{\int_0^{LT_s} R(\tau)e^{-j2\pi f\tau}d\tau + \frac{e^{-j2\pi fLT_s}}{1 - C_\alpha e^{-j2\pi fT_s}} \int_0^{T_s} T_s R(\tau + LT_s)e^{-j2\pi f\tau}d\tau\} \tag{7.55}$$

where

$$C_\alpha = \sum_{\substack{k=-(M-1) \\ k \text{ odd}}}^{M-1} p_k e^{jh\pi k} \tag{7.56}$$

In this particular situation, h is equal to 1 (after the power-law device). This yields $|C_\alpha| = 1$. It is shown in [9] that this situation causes the autocorrelation function to be periodic outside $|\tau| = LT_s$. Therefore, $R(\tau)$ can be written as:

$$R(\tau) = R_{con}(\tau) + R_{dis}(\tau) \tag{7.57}$$

where $R_{dis}(\tau)$ is periodic, causing the discrete components in $S(f)$. In [12] it is also shown that when $|C_\alpha| = 1$, $R_{con}(\tau) \equiv 0$; $|\tau| \geq LT_s$. In this instance, $R_{con}(\tau)$ yields the continuous part of the spectrum, and $R_{dis}(\tau)$ yields the discrete components. Therefore, the complete spectrum is found by taking the Fourier transform of $R_{con}(\tau)$, and finding the coefficients of the Fourier series of $R_{dis}(\tau)$.

To determine $R_{dis}(\tau)$, we use the fact that $R_{con}(\tau) \equiv 0$; $|\tau| \geq LT_s$. This means that $R_{dis}(\tau) = R(\tau)$; $|\tau| \geq LT_s$. It also means that $R_{dis}(\tau)$ is completely defined over a period of $2T_s$, since we already know that the spectrum has discrete components at $R_s/2$. Therefore, we calculate $R_{dis}(\tau)$ over the range $2LT_s \leq \tau < 4LT_s$, and extend it in either direction to get the complete signal. Now, subtracting $R_{dis}(\tau)$ from $R(\tau)$ gives $R_{con}(\tau)$.

The continuum part of the spectrum is calculated by taking the Fourier transform of $R_{con}(\tau)$:

$$\begin{aligned} S_{con}(f) &= \int_{-\infty}^{\infty} R_{con}(\tau) e^{-j2\pi f\tau} d\tau \\ &= 2\,\mathrm{Re}\left\{ \int_0^{LT} R_{con}(\tau) e^{-j2\pi f\tau} d\tau \right\} \end{aligned} \tag{7.58}$$

where the limits of integration are reduced due to the known characteristics of $R_{con}(\tau)$.

Finally, the Fourier series coefficients of $R_{dis}(\tau)$ are calculated:

$$c_n = \frac{R_s}{2} \int_0^{2/R_s} R_{dis}(\tau) e^{-j\pi n R_s \tau} d\tau \tag{7.59}$$

The results of numerically evaluating equations (7.58) and (7.59) are plotted in Figs. 7.22 and 7.23, with the magnitude of the spectral lines equal to the power in each one.

The spectrum for the 1-REC pulse is shown in Fig. 7.22, and for the 1-RC pulse in Fig. 7.23. Notice how much greater the ratio of the spectral line to continuum is in the 1-RC case than in the 1-REC case. Using 1-RC gives a 9 dB gain in this ratio. The ideal case (ideal in the sense that it produces the strongest spectral lines) is an impulse, which produces a differential phase shift keyed signal (DPSK). In that case,

$$g(t) = \frac{1}{2}\delta(t - \frac{T_s}{2}) \tag{7.60}$$

When integrated, $q(t)$ becomes:

$$q(t) = \begin{cases} 0; & 0 \leq t < \frac{T_s}{2} \\ \frac{1}{2}; & \frac{T_s}{2} \leq t < T_s \end{cases} \tag{7.61}$$

In this system, the phase jumps abruptly at $T_s/2$, and always by an odd integral multiple of π. So, $\phi(t, \bar{\alpha})$ assumes values that always increment by

π over a symbol time, producing a signal whose complex envelope is a square wave. Therefore, the DPSK spectrum consists *only* of spectral lines, with no continuum, since a square wave can be expressed as a sum of sinusoids. Given the above, an intuitive reason why 1-RC produces a better spectrum (as far as tracking performance goes) than 1-REC is that $g(t)$ is closer to an impulse for the 1-RC pulse than for the 1-REC pulse.

However, this change in pulse shape is not without problems. The original CPM spectrum using 1-RC has a wider main lobe than with 1-REC. The sidelobes, however, are eventually lower, partially reducing the affect of the wider main lobe on the out-of-band power. This seems to be a minor price to pay, given the ease of synchronization of the recovered signal.

Filter action

Given the relatively strong spectral lines of the 1-RC system, we can now illustrate the action of NBF1 and NBF2. As referenced in earlier chapters, NBF1 gets excited periodically, then decays between excitations. For $M = 8$, it gets excited an average of 1 time in 8, specifically when a $\{+1\}$ symbol is transmitted. This phenomenon is illustrated in Fig. 7.24 for NBF1, and in Fig. 7.25 for NBF2, using one-sided filter bandwidths of $2R_s/3 = 1600$ Hz for each filter. In the ideal situation, we expect each filter to oscillate continuously at its center frequency, which means that the complex envelope, relative to its center frequency, should remain constant. Obviously, from the graphs, this is not happening. In our situation, the filters decay greatly between excitations, and especially between symbols. Because of the short decay time, the filters lose their memory quickly, and the phase is no longer useful after the filters are completely decayed. At that point, the phase begins to drift, but adding a narrow post-detection filter alleviates some of the phase drifting by increasing the memory of the effective combination of filters NBF1, NBF2, and LBPF.

It is fairly obvious that a smaller alphabet size, M, would increase the likelihood that NBF1 would be excited (a $\{+1\}$ symbol would be sent more frequently), allowing a shorter decay time between excitations. This is equivalent to increasing the spectral line power in the $n = 1$ line. This would improve the tracking performance also, but at a cost of lower information throughput.

Pulse Shape	E_b/N_0 (dB)	K (dB)	ΔF (Hz)	Normalized Jitter Variance
1-RC	0	60	0	1.0×10^{-3}
	5	60	0	1.8×10^{-4}
	10	60	0	6.9×10^{-5}
	120	10	0	1.6×10^{-6}
	120	13	0	1.3×10^{-6}
	10	10	0	1.1×10^{-4}
	10	10	150	1.3×10^{-4}

Figure 7.20: Final simulation results

Recovered phase

Figs. 7.26 and 7.27 show two examples of phase recovery, the only difference being in the delay time between when the signal is transmitted and when it is received. In Fig. 7.26, a zero delay is used, producing a recovered phase whose average value is 0. In Fig. 7.27, a delay of $0.25T_s$ is used, producing a phase whose average value is $-\pi/2$. Note that a delay of T_s is equivalent to zero delay, and would produce a recovered phase of 0. Since the synchronizer produces an output that is proportional to the delay time, it is now clear that the synchronizer is performing its intended task. In order to illustrate the effects of Doppler shift, noise magnitude, and fading severity on the variance of the recovered phase, some simulation results are tabulated below.

Interestingly, the variance for the no-noise, no-fading, no-Doppler shift case is not exactly zero, though it is quite small. The reason is due to *data noise*, which surfaces because of the randomness of the transmitted data symbols. Most importantly, it is related to the probability and of $\{+1\}$ and $\{-1\}$ symbol transmissions, and the autocorrelation function of the symbol generating source function (usually the source symbols are assumed to be uncorrelated with one another.) A deterministic case, in which the symbol pattern is periodic (alternating $\{+1\}$, $\{-1\}$ symbols, for example) does produce zero variance, because the filters (NBF1 and NBF2) reach a steady-state after a few symbols are sent.

In the worst-case noise situation without fading, $E_b/N_0 = 0$ dB, and the jitter variance is 10^{-3}. This means that, on average, the timing jitters about $\pm(10^{-3})^{1/2} = \pm 0.032$ of a symbol time, which is acceptable. In the worst case fading situation, without noise, $K = 10$ dB, and the timing jitters

about $\pm(1.6 \times 10^{-6})^{1/2} = \pm 0.0013$ of a symbol time. This suggests that, in the expected environment, the noise is more of a problem than the fading.

Several combinations of noise and fading levels are included in Fig. 7.20, but perhaps the most important two are the ones closest to the expected case; namely the situation when $E_b/N_0 = 10$ dB, $K = 10$ dB, with varying values of Δf. Without any Doppler shift ($\Delta f = 0$), the variance of the phase jitter is 1.1×10^{-4}, which means that the timing typically jitters $\pm(1.1 \times 10^{-4})^{1/2} = \pm 0.01$ of a symbol time, which is acceptable. With a maximum Doppler shift of 150 Hz (larger than we expect), the timing jitter increases slightly, to $\pm(1.3 \times 10^{-4})^{1/2} = \pm 0.011$ of a symbol time. The reason why the value is slightly higher for the Doppler-shifted case is a combination of several factors. First, the spectral lines are shifted close to the edge of the filters (NBF1 and NBF2), so their amplitudes are starting to be reduced, due to the rolloff of the filters at the edge of their bandwidths. Also, the filters used in the simulation are IIR, which means they do not have linear phase, but they are easier to use, in terms of memory requirements and speed of execution. Since they are not linear phase, especially at the outer edges of the frequency band, the signals that are near the edge experience some additional phase distortion, which, combined with the amplitude reduction at the filter edge, increases the jitter variance. In addition, a factor that is always present is simulation "noise" which translates into slight uncertainty in the accuracy of the simulation results, due mostly to finite averaging time in the simulation. However, even with the 11 percent increase in standard deviation between the no-Doppler and maximum-Doppler cases, the system is still quite useful.

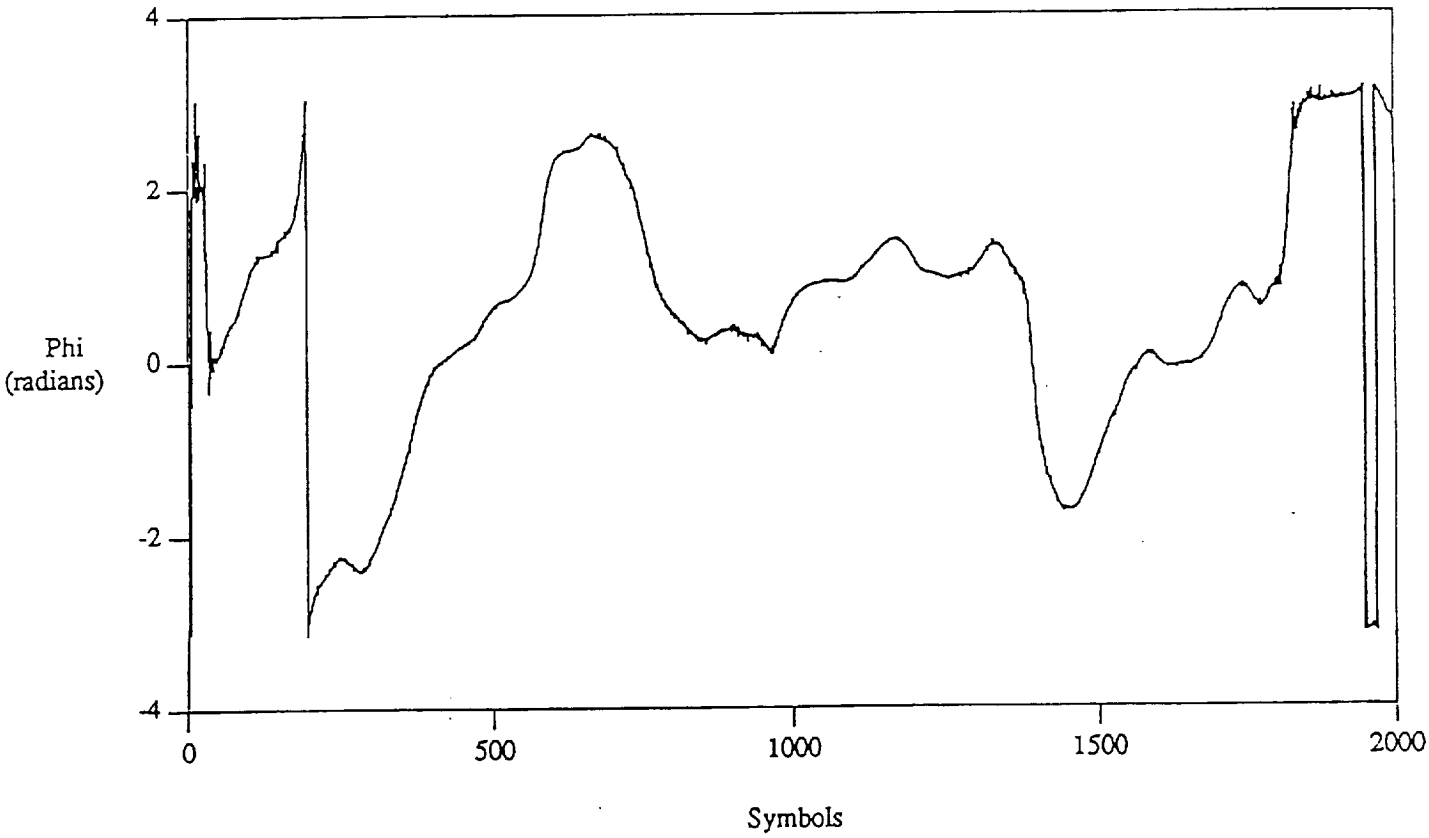

Figure 7.21: Recovered Phase with a 1-REC Pulse Shape

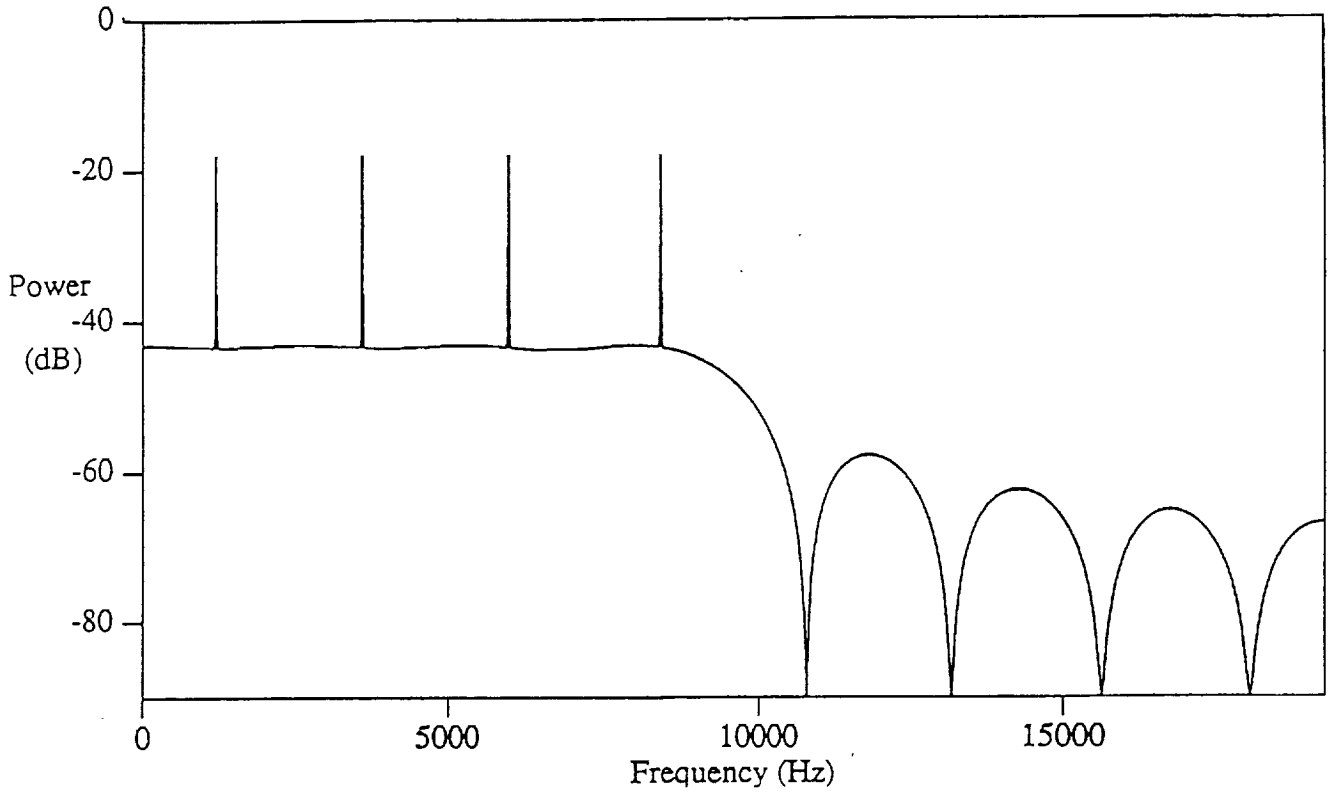

Figure 7.22: Power Spectrum of Integer-h CPM, 1-REC Pulse Shape

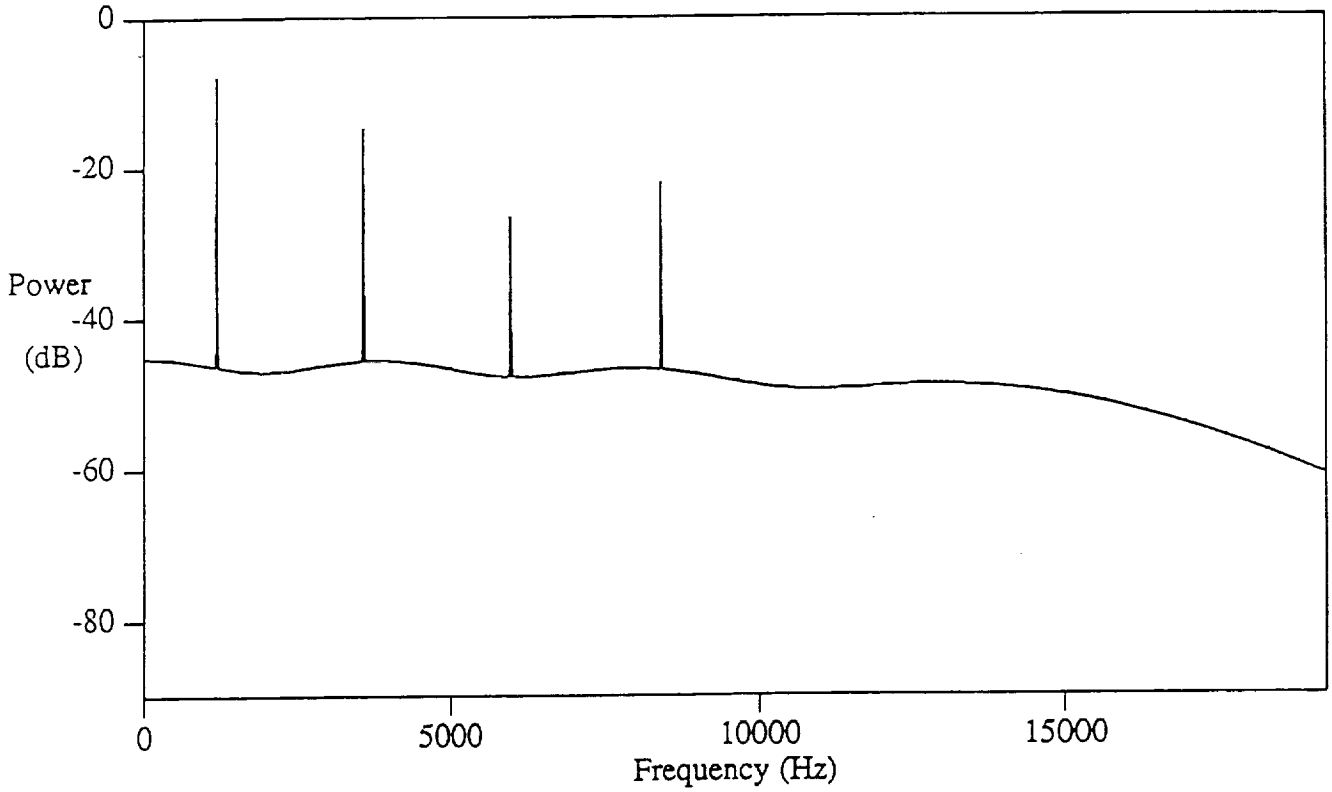

Figure 7.23: Power Spectrum of Integer-h CPM, 1-RC Pulse Shape

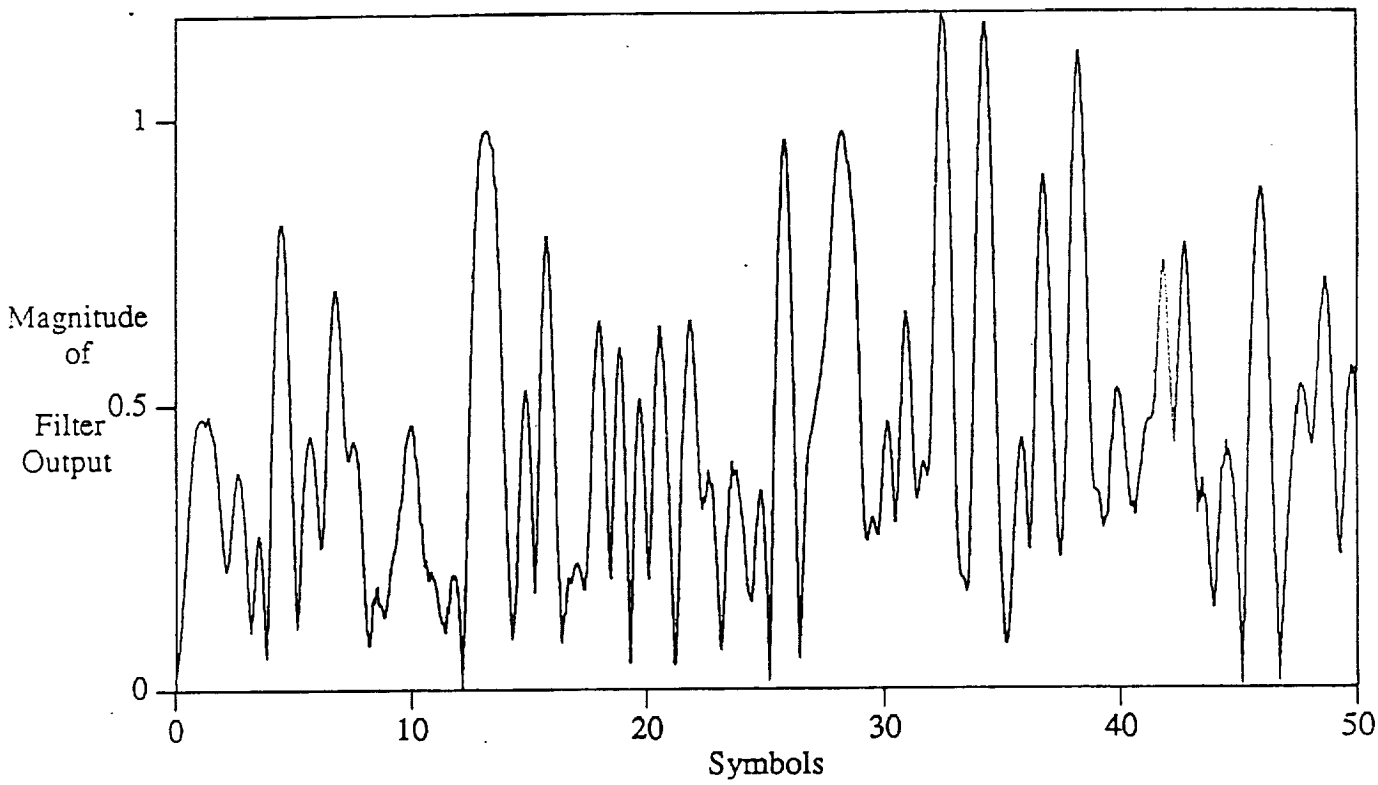

Figure 7.24: Action of filter NBF1

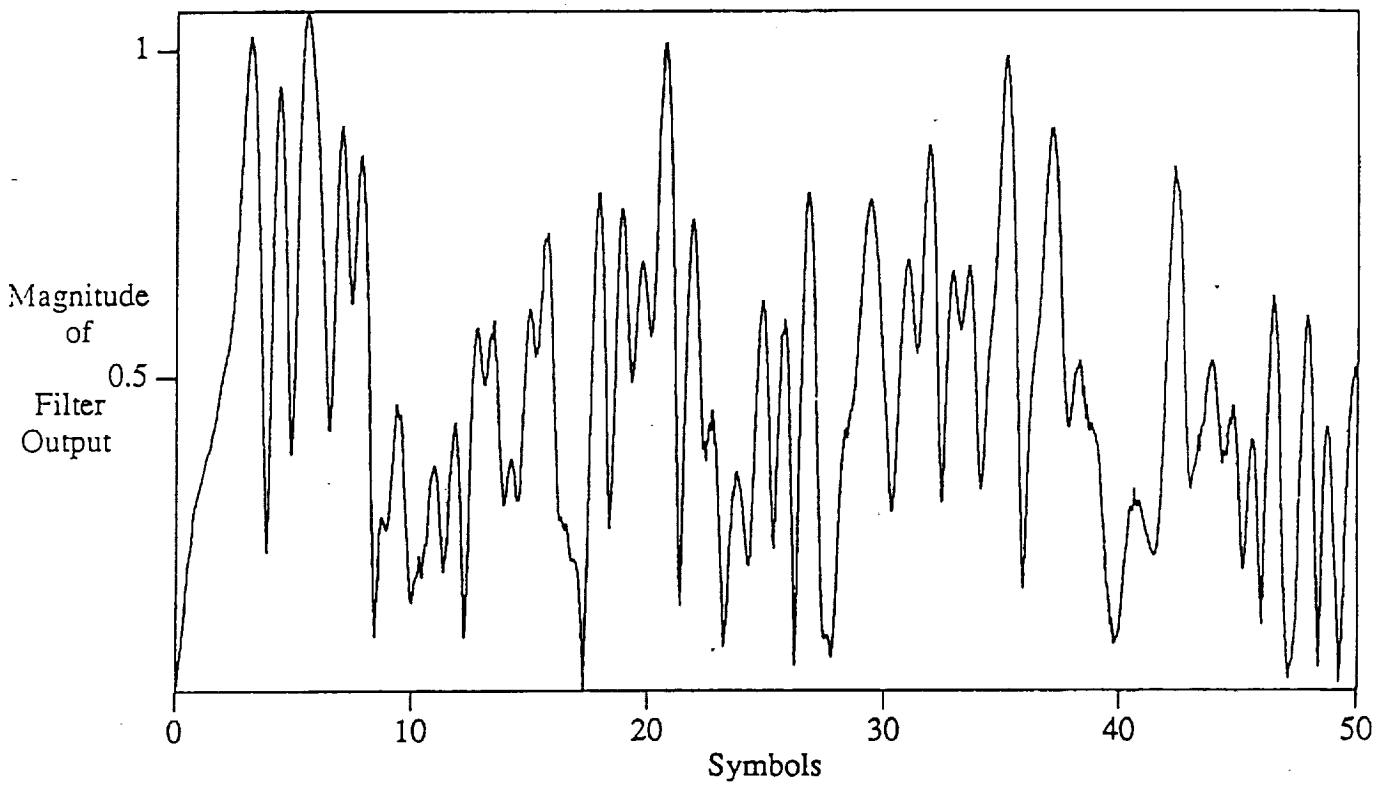

Figure 7.25: Action of filter NBF2

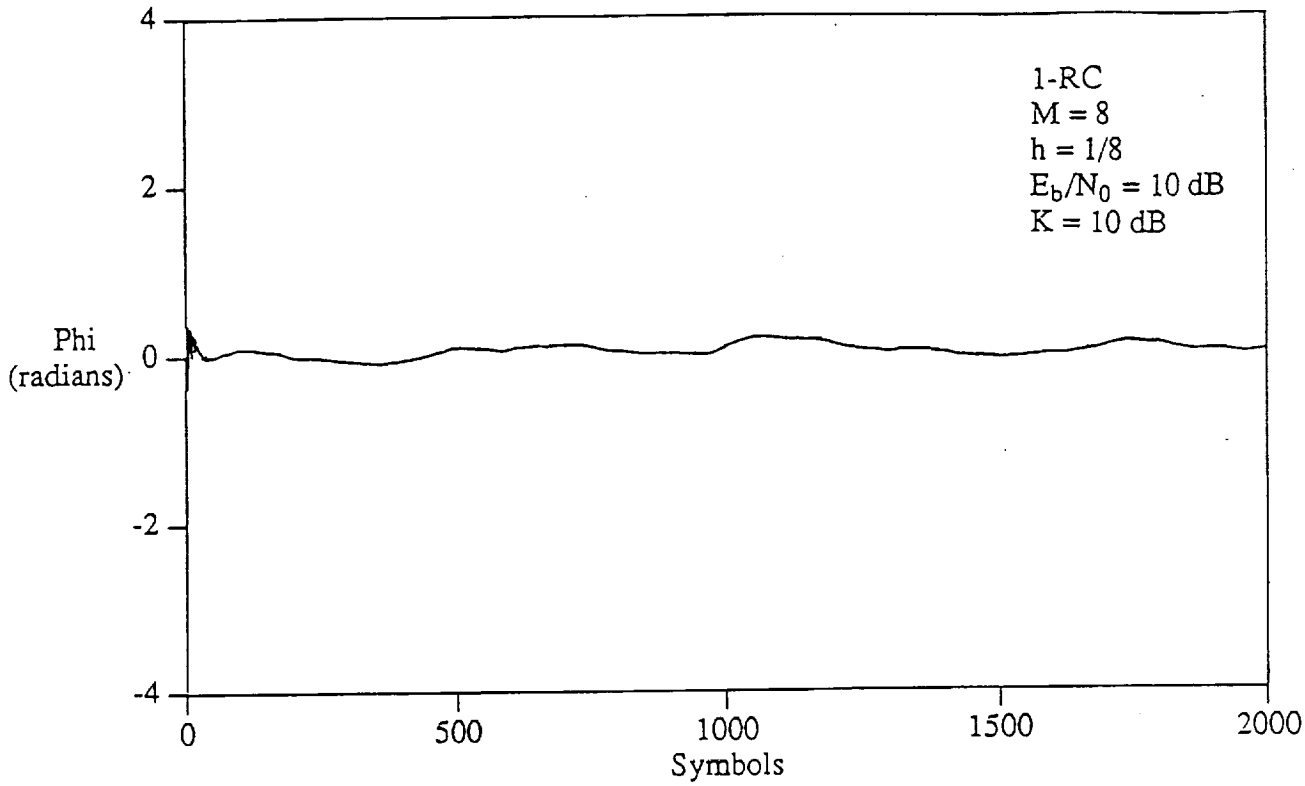

Figure 7.26: Recovered Phase, 1-RC, Time Delay = 0

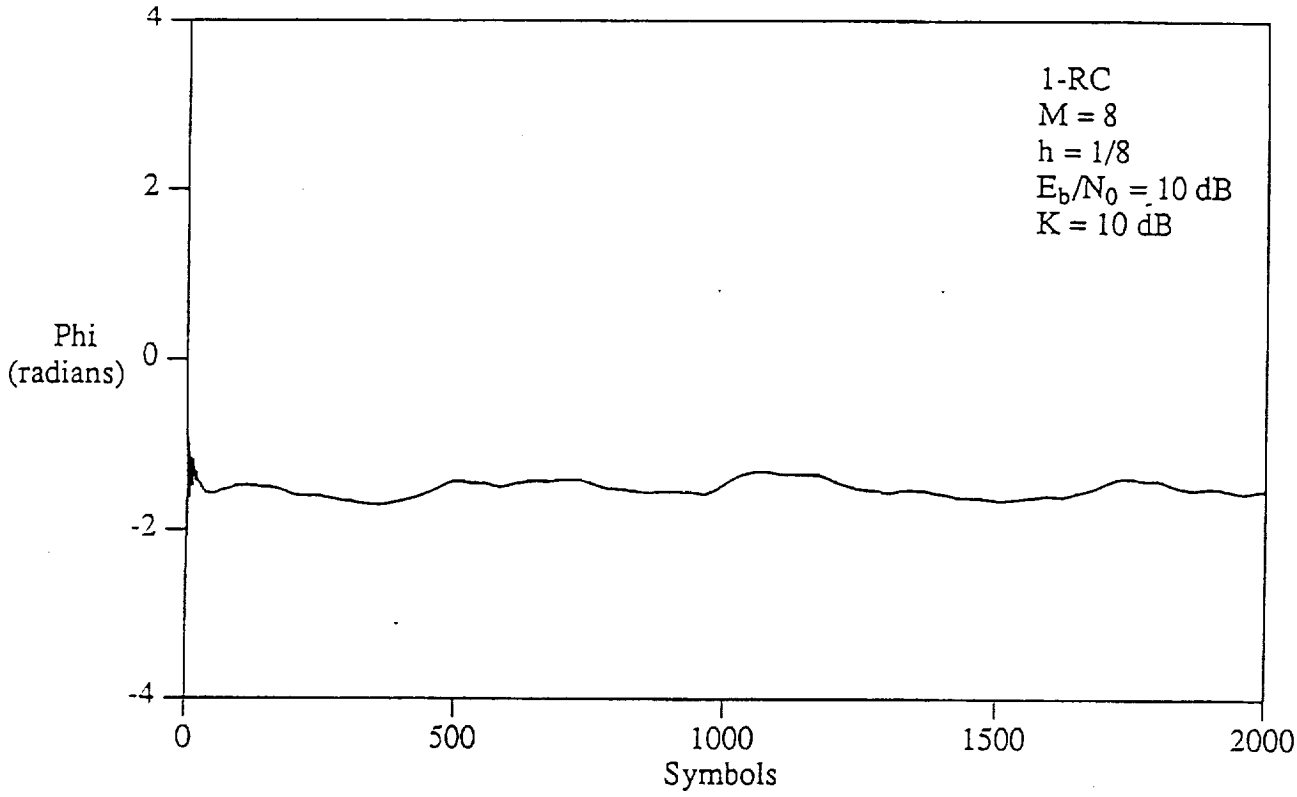

Figure 7.27: Recovered Phase, 1-RC, Time Delay = 1/4 Symbol Time

Chapter 8

Simulation results

In this Chapter we present simulation results that allow a comparison between different classes of trellis-encoded continuous-phase modulation (CPM) schemes with differential demodulation and optimum (maximum-likelihood, i.e., Viterbi) decoding. The performance analysis will be based on bit error probability versus the ratio $\mathcal{E}_b/N_0$ between the average energy per information bit and the noise power spectral density of the additive white Gaussian noise affecting the transmission. The baseline for our comparison has been chosen to be the performance of differentially-demodulated phase-shift keying (DPSK) with 8 levels. In fact, DPSK offers constant-envelope signals (like CPM) and is demodulated differentially (like our scheme). DPSK turns out to be more power-efficient than CPM, but on the other hand it occupies a broader bandwidth than CPM: thus, this comparison will show how our trellis-encoded CPM scheme will trade bandwidth efficiency for power efficiency. However, as will be demonstrated, *trellis coded CPM comes fairly close, and indeed somewhat better, in performance to the filtered DPSK particularly in a Rician fading environment.*

Our simulation will include the effects of additive white Gaussian noise channel, Rician fading, and Doppler frequency shift. Our goal is to get the best combination of

- Frequency shaping pulse $g(t)$.
- Full- or partial-response CPM.
- Receiver filter shape and bandwidth.
- Trellis-coded modulation (TCM) scheme.

Hereafter, the modulation index h for CPM has always been chosen equal to $1/M$, M the number of symbol carried by CPM. We hasten to observe that if the demodulation were optimum, i.e., coherent and based on Viterbi algorithm, then the optimum choice of h would involve a subtle tradeoff between power and bandwidth. With differential detection, it is known that increasing h will increase the phase difference among CPM signals associated with different symbols, and hence increase the signal distance, which will ultimately result into a smaller error probability. Since increasing h will also increase the bandwidth occupancy, the strategy that we have chosen is the following: choose $h = 1/M$, and the phase pulse shapes that satisfy the bandwidth constraints for that value of the modulation index. Soft decision demodulation was optimized based on analysis of the eye patterns. A complete set of precoded partial response signals have been studied under the AWGN model. It was observed that partial response systems shows a performance degradation larger than full-response CPM. For this reason, full-response CPM was analyzed more thoroughly with the aim of choosing the final candidate system. The selected full-response scheme was then tested under the Rician fading environment.

8.1 Description of simulation results

In this section we present the best combinations of TCM schemes, continuous-phase modulations, and receiving filters for a number of channels. The following situations are considered:

1. Frequency pulse shapes as shown in Table 8.1. In particular:
   - LREC denotes rectangular frequency pulse with duration LT_s (in particular, $L = 1$ denotes full-response signaling).
   - LHCS denotes "half-cycle sinusoidal" frequency pulse with duration LT_s.
   - LSRC denotes "spectral raised cosine" with duration LT_s and "rolloff" factor α.
   - GMSK denotes a Gaussian frequency pulse. This has a theoretical infinite duration, and is truncated to duration LT_s.
2. Receiver filter shapes:
   - LREC filter.

- Butterworth filter (unless otherwise specified, the Butterworth considered here has order 6 and a 3-dB bandwidth of 4800 Hz).
- L_ARC (raised cosine) filter (see Table 8.2).
- L_BSRC (spectral raised cosine) filter (see Table 8.2). Here β_f is the rolloff factor, and a_0 is a normalization constant chosen such that $\int h^2(t)dt = 1$.
- Gaussian filter

3. Trellis-coded modulation schemes:
   - Rate-2/3, 4 states (see Fig. 1)
   - Rate-2/3, 8 states (see Fig. 2)
   - Rate-2/3, 16 states (see Fig. 3)
4. Interleaving/deinterleaving sizes and depths:
   - No interleaving
   - (128,16) interleaving
   - (256,16) interleaving

It should be observed here that we limited our consideration of TCM to schemes with no more than 16 states, and this for two reasons:

1. While it is known that by increasing the number of states the performance of TCM increases, it has been observed that above a certain number of states the returns are diminishing, thus rendering less and less attractive the increase in complexity entailed.
2. We are interested in system performance at relatively small values of signal-to-noise ratio (typically, they correspond to error probabilities around 10^{-3}. In this range, *TCM schemes with a large number of states perform more poorly than simpler schemes.* In fact, the higher is the number of states, the higher is the signal-to-noise ratio necessary to take full advantage of the potential coding gain generated by the introduction of trellis-coded modulation.

Interleaving the symbols after the TCM encoder and deinterleaving them before the TCM decoder would make the equivalent channel, as seen by the TCM scheme, more similar to a memoryless one. Since the decoding strategy is based on the simplifying assumption that the channel is indeed memoryless, it is expected that interleaving prove beneficial in the present context.

LREC	$g(t) = \begin{cases} \frac{1}{2LT_s}, & 0 \le t \le LT_s \\ 0, & \text{otherwise} \end{cases}$
GMSK	$g(t) = \frac{1}{2T_s}\left[Q\left(2\pi B\frac{t-T_s/2}{\sqrt{\ln 2}}\right) - Q\left(2\pi B\frac{t+T_s/2}{\sqrt{\ln 2}}\right)\right]$
HCS	$g(t) = \frac{\pi}{2LT_s}\sin\frac{\pi T_s}{LT_s}$
SRC	$g(t) = \begin{cases} \frac{1+\alpha}{2LT_s}, & \|t-LT_s/2\| \le \frac{LT_s}{2}\frac{1-\alpha}{1+\alpha} \\ \frac{1+\alpha}{2LT_s}\left\{1-\sin\left[\frac{\pi}{2}\frac{1+\alpha}{\alpha}\left(t-\frac{LT_s}{2(1+\alpha)}\right)\right]\right\} & \frac{LT_s}{2}\frac{1-\alpha}{1-\alpha} \le \|t-LT_s/2\| \le \frac{LT_s}{2} \\ 0 & \|t-LT_s/2\| \ge \frac{LT_s}{2} \end{cases}$

Table 8.1: Frequency pulses used in the simulation.

L_ARC	$h(t) = \begin{cases} \sqrt{\frac{2}{3L_AT_s}}\left(1-\cos\frac{2\pi t}{L_AT_s}\right) & 0 \le t \le L_AT_s \\ 0 & \text{otherwise} \end{cases}$
L_BSRC	$h(t) = a_0\frac{\sin 2\pi t/L_BT_s}{2\pi t/L_BT_s}\frac{\cos\beta_f 2\pi t/L_BT_s}{1-(4\beta_f t/L_BT_s)^2}$ $\quad 0 \le \beta_f \le 1$

Table 8.2: Impulse responses of filters pulses used in the simulation.

8.1.1 Gaussian channel

In this section simulation results will be provided in the form of error probability charts corresponding to a transmission system operating over the additive white Gaussian noise (AWGN) channel, with intersymbol interference generated by non-ideal filters.

- Fig. 8.4 shows the performance of 4-state, TCM-encoded CPM signals with full response signaling, HCS1 frequency pulse, $M = 8$ levels, $h = 0.125$, and differential detection. This scheme carries 2 information bits per symbol. Here we compare the effect of different receiver filters, namely:

  1. 1RC
  2. 2RC
  3. 2RC with (256,16) block interleaving
  4. SRC with $L_B = 1.01$ and rolloff $\beta_f = 0.4$
  5. Same as above, with (256,16) block interleaving
  6. Butterworth
  7. Same as above, with (256,16) interleaving

  Comparison of the performance with and without interleaving shows the benefit of introducing the latter. SRC filters provide the best performance in this situation.

- Fig. 8.5 shows the performance of 4-state, TCM-encoded CPM signals with partial response signaling, 2REC frequency pulse, $M = 8$ levels, $h = 0.125$, and differential detection. This scheme carries 2 information bits per symbol. Here we compare the effect of different receiver filters, namely:

  1. 1REC
  2. 1RC
  3. 3RC
  4. Gaussian filter with 3-dB bandwidth 0.95
  5. SRC with $L_B = 1.01$ and rolloff $\beta_f = 0.4$

  This chart shows that the 2REC pulse offers poor performance for this system.

- Fig. 8.6 refers to the same situation as in Fig. 8.5, with the only change of an 8-state trellis in lieu of a 4-state trellis. The increase in complexity does not help.

- Fig. 8.7 refers to the same situation as in Fig. 8.6, with the complexity of the TCM scheme further increased to 16 states. The same conclusion reached before about 2REC is still valid under the new conditions.

- Fig. 8.8 shows the performance of 4-state, TCM-encoded CPM signals with partial response signaling, 2RC frequency pulse, $M = 8$ levels, $h = 0.125$, and differential detection. This scheme carries 2 information bits per symbol. Here we compare the effect of different receiver filters, namely:

  1. 1REC
  2. 1RC
  3. 3RC
  4. Gaussian filter with 3-dB bandwidth 0.95
  5. SRC with $L_B = 1.01$ and rolloff $\beta_f = 0.4$

  This chart shows that the 2RC pulse offers a performance for this system which is better than 2REC, but still worse than the HCS1 pulse considered before.

- Fig. 8.9 refers to the same situation as in Fig. 8.8, with the only change of an 8-state trellis in lieu of a 4-state trellis. The increase in complexity causes only a marginal performance improvement.

- Fig. 8.10 refers to the same situation as in Fig. 8.8, with the complexity of the TCM scheme further increased to 16 states. The performance improvement is modest.

- Fig. 8.11 shows the performance of 4-state, TCM-encoded CPM signals with partial response signaling, GMSK frequency pulse with $BT = 0.4$ and truncated at $LT_s = 2$, $M = 8$ levels, $h = 0.125$, and differential detection. This scheme carries 2 information bits per symbol. Here we compare the effect of different receiver filters, namely:

  1. 1REC
  2. 1RC

3. 3RC
4. Gaussian filter with 3-dB bandwidth 0.95
5. SRC with $L_B = 1.01$ and rolloff $\beta_f = 0.4$

This chart shows that the GMSK pulse offers a performance similar to 2RC.

- Fig. 8.12 refers to the same situation as in Fig. 8.11, with the only change of an 8-state trellis in lieu of a 4-state trellis. The increase in complexity causes no performance improvement.

- Fig. 8.13 refers to the same situation as in Fig. 8.11, with the complexity of the TCM scheme further increased to 16 states. The performance improvement is modest.

- Fig. 8.14 shows the performance of 4-state, TCM-encoded CPM signals with partial response signaling, HCS2 frequency pulse, $M = 8$ levels, $h = 0.125$, and differential detection. This scheme carries 2 information bits per symbol. Here we compare the effect of different receiver filters, namely:

  1. 1REC
  2. 1RC
  3. 3RC
  4. Gaussian filter with 3-dB bandwidth 0.95
  5. SRC with $L_B = 1.01$ and rolloff $\beta_f = 0.4$

  This chart shows that the GMSK pulse offers a performance similar to 2RC.

- Fig. 8.15 refers to the same situation as in Fig. 8.14, with the only change of an 8-state trellis in lieu of a 4-state trellis. The increase in complexity causes no performance improvement.

- Fig. 8.16 refers to the same situation as in Fig. 8.15, with the complexity of the TCM scheme further increased to 16 states. There is no evident performance improvement.

- Fig. 8.17 compares the performance of two TCM schemes with different number of states (and consequently, different complexity) under

the same conditions, namely, TCM-encoded CPM signals with partial response signaling, 2RC frequency pulse, $M = 8$ levels, $h = 0.125$, and differential detection. The receiver filter is SRC with $L_B = 1.01$ and rolloff $\beta_f = 0.4$. It is seen that, at least for large enough signal-to-noise ratios, increase in complexity involves a performance improvement. It should be noticed, however, that this improvement depends on the specific receiver filter involved, and different filters give different returns, as shown by comparison of Figs. 8 and 9.

- Fig. 8.18 compares the performance of two TCM schemes with different number of states (and consequently, different complexity) under the same conditions, namely, TCM-encoded CPM signals with partial response signaling, GMSK frequency pulse truncated at $LT_s = 2$ and with $BT = 0.4$, $M = 8$ levels, $h = 0.125$, and differential detection. The receiver filter is 1RC. The same conclusions reached in the examination of Fig. 8.17 still hold true.

- Fig. 8.19 compares the performance of three TCM schemes with different number of states (and consequently, different complexity) under the same conditions, namely, TCM-encoded CPM signals with partial response signaling, HCS2 frequency pulse, $M = 8$ levels, $h = 0.125$, and differential detection. The receiver filter is Gaussian with $BT_s = 0.95$. As expected, a 16-state scheme provides a larger coding gain, but this is true only at higher values of signal-to-noise ratio. The overall performance is slightly worse than with 2RC pulses.

- Fig. 8.20 shows the performance of 4-state, TCM-encoded CPM signals with full response signaling, 1REC frequency pulse, $M = 8$ levels, $h = 0.125$, and differential detection. This scheme carries 2 information bits per symbol. Here we compare the effect of different receiver filters, namely:

  1. 1REC
  2. 1RC
  3. 2RC
  4. Gaussian filter with $BT_s = 0.95$
  5. SRC with $L_B = 1.01$ and rolloff $\beta_f = 0.4$
  6. Butterworth

Butterworth filters provide the best performance in this situation, but the system performance is worse than with full-response HCS1 pulse (See Fig. 8.4 above).

- Fig. 8.21 refers to the same situation as Fig. 8.20, with the only change of an 8-state TCM scheme instead of a 4-state scheme.
- Fig. 8.22 refers to the same situation as Fig. 8.20, with the only change of an 16-state TCM scheme instead of a 4-state scheme.
- Fig. 8.23 shows the performance of 4-state, TCM-encoded CPM signals with full response signaling, 1RC frequency pulse, $M = 8$ levels, $h = 0.125$, and differential detection. This scheme carries 2 information bits per symbol. Here we compare the effect of different receiver filters, namely:

  1. 1REC
  2. 1RC
  3. 2RC
  4. Gaussian filter with $BT_s = 0.95$
  5. SRC with $L_B = 1.01$ and rolloff $\beta_f = 0.4$
  6. Same as above, with (256,16) block interleaving
  7. Butterworth

  The SRC filter with interleaving provide the best performance in this situation. The resulting performance is only slightly worse than that of 8DPSK.

- Fig. 8.24 refers to the same situation as the previous figure, but it emphasizes the effect of interleaving. It is seen that for an error probability of 10^{-3} interleaving improves the signal-to-noise ratio of about 0.8 dB.
- Fig. 8.25 refers to the same situation as Fig. 8.23, with the only change of an 8-state TCM scheme instead of a 4-state scheme. Also, interleaved SRC filtering is not considered here.
- Fig. 8.26 refers to the same situation as the previous figure, but it emphasizes the effect of interleaving. It is seen that for an error probability of 10^{-3} interleaving improves the signal-to-noise ratio of about

0.8 dB, although RC filters do not provide as good a performance as SRC filters.

- Fig. 8.27 refers to the same situation as Fig. 8.25. It emphasizes the effect of interleaving. It is seen that for an error probability of 10^{-3} interleaving improves the signal-to-noise ratio of about 0.8 dB. Here SRC filters are considered, which improves the performance with respect to RC filters.

- Fig. 8.28 refers to the same situation as Fig. 8.25. It emphasizes the effect of interleaving and of the interleaving size and depth.

- Fig. 8.29 refers to the same situation as Fig. 8.27, with the receiving filter changed from SRC into Butterworth. This proves once again the benefits of interleaving, but the performance is not as good as with SRC filter.

- Fig. 8.30 compares 4-state and 8-state TCM schemes in the same situation as in Fig. 8.28. Once again, it is seen that an increase in the number of states improves the performance at higher values of the signal-to-noise ratio.

- Fig. 8.31 shows the performance of 16-state, TCM-encoded CPM signals with full response signaling, 1RC frequency pulse, $M = 8$ levels, $h = 0.125$, and differential detection. This scheme carries 2 information bits per symbol. Here we compare the effect of different receiver filters, namely:

  1. 1RC
  2. 2RC
  3. 2RC with (256,16) block interleaving
  4. SRC with $L_B = 1.01$ and rolloff $\beta_f = 0.4$
  5. Same as above, with (256,16) block interleaving
  6. Butterworth
  7. Butterworth, with (256,16) block interleaving

  The SRC filter with interleaving provide the best performance in this situation. The resulting performance is only slightly worse than that of 8DPSK.

- In the same situation as in the previous figure, Fig. 8.32 compares interleaved and non-interleaved transmission with SRC filtering. Here interleaving provides a gain of 0.6 dB in signal-to-noise ratio.

- In the same situation as in Fig. 8.31, Fig. 8.33 compares interleaved and non-interleaved transmission with Butterworth filtering. Once more, interleaving provides a gain of 0.6 dB in signal-to-noise ratio.

- Fig. 8.34 shows the performance of 4-state, TCM-encoded CPM signals with full response signaling, GMSK1 frequency pulse with $BT_s = 0.7$, $M = 8$ levels, $h = 0.125$, and differential detection. This scheme carries 2 information bits per symbol. Here we compare the effect of different receiver filters, namely:

  1. 1REC
  2. 1RC
  3. 2RC
  4. Gaussian filter with $BT_s = 0.95$
  5. SRC with $L_B = 1.01$ and rolloff $\beta_f = 0.4$
  6. Butterworth

  The Butterworth filter provides the best performance in this situation, although the resulting performance is several dB worse than that of 8DPSK.

- In the same situation as in the previous figure, Fig. 8.35 considers an 8-state TCM scheme.

- In the same situation as in Fig. 8.34, Fig. 8.36 considers a 16-state TCM scheme.

- Fig. 8.37 compares 4-, 8-, and 16-state TCM scheme for full response signaling, GMSK1 frequency pulse with $BT_s = 0.7$, $M = 8$ levels, $h = 0.125$, and differential detection. The receiver filter here is Butterworth. The same conclusions listed before about the effect of an increase in the number of states of the TCM scheme hold here: such increase is beneficial only at high-enough signal-to-noise ratio.

- Fig. 8.38 shows the performance of 4-state, TCM-encoded CPM signals with full response signaling, HCS1 frequency pulse, $M = 8$ levels, $h =$

0.125, and differential detection. This scheme carries 2 information bits per symbol. Here we compare the effect of different receiver filters, namely:

1. SRC with $L_B = 1.01$ and rolloff $\beta_f = 0.4$
2. Same as above, with (256,16) block interleaving
3. Butterworth
4. Butterworth with (256,16) block interleaving

The SRC filter with interleaving provides the best performance in this situation.

- In the same situation as in the previous figure, Fig. 8.39 compares interleaved and non-interleaved transmission with SRC filtering. Here interleaving provides a gain of 0.9 dB in signal-to-noise ratio.

- In the same situation as in Fig. 8.38, Fig. 8.40 compares interleaved and non-interleaved transmission with Butterworth filtering. Here interleaving provides a gain of 0.8 dB in signal-to-noise ratio.

- Fig. 8.41 shows the performance of 8-state, TCM-encoded CPM signals with full response signaling, HCS1 frequency pulse, $M = 8$ levels, $h = 0.125$, and differential detection. This scheme carries 2 information bits per symbol. Here we compare the effect of different receiver filters, namely:

  1. 1RC
  2. 2RC
  3. 2RC with (256,16) block interleaving
  4. Gaussian filter with $BT_s = 0.95$
  5. SRC with $L_B = 1.01$ and rolloff $\beta_f = 0.4$
  6. Same as above, with (256,16) block interleaving
  7. Butterworth

  The SRC filter with interleaving provides the best performance in this situation.

- In the same situation as in the previous figure, Fig. 8.42 compares interleaved and non-interleaved transmission with SRC filtering. Here interleaving provides a gain of 0.9 dB in signal-to-noise ratio.

- Fig. 8.43 shows the performance of 16-state, TCM-encoded CPM signals with full response signaling, HCS1 frequency pulse, $M = 8$ levels, $h = 0.125$, and differential detection. This scheme carries 2 information bits per symbol. Here we compare the effect of different receiver filters, namely:

  1. 1RC
  2. 2RC
  3. 2RC with (256,16) block interleaving
  4. SRC with $L_B = 1.01$ and rolloff $\beta_f = 0.4$
  5. Same as above, with (256,16) block interleaving
  6. Butterworth
  7. Butterworth with (256,16) block interleaving

  The SRC filter with interelaving provides the best performance in this situation.

- In the same situation as in the previous figure, Fig. 8.44 compares interleaved and non-interleaved transmission with SRC filtering. Here (256,16) block interleaving provides a gain of about 1 dB in signal-to-noise ratio, while (128,16) interleaving offers only 0.4 dB.

- Fig. 8.45 refers to the same situation as the previous figure, with Butterworth receiving filter. Comparison of interleaving schemes of different size shows that (256,16) block interleaving provides a gain of about 0.8 dB in signal-to-noise ratio, while (128,16) interleaving offers only 0.4 dB.

- Fig. 8.46 compares the performance of 4-state and 8-state TCM-encoded CPM signals with full response signaling, HCS1 frequency pulse, $M = 8$ levels, $h = 0.125$, and differential detection. This scheme carries 2 information bits per symbol. The receiver filter is Butterworth.

In conclusion, for the AWGN channel model (i.e., in the absence of fading) an 8-state TCM-encoded CPM signals with full response signaling, 1RC frequency pulse, $M = 8$ levels, $h = 0.125$, and differential detection, in conjunction with an SRC receiver filter with $L_B = 1.01$ and rolloff $\beta_f = 0.4$, and (256,16) block interleaving, offers the best compromise between complexity and performance in the signal-to-noise range and among the candidate schemes considered in this Report.

8.1.2 Fading channel

We now consider a channel affected by additive Gaussian noise, intersymbol interference due to filtering effects, Doppler frequency spread, and Rician fading. The following parameters were selected:

1. Rician parameter K: chosen to be 10 .
2. Doppler frequency spread : chosen to be 20 and 40 Hz.

In our simulations we have examined the behavior of the best schemes found for the AWGN channel, i.e., **1RC** and **1HCS**. The latter has a higher degradation (as shown in Fig. 8.44), but is spectrally more efficient than 1RC.

The results obtained are illustrated in the figures that follow.

- Fig. 8.47 illustrates the performance of the full-response 4-state trellis coded CPM with HCS pulse shape, SRC filtering, two different interleaving sizes, and a Doppler spread of 20 Hz.
- Fig. 8.48 shows the performance of the previous system with an 8-state code.
- Fig. 8.49 refers to the same situation as the previous figure. The only change is in the number of TCM states, that is 16 here. Here, a comparison is made between the proposed CPM system (which has constant envelope) and the filtered 16-state 8DPSK (whose envelope is not constant).

  With *(256, 16) interleaving* the CPM system offers the same performance as the non-constant envelope filtered 8DPSK with (128, 16) interleaving. *This will make the CPM relatively superior the 8DPSK system.*

  With *(128, 16) interleaving*, our CPM system shows a degradation of only .5 dB with respect to 8DPSK. *In the presence of significant channel nonlinearities due to power amplifiers driven at or near saturation for better power efficiency, CPM will perform better than 8DPSK because in the latter scheme envelope fluctuations will cause phase fluctuations, which in turn will be reflected into further performance degradation.*

- Fig. 8.50 shows the performance of the full response 4-state trellis coded CPM signal, over the Rician fading channel with a Doppler spread of 40 Hz, with HCS pulse shape, SRC filter, and two different interleaving sizes.
- Fig. 8.51 demonstrates the expected 2 dB loss, for a 4-state trellis coded CPM signal, due to the presence of fading, with and without interleaving.
- Fig. 8.52 is the same as Fig. 8.50 with an 8-state TCM scheme.
- Fig. 8.53 compares the performance of the 8-state trellis coded full response CPM signal over AWGN channel with Rician fading and 40 Hz Doppler spread, with and without interleaving. This system shows a performance degradation, due to fading, of only .9 dB.
- Fig. 8.54 is the same as Fig. 8.50 with a 16-state code.
- Fig. 8.55 compares the performance of full-response CPM signal with HCS pulse shape over AWGN channel with Rician fading and a 40 Hz Doppler spread for 4, 8, and 16-state codes. A performance improvement of about 2 dB caused by the increase in the number of code states from 4 to 16 is observed here.
- Fig. 8.56 compares the performance, over two different Rician fading channels with the same interlaving scheme, of the following two systems:

  8DPSK : 16-state trellis coded, filtered, over Rician fading with 20 Hz Doppler spread, and (128, 16) interleaving.

  Differential CPM ; 16-state trellis coded, over Rician fading with 40 Hz Doppler spread, and (128, 16) interleaving.
- Fig. 8.57 illustrates the performances of 4-state trellis coded CPM signal, over the Rician fading channel, with 1RC pulse shape for two different interleaving sizes.
- Fig. 8.58 illustrates the performancs of 8-state trellis coded CPM signal, over the Rician fading channel, with 1RC pulse shape for two different interleaving sizes. Comparison is drawn with the 16-state non-constant envelope interleaved, with the same Doppler spread of 20 Hz, filtered 8DPSK, indicating a loss of only 1 dB.

- Fig. 8.59 illustrates the performancs of 16-state trellis coded CPM signal, over the Rician fading channel, with 1RC pulse shape for two different interleaving sizes. Comparison is drawn with the 16-state non-constant envelope interleaved, with the same Doppler of 20 Hz., filtered 8DPSK, indicating a loss of only 1.1 dB.

- Fig. 8.60 is the same as fig. 8.57 except, the Doppler spread is 40 Hz.

- Fig.8 61 is the same as fig. 8.58 except, the Doppler spread is 40 Hz.

- Fig. 8.62 compares the performance, over two different Rician fading channels with the same interleaving scheme, of the following two systems:

  8DPSK : 16-state trellis coded, filtered, over Rician fading with 20 Hz Doppler spread, and (128, 16) interleaving.

  Differential CPM ; 16-state trellis coded, over Rician fading with 40 Hz Doppler spread, and (128, 16) interleaving.

- Fig. 8.63 compares the performance, over the same Rician fading channel with 20 Hz. Doppler spread, of:

  8DPSK : 16-state trellis coded, filtered, and (128, 16) interleaving.

  Differential CPM ; 8 and 16-state trellis coded, and (128, 16) interleaving.

We observe that, under the conditions of our simulation, the CPM scheme offers the same performance as a filtered 8DPSK signal, but with the additional positive feature of a constant envelope. This, in essence, will make the CPM a more attractive system. We also observe that, in the presence of a finite-size block interleaving, larger Doppler spreads may cause a smaller performance degradation than smaller spreads. This is apparently due to the fact that Doppler frequency spread causes a *reduction* of the length of the bursts, which are not completely interspersed by a finite-depth interleaver.

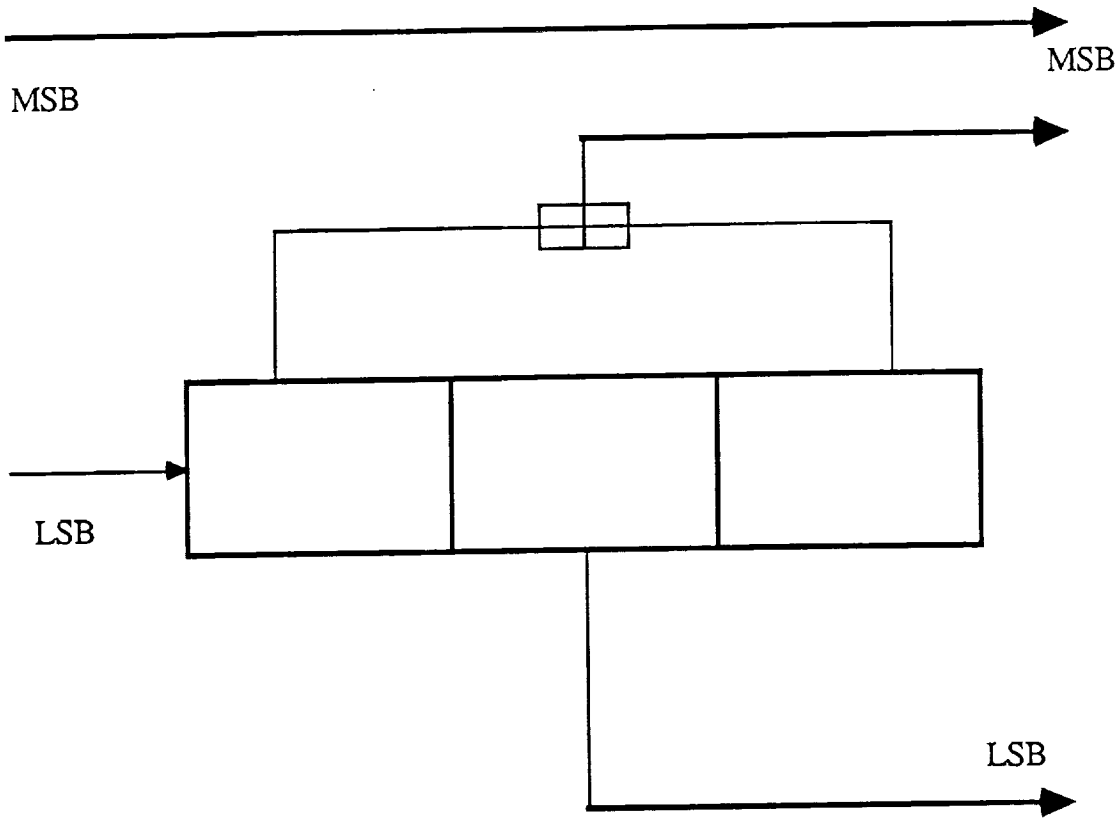

4-state code

Figure 8.1

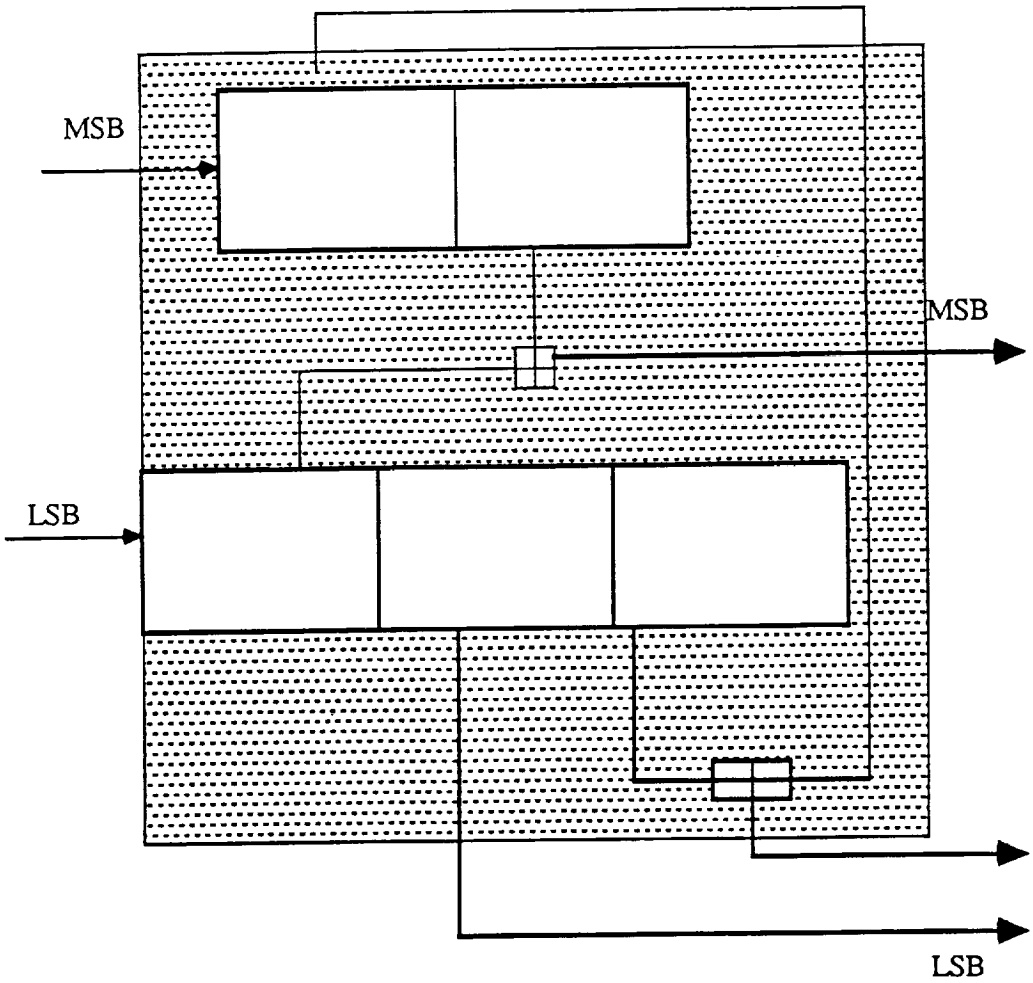

8-state code

Figure 8.2

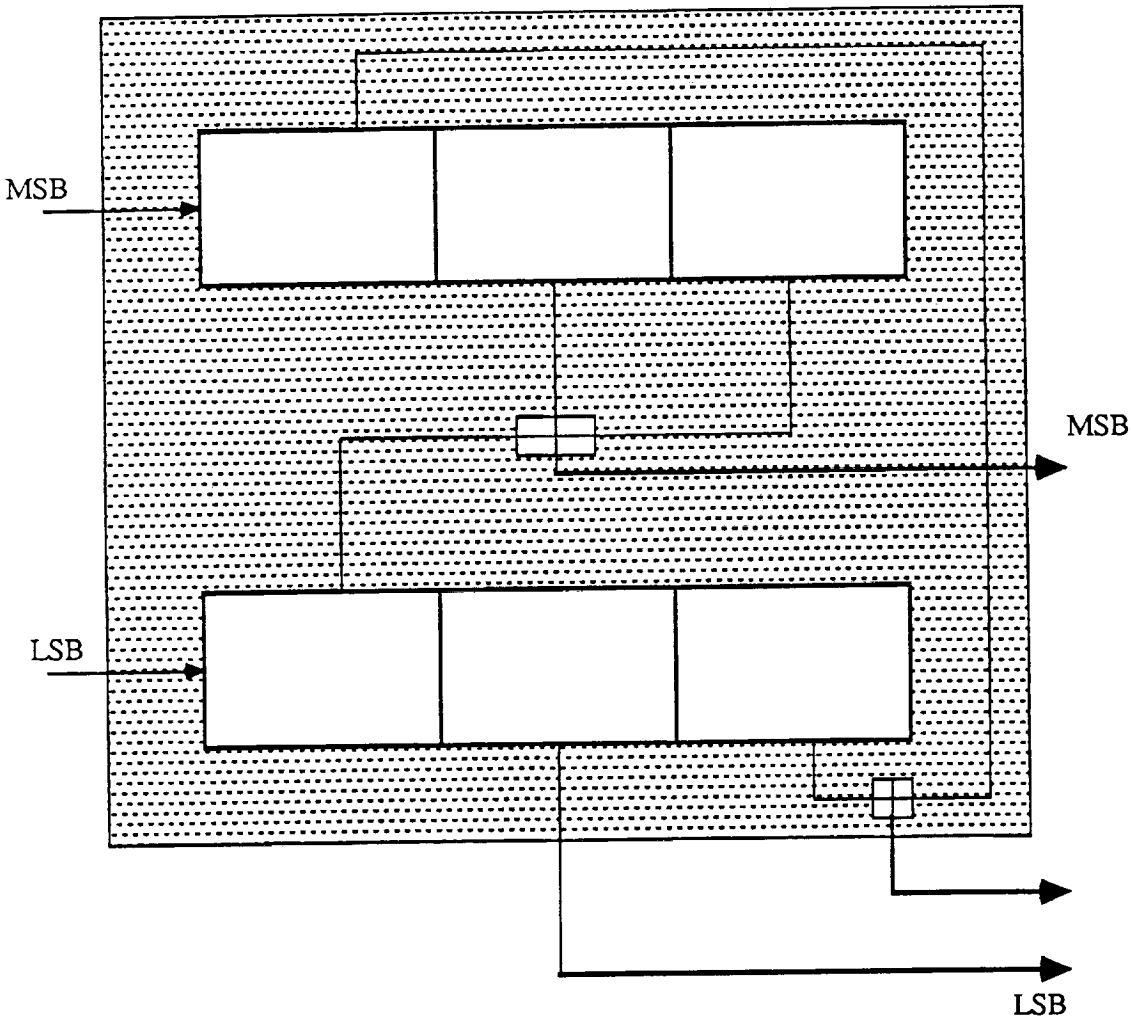

16-state code

Figure 8.3

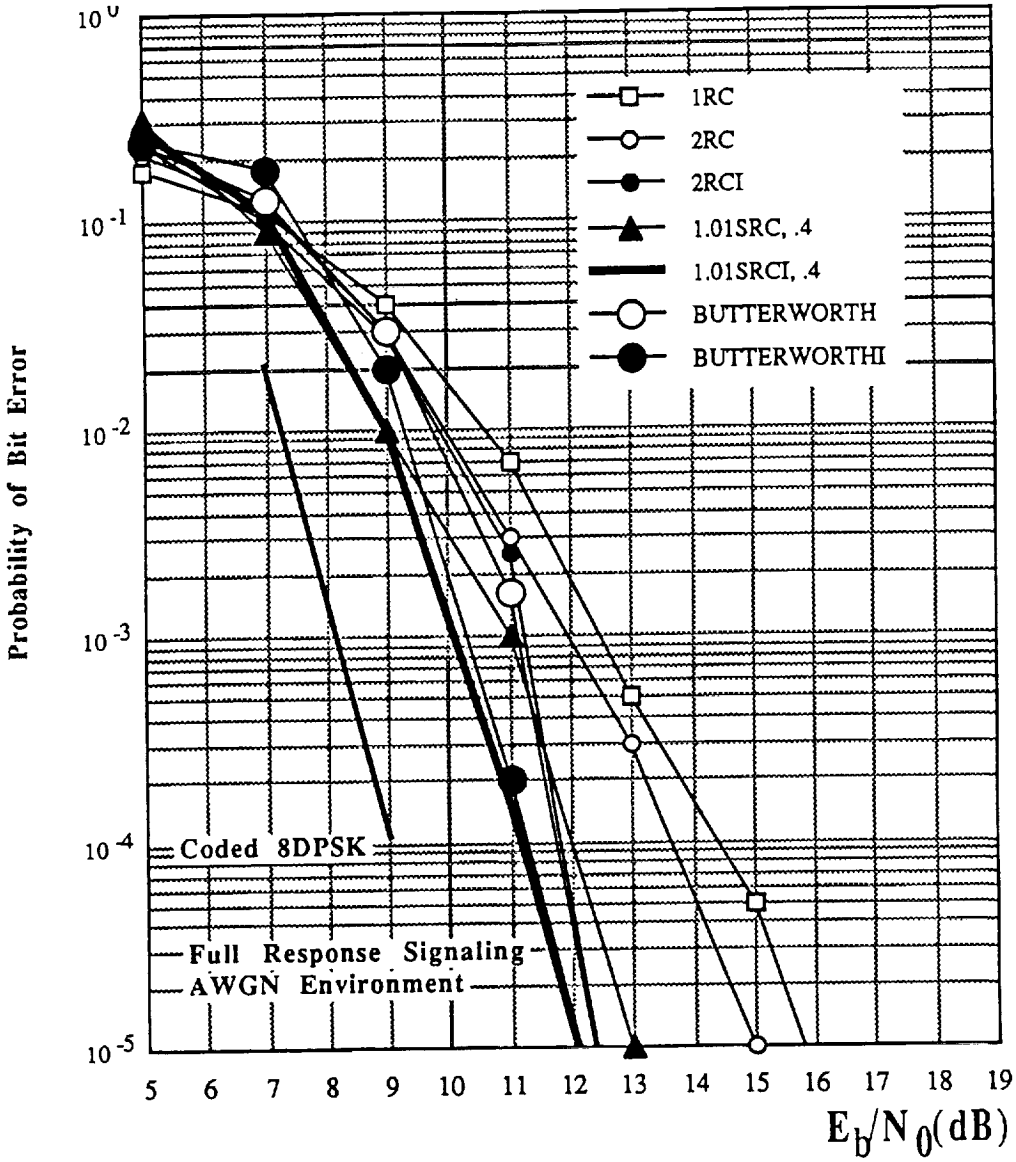

Performance of 4-state trellis coded 8-level CPM signal with HCS1 pulse shape, h=0.125, and differential detection for various receiver filtering. Trellis coded 8-level DPSK is also shown for comparison.

Figure 8.4

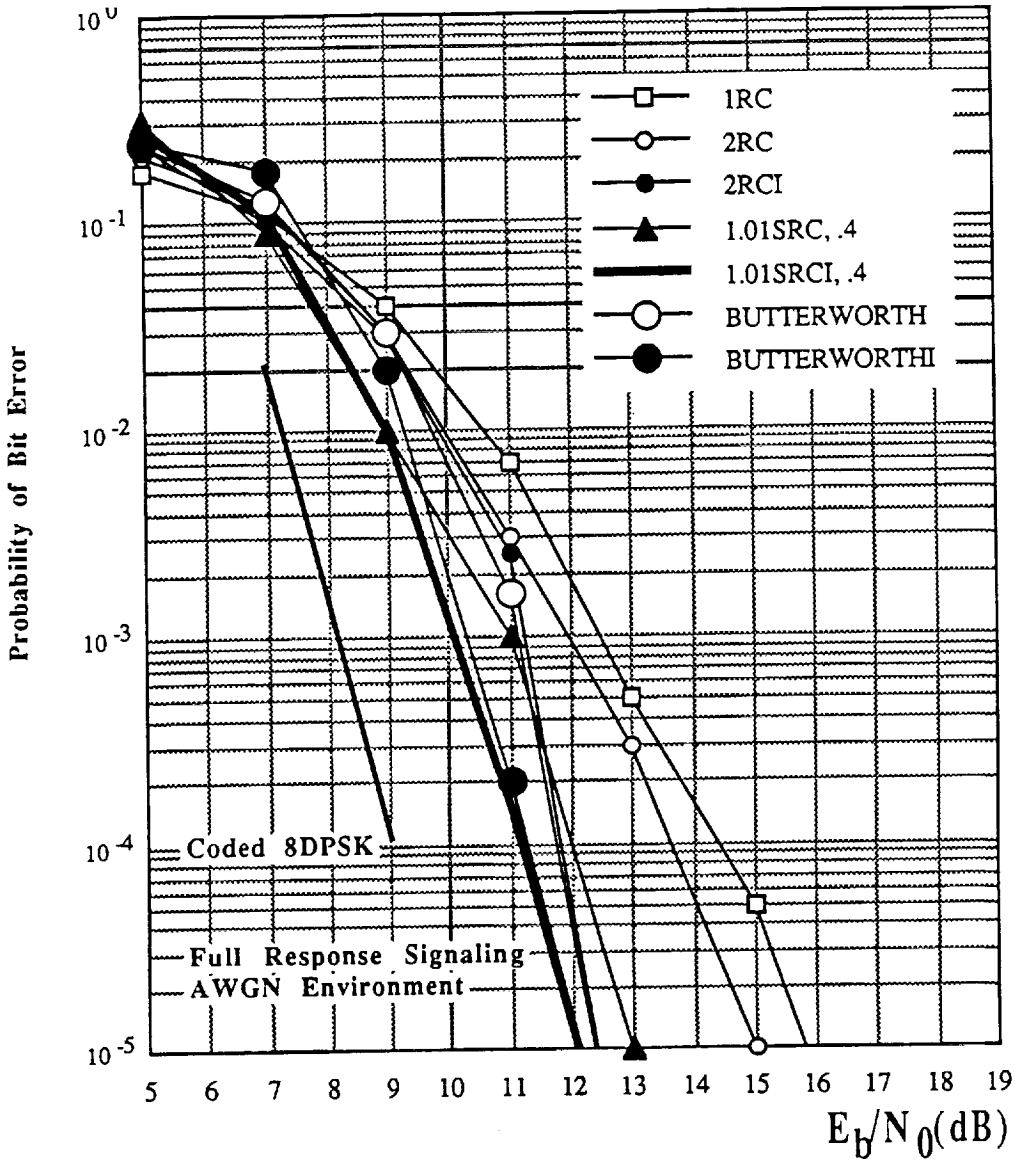

Performance of 4-state trellis coded 8-level CPM signal with HCS1 pulse shape, h=0.125, and differential detection for various receiver filtering. Trellis coded 8-level DPSK is also shown for comparison.

Figure 8.5

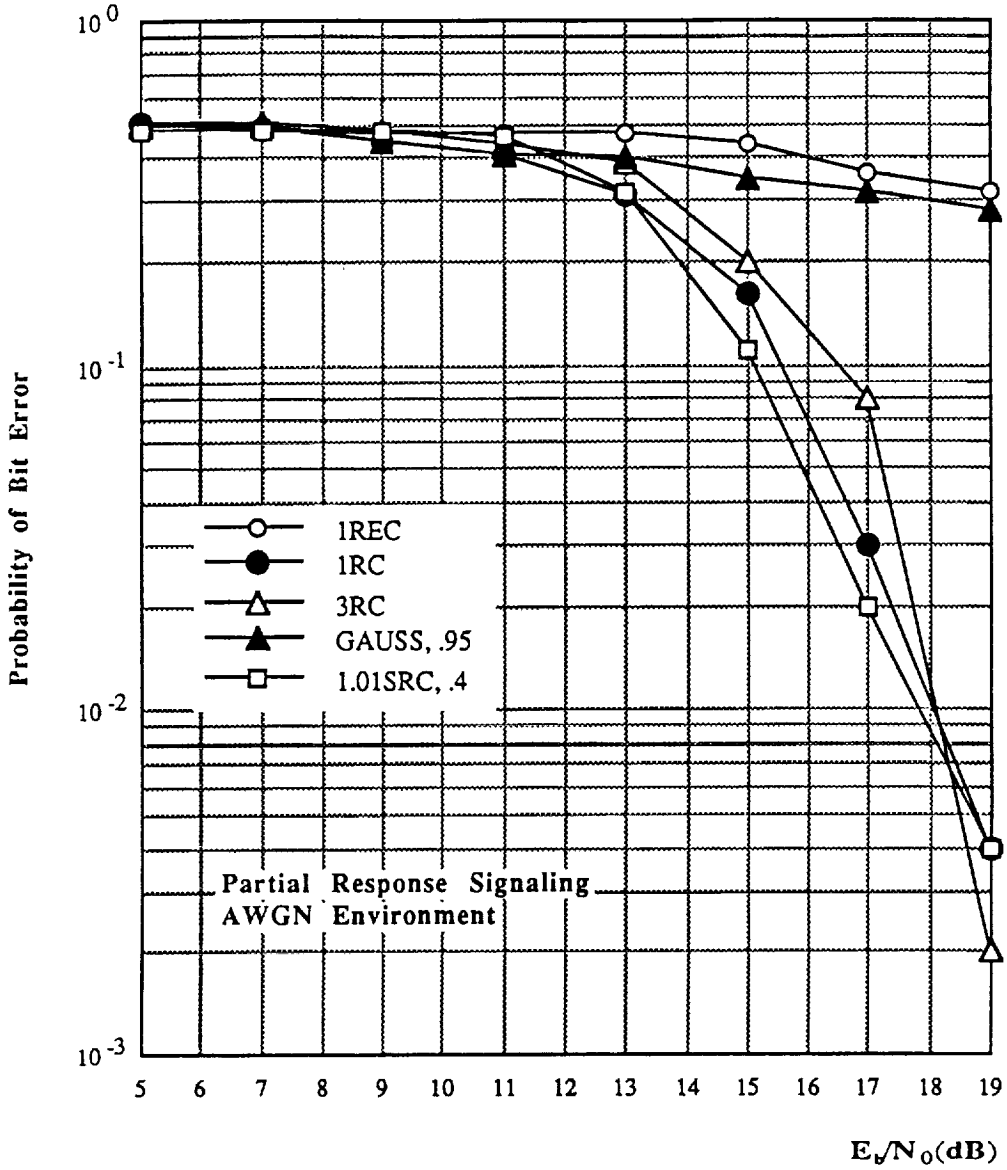

Performance of 8-state trellis coded 8-level CPM signal with 2REC pulse shape, h=0.125, and differential detection for various receiver filtering.

Figure 8.6

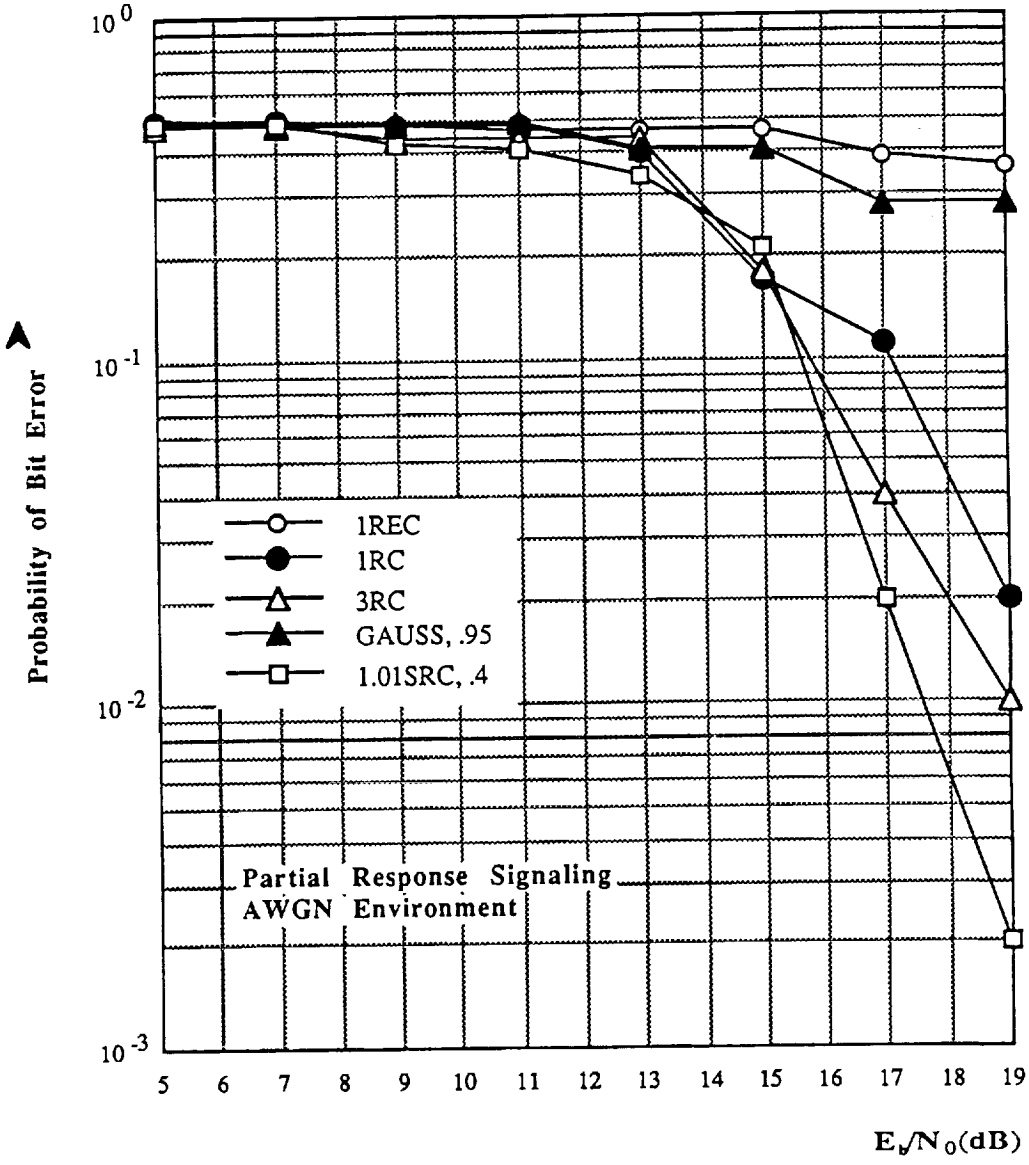

Performance of 8-state trellis coded 8-level CPM signal with 2REC pulse shape, h=0.125, and differential detection for various receiver filtering.

Figure 8.7

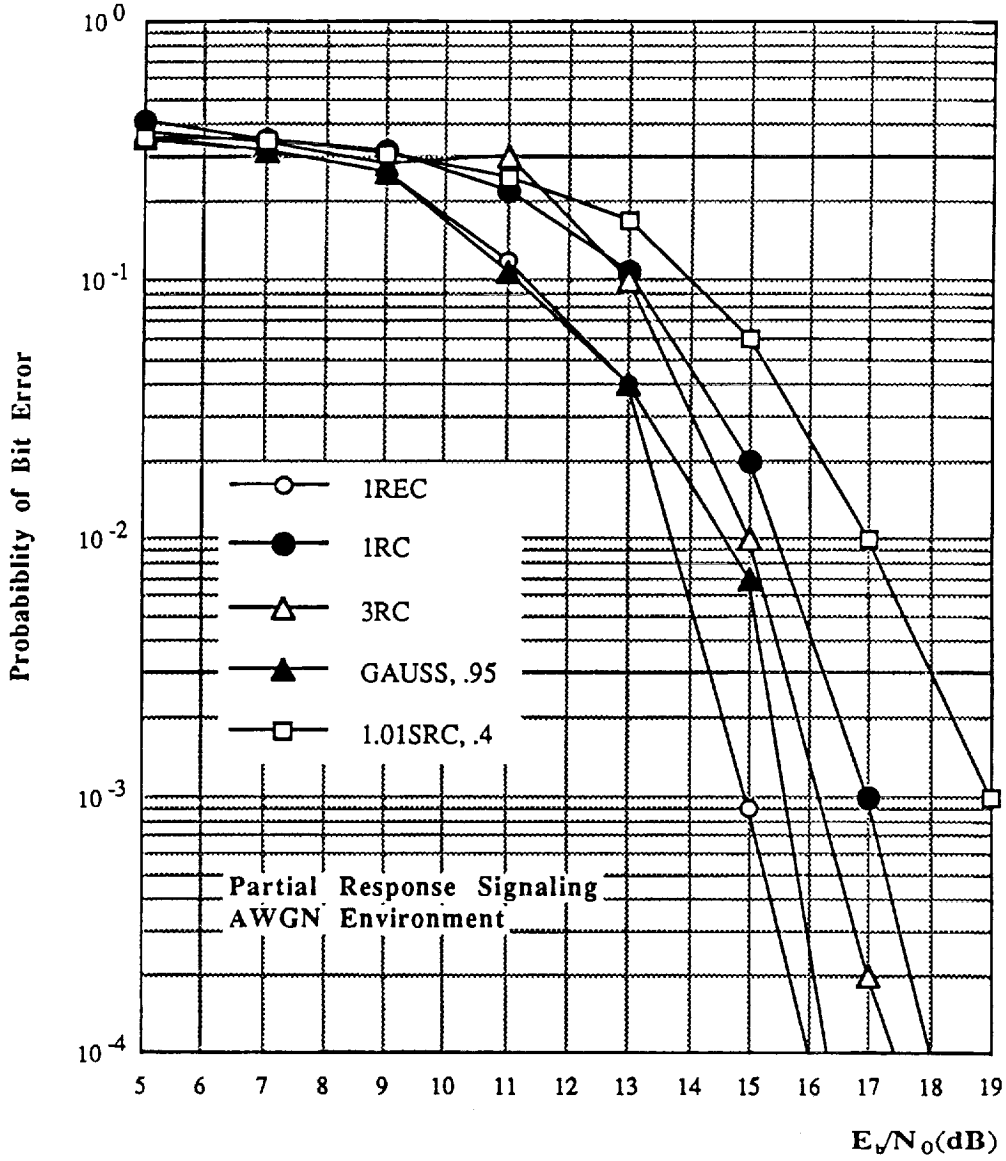

Performance of 4-state trellis coded 8-level CPM signal with 2RC pulse shape, h=0.125, and differential detection for various receiver filtering.

Figure 8.8

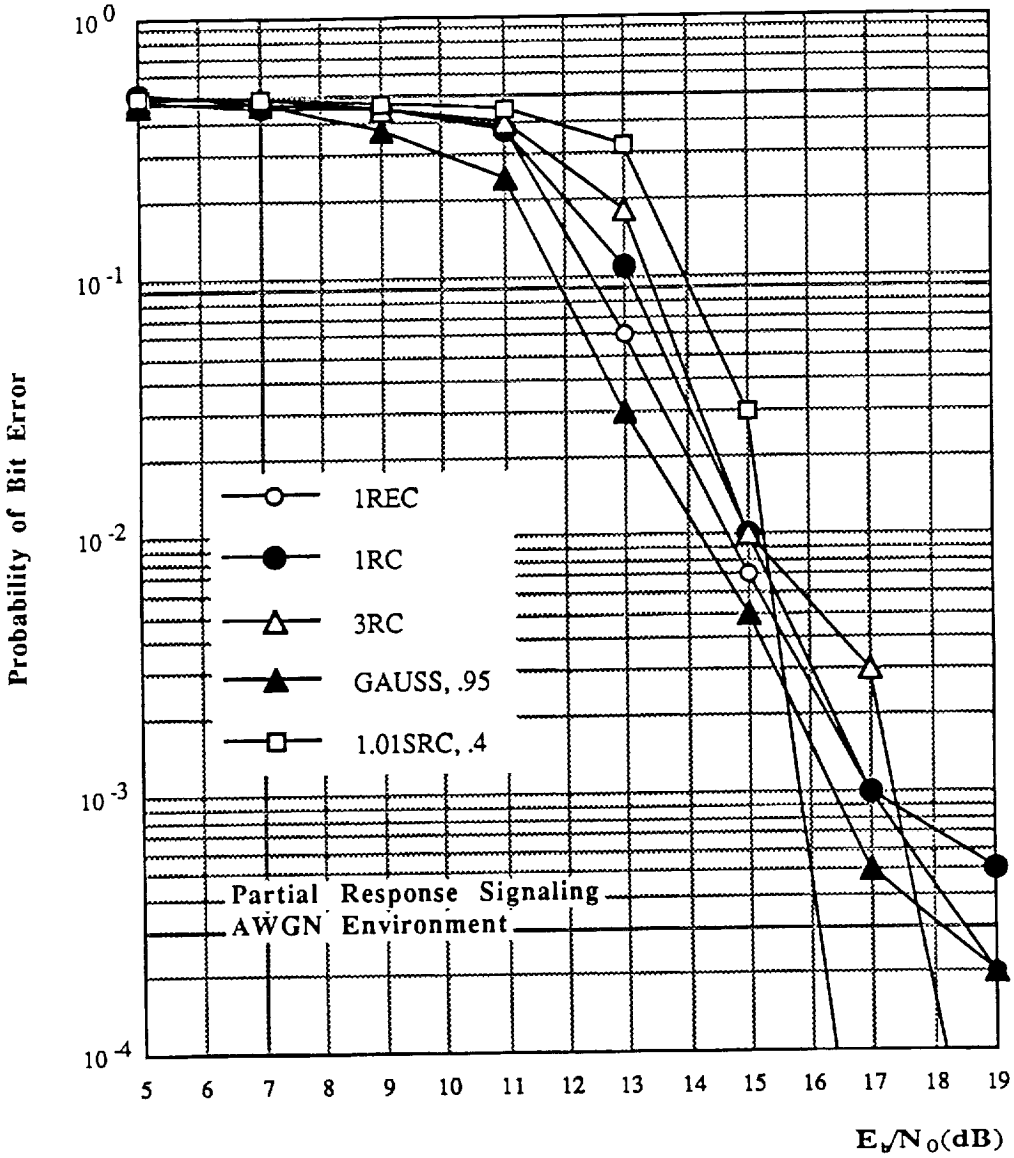

Performance of 8-state trellis coded 8-level CPM signal with 2RC pulse shape, h=0.125, and differential detection for various receiver filtering.

Figure 8.9

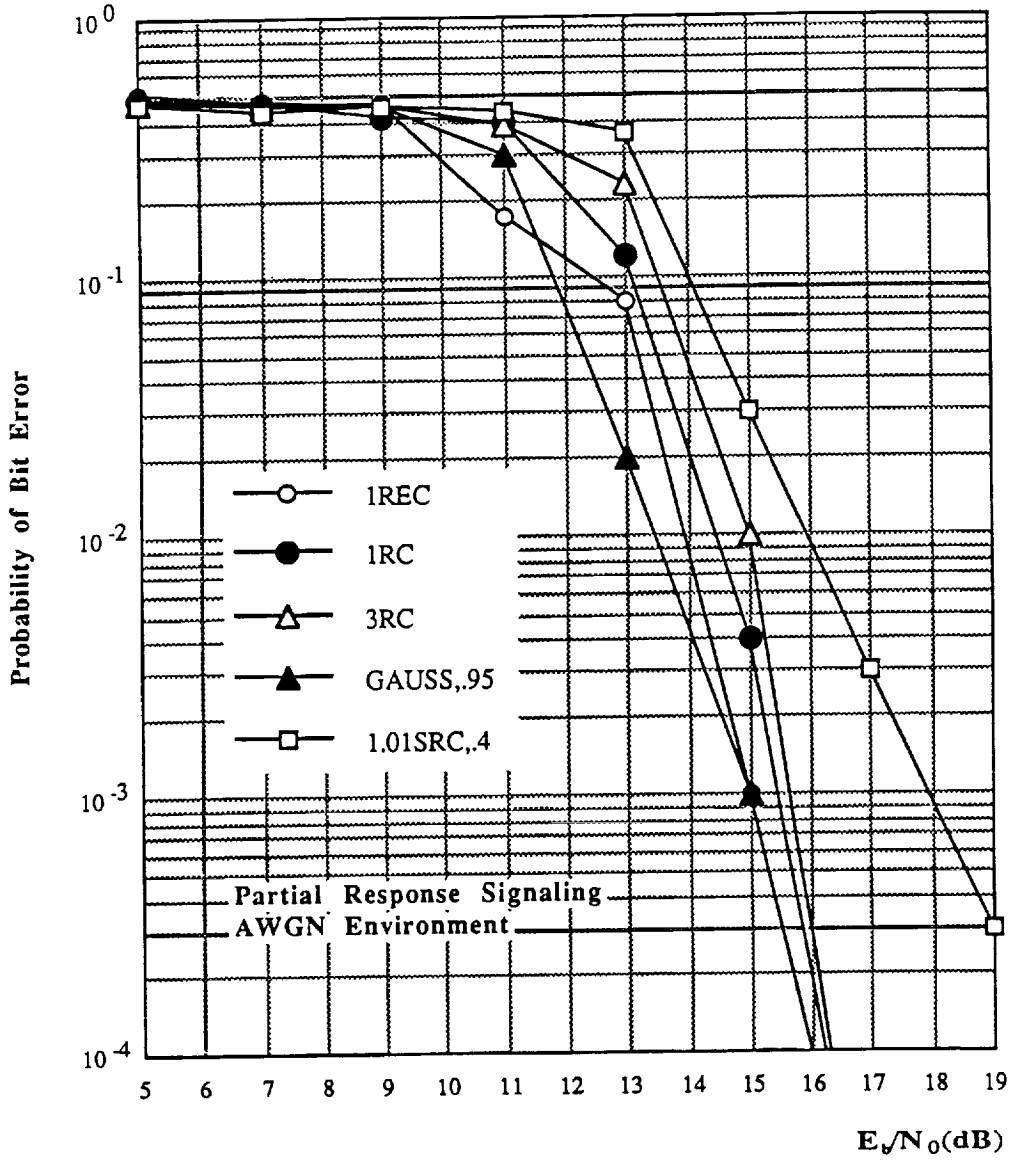

Performance of 16-state trellis coded 8-level CPM signal with 2RC pulse shape, h=0.125, and differential detection for various receiver filtering.

Figure 8.10

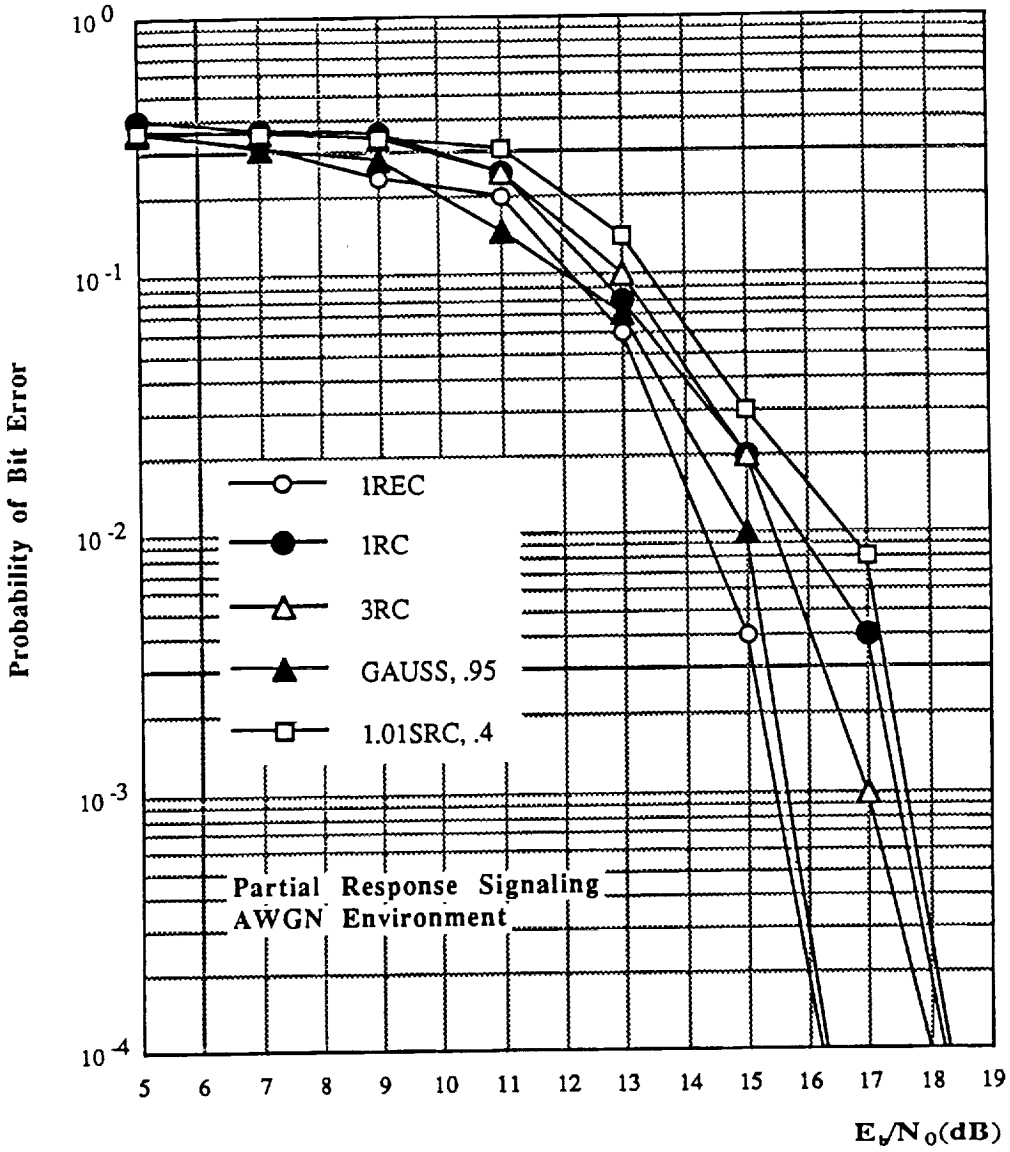

Performance of 4-state trellis coded 8-level CPM signal with GMSK2, BT=.4 pulse shape, h=0.125, and differential detection for various receiver filtering.

Figure 8.11

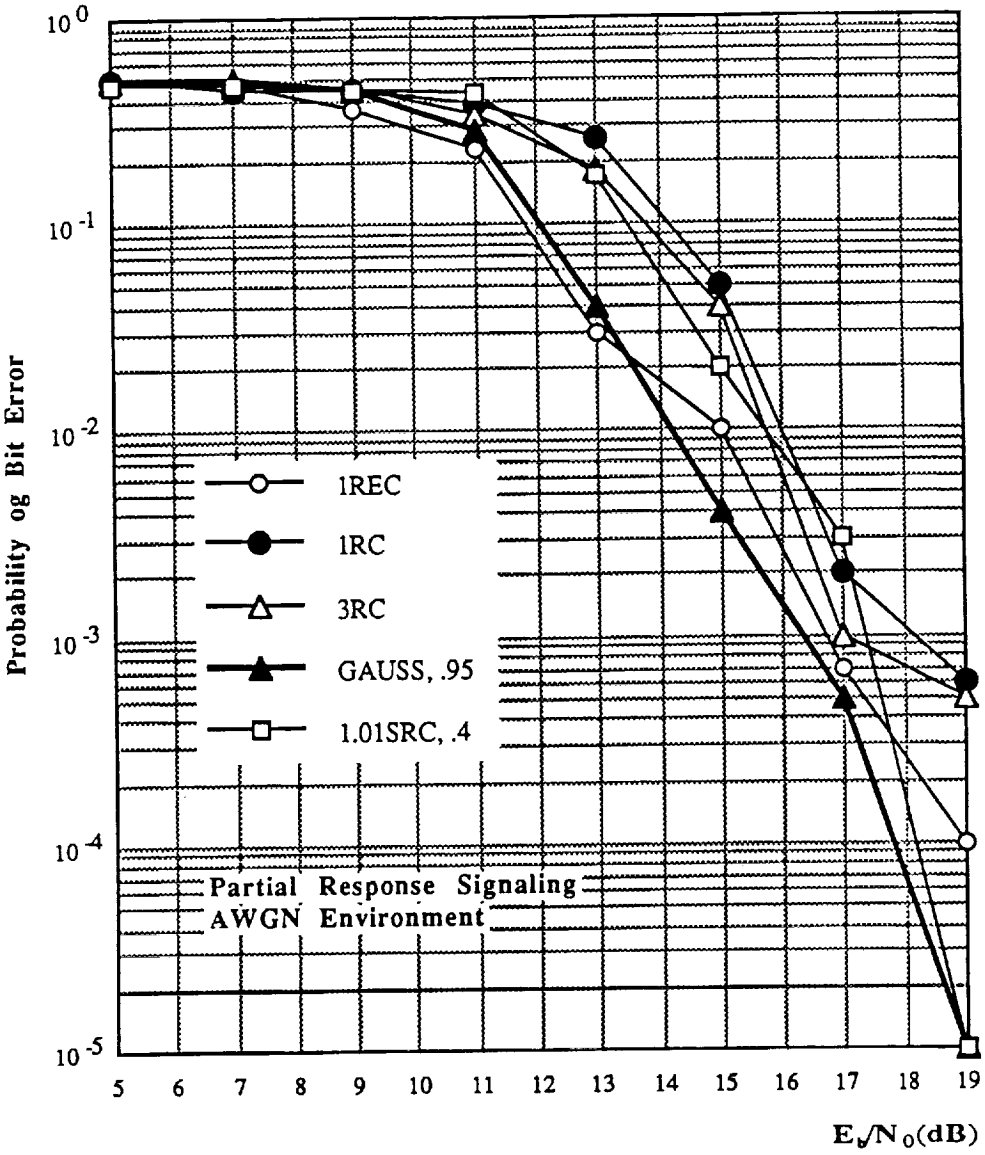

Performance of 8-state trellis coded 8-level CPM signal with GMSK2, BT=.4 pulse shape, h=0.125, and differential detection for various receiver filtering.

Figure 8.12

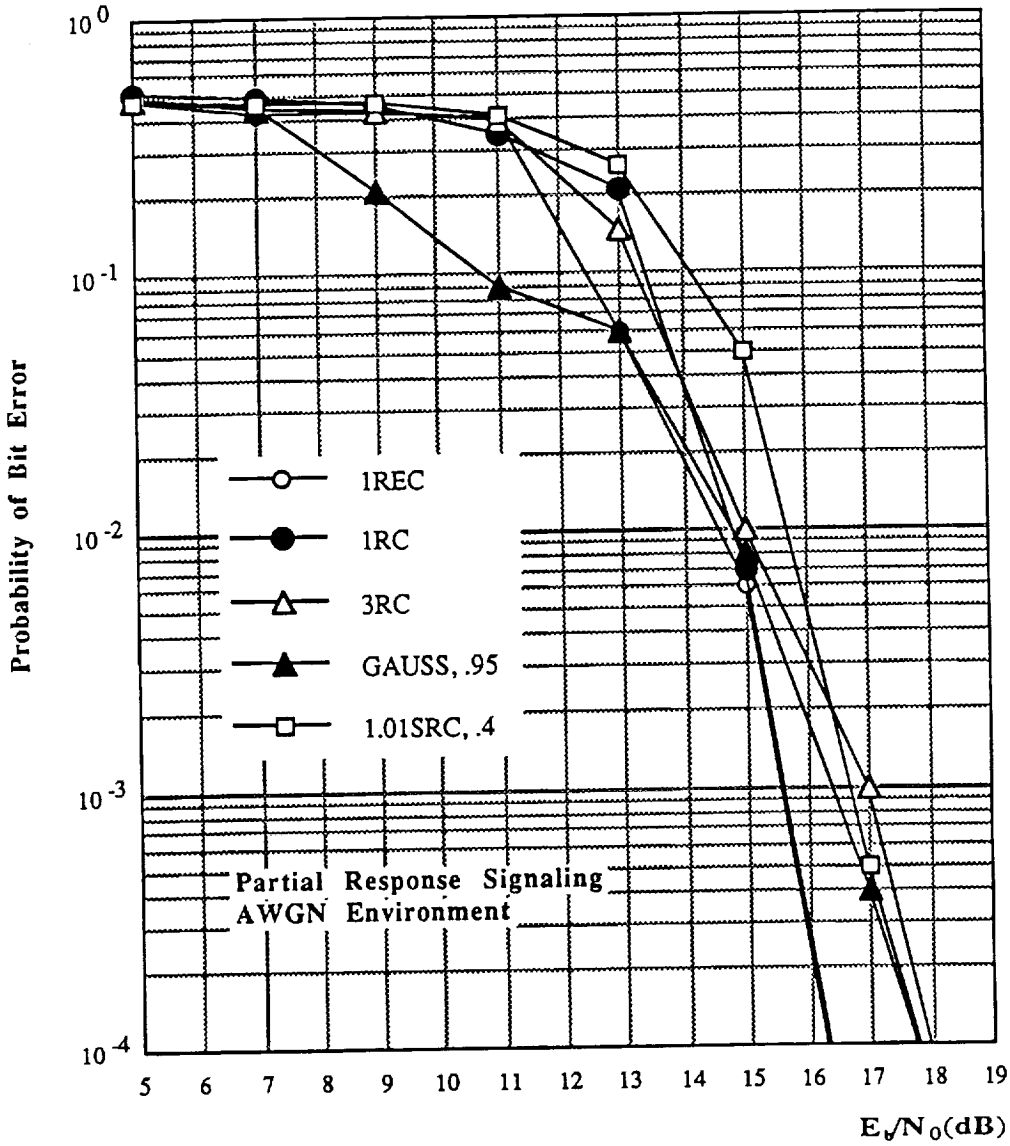

Performance of 16-state trellis coded 8-level CPM signal with GMSK2, BT=.4 pulse shape, h=0.125, and differential detection for various receiver filtering.

Figure 8.13

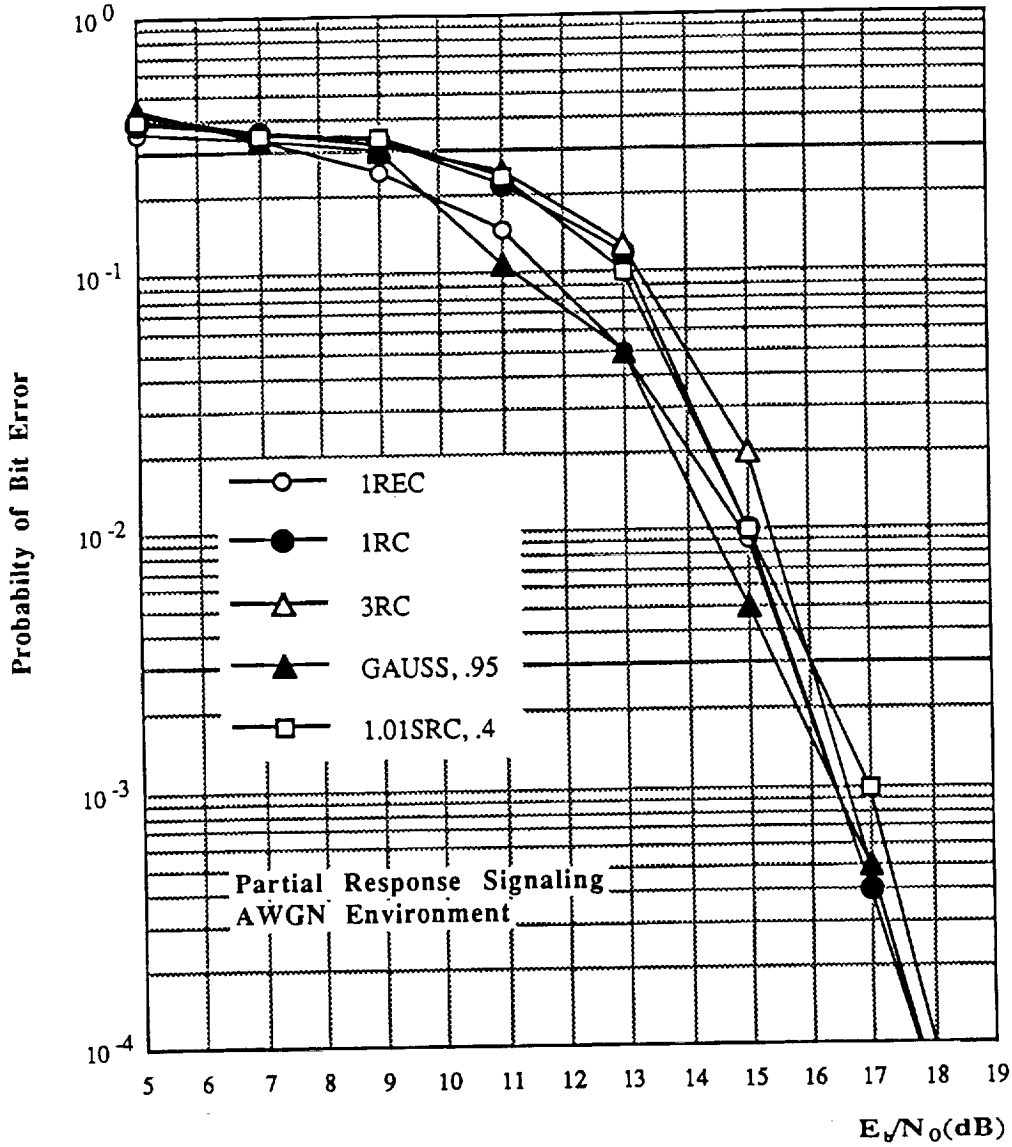

Performance of 4-state trellis coded 8-level CPM signal with HCS2 pulse shape, h=0.125, and differential detection for various receiver filtering.

Figure 8.14

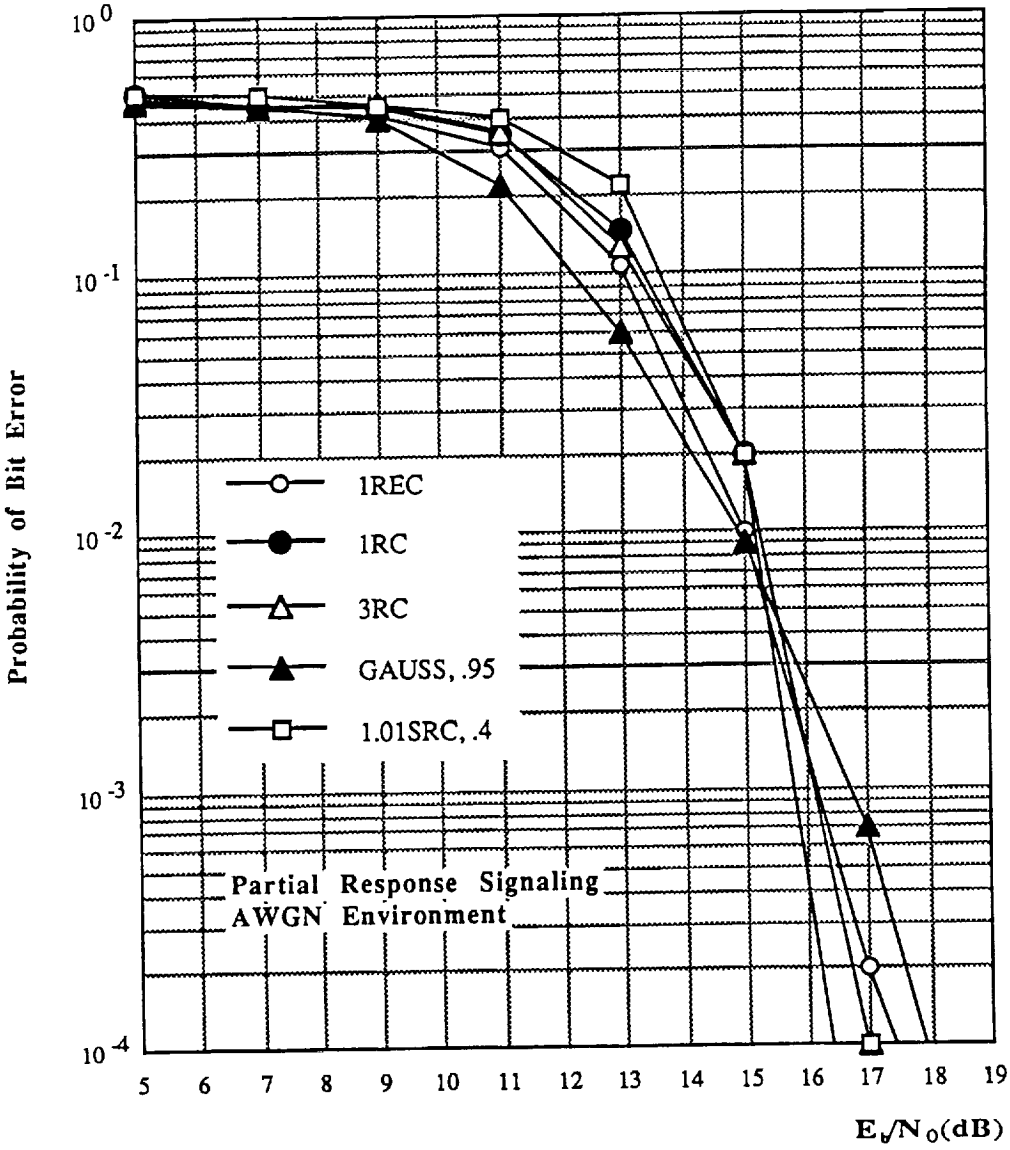

Performance of 8-state trellis coded 8-level CPM signal with HCS2 pulse shape, h=0.125, and differential detection for various receiver filtering.

Figure 8.15

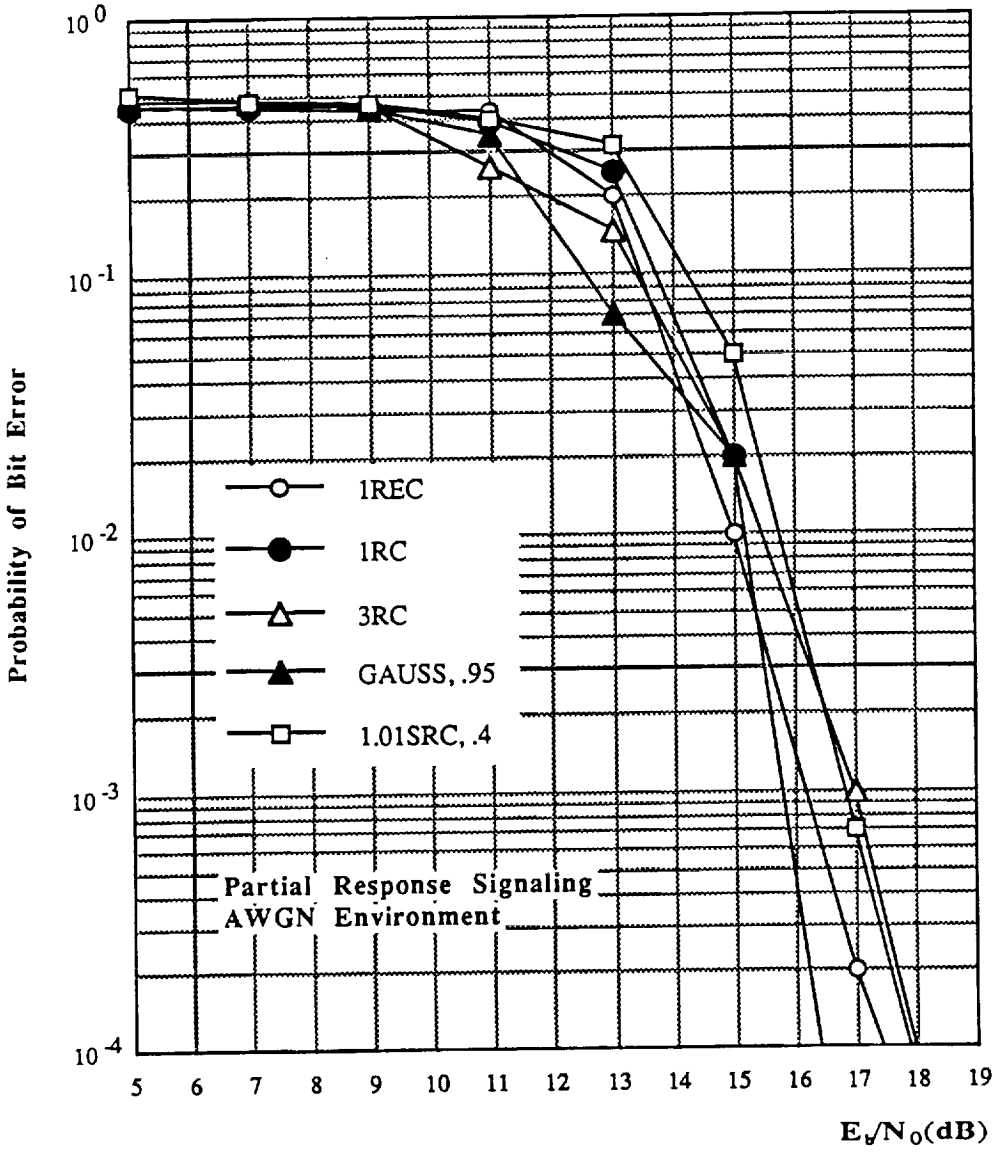

Performance of 16-state trellis coded 8-level CPM signal with HCS2 pulse shape, h=0.125, and differential detection for various receiver filtering.

Figure 8.16

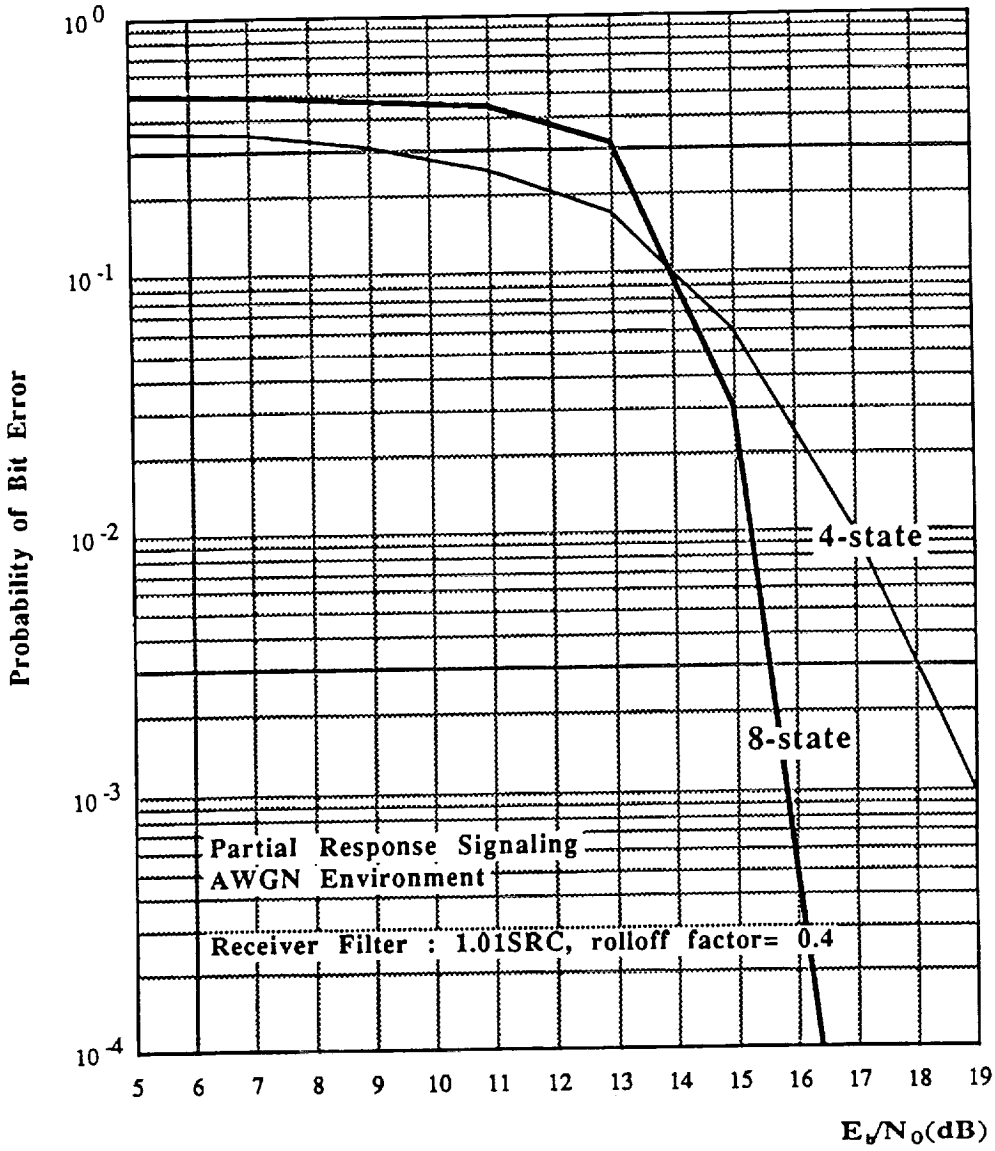

Performance of trellis coded 8-level CPM signal with 2RC pulse shape, h=0.125, and differential detection for 4 and 8-state codes.

Figure 8.17

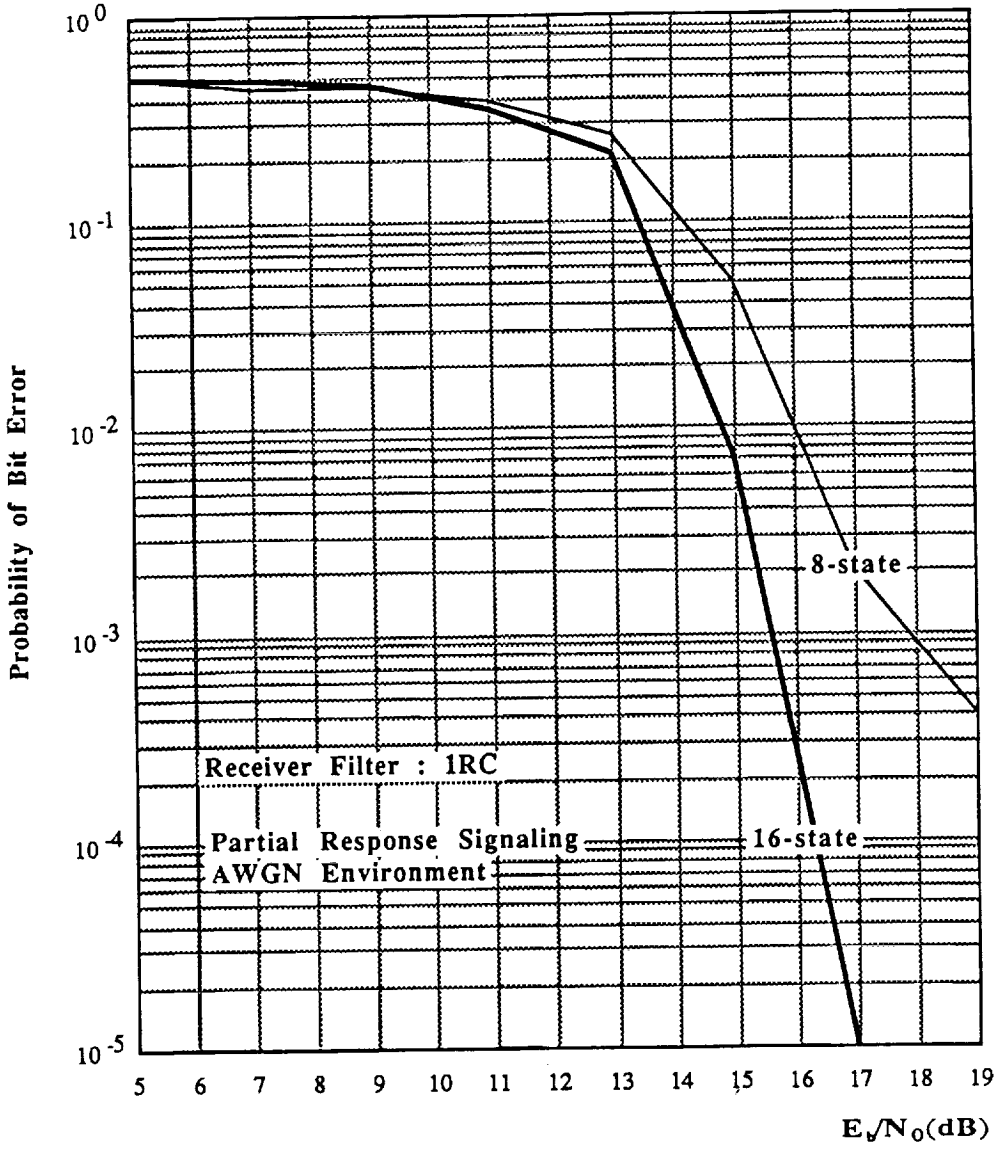

Performance of trellis coded 8-level CPM signal with GMSK2, BT=.4 pulse shape, h=0.125, and differential detection for 8 and 16-state codes.

Figure 8.18

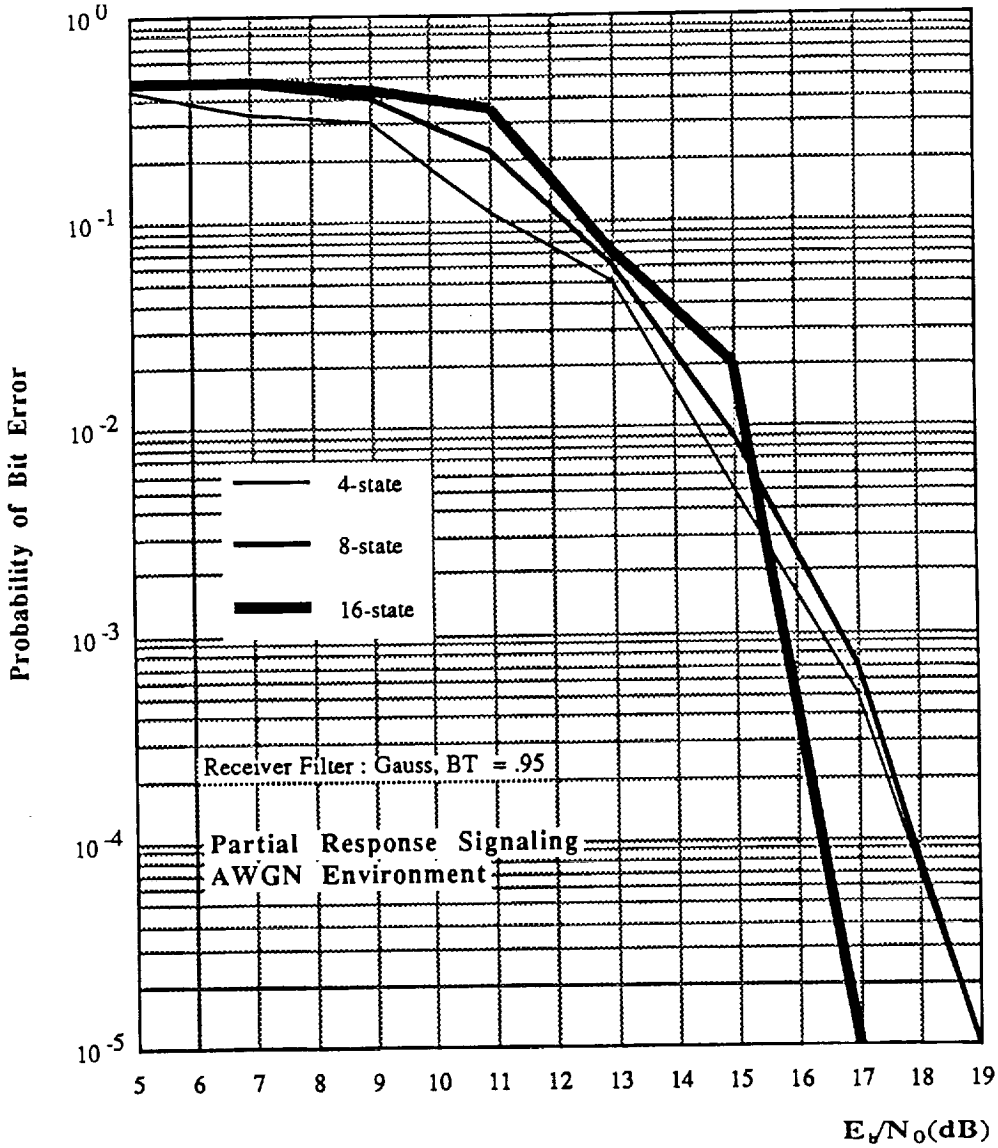

Performance of trellis coded 8-level CPM signal with HCS2 pulse shape, h=0.125, and differential detection for 4, 8, and 16-state codes.

Figure 8.19

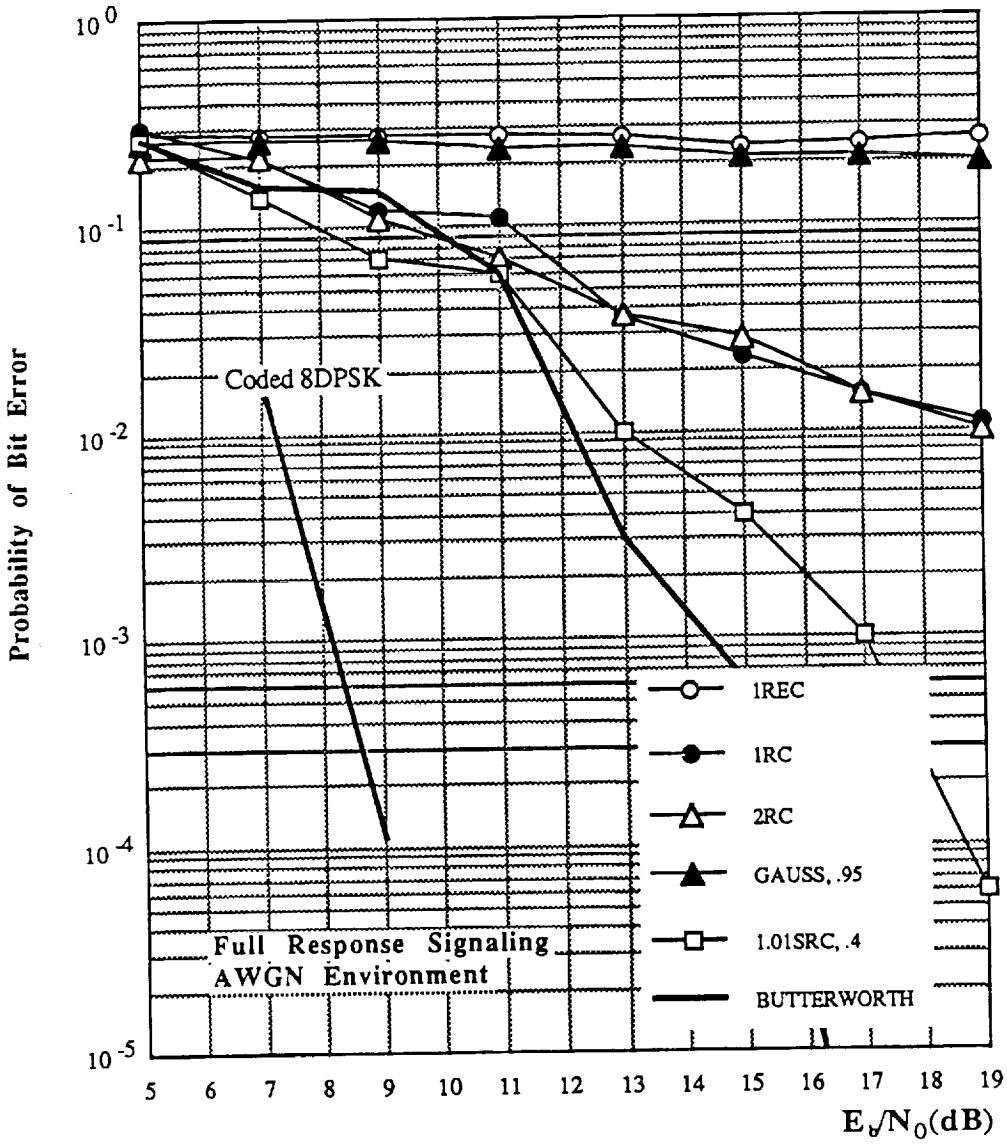

Performance of 4-state trellis coded 8-level CPM signal with 1REC pulse shape, h=0.125, and differential detection for various receiver filtering. Trellis coded 8-level DPSK is also shown for comparison.

Figure 8.20

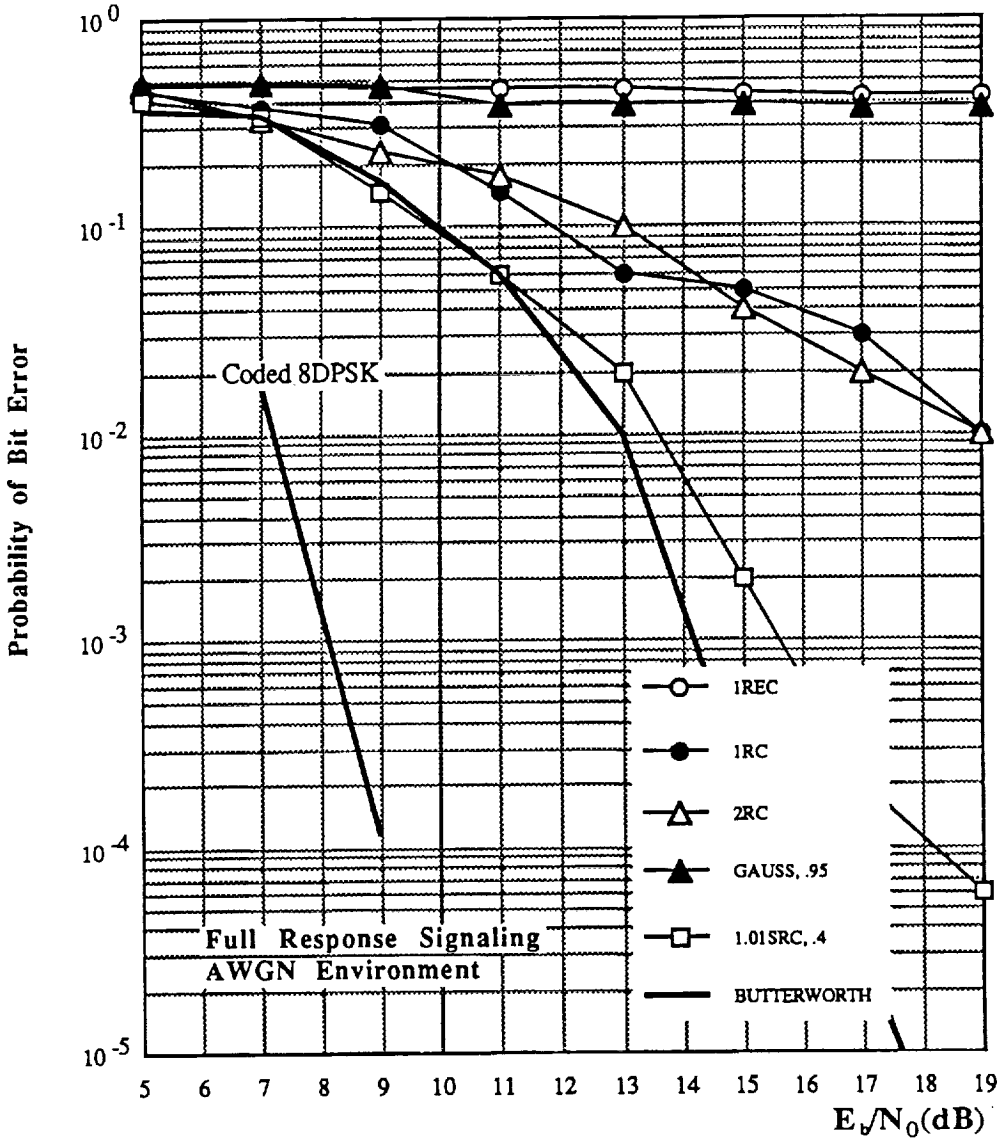

Performance of 8-state trellis coded 8-level CPM signal with 1REC pulse shape, h=0.125, and differential detection for various receiver filtering. Trellis coded 8-level DPSK is also shown for comparison.

Figure 8.21

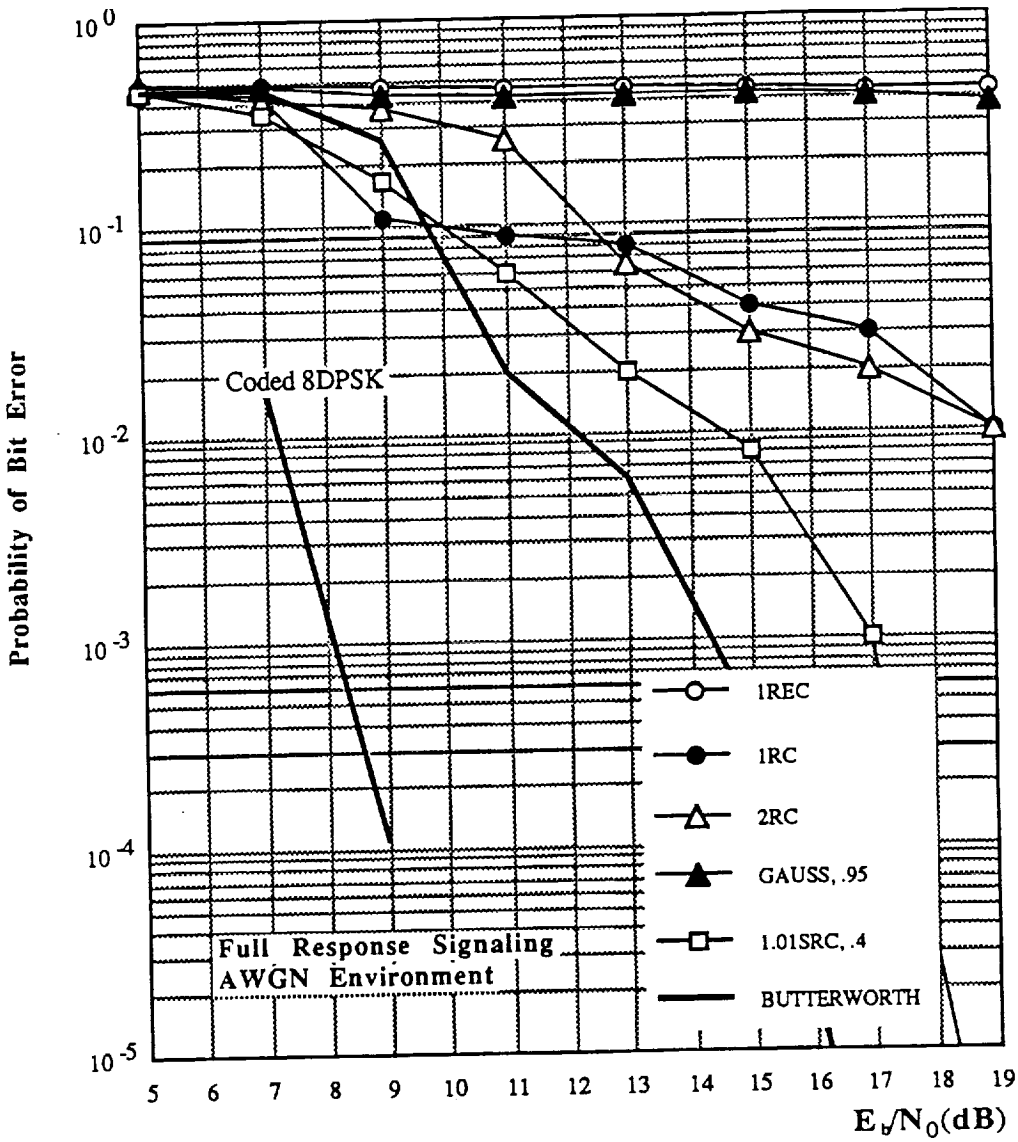

Performance of 16-state trellis coded 8-level CPM signal with 1REC pulse shape, h=0.125, and differential detection for various receiver filtering. Trellis coded 8-level DPSK is also shown for comparison.

Figure 8.22

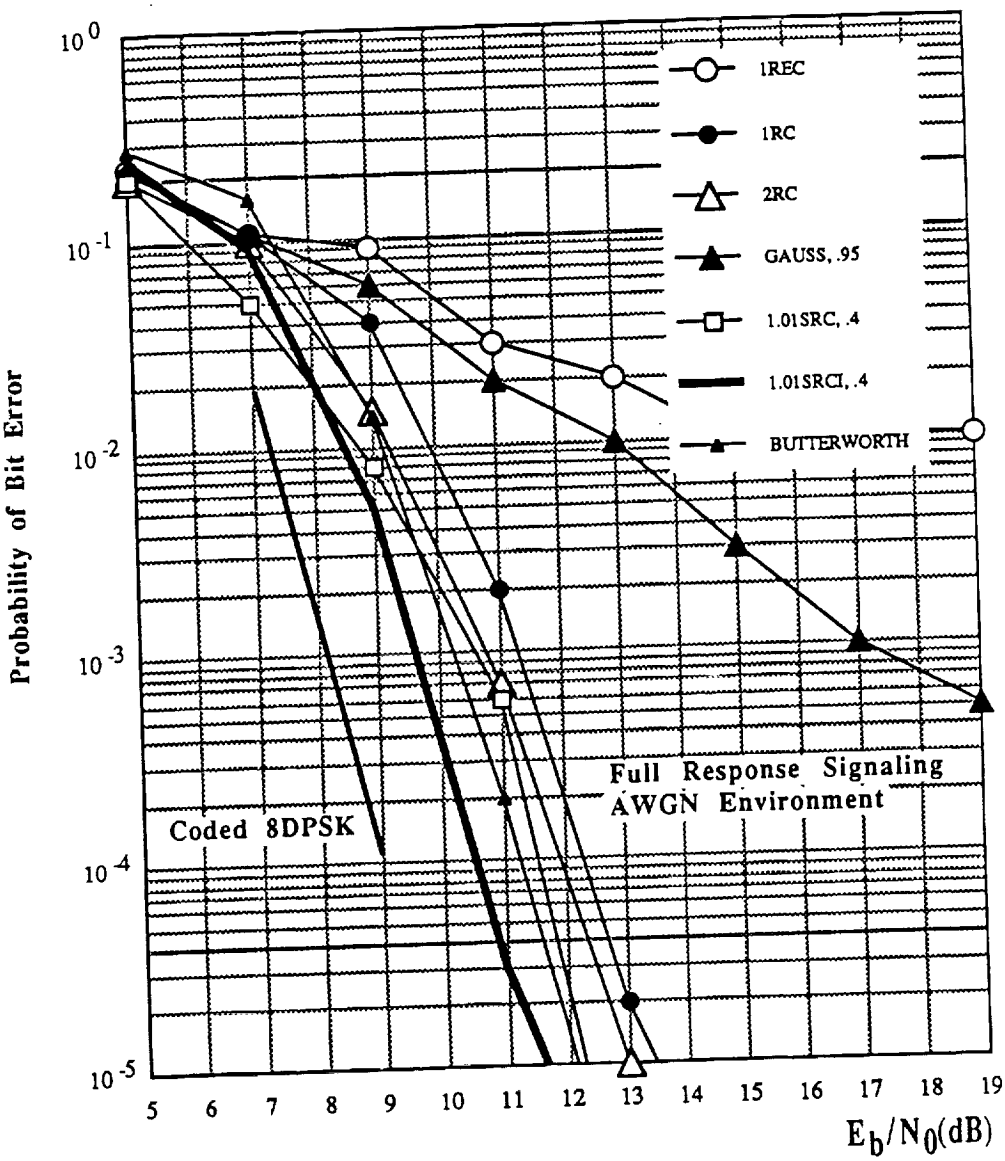

Performance of 4-state trellis coded 8-level CPM signal with 1RC pulse shape, h=0.125, and differential detection for various receiver filtering. Trellis coded 8-level DPSK is also shown for comparison.

Figure 8.23

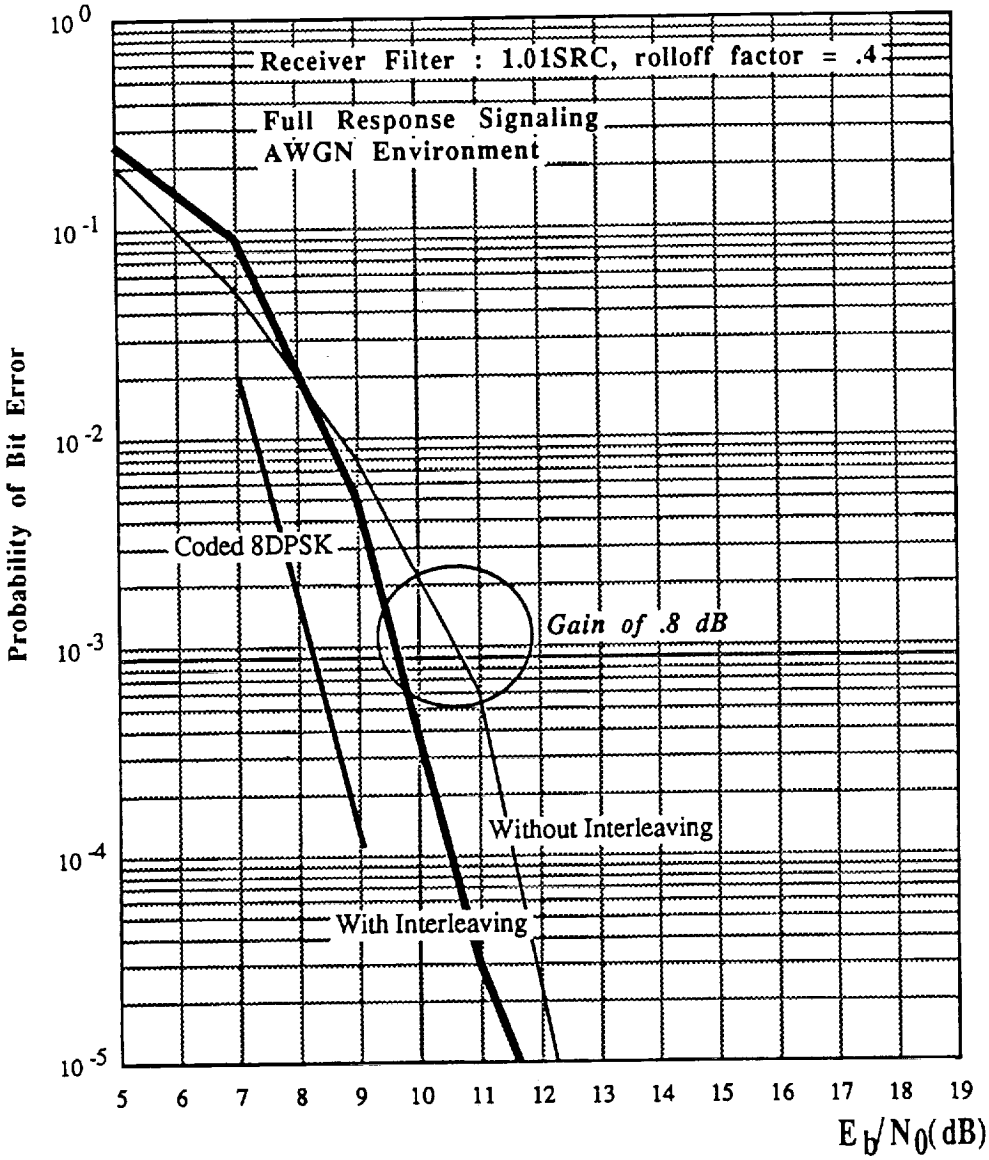

Performance of 4-state trellis coded 8-level CPM signal with 1RC pulse shape, h=0.125, and differential detection with and without interleaving. Trellis coded 8-level DPSK is also shown for comparison.

Figure 8.24

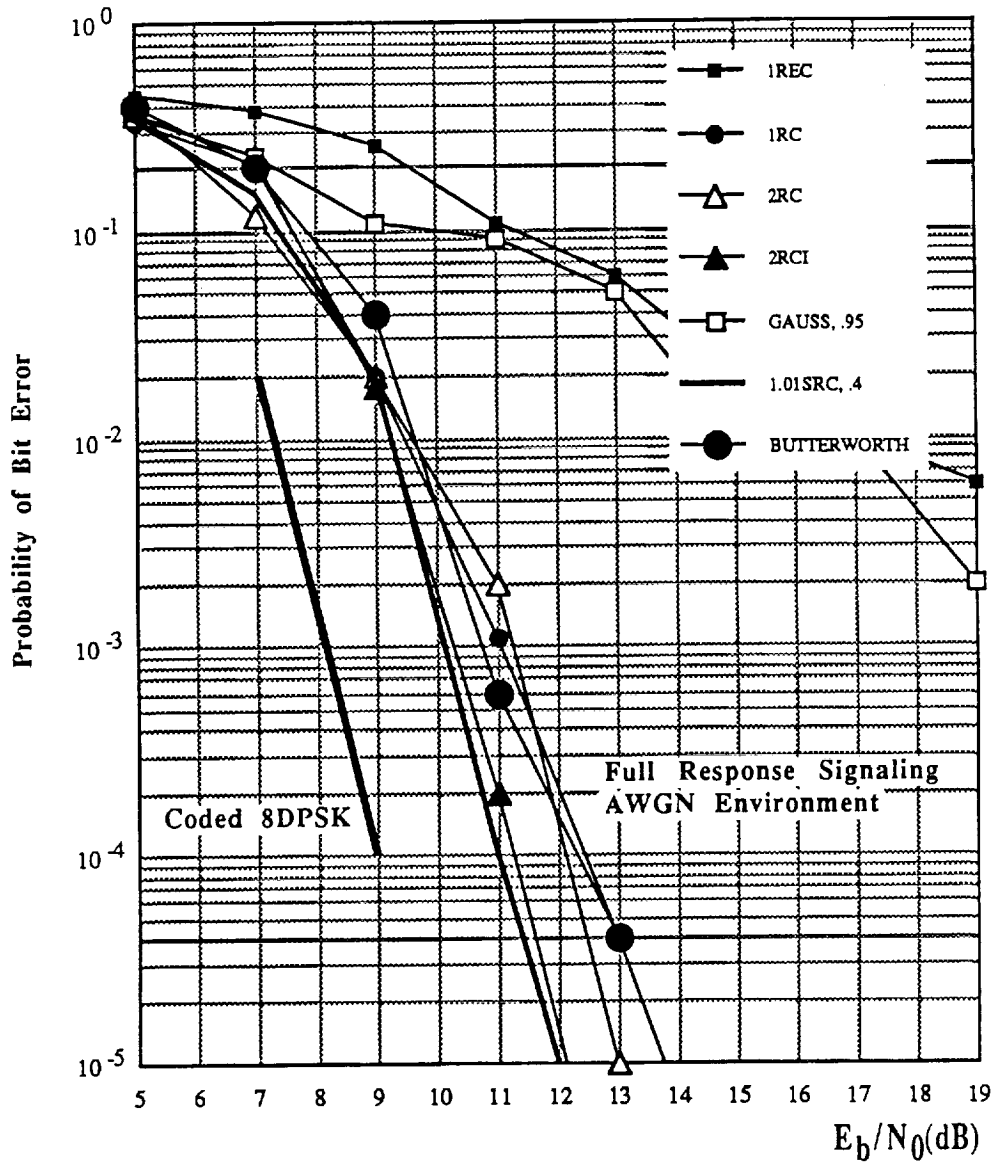

Performance of 8-state trellis coded 8-level CPM signal with 1RC pulse shape, h=0.125, and differential detection for various receiver filtering. Trellis coded 8-level DPSK is also shown for comparison.

Figure 8.25

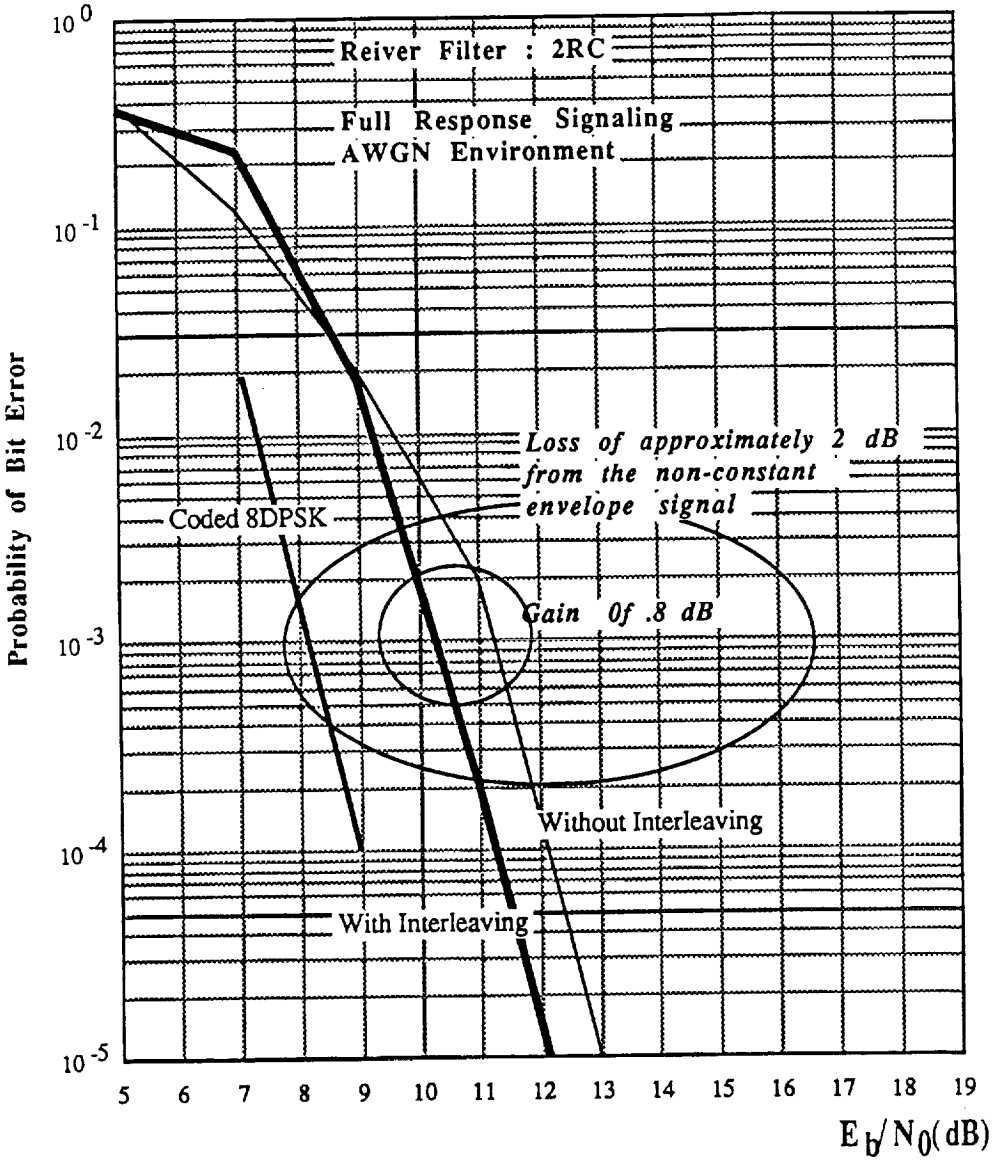

Performance of 8-state trellis coded 8-level CPM signal with 1RC pulse shape, h=0.125, and differential detection with and without interleaving. Trellis coded 8-level DPSK is also shown for comparison.

Figure 8.26

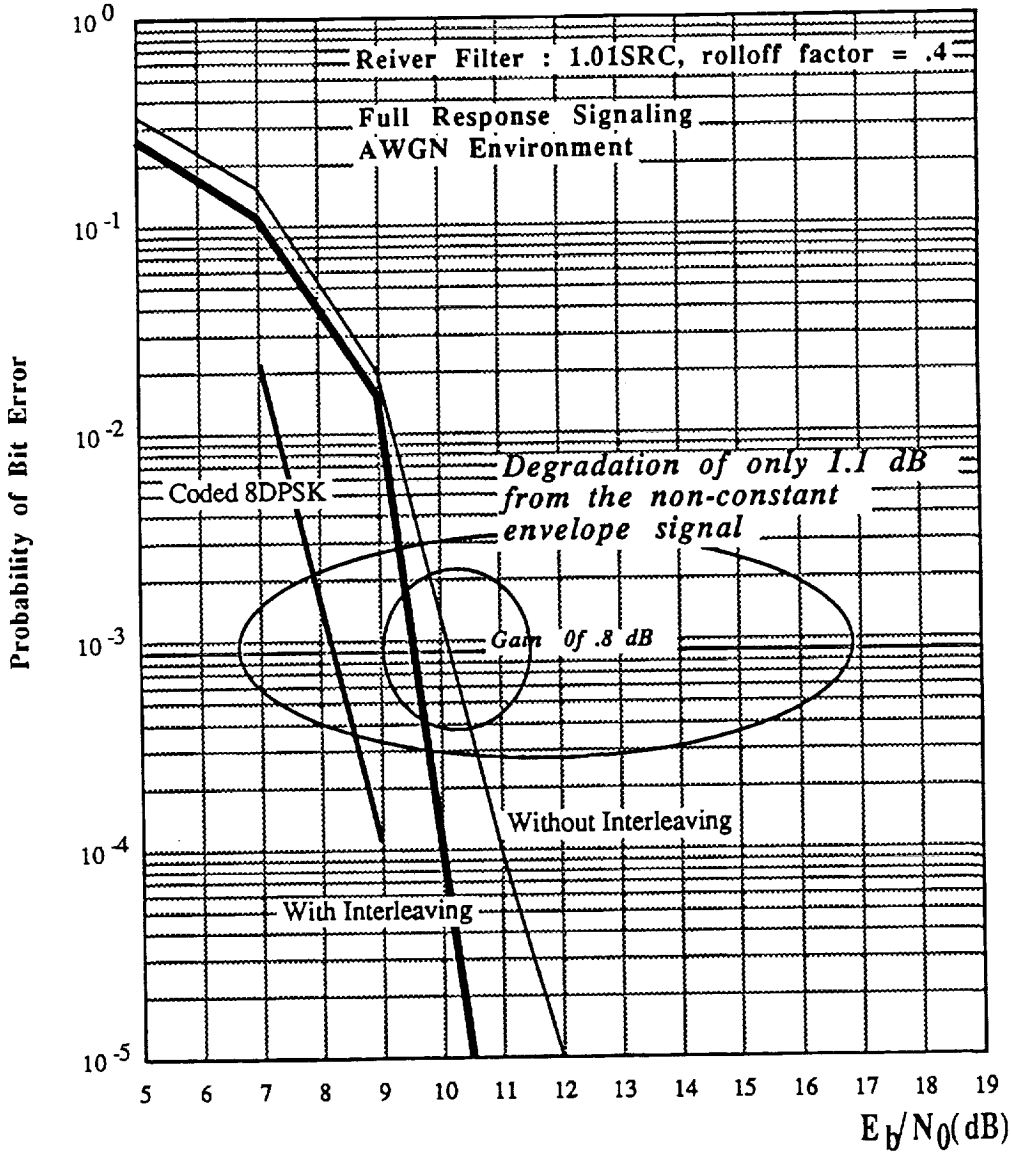

Performance of 8-state trellis coded 8-level CPM signal with 1RC pulse shape, h=0.125, and differential detection with and without interleaving. Trellis coded 8-level DPSK is also shown for comparison.

Figure 8.27

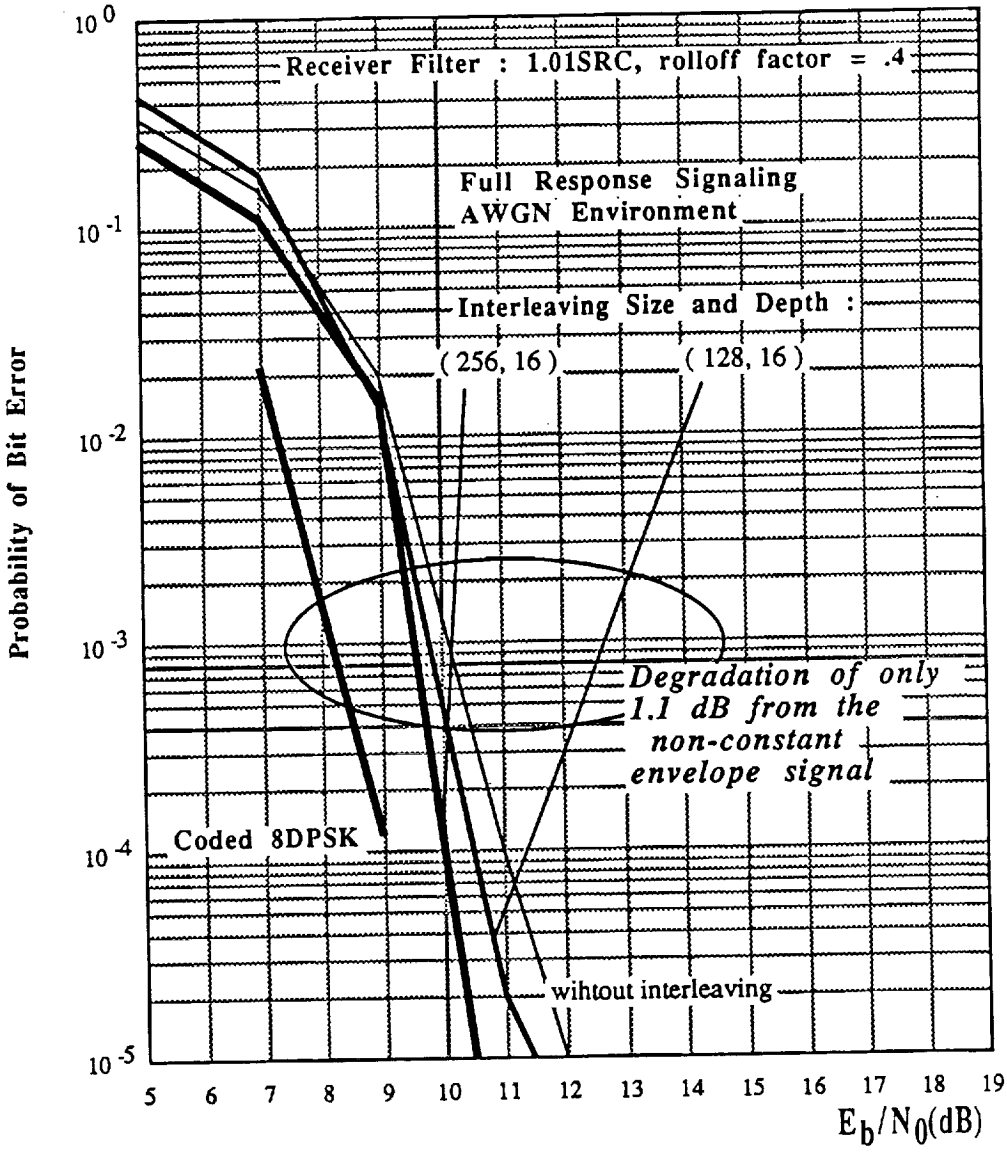

Performance of 8-state trellis coded 8-level CPM signal with 1RC pulse shape, h=0.125, and differential detection with and without interleaving. Trellis coded 8-level DPSK is also shown for comparison.

Figure 8.28

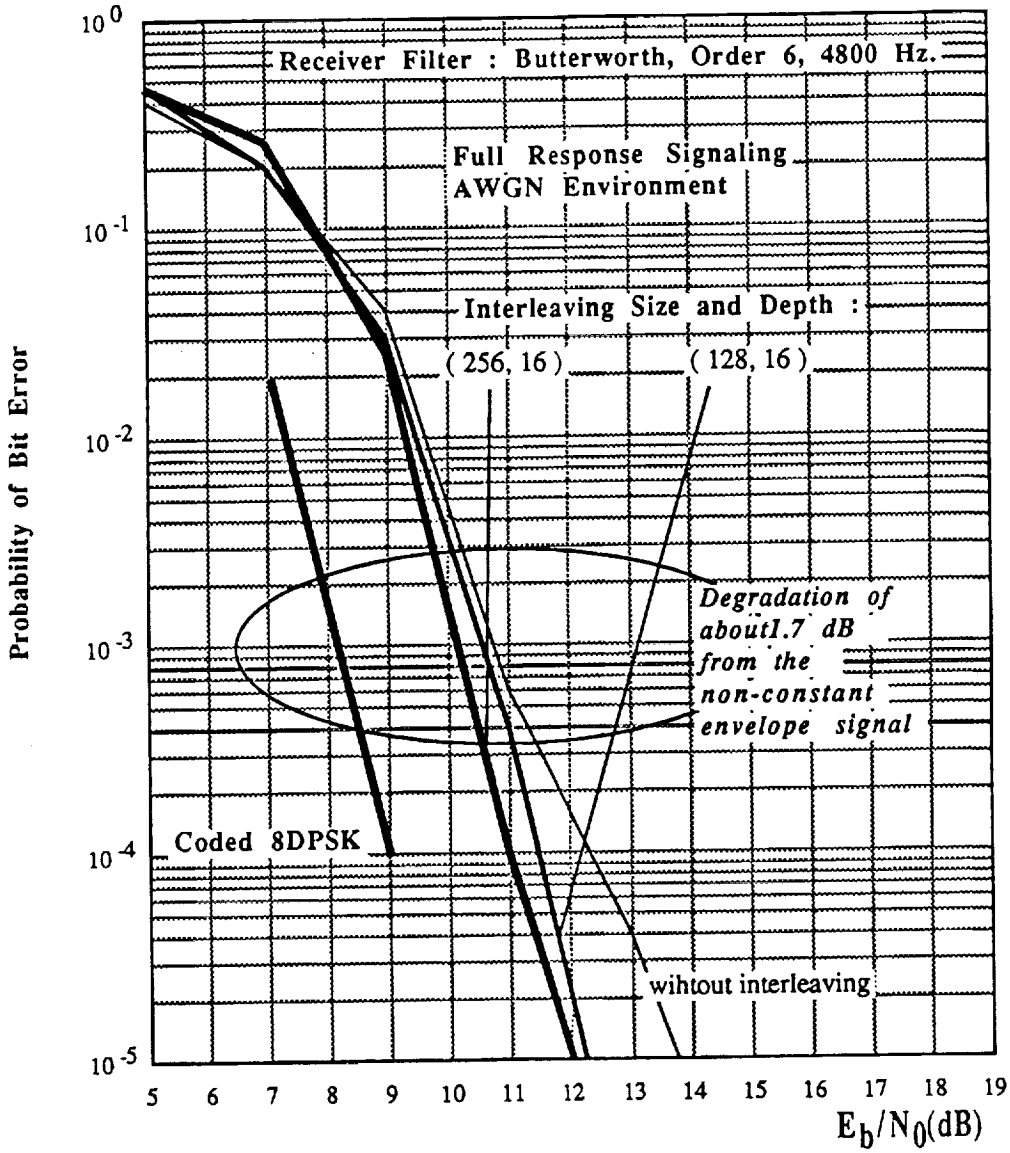

Performance of 8-state trellis coded 8-level CPM signal with 1RC pulse shape, h=0.125, and differential detection with and without interleaving. Trellis coded 8-level DPSK is also shown for comparison.

Figure 8.29

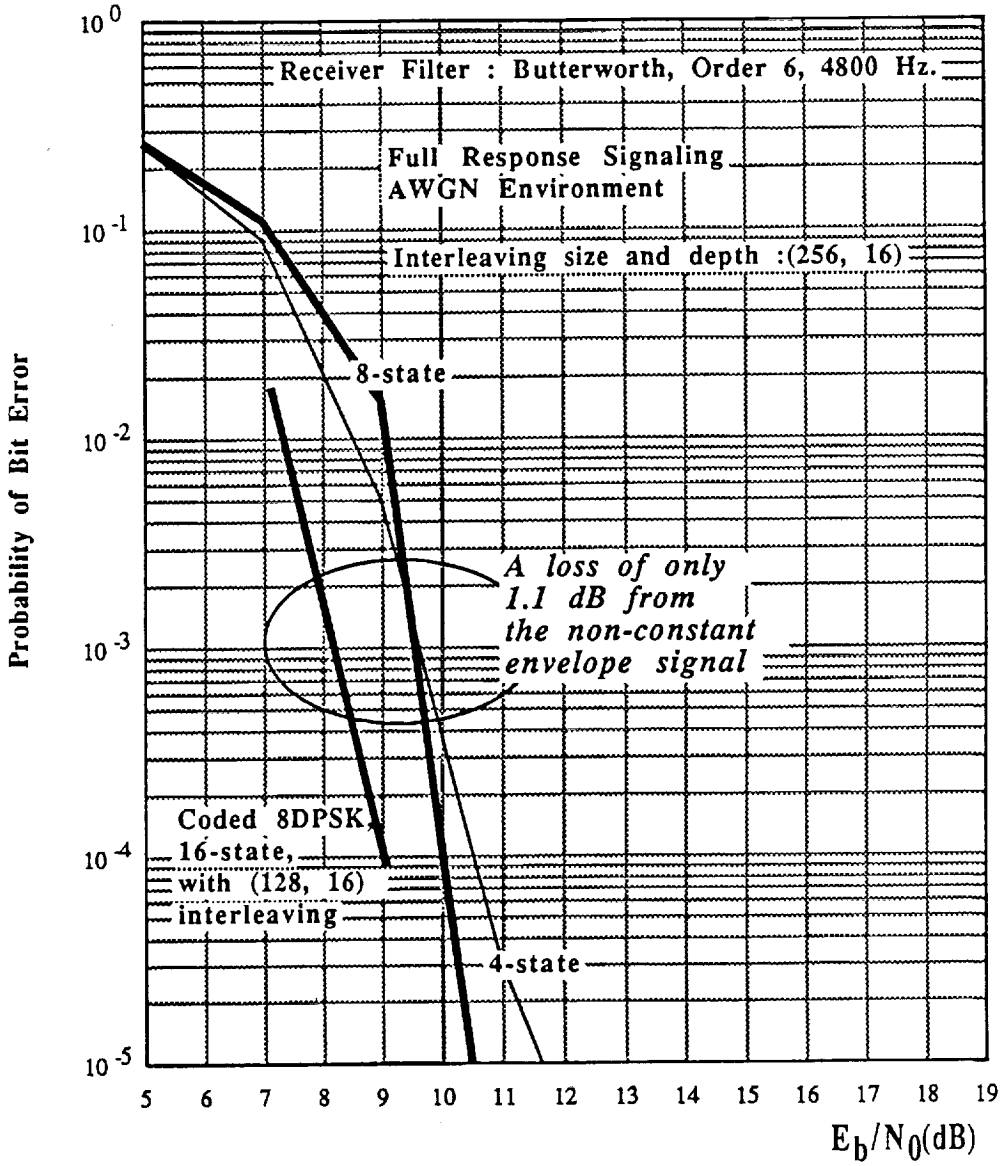

Performance of 8-state trellis coded 8-level CPM signal with 1RC pulse shape, h=0.125, and differential detection for 4 and 8-state codes.Trellis coded 8-level DPSK is also shown for comparison.

Figure 8.30

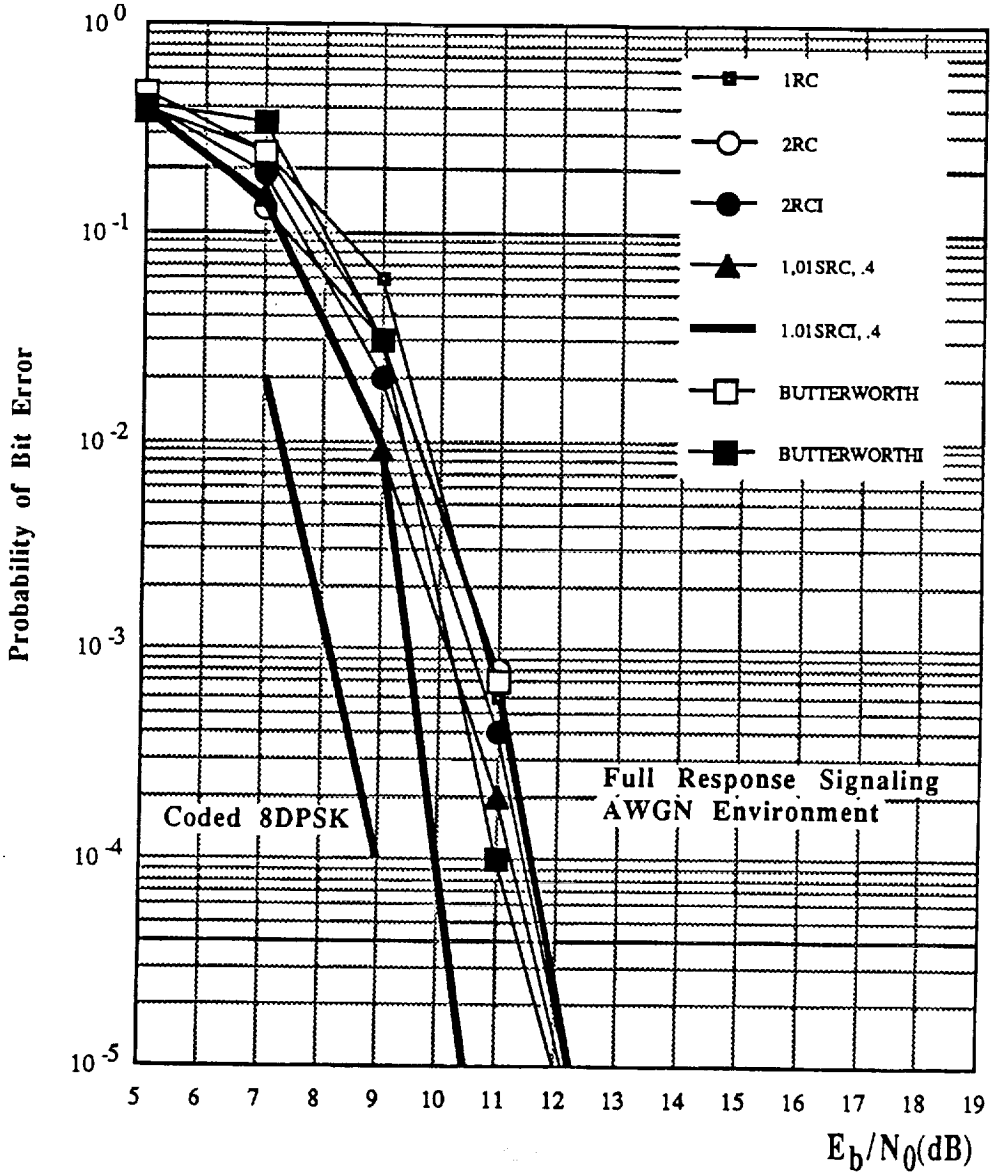

Performance of 16-state trellis coded 8-level CPM signal with 1RC pulse shape, h=0.125, and differential detection for various receiver filtering. Trellis coded 8-level DPSK is also shown for comparison.

Figure 8.31

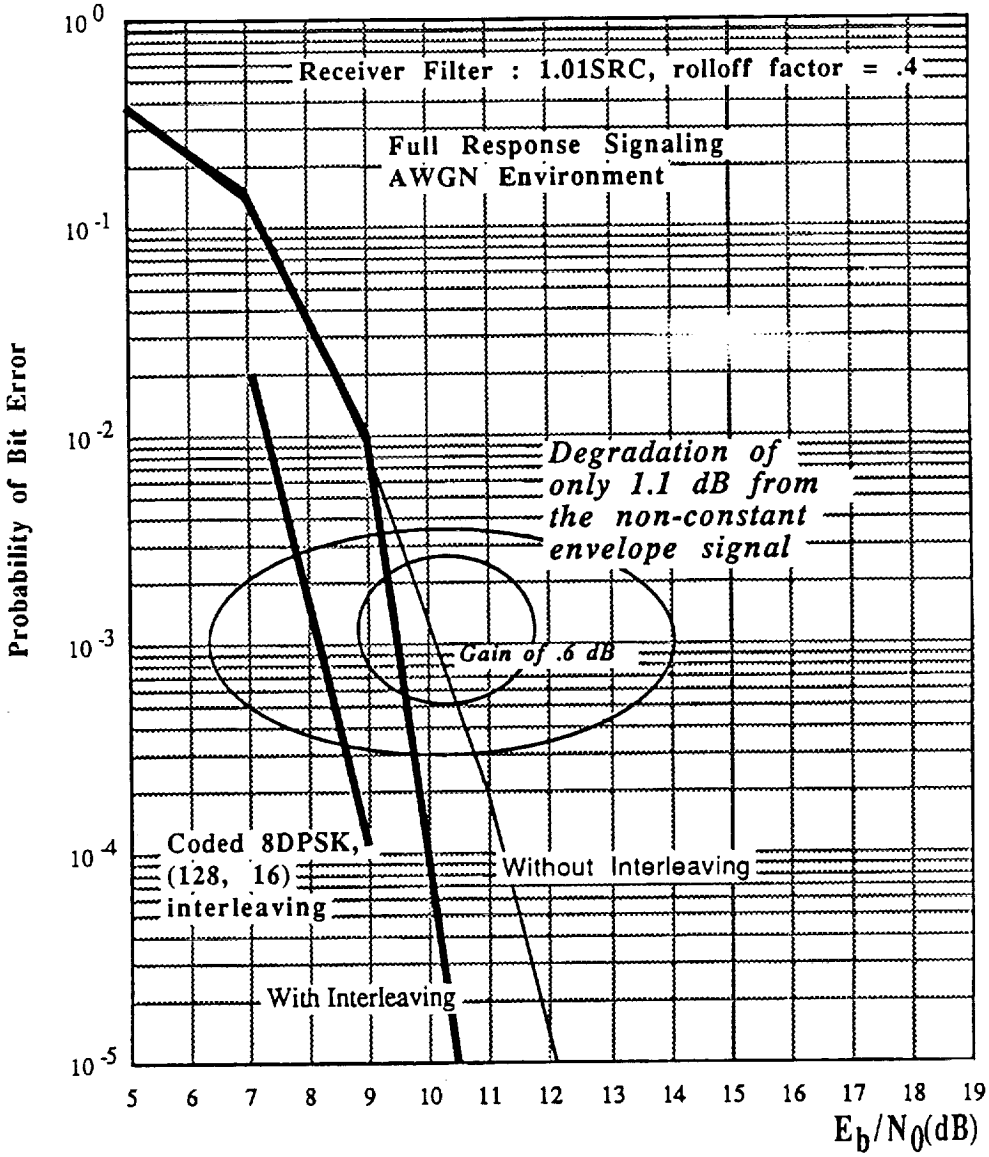

Performance of 16-state trellis coded 8-level CPM signal with 1RC pulse shape, h=0.125, and differential detection with and without interleaving. Trellis coded 8-level DPSK is also shown for comparison.

Figure 8.32

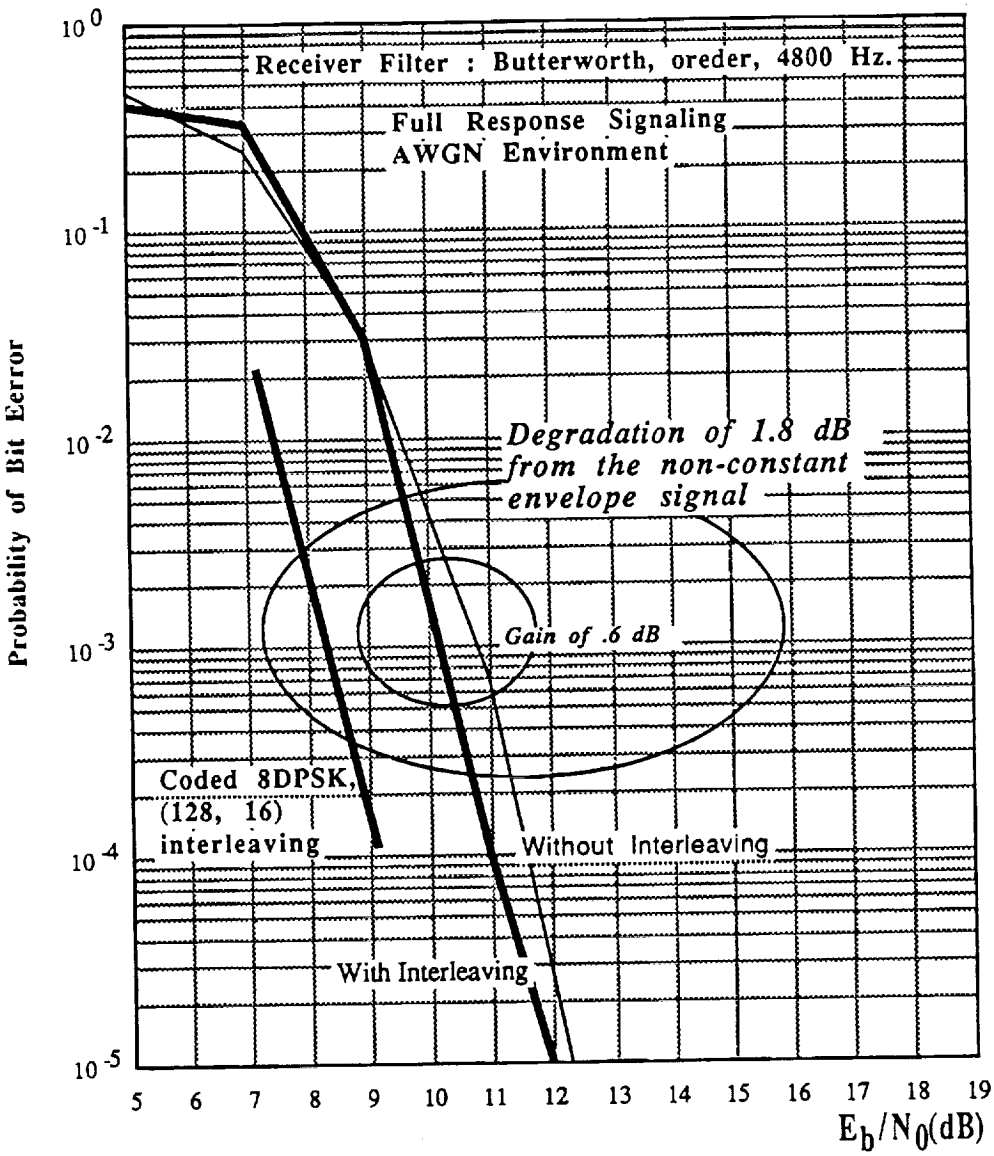

Performance of 16-state trellis coded 8-level CPM signal with 1RC pulse shape, h=0.125, and differential detection with and without interleaving. Trellis coded 8-level DPSK is also shown for comparison.

Figure 8.33

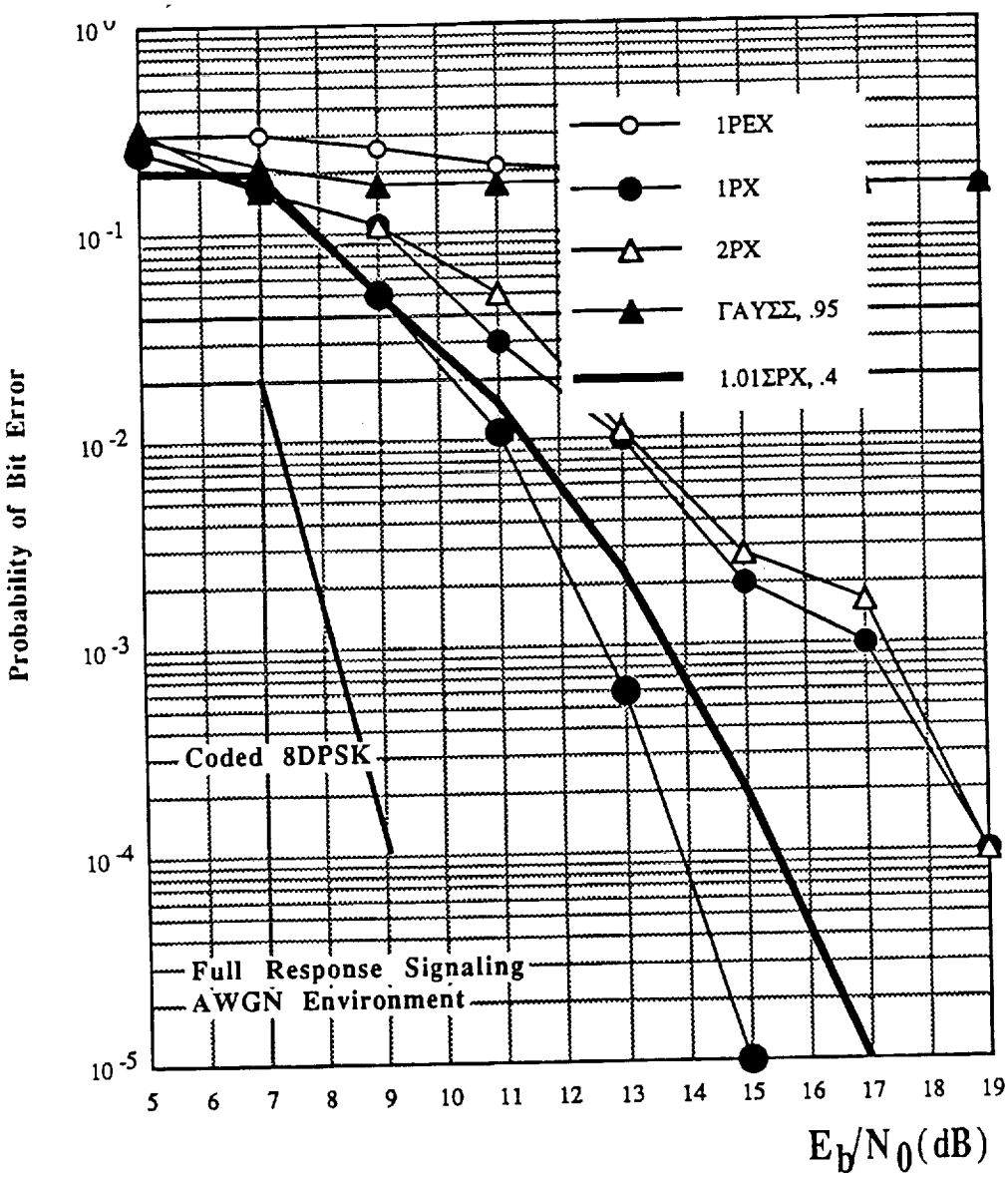

Performance of 4-state trellis coded 8-level CPM signal with GMSK1, BT=.7 pulse shape, h=0.125, and differential detection for various receiver filtering. Trellis coded 8-level DPSK is also shown for comparison.

Figure 8.34

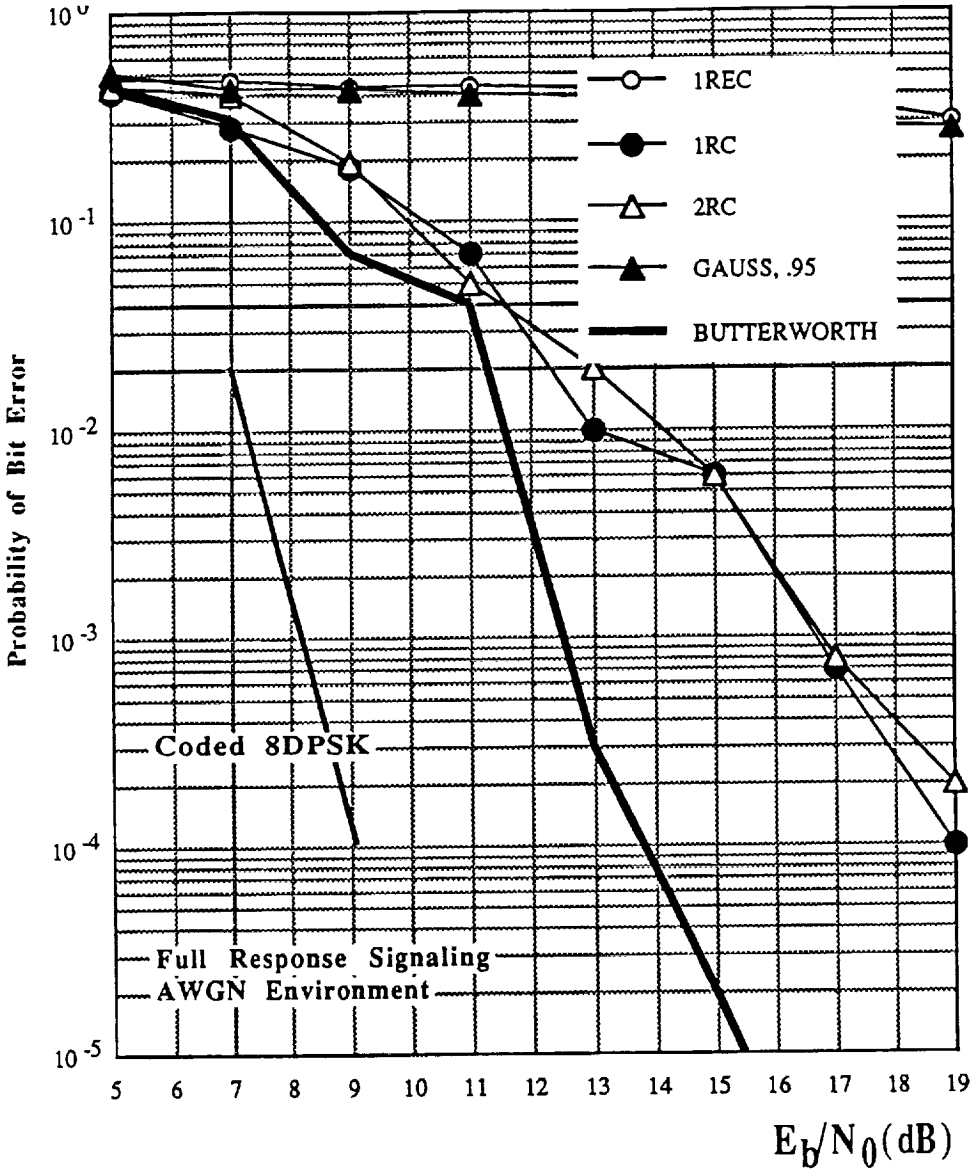

Performance of 8-state trellis coded 8-level CPM signal with GMSK1, BT=.7 pulse shape, h=0.125, and differential detection for various receiver filtering. Trellis coded 8-level DPSK is also shown for comparison.

Figure 8.35

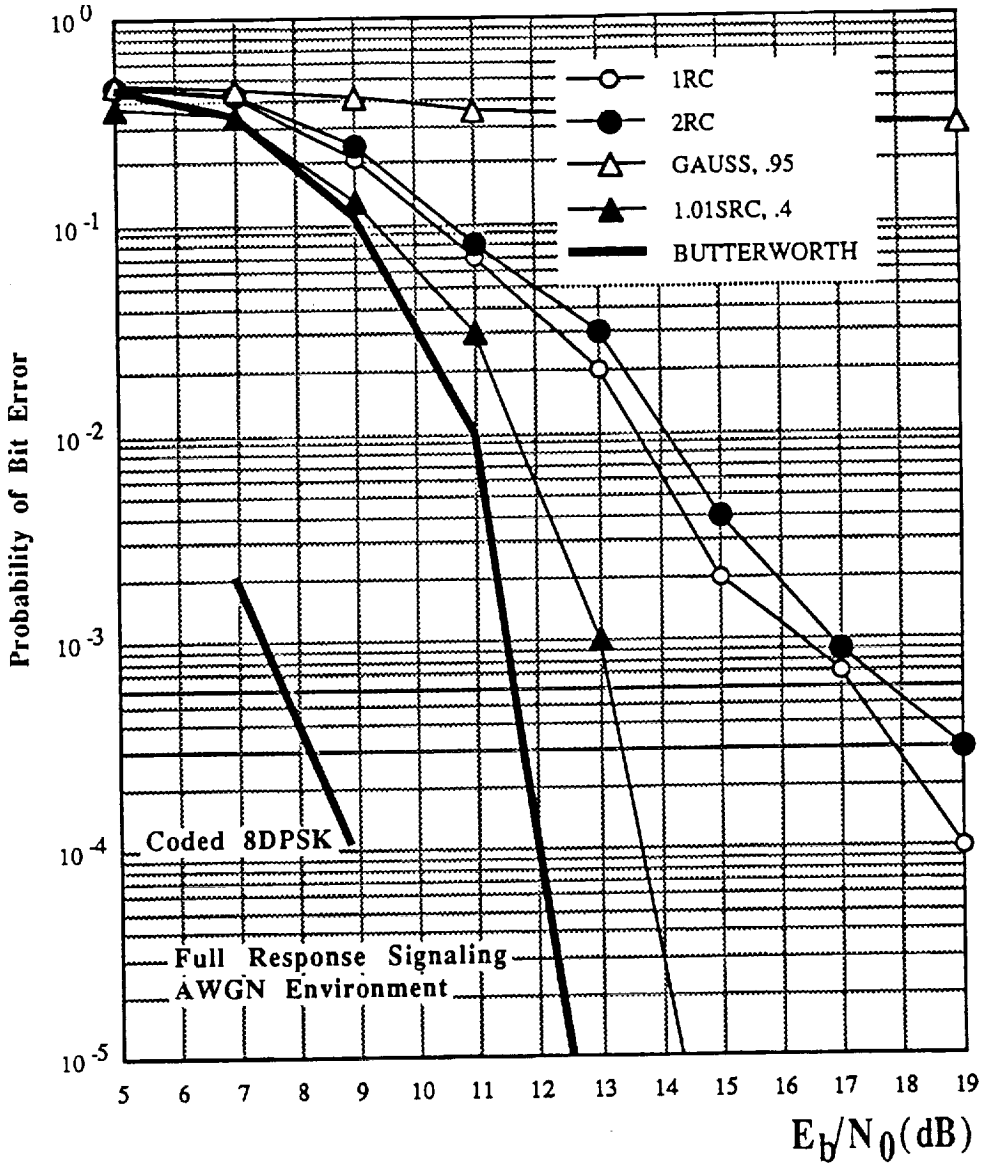

Performance of 16-state trellis coded 8-level CPM signal with GMSK1, BT=.7 pulse shape, h=0.125, and differential detection for various receiver filtering. Trellis coded 8-level DPSK is also shown for comparison.

Figure 8.36

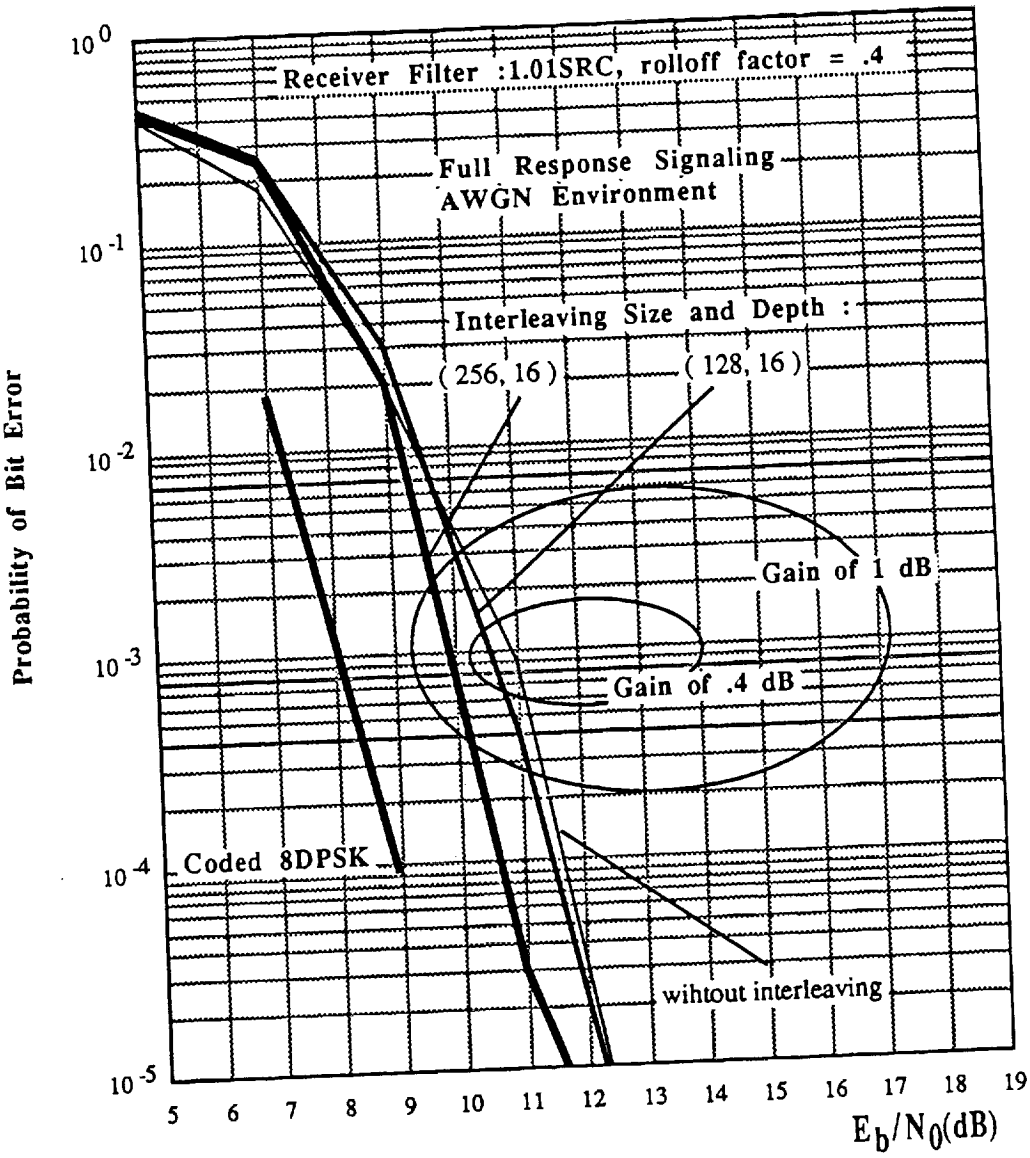

Performance of 8-state trellis coded 8-level CPM signal with HCS1 pulse shape, h=0.125, and differential detection with and without interleaving. Trellis coded 8-level DPSK is also shown for comparison.

Figure 8.37

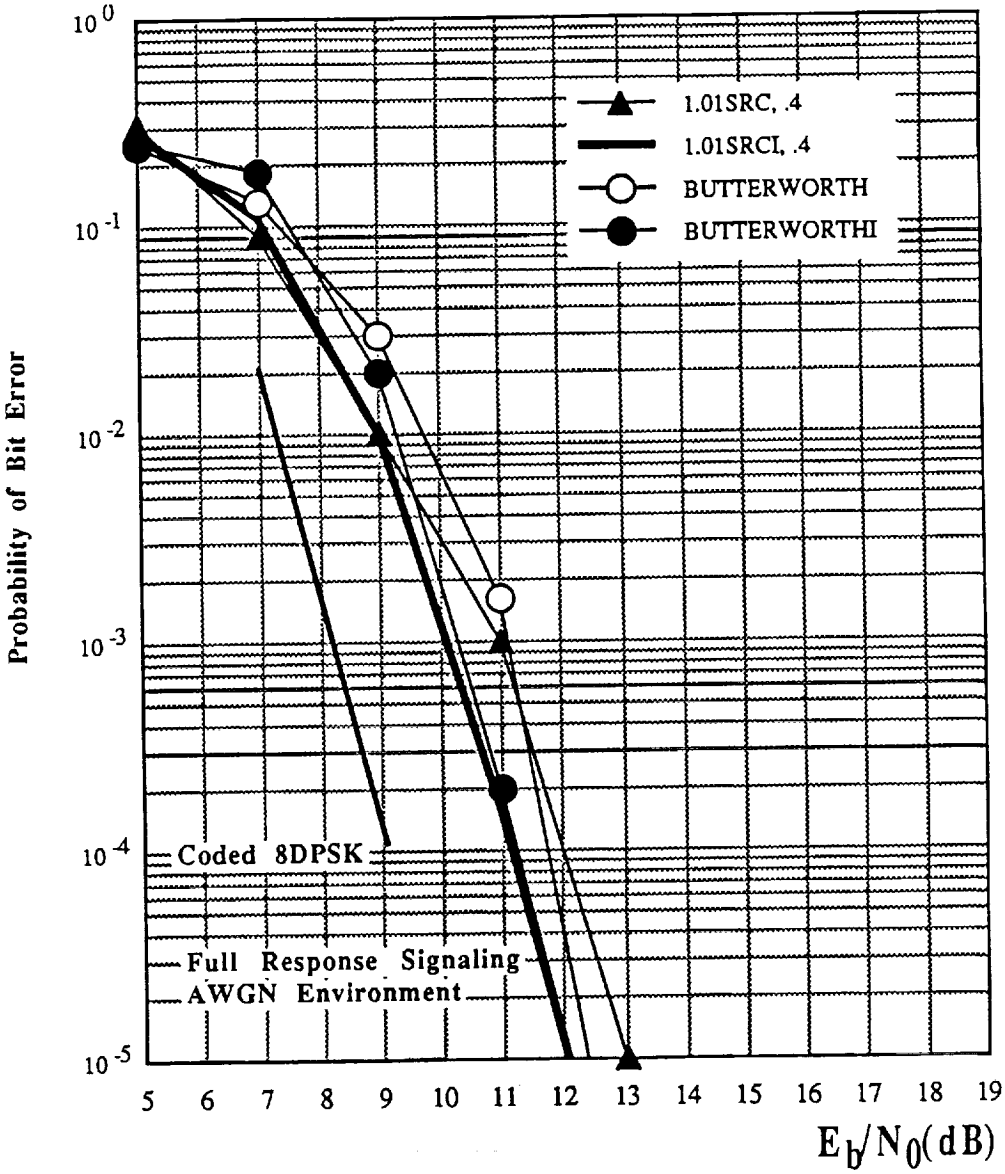

Performance of 4-state trellis coded 8-level CPM signal with HCS1 pulse shape, h=0.125, and differential detection for various receiver filtering. Trellis coded 8-level DPSK is also shown for comparison.

Figure 8.38

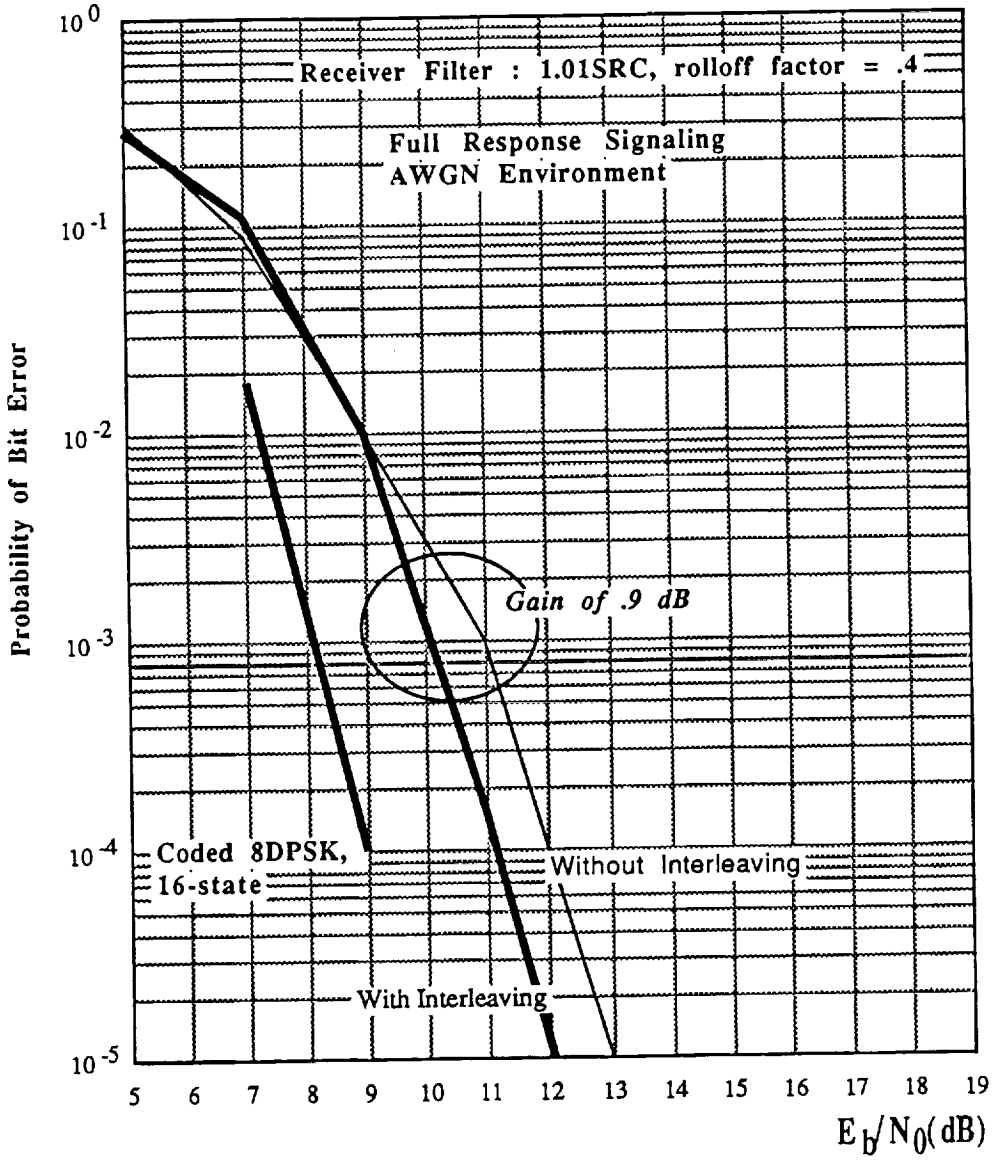

Performance of 4-state trellis coded 8-level CPM signal with HCS1 pulse shape, h=0.125, and differential detection with and without interleaving. Trellis coded 8-level DPSK is also shown for comparison.

Figure 8.39

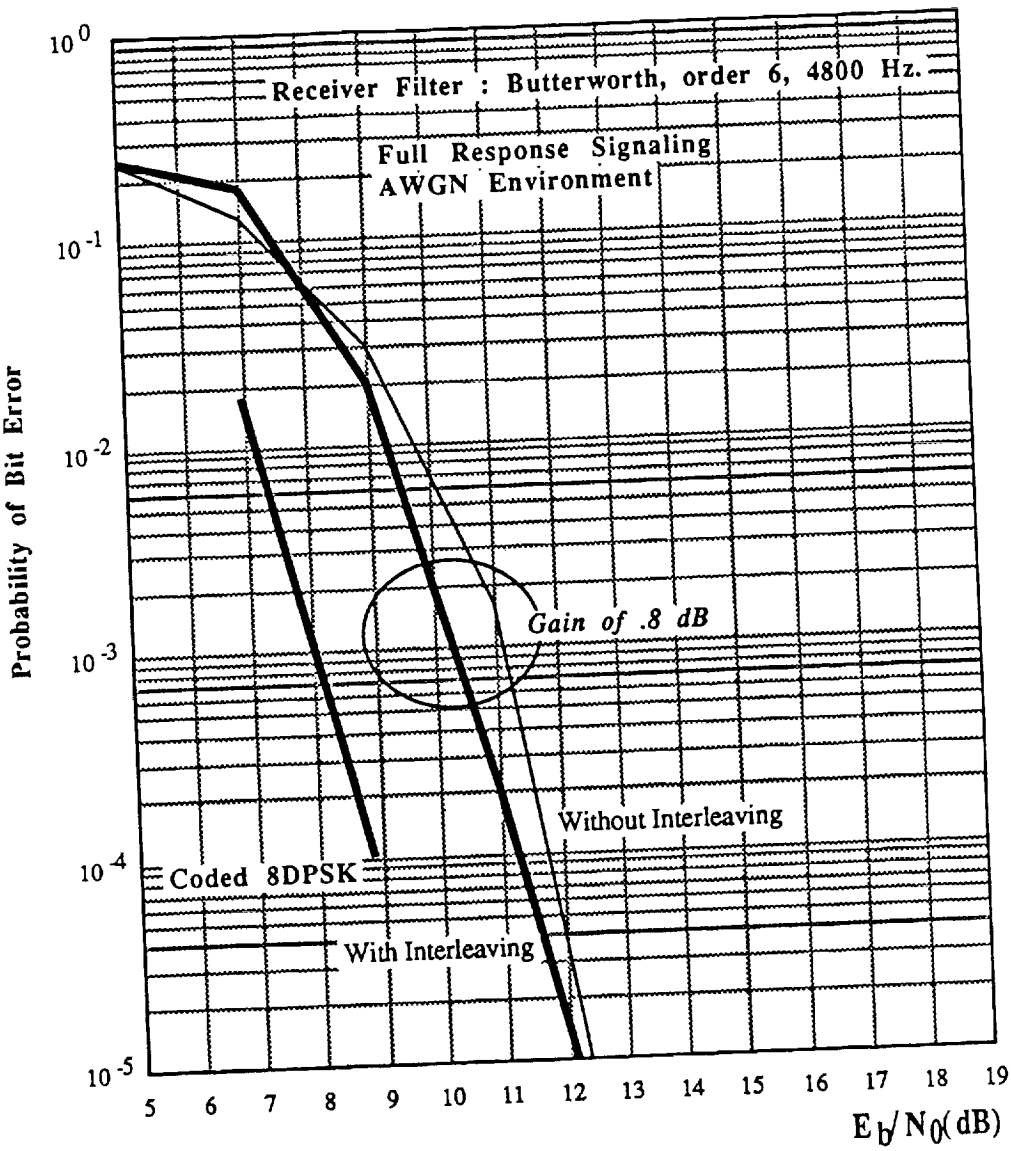

Performance of 4-state trellis coded 8-level CPM signal with HCS1 pulse shape, h=0.125, and differential detection with and without interleaving. Trellis coded 8-level DPSK is also shown for comparison.

Figure 8.40

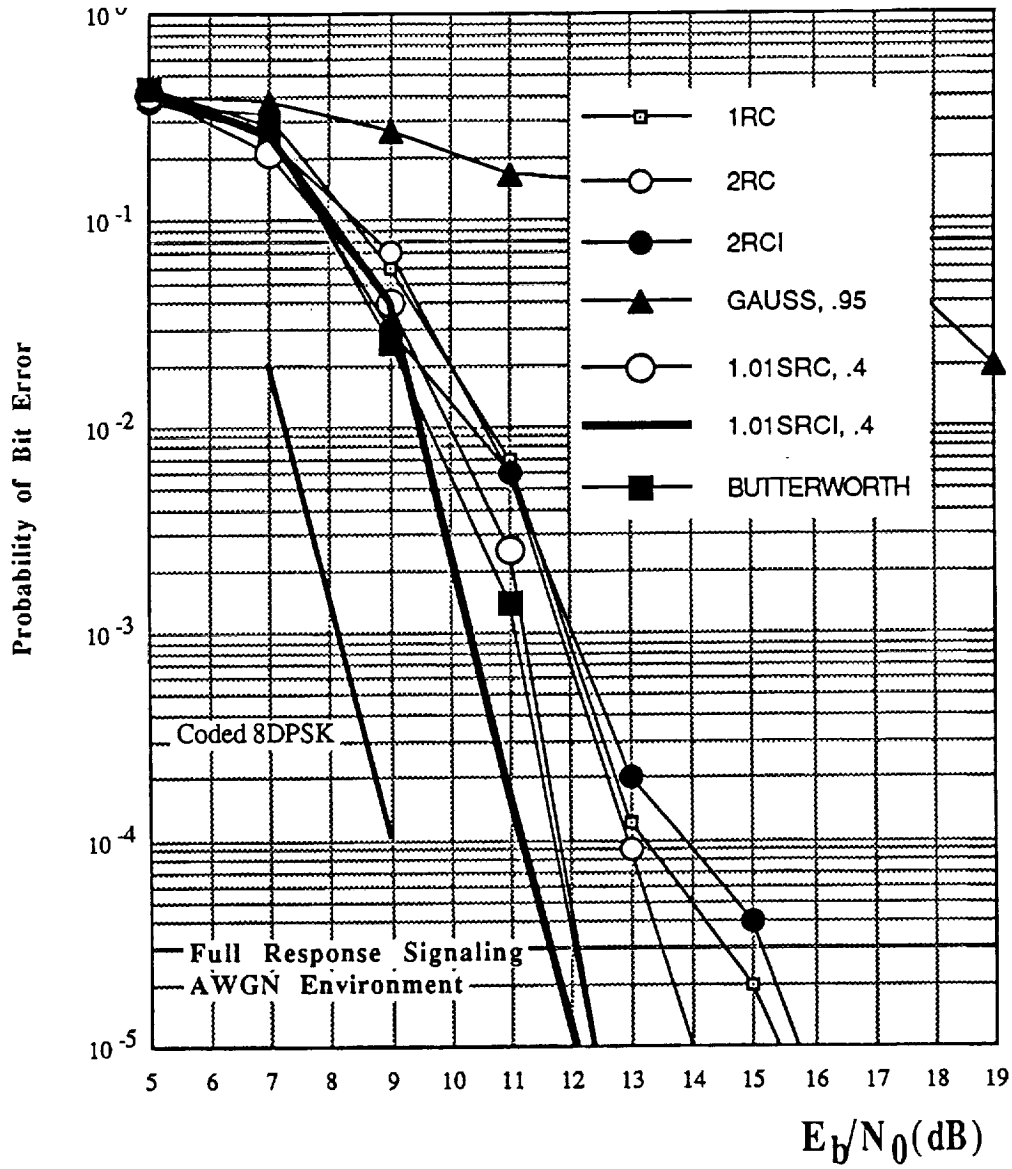

Performance of 8-state trellis coded 8-level CPM signal with HCS1 pulse shape, h=0.125, and differential detection for various receiver filtering. Trellis coded 8-level DPSK is also shown for comparison.

Figure 8.41

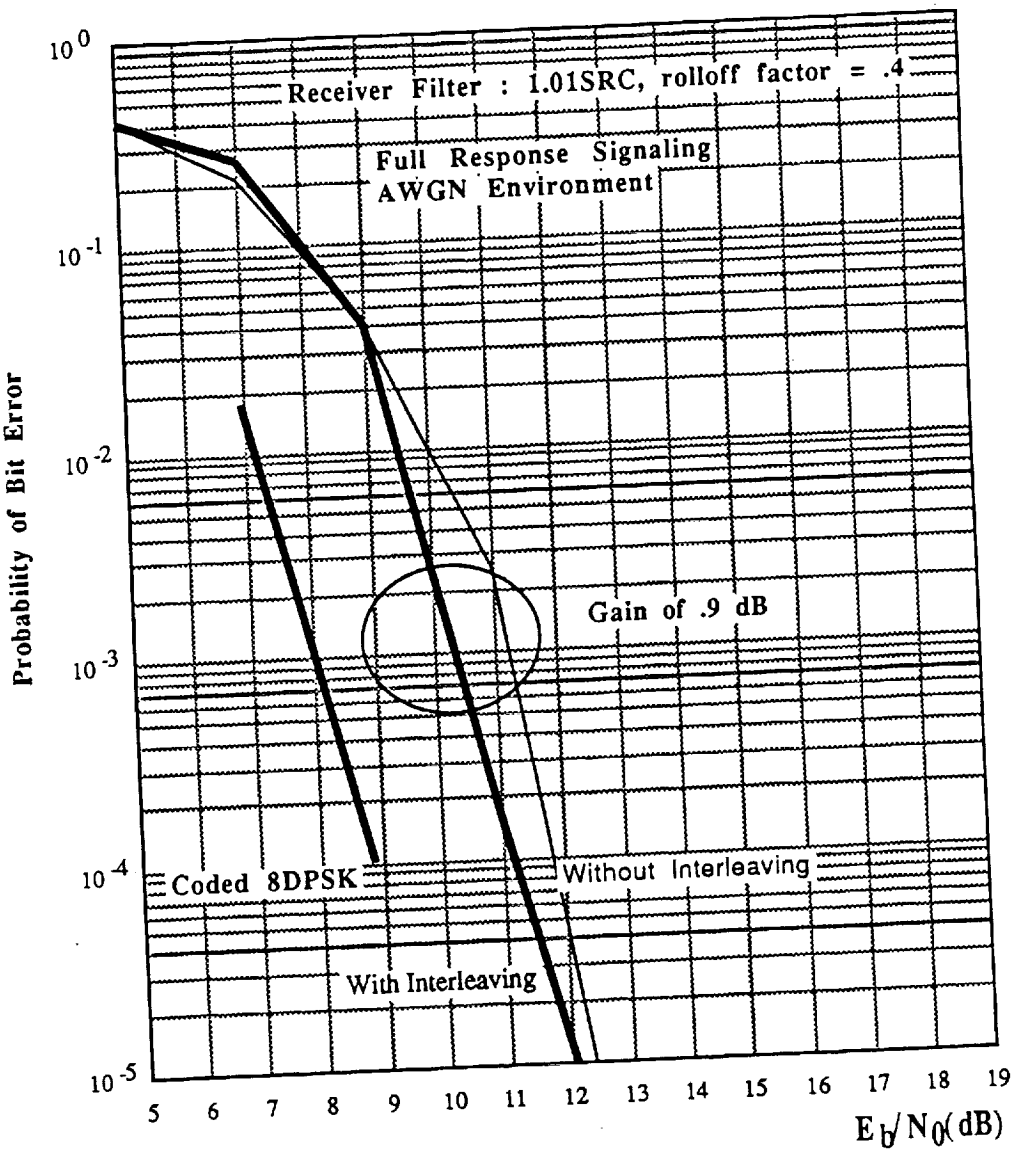

Performance of 8-state trellis coded 8-level CPM signal with HCS1 pulse shape, h=0.125, and differential detection with and without interleaving. Trellis coded 8-level DPSK is also shown for comparison.

Figure 8.42

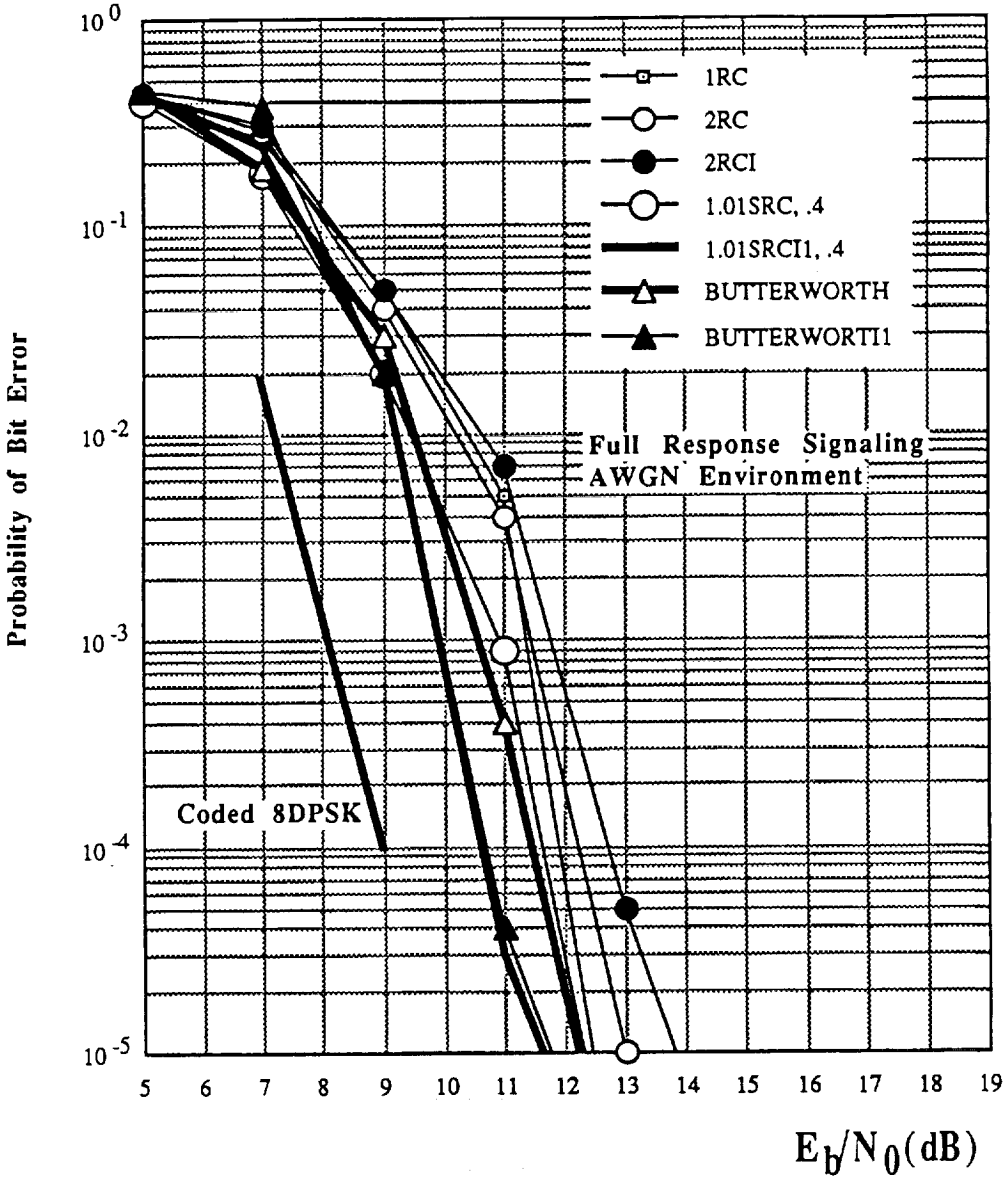

Performance of 16-state trellis coded 8-level CPM signal with HCS1 pulse shape, h=0.125, and differential detection for various receiver filtering. Trellis coded 8-level DPSK is also shown for comparison.

Figure 8.43

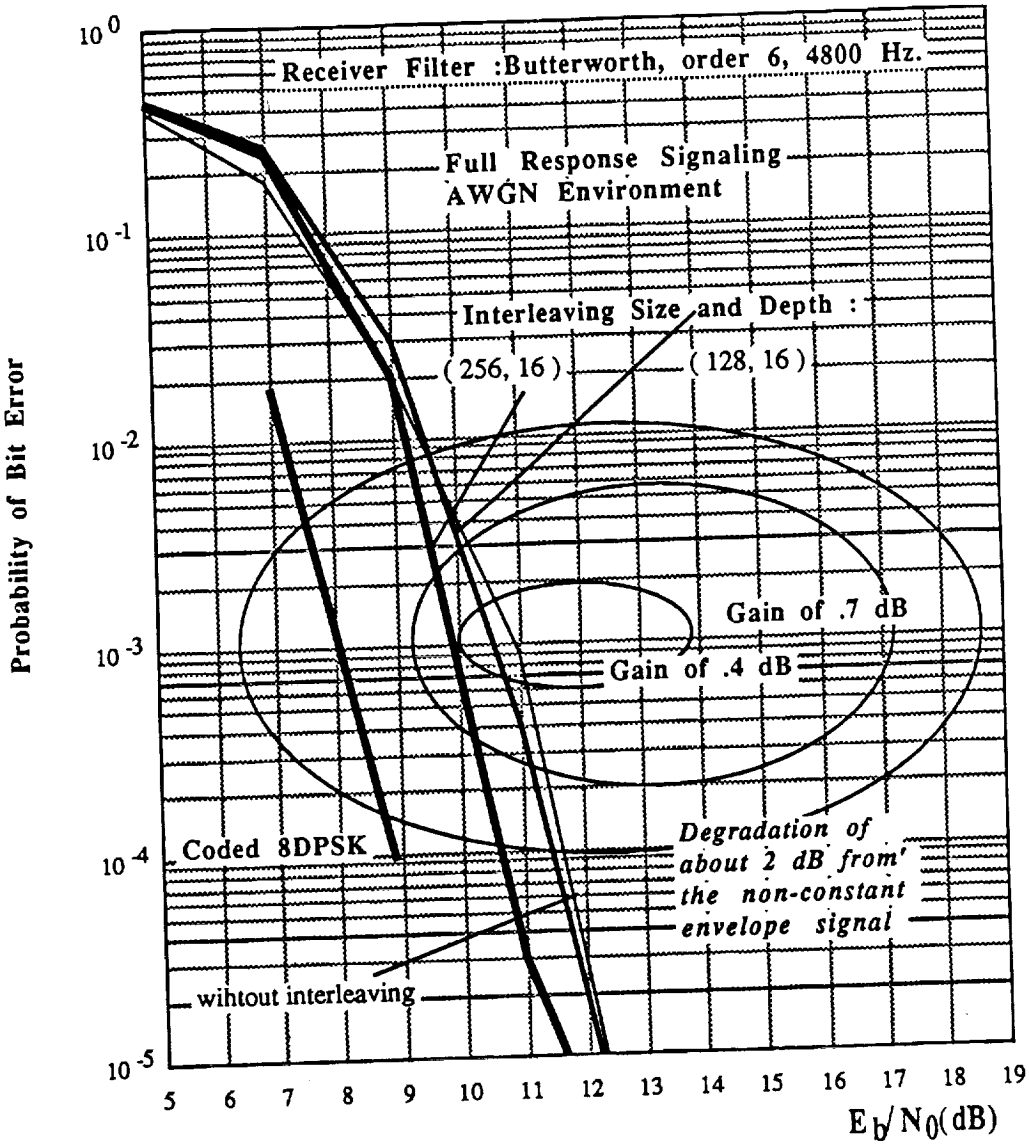

Performance of 8-state trellis coded 8-level CPM signal with HCS1 pulse shape, h=0.125, and differential detection with and without interleaving. Trellis coded 8-level DPSK is also shown for comparison.

Figure 8.44

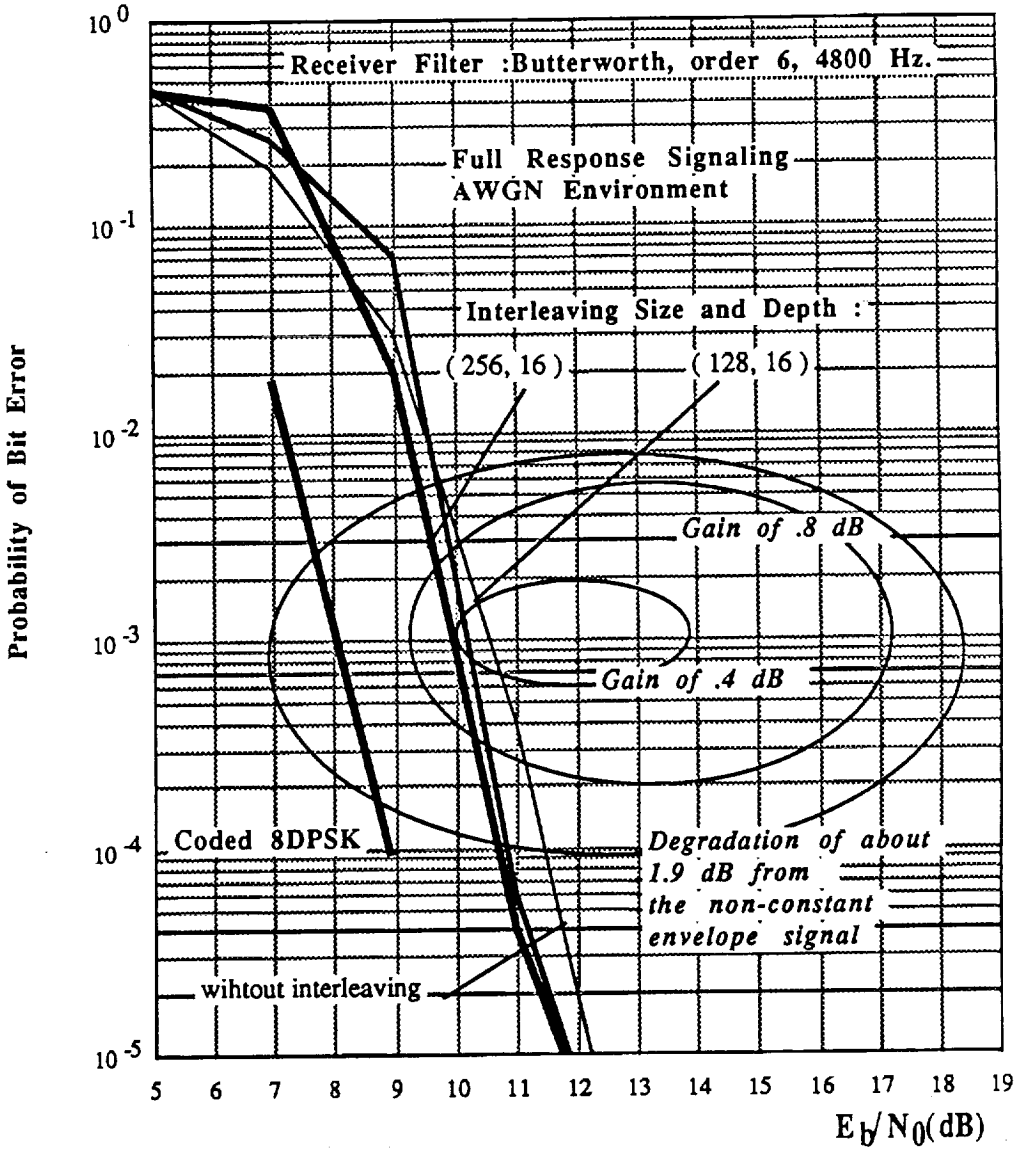

Performance of 16-state trellis coded 8-level CPM signal with HCS1 pulse shape, h=0.125, and differential detection with and without interleaving. Trellis coded 8-level DPSK is also shown for comparison.

Figure 8.45

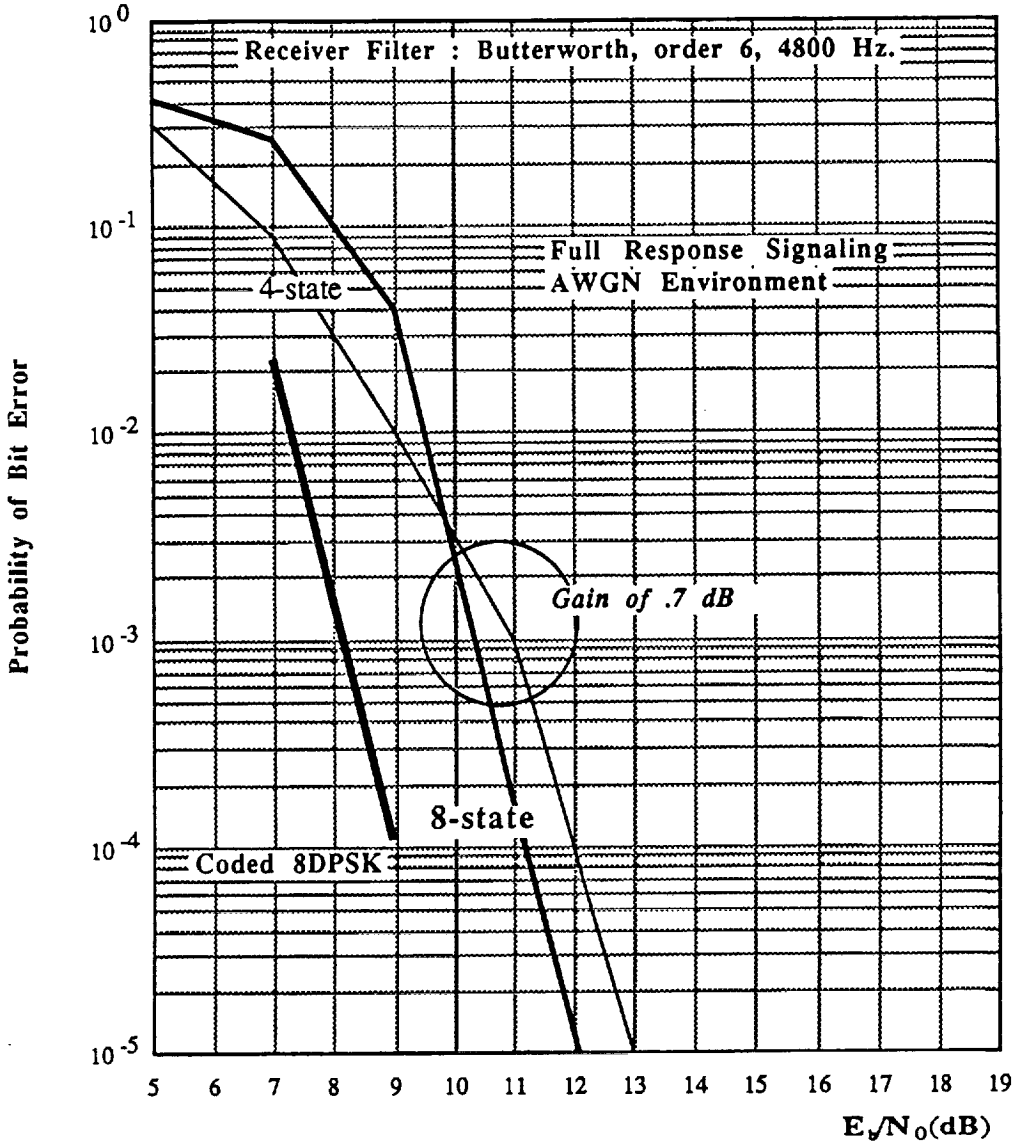

Performance of trellis coded 8-level CPM signal with HCS1 pulse shape, h=0.125, and differential detection for 4 and 8-state codes.

Figure 8.46

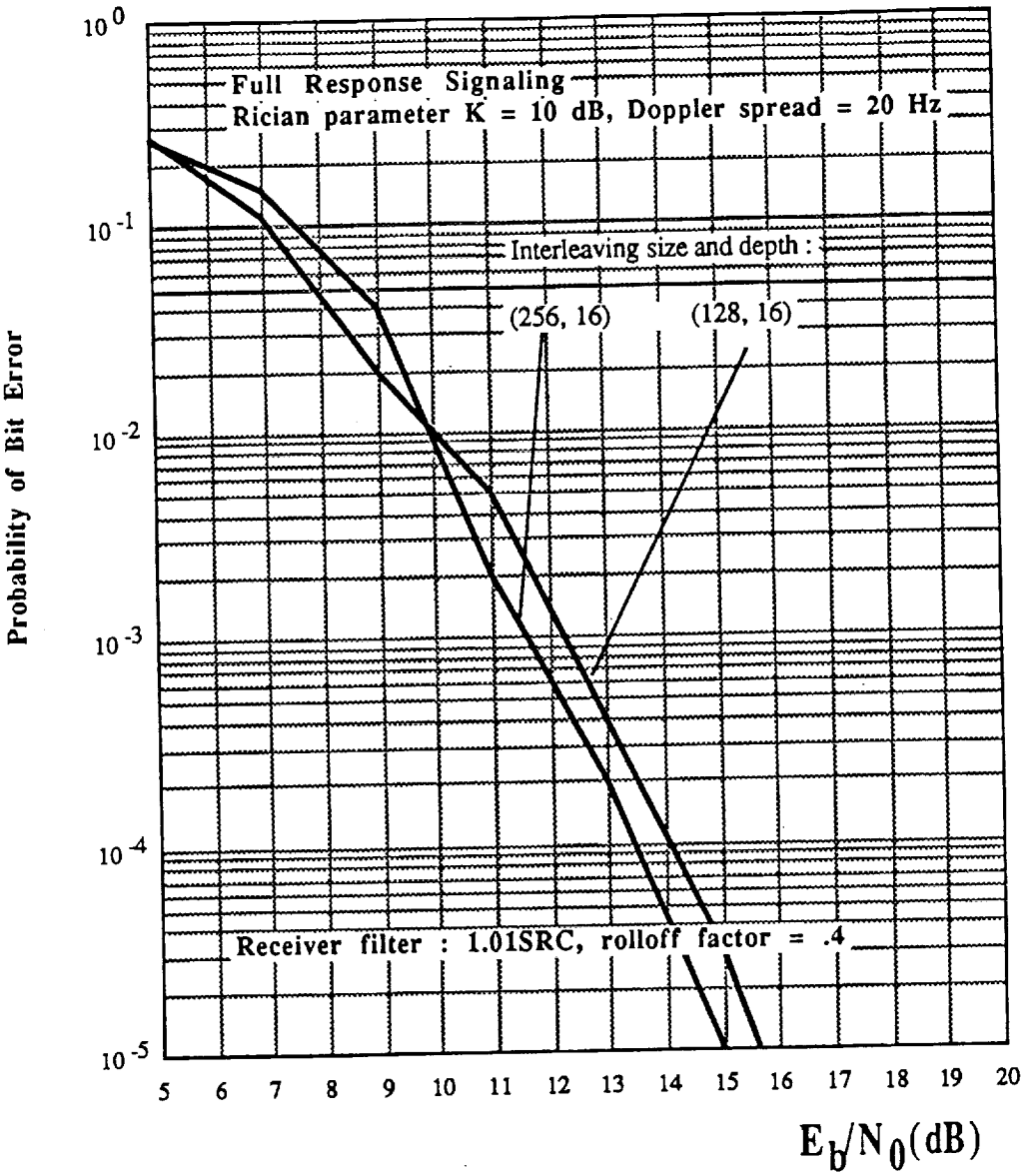

Performance of 4-state trellis coded 8-level CPM signal with HCS1 pulse shape, h=0.125, and differential detection over Rician fading and AGWN channel.

Figure 8.47

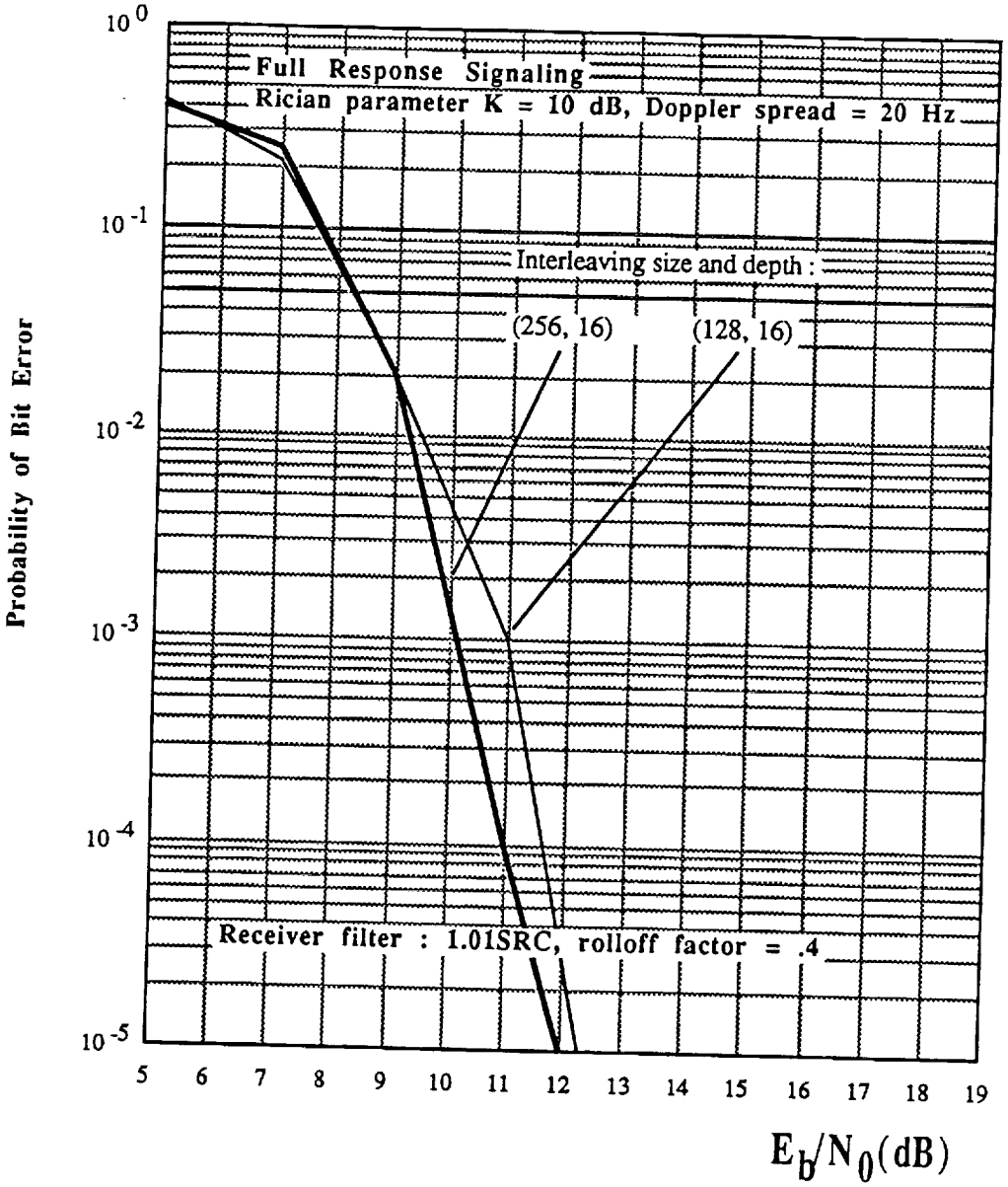

Performance of 8-state trellis coded 8-level CPM signal with HCS1 pulse shape, h=0.125, and differential detection over Rician fading and AGWN channel.

Figure 8.48

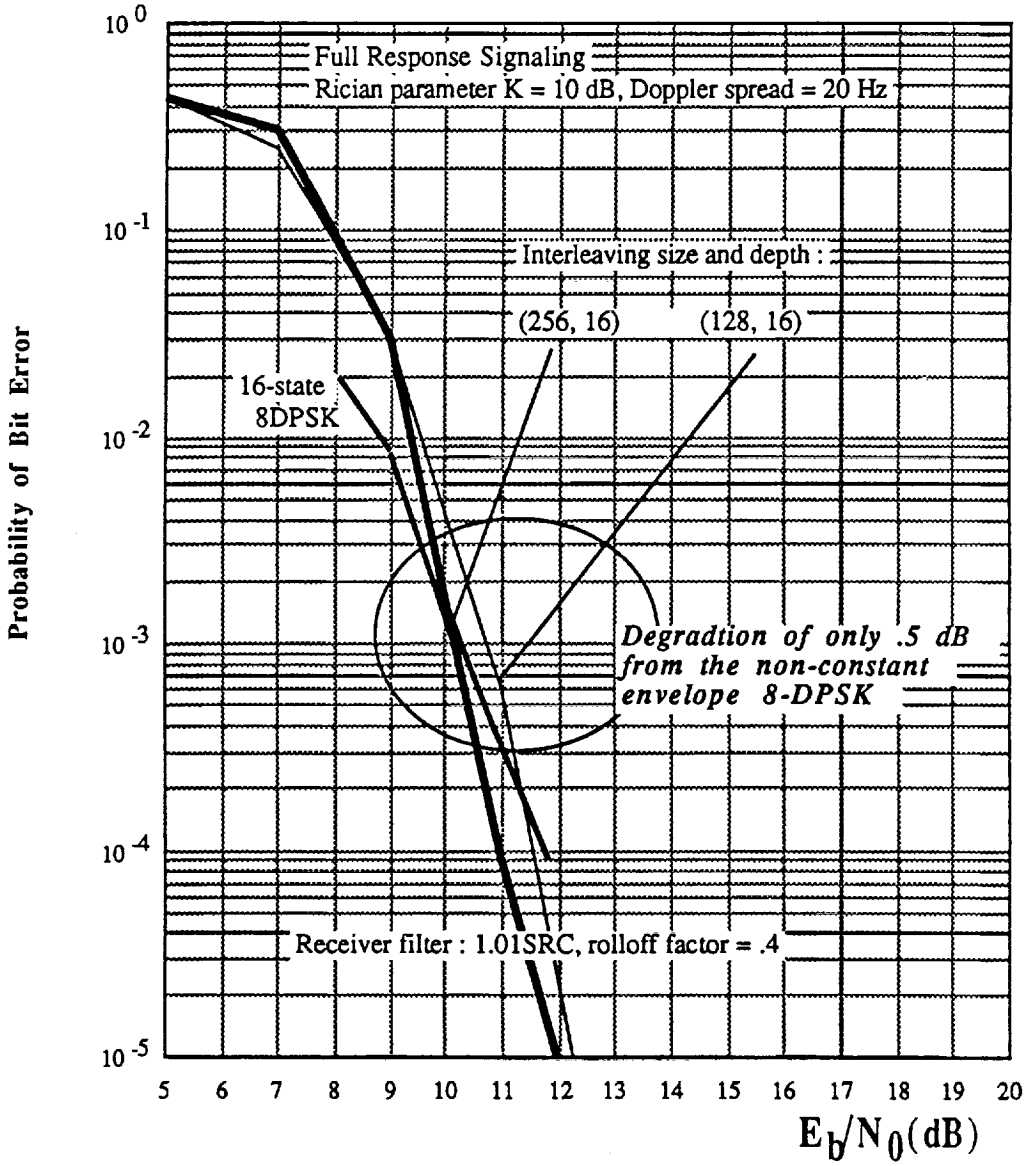

Performance of 16-state trellis coded 8-level CPM signal with HCS1 pulse shape, h=0.125, and differential detection over Rician fading and AGWN channel. 16-state trellis coded 8-DPSK is also shown for comparison.

Figure 8.49

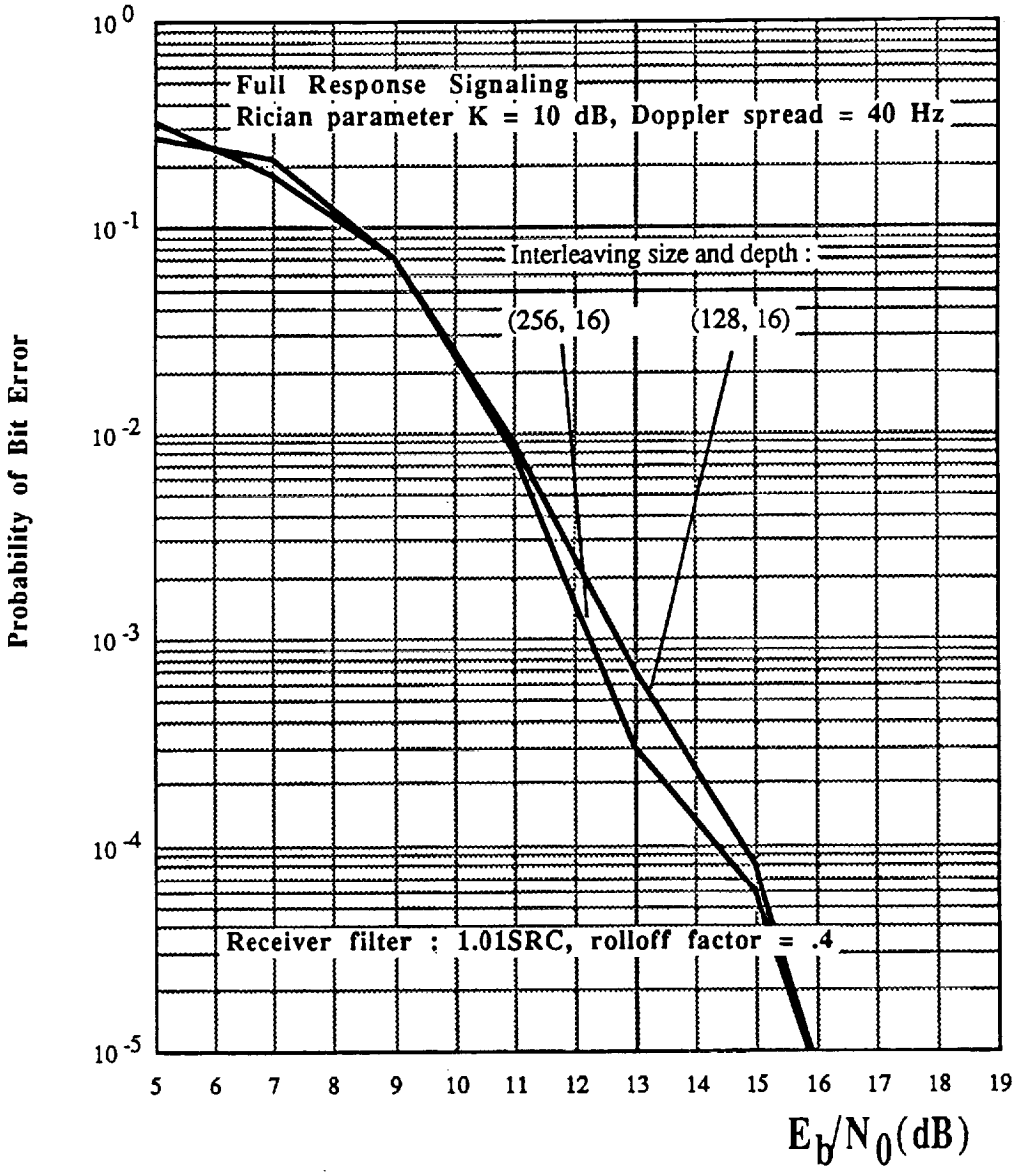

Performance of 4-state trellis coded 8-level CPM signal with HCS1 pulse shape, h=0.125, and differential detection over Rician fading and AGWN channel.

Figure 8.50

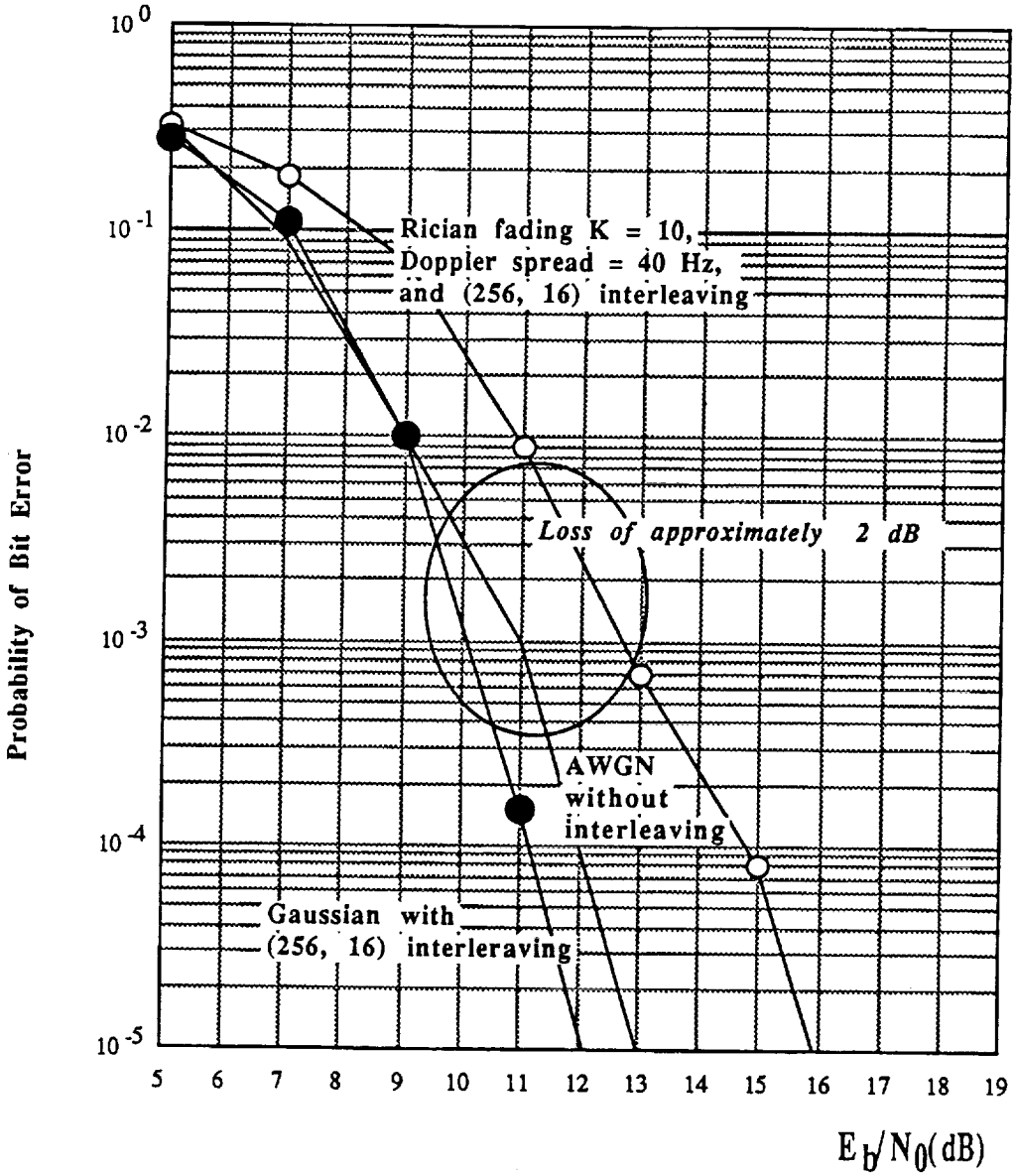

Preformance of 4-state treliis coded 8-level CPM signal with HCS1 pulse shape, h = .125, and differential detection over diffferent channels.

Figure 8.51

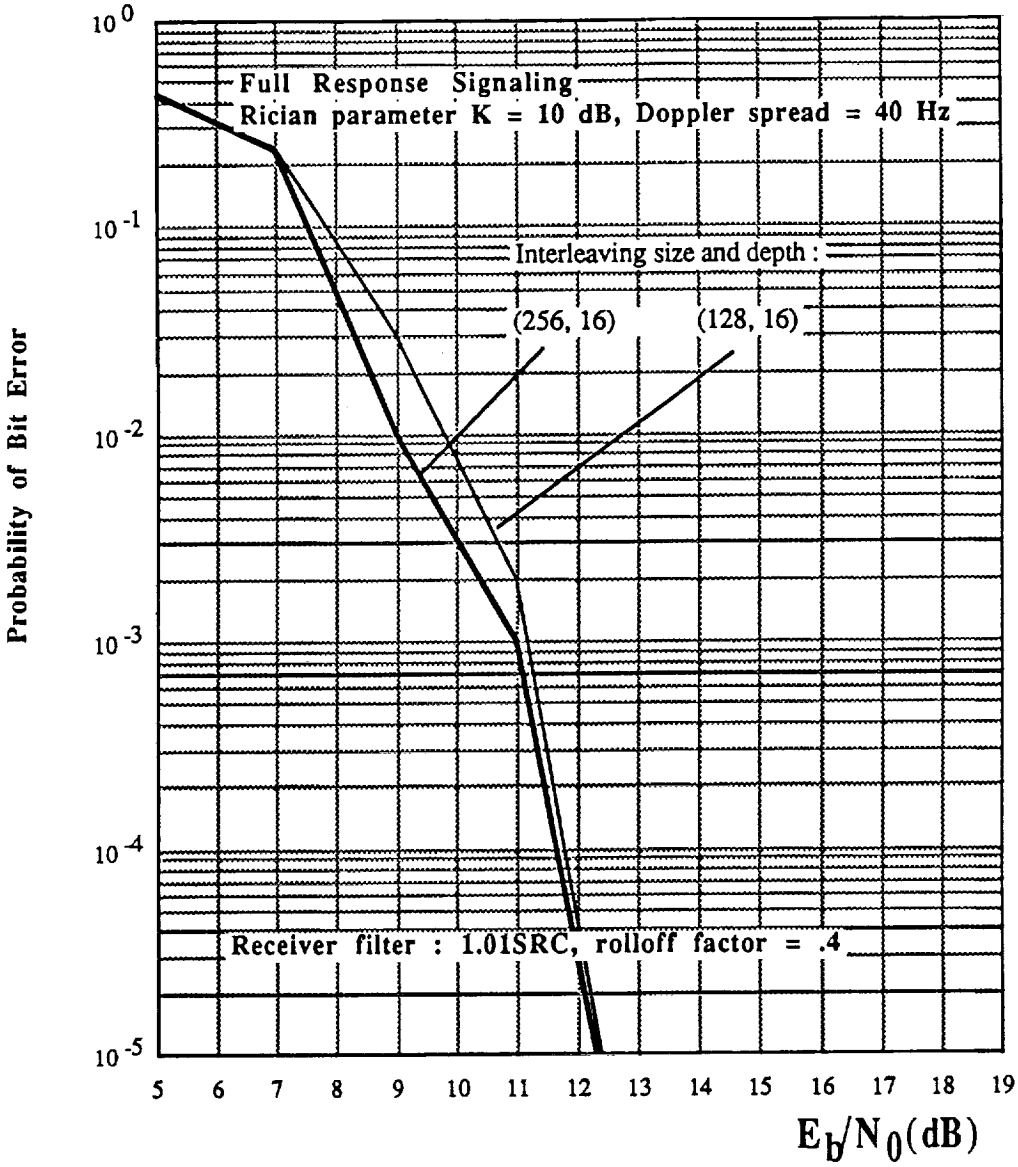

Performance of 8-state trellis coded 8-level CPM signal with HCS1 pulse shape, h=0.125, and differential detection over Rician fading and AGWN channel.

Figure 8.52

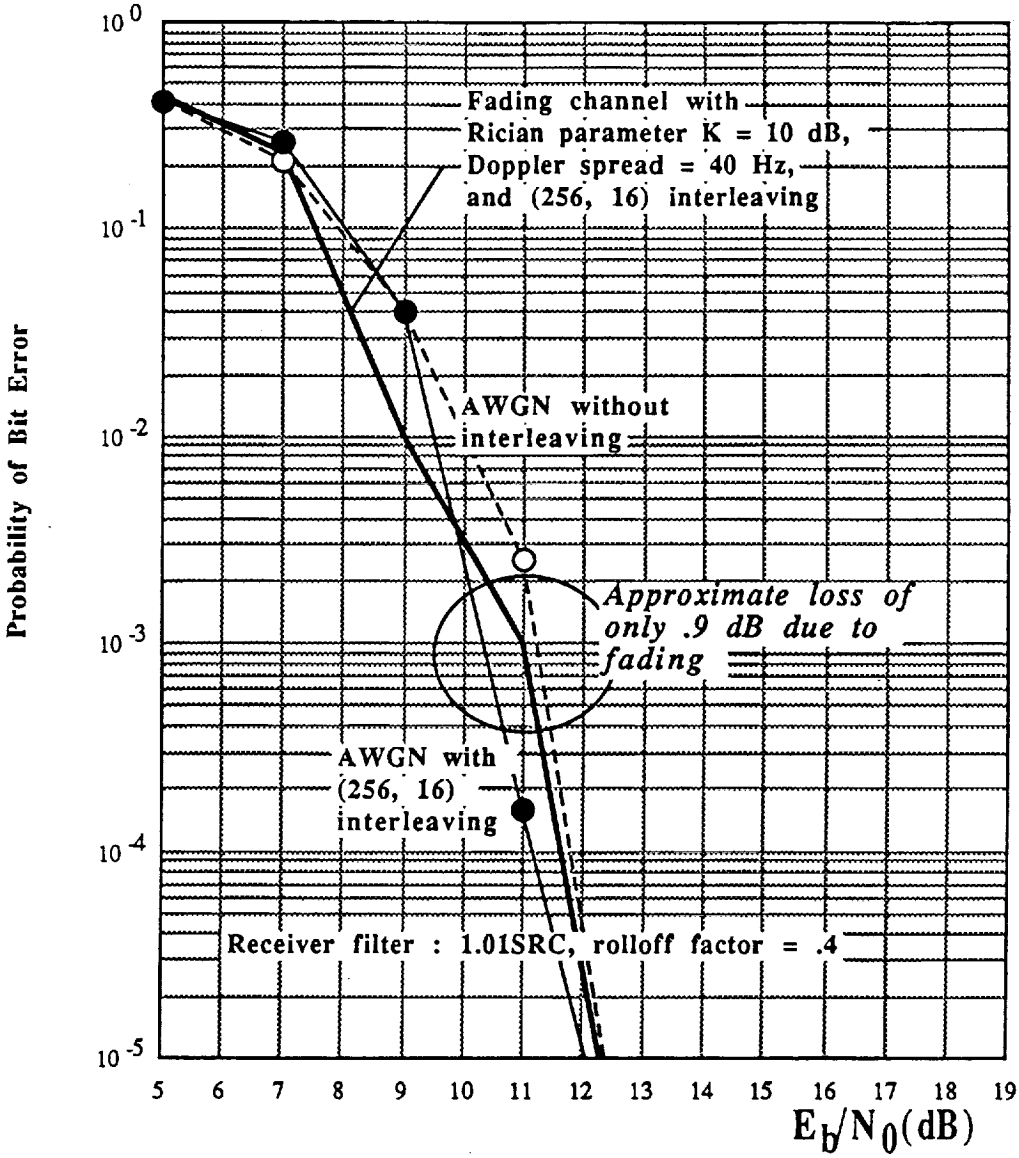

Performance of 8-state trellis coded 8-level CPM signal with HCS1 pulse shape, h=0.125, and differential detection over different channels.

Figure 8.53

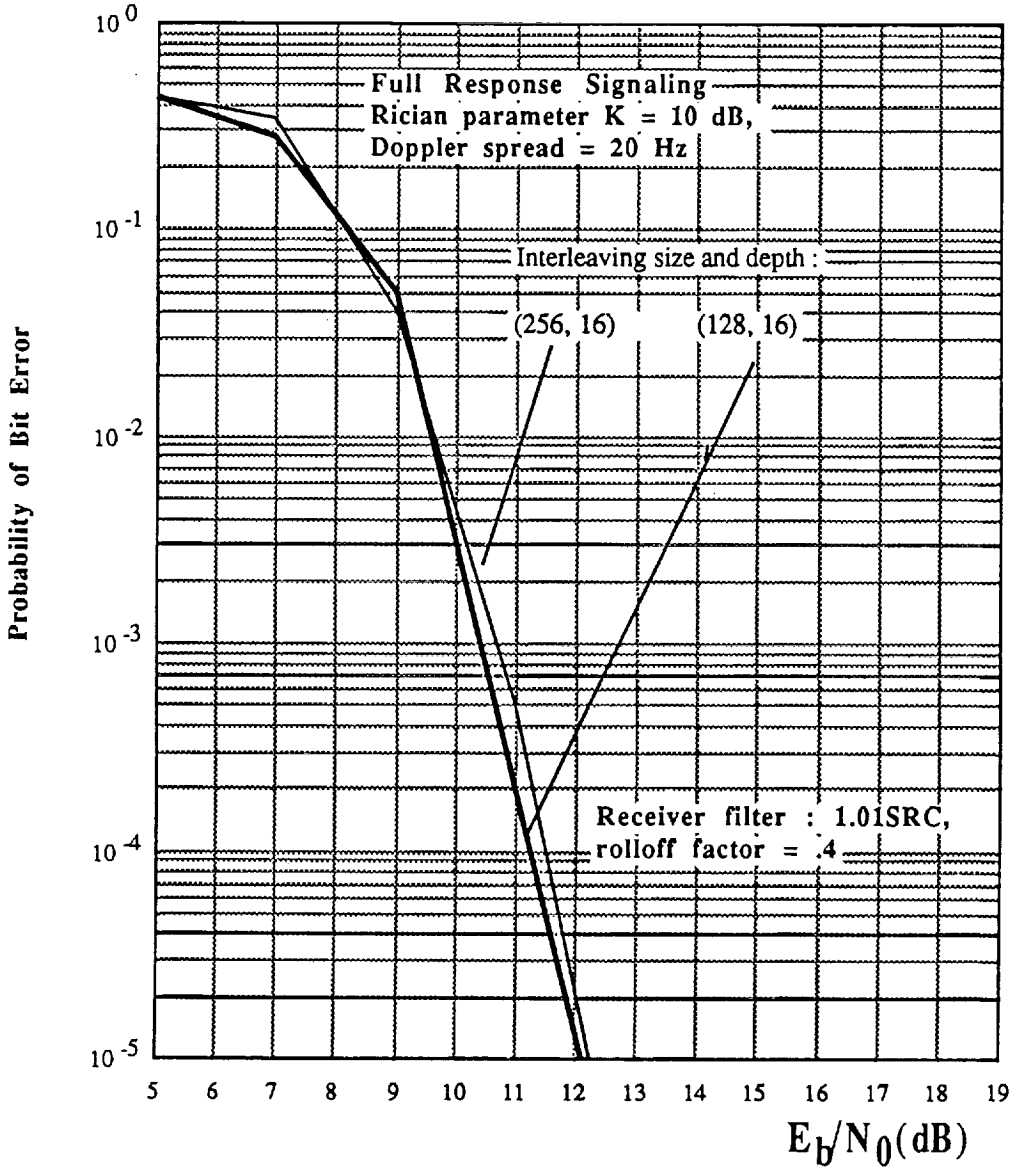

Performance of 16-state trellis coded 8-level CPM signal with HCS1 pulse shape, h=0.125, and differential detection over Rician fading and AGWN channel.

Figure 8.54

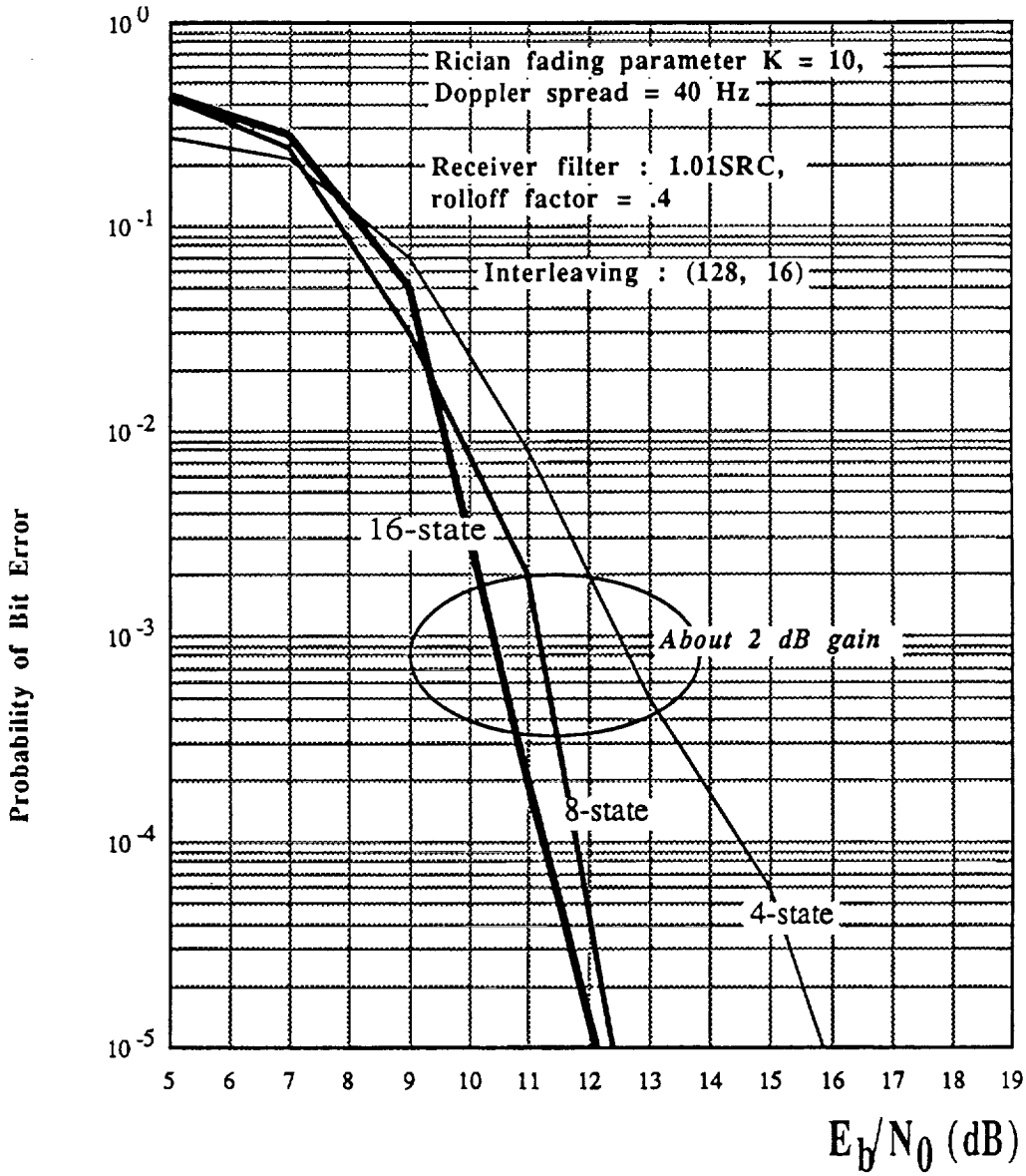

Performance of trellis coded 8-level CPM signal with HCS1 pulse shape, h = .125, and differential detection, over Rician fading and AWGN channel, for 4, 6, and 16-state codes.

Figure 8.55

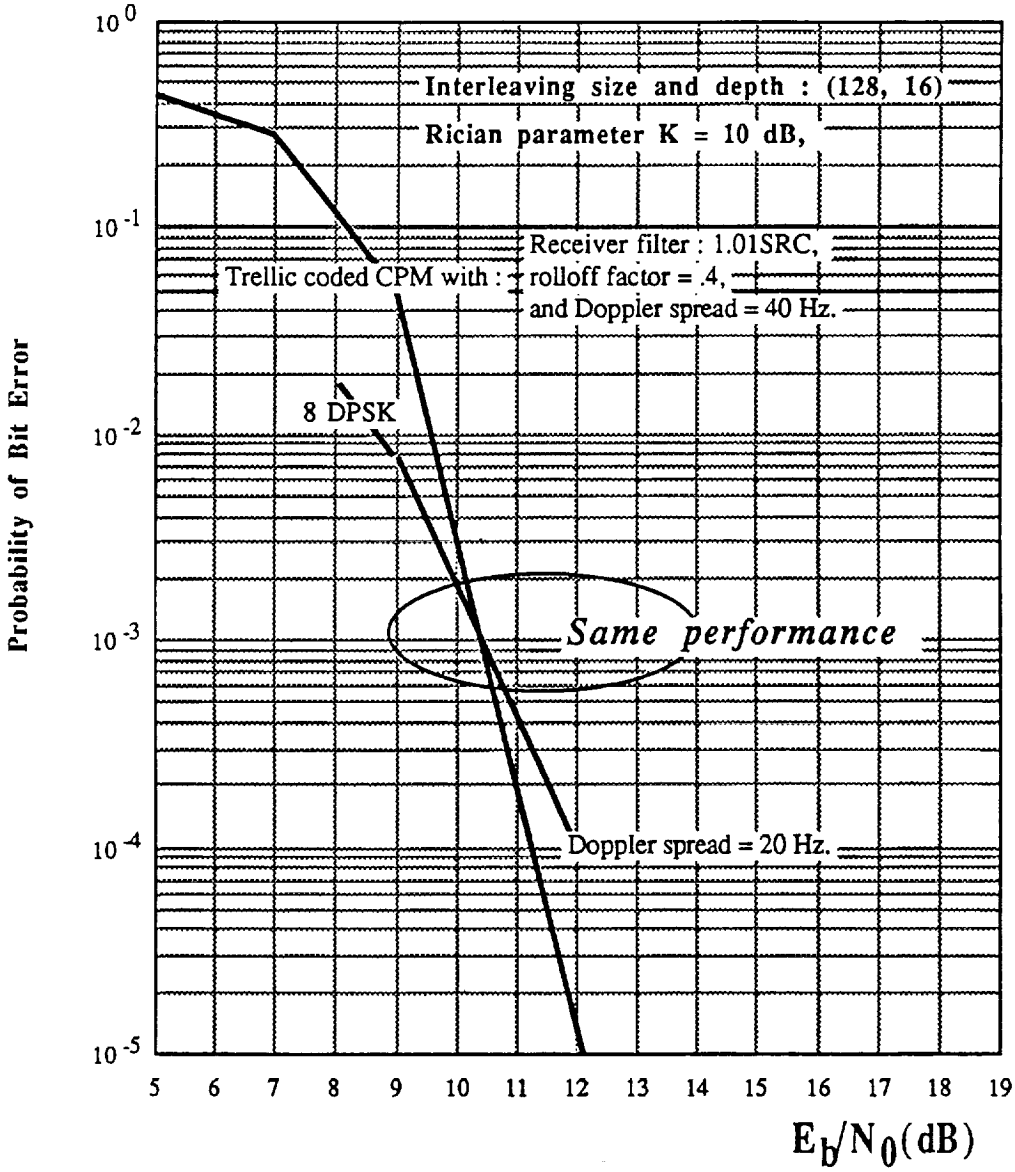

Comparison between the performance of 16-state trellis coded 8-level CPM signal with HCS1 pulse shape, h=0.125, with differential detection and 16-state 8DPK, over the Rician fading and AGWN channel, for two different Duppler spreads.

Figure 8.56

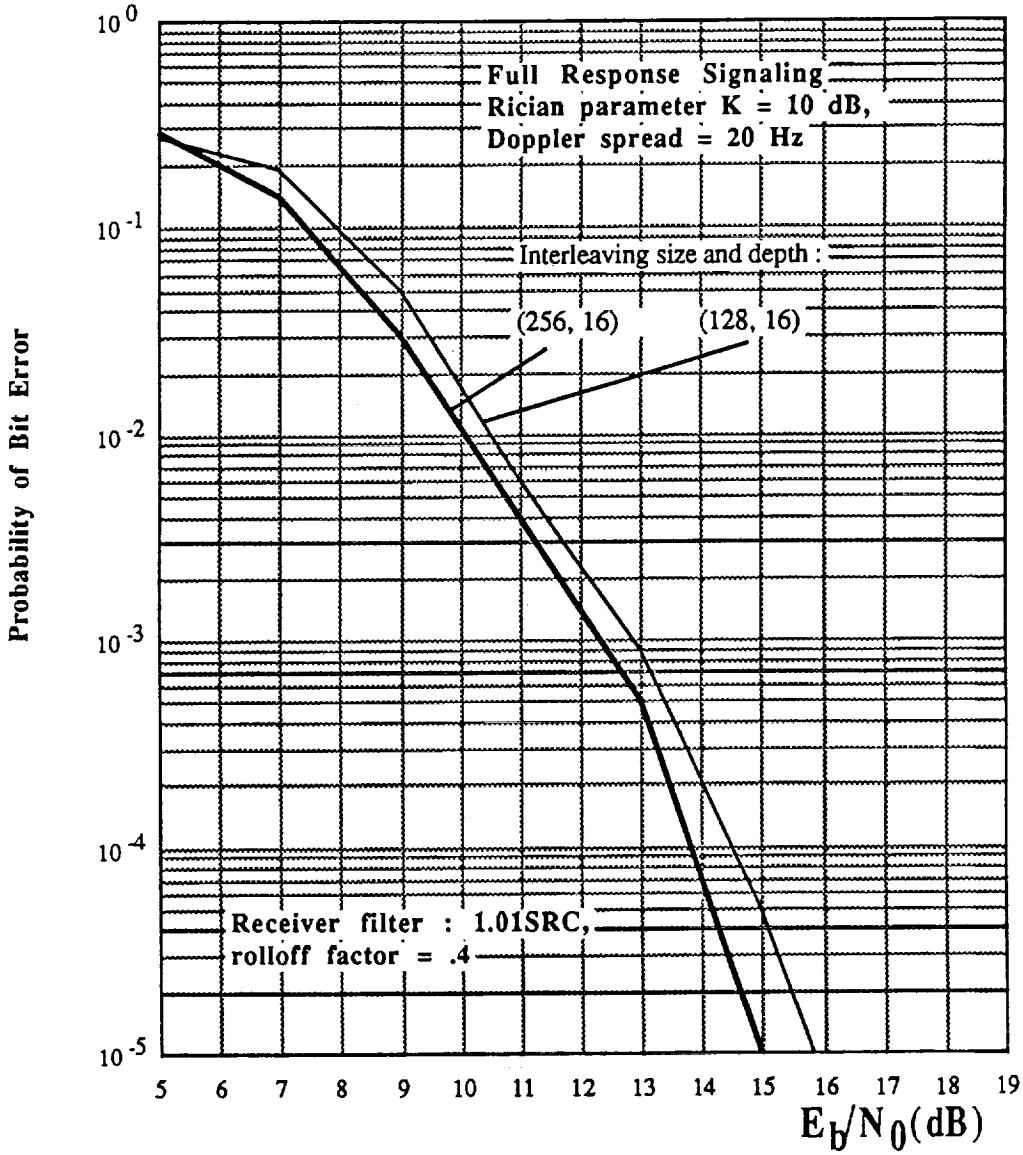

Performance of 4-state trellis coded 8-level CPM signal with 1RC pulse shape, h=0.125, and differential detection over Rician fading and AGWN channel.

Figure 8.57

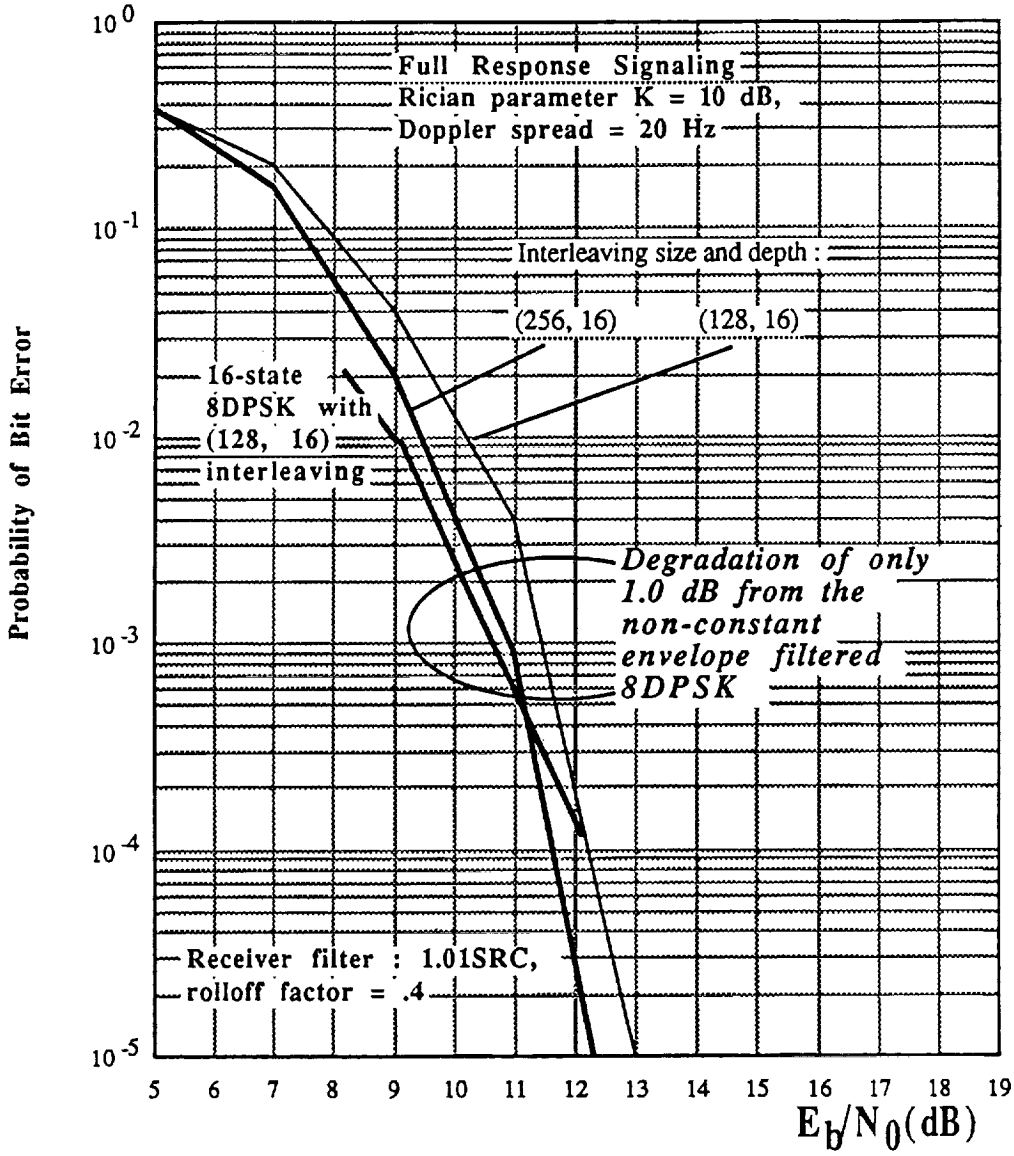

Performance of 8-state trellis coded 8-level CPM signal with 1RC pulse shape, h=0.125, and differential detection over Rician fading and AGWN channel. 16-state trellis coded 8-DPSK is also shown for comparison.

Figure 8.58

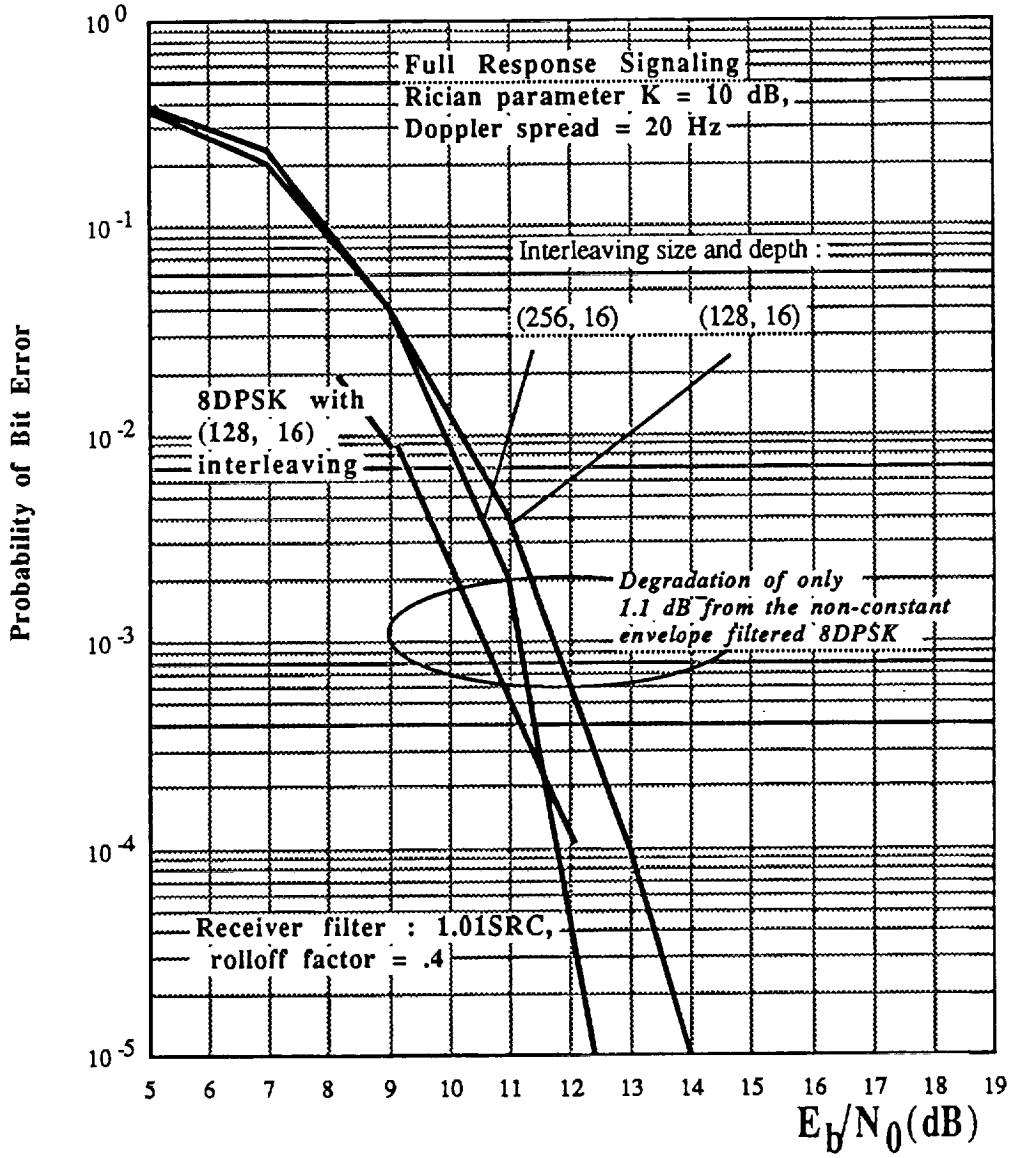

Performance of 16-state trellis coded 8-level CPM signal with 1RC pulse shape, h=0.125, and differential detection over Rician fading and AGWN channel. 16-state trellis coded 8-DPSK is also shown for comparison.

Figure 8.59

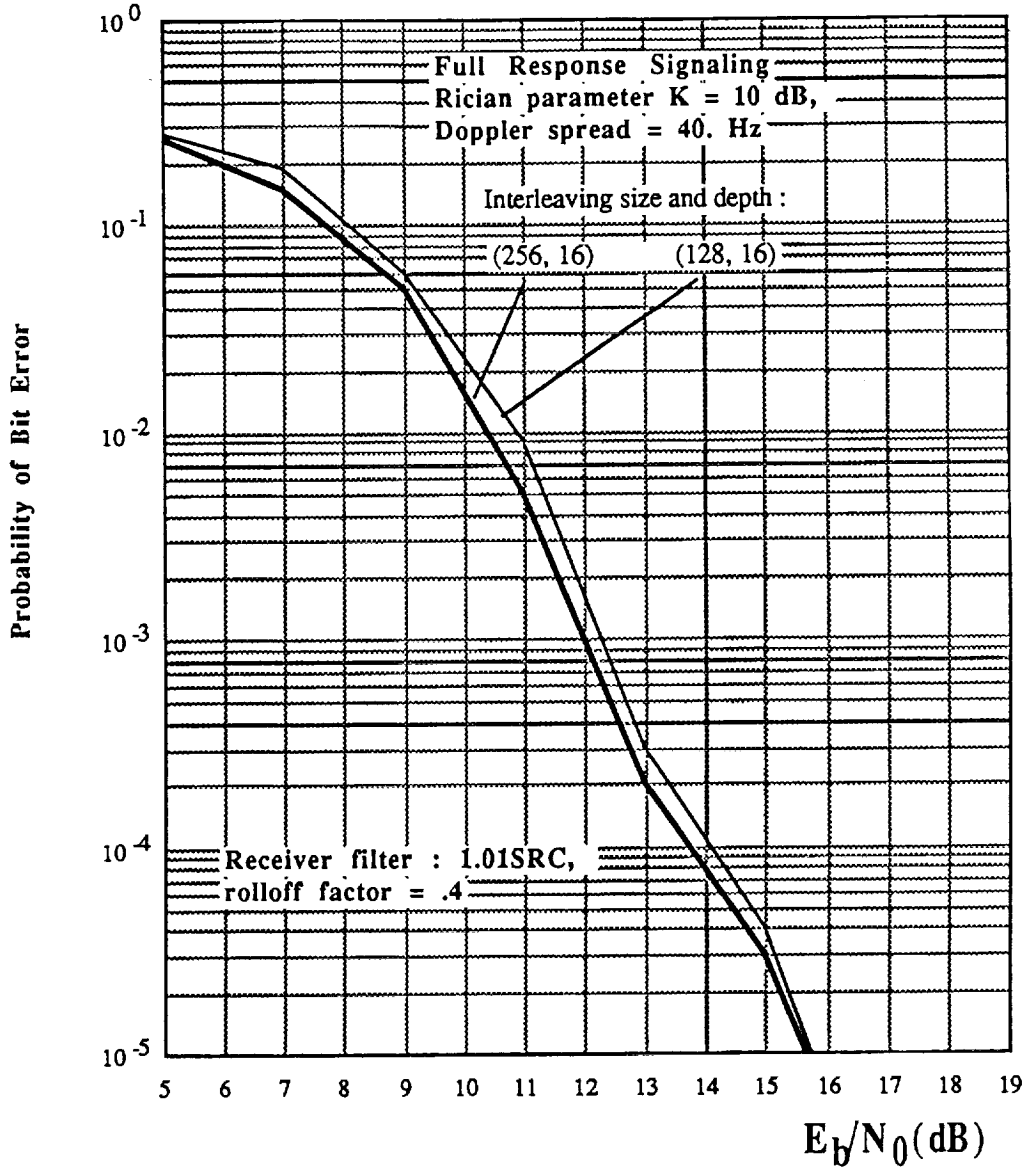

Performance of 4-state trellis coded 8-level CPM signal with 1RC pulse shape, h=0.125, and differential detection over the Rician fading and AGWN channel. 16-state trellis coded 8-DPSK is also shown for comparison.

Figure 8.60

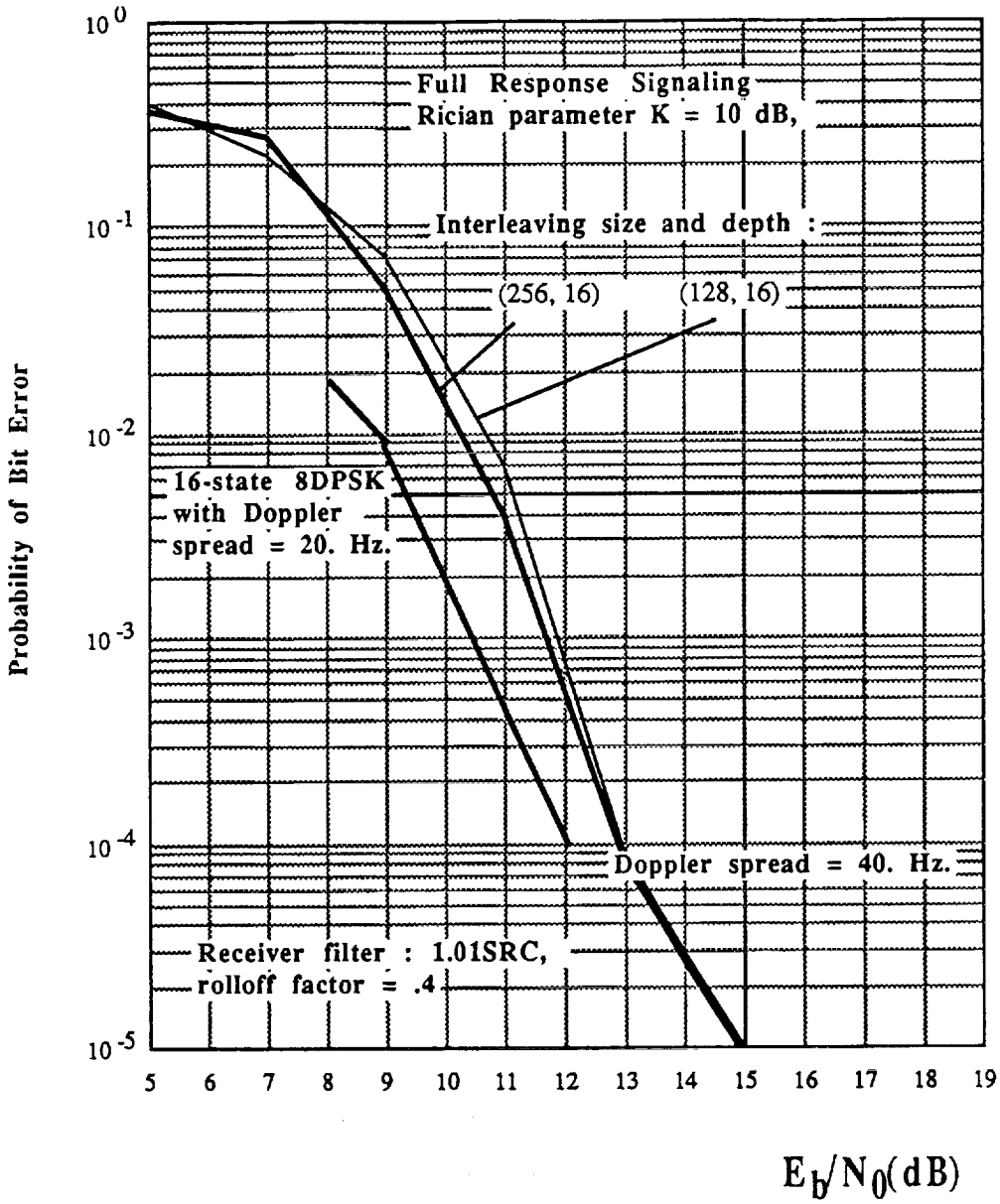

Performance of 8-state trellis coded 8-level CPM signal with 1RC pulse shape, h=0.125, and differential detection over Rician fading and AGWN channel. 16-state trellis coded 8-DPSK is also shown for comparison.

Figure 8.61

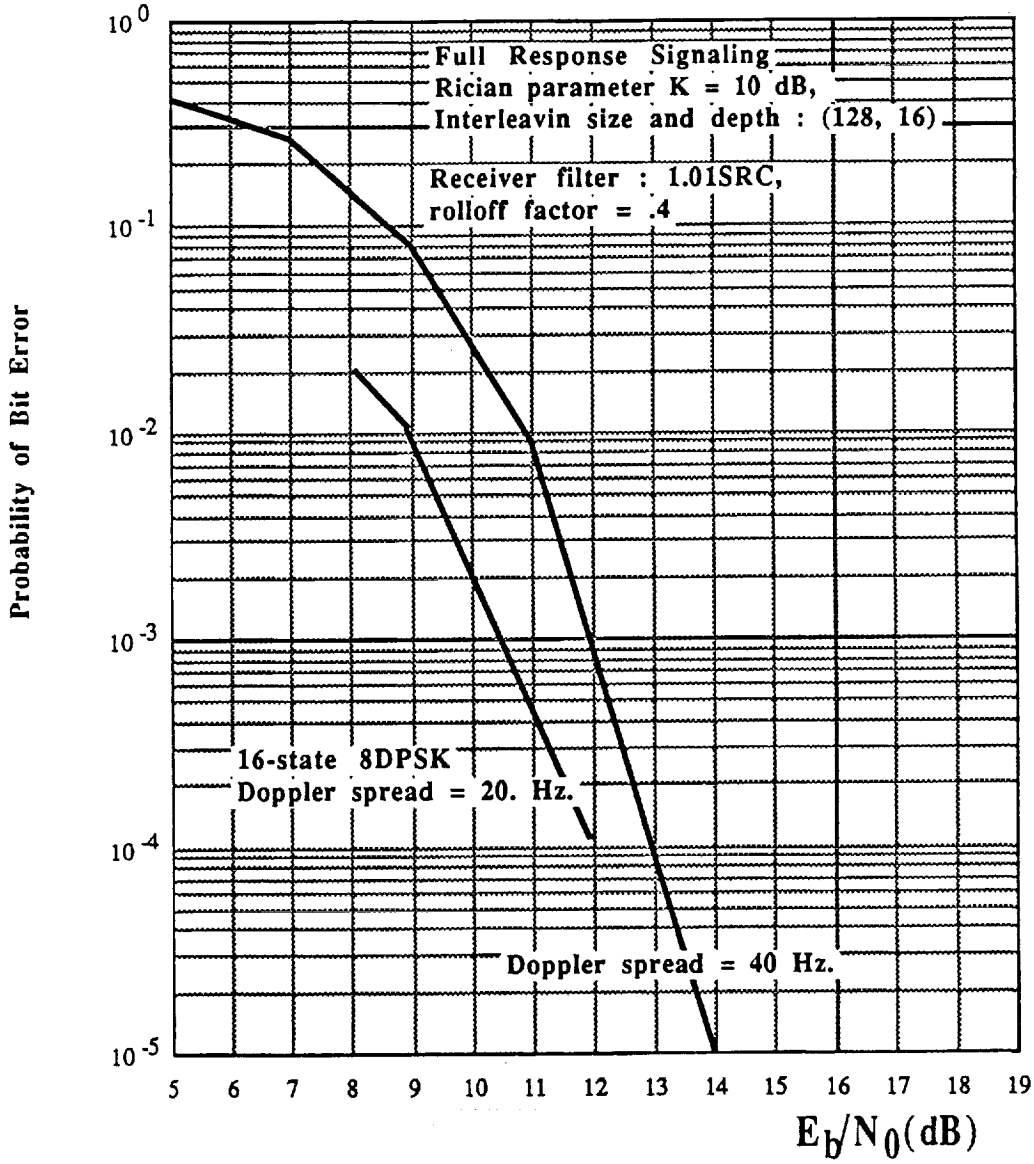

Performance of 16-state trellis coded 8-level CPM signal with 1RC pulse shape, h=0.125, and differential detection over the Rician fading and AGWN channel. 16-state trellis coded 8-DPSK is also shown for comparison.

Figure 8.62

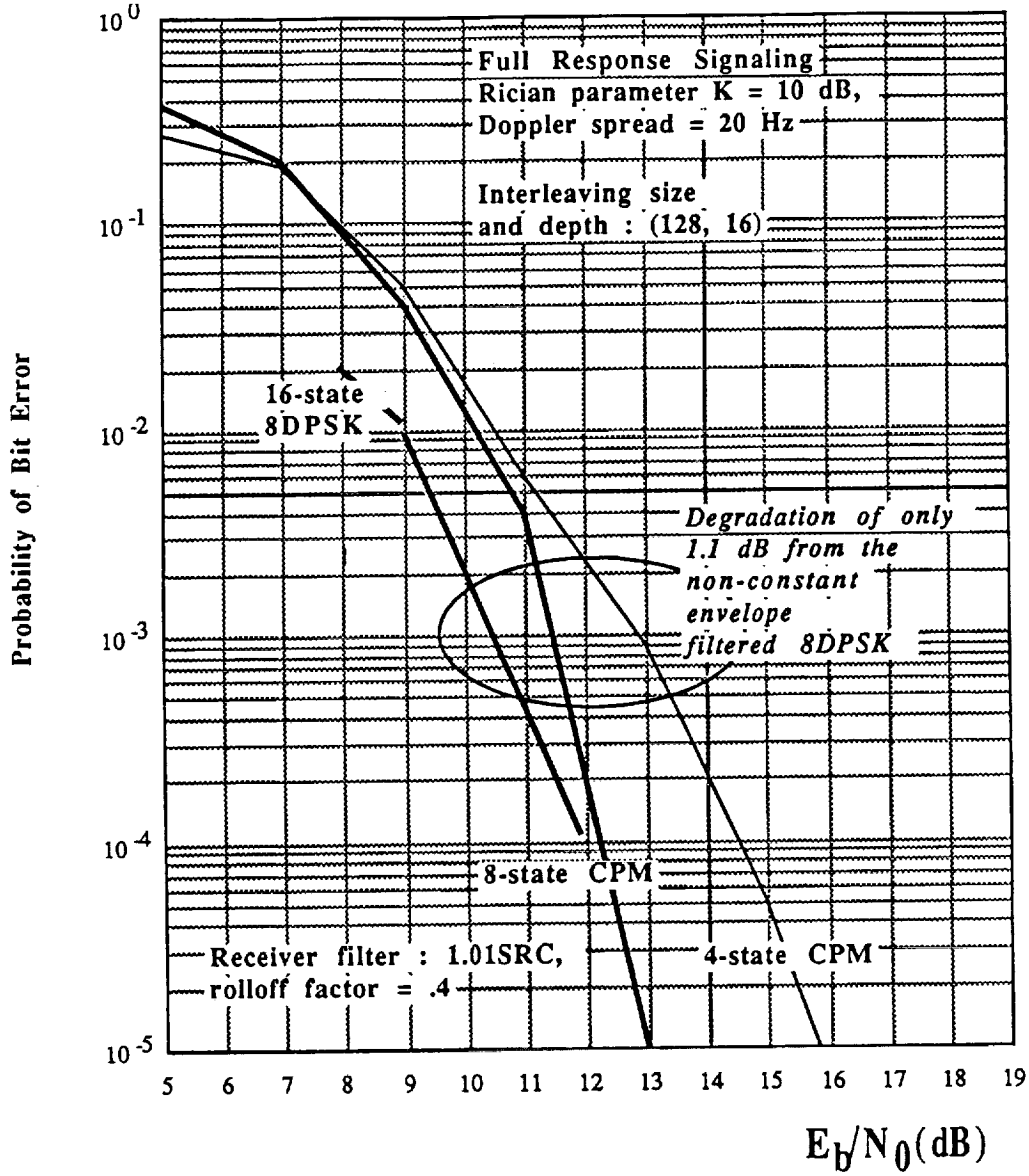

Performance of trellis coded 8-level CPM signal with 1RC pulse shape, h=0.125, and differential detection , over Rician fading and AGWN channel, for 4 and 8-state codes. 16-state trellis coded 8-DPSK is also shown for comparison.

Figure 8.63

Chapter 9

Conclusions

We have considered a satellite-based mobile communication scheme based on continuous-phase modulated (CPM) signals used in conjunction with trellis-coded modulation (TCM). We have proved that the synergy between TCM, which improves error probability, and CPM signals, which provide constant envelope and low spectral occupancy, provides a satisfactory solution to the problem of transmitting on mobile satellite channels.

CPM signals are differentially demodulated symbol-by-symbol. By doing this, the power efficiency of CPM is not exploited, but its spectral properties are retained, and interleaving/deinterleaving is made possible.

This transmission scheme was extensively simulated under several conditions. Several frequency pulse shapes, receiver filter shapes, TCM schemes, interleaving/deinterleaving sizes and depths, and fading channels were considered. It has been found that, over the AWGN channel model (i.e., in the absence of fading) an 8-state TCM-encoded CPM signals with full response signaling, 1RC frequency pulse, $M = 8$ levels, $h = 0.125$, and differential detection, in conjunction with an SRC receiver filter with $L_B = 1.01$ and rolloff $\beta_f = 0.4$, and (256,16) block interleaving, offers the best compromise between complexity and performance in the signal-to-noise range and among the candidate schemes considered in this Report. For fading channels, full-response CPM with 1HCS pulses offers the same performance as a filtered 8DPSK signal, but with the additional positive feature of a constant envelope. This, in essence, will make the CPM a system more attractive than DPSK.

In conclusion, our results show that, for a careful selection of system parameters, on satellite-based land mobile communication channels a differentially-detected CPM scheme can offer an error performance which is essentially the

same as differentially coherent PSK. Since PSK does not use bandwidth in a very efficient way, it has to be band-pass filtered to meet the requirements of closely-spaced mobile-radio channelization. As a result, its envelope is not constant, and its performance would be degraded by power amplifiers operated at or near saturation for better power efficiency. Since CPM with the parameters chosen is bandwidth efficient it does not require narrow filtering, and consequently offers constant or near-constant envelope, thus preventing a possible cause of serious performance degradation.

Bibliography

[1] C. E. Sundberg, "Continuous phase modulation," *IEEE Commun. Mag.*, vol. COM-24, No. 4, April 1986.

[2] J. B. Anderson, T. Aulin and C. E. Sundberg. *Digital Phase Modulation*, New York, 1986, Plenum Press.

[3] T. Aulin and C. E. Sundberg, "Synchronization properties of continuous phase modulation," *Globecomm*, 1982, Miami.

[4] A. N. D'Andrea, U. Mengali and R. Reggiannini, "Carrier phase and clock recovery for continuous phase modulated signals," *IEEE Trans. Commun.*, vol. COM-35, No. 10, October 1987.

[5] T. Aulin, N. Rydbeck and C. E. Sundberg, "Transmitter and receiver structures for M-ary partial response FM - synchronization considerations," Technical Report TR-121, Telecommunication Theory, University of Lund, Sweden, December 1978.

[6] T. Aulin and C. E. Sundberg, "Differential detection of continuous phase modulated signals," Technical Report TR-138, Telecommunication Theory, University of Lund, Sweden, February 1980.

[7] T. Aulin and C. E. Sundberg, "Partially coherent detection of digital full response continuous phase modulated signals," *IEEE Trans. Commun.*, vol. COM-30, No. 5, May 1982.

[8] A. Svensson, "On an improved differential detector for continuous phase modulation," Technical Report TR-197, Telecommunication Theory, University of Lund, Sweden, August 1985.

[9] T. Aulin and C. E. Sundberg, "An easy way to calculate power spectra for digital FM," *IEE Proceedings, Part F, Communications, Radar and Signal Processing*, October 1983.

[10] Simon Haykin, *Communication Systems*, New York, 1983, John Wiley & Sons.

[11] S. V. Pizzi and S. G. Wilson, "Convolutional coding combined with continuous phase modulation," *IEEE Trans. Commun.*, vol. COM-33, No. 1, January 1985.

[12] T. Aulin and C. E. Sundberg, "On synchronization for CPM," Technical Report TR-156, Telecommunication Theory, University of Lund, Sweden, September 1981.

[13] R. de Buda, "Coherent demodulation of frequency shift keying with low deviation ratio," *IEEE Trans. Commun.*, vol. COM-20, No. 6, pp.429-435, June 1972.

[14] W. U. Lee, "Carrier synchronization of CPFSK signals," in *Proc. Nat. Telecommun. Conf.*, Los Angeles, CA, December 1977, pp.30.2.1-30.2.4.

[15] A. V. Oppenheim and R. W. Schafer, *Digital Signal Processing*, Englewood Cliffs, 1975, Prentice-Hall, Inc.

[16] Phase I SBIR Report 1405.6455, "Trellis coding with continuous phase modulation (CPM) for satellite-based land mobile communications," Technology Group, 1986, Los Angeles, CA.

[17] J. G. Proakis, *Digital Communications*, New York, 1983, McGraw-Hill, Inc.

[18] F. Abrishamkar and E. Biglieri, "Doppler frequency shift estimation for differentially coherent CPM," submitted for publication

[19] J.B.Anderson, T.Aulin, and C.-E.Sundberg, *Digital Phase Modulation.* New York: Plenum Publ. Co., 1986

[20] S.Benedetto, E.Biglieri, and V.Castellani, *Digital Transmission Theory.* Englewood Cliffs, NJ: Prentice-Hall Publ. Co, 1987

[21] E.Biglieri, "Ungerboeck codes do not shape the signal power spectrum," *IEEE Trans. Inform. Th.*, vol. IT-32, July 1986

[22] A.P.Clark, "Digital modems for land mobile radio," *IEE Proceedings,* Vol.132, pt. F, No. 5, pp.348-362, August 1985

[23] G. C. Clark, Jr. , and J. B. Cain, *Error-Correction Coding for Digital Communications.* New York: Plenum Press, 1981

[24] D.Divsalar and M.K.Simon, "Trellis code modulation for 4800-9600 bits/s transmission over a fading mobile satellite channel," *IEEE Journal on Selected Areas in Communications,* vol.SAC-5, No.2, pp.162-175, February 1987

[25] G.Lindell and C.-E.Sundberg, "Multilevel continuous phase modulation with high rate convolutional codes," *GLOBECOM'83,* San Diego, CA, Nov. 1983

[26] S.V.Pizzi and S.G.Wilson, "Convolutional coding combined with continuous phase modulation," *IEEE Trans. on Communications,* vol.COM-33, No.1, pp.20-29, Jan. 1965

[27] B.Rimoldi, "A decomposition approach to CPM," *IEEE Trans. on Inform. Theory,* Vol. 34, No. 2, pp.260-270, March 1988

[28] M. K. Simon and D. Divsalar, "Open loop frequency synchronization of MDPSK with Doppler," *ICC'87,* Seattle, WA, June 7-10, 1987

[29] M. K. Simon and D. Divsalar, "Doppler-corrected differential detection of MPSK," *IEEE Trans. on Commun.*, to be published

[30] G. Ungerboeck, "Channel coding with multilevel/phase signals," *IEEE Trans. Inform. Th.*, vol. IT-28, pp. 56-67, January 1982

[31] A.J.Viterbi and A.M.Viterbi, "Nonlinear estimation of PSK-modulated carrier phase with application to burst digital transmission," *IEEE Trans. on Inform. Theory,* vol.IT-29, No.4, pp.543-551, July 1983

[32] A. M. Gerrish and R. D. Howson, "Multilevel Partial-Response Signaling," *Conf. Record, IEEE Int'l. Conf. on Communications*, 1967, p. 186.

[33] P. Kabal and S. Pasupathy, "Partial-Response Signalling," Commun. Tech. Rep. 75-1, Dept. of Elec. Eng., Univ. of Toronto, Toronto, Ont., Canada, January 1975.

[34] B. E. Rimoldi, "A Decomposition Approach to CPM," *IEEE Trans. on Info. Theory*, Vol. 34, March 1988, pp. 260–270.

[35] T. Thesken and E. Biglieri, "Cutoff rate for channel having precoding, continuous-phase modulation, and differential decoding," MILCOM'89, Boston, MA, October 1989

[36] F. Abrishamkar and E. Biglieri, "Doppler frequency shift estimation for differentially coherent CPM," submitted for publication

[37] J.B.Anderson, T.Aulin, and C.-E.Sundberg, *Digital Phase Modulation.* New York: Plenum Publ. Co., 1986

[38] T. Aulin and C.-E. Sundberg, "Synchronization properties of continuous phase modulation," *GLOBECOM 1982*, Miami, FL

[39] T. Aulin and C.-E. Sundberg, "Partially coherent detection of digital full response continuous phase modulated signals," *IEEE Trans. on Communications*, vol. COM-30, No. 5, pp. 1096-1117, May 1982

[40] S.Benedetto, E.Biglieri, and V.Castellani, *Digital Transmission Theory.* Englewood Cliffs, NJ: Prentice-Hall Publ. Co, 1987

[41] G. C. Clark, Jr., and J. B. Cain, *Error-Correction Coding for Digital Communications.* New York: Plenum Press, 1981

[42] A. N. D'Andrea, U. Mengali, and R. Reggiannini, "Carrier phase and clock recovery for continuous phase modulated signals," *IEEE Trans. Commun.*, Vol. COM-35, No. 10, October 1987

[43] D.Divsalar and M.K.Simon, "Trellis code modulation for 4800-9600 bits/s transmission over a fading mobile satellite channel," *IEEE Journal on Selected Areas in Communications*, vol.SAC-5, No.2, pp.162-175, February 1987

[44] D. Divsalar and M. K. Simon, "The design of trellis codes for fading channels: Performance criteria," *IEEE Trans. on Communications*, vol. 36, No. 9, pp. 1004-1012, and "The design of trellis codes for fading channels: Set partitioning for optimum code design," *IEEE Trans. on Communications*, vol. 36, No. 9, pp. 1013-1021

[45] D. Divsalar, M. K. Simon, and T. Jedrey, "Trellis coding techniques for mobile communications," *MILCOM'88*, San Diego, CA, October 23-26, 1988

[46] G.Lindell and C.-E.Sundberg, "Multilevel continuous phase modulation with high rate convolutional codes," *GLOBECOM'83*, San Diego, CA, Nov. 1983

[47] J. L. Massey, "Coding and modulation in digital communications," *Proc. Int. Zürich Seminar on Digital Communications*, 1974, pp. E2(1)-E2(4)

[48] W. P. Osborne and M. B. Luntz,"Coherent and noncoherent detection of CPFSK," *IEEE Trans. on Communications*, vol. COM-22, No. 8, pp. 1023-1036, August 1974

[49] S.V.Pizzi and S.G.Wilson, "Convolutional coding combined with continuous phase modulation," *IEEE Trans. on Communications*, vol.COM-33, No.1, pp.20-29, Jan. 1965

[50] W. Rafferty (ed.), *Proceeding of the Mobile Satellite Conference*. JPL Publication 88-9, Jet Propulsion Laboratory, California Institute of Technology, Pasadena, CA, May 1988

[51] B. Rimoldi, "A decomposition approach to CPM," *IEEE Trans. on Inform. Theory*, Vol. 34, No. 2, pp.260-270, March 1988

[52] A. Svensson, T. Aulin, and C.-E. Sundberg, "Symbol error probability behaviour for continuous phase modulation with partially coherent detection," *A.E.Ü.*, vol. 40, pp. 37-45, 1986

[53] G. Ungerboeck, "Channel coding with multilevel/phase signals," *IEEE Trans. Inform. Th.*, vol. IT-28, pp. 56-67, January 1982

[54] A.J.Viterbi and A.M.Viterbi, "Nonlinear estimation of PSK-modulated carrier phase with application to burst digital transmission," *IEEE Trans. on Inform. Theory*, vol.IT-29, No.4, pp.543-551, July 1983

[55] J.B.Anderson, T.Aulin, and C.-E.Sundberg, *Digital Phase Modulation*. New York: Plenum Publ. Co., 1986

[56] T.Aulin and C.-E. Sundberg, "Calculating digital FM spectra by means of autocorrelation," *IEEE Trans. on Communications*, Vol.COM-30, No.5, pp.1199-1208, May 1982

[57] T.Aulin and C.-E.Sundberg, "Synchronization properties of continuous phase modulation," *ICC'82*, Philadelphia, PA, June 1982

[58] S.Benedetto, E.Biglieri, and V.Castellani, *Digital Transmission Theory.* Englewood Cliffs, NJ: Prentice-Hall Publ. Co, 1987

[59] E.Biglieri, "High-level modulation and coding for nonlinear satellite channels," *IEEE Trans. Commun.*, vol. COM-32, No.5, pp.616-626, May 1984

[60] E.Biglieri, "Ungerboeck codes do not shape the signal power spectrum," *IEEE Trans. Inform. Th.*, vol. IT-32, July 1986

[61] A.P.Clark, "Digital modems for land mobile radio," *IEE Proceedings,* Vol.132, pt. F, No. 5, pp.348-362, August 1985

[62] A.N.D'Andrea, U.Mengali, and R.Reggiannini, "Carrier phase and clock recovery for continuous phase modulated signals," *IEEE Trans. Commun.,* Vol.COM-35, No.10, pp.1095-1101, October 1987

[63] R. de Buda, "Coherent demodulation of frequency shift keying with low deviation ratio," *IEEE Trans. Commun.*, Vool.COM-20, pp.429-435, June 1972

[64] D.Divsalar and M.K.Simon, "Trellis code modulation for 4800-9600 bits/s transmission over a fading mobile satellite channel," *IEEE Journal on Selected Areas in Communications,* vol.SAC-5, No.2, pp.162-175, February 1987

[65] G.D.Forney, Jr., *et al.*, "Efficient modulation for band-limited channels," *IEEE Journal on Selected Areas in Communications,* vol. SAC-2, No.5, pp. 632-647, September 1984

[66] R.G.Gallager, *Information Theory and Reliable Communication.* New York: Wiley, 1968

[67] P.Ho and P.J.McLane, "Spectrum, distance and receiver complexity of encoded continuous phase modulation," *IEEE Trans. Inform. Theory,* to be published

[68] G.Lindell and C.-E.Sundberg, "Multilevel continuous phase modulation with high rate convolutional codes," *GLOBECOM'83,* San Diego, CA, Nov. 1983

[69] G.Lindell and C.-E.W.Sundberg, "Power and bandwidth efficient coded modulation schemes with constant amplitude," *Archiv für Elektronik*

and Übertragungstechnik, Band 39, Heft 1, pp.45-56, January/February 1985

[70] G.Lindell, C.-E.K.Sundberg and T.Aulin, "Minimum Euclidean distance for the best combination of short rate 1/2 convolutional codes and CPFSK modulation," *IEEE Trans. Inform. Theory,* Vol.IT-30, pp.509-520, May 1984

[71] C.Loo, "A statistical model for a land mobile satellite link," *ICC'84,* Amsterdam, The Netherlands, 1984

[72] C.Loo, "Measurements and models of a mobile-satellite link with applications," *GLOBECOM'85,* December 1985, New Orleans, LA

[73] C.Loo, "A statistical model for a land mobile satellite link," *IEEE Trans. Vehicular Technology,* Vol.VT-34, pp.122-127, August 1985

[74] P.J.McLane, P.H.Wittke, P.K.-M.Ho, and C.Loo, "PSK and DPSK trellis codes for fast fading, shadowed mobile satellite communication channels," *ICC'87,* Seattle, Washington, 1987

[75] S.V.Pizzi and S.G.Wilson, "Convolutional coding combined with continuous phase modulation," *IEEE Trans. on Communications,* vol.COM-33, No.1, Jan. 1965, pp.20-29

[76] B.Rimoldi, "Design of coded CPFSK modulation systems for bandwidth and energy efficiency," *IEEE Trans. on Commun.,* 1989, to be published

[77] R.C.P.Saxena, *Optimum Encoding in Finite State Coded Modulation,* Report TR83-2, Department of Electrical, Computer and System Engineering, Rensselaer Polytechnic Institute, Troy, N.Y., 1983

[78] M.K.Simon and D.Divsalar, "Open loop frequency synchronization of MDPSK with Doppler," *ICC'87,* Seattle, WA, June 7-10, 1987

[79] M.K.Simon and D.Divsalar, "The performance of trellis code multilevel DPSK on a fading mobile satellite channel," *ICC'87,* Seattle, Washington, June 1987

[80] G. Ungerboeck, "Channel coding with multilevel/phase signals," *IEEE Trans. Inform. Th.,* vol. IT-28, pp. 56-67, January 1982

[81] G.Ungerboeck, "Trellis-coded modulation with redundant signal sets – Part I: Introduction," *IEEE Communications Magazine,* vol.25, No.2, pp.5-11, February 1987. "Trellis-coded modulation with redundant signal sets – Part II:State of the art," *Ibidem*, pp.12-21

[82] A.J.Viterbi and A.M.Viterbi, "Nonlinear estimation of PSK-modulated carrier phase with application to burst digital transmission," *IEEE Trans. on Inform. Theory,* vol.IT-29, No.4, pp.543-551, July 1983

[83] S.G.Wilson, "Bandwidth-efficient modulation and coding: A survey of recent results," *ICC'86*

[84] S.G.Wilson and Y.S.Leung, "Trellis-coded phase modulation on Rayleigh channels," *ICC'87,* Seattle, Washington, 1987

[85] S.G. Wilson, H.A. Sleeper, P.J. Schottler, and M.T. Lyons, "Rate 3/4 convolutional coding of 16-PSK: Code design and performance study," *IEEE Trans. Commun.,* vol.COM-32, pp.1308-1315, 1984

Appendix A

The simulation package

A.1 Structure of the simulation package

The computer simulation package developed for the analysis and design of the trellis-encoded CPM scheme includes the following subpackages:

1. Input/Output blocks. They input the various parameters affecting system performance and store them into an assigned file. They also store the output quantities and store them into files for graphical presentation.

2. TCM encoder and Viterbi decoder.

3. CPM modulator and demodulator. These blocks generate different pulse shapes according to the input parameters, and demodulate the received signal by using a differential or non-coherent demodulator.

4. Channel simulators. Addition of Gaussian noise and fading with or without shadowing.

5. Filter simulators. Modules are available to simulate the following filter families: 1REC, LRC, Gaussian, Chebychev, Butterworth, and LSRC. Gaussian and LSRC use the frequency-domain exact form, the other filter models are based on approximations.

6. Simulator of the Doppler-frequency shift estimation and removal.

7. Simulator of the timing recovery circuit.

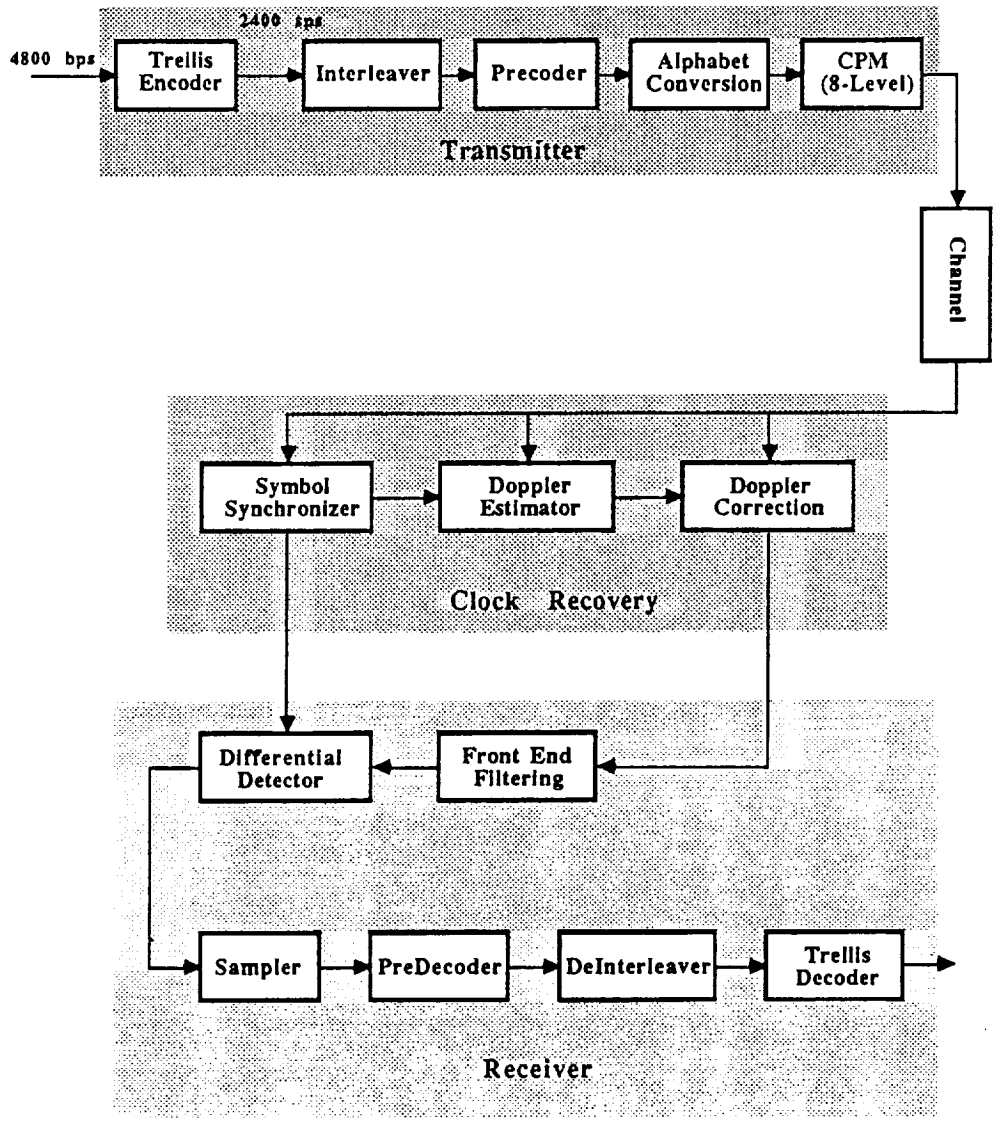

Figure A.1: Flow chart of the simulation program.

Fig. A.1 shows the flow chart of the package as used to simulate the behavior of the TCM-encoded CPM system. The number of CPM symbol levels generated by the transmitter may be 2, 4, ar 8. The binary and quaternary case have been validated by comparing our simulation results with results previously published. The pulse shapes chosen were LREC, LRC, and GMSK. The binary cases considered are without precoding, and the samples at the output of the differential detector were taken at integer multiples of signal symbol time, i.e., $t_n = nT_s$. For for quaternary GMSK precoding was used on the source data. The precoding rules are described in the following:

Transmitter:	output of data generator	$b_n \in \{0,1,2,3\}$
	output of precoder	$a_n = b_n - a_{n-1} \mod 4$
		$a_n \in \{0,1,2,3\}$
	input of CPM modulator	$c_n = 2a_n - 3$
		$c_n \in \{\pm 1, \pm 3\}$
Receiver:	detector output	$y_n = c_n + c_{n-1} = 2(a_n + a_{n-1}) - 6$
		$= 2[(b_n - a_{n-1} \bmod 4) + a_{n-1}] - 6$
		$\in \{0, \pm 2, \pm 4, \pm 6\}$

The decoding rules are:

$$\begin{aligned} y_n = -6 \text{ or } 2 &\implies b_n = 0 \\ y_n = -4 \text{ or } 4 &\implies b_n = 1 \\ y_n = -2 \text{ or } 6 &\implies b_n = 2 \\ y_n = 0 &\implies b_n = 3 \end{aligned}$$

The relations among b_n, a_{n-1}, and y_n are summarized in Table A.1.

A.1.1 Multipath fading simulator

In our description of the channel used in this Report, we have listed three fading models, namely, the Rayleigh, Rice, and Loo models. Here we describe the structure of the software written to simulate these channel models, and provide their validation based on simulation results.

The commonly accepted signal propagation model for satellite-based mobile communication is based upon consideration of three signal paths from the satellite to the mobile, namely, a *line-of-sight* or *direct* path, a *specular* path, and a *scatter path* or *multipath*. The specular and direct path are combined to form the coherent component, while the diffuse path forms the noncoherent component.

b_n	a_{n-1}	y_n
0	0	-6
0	1	2
0	2	2
0	3	2
1	0	-4
1	1	-4
1	2	4
1	3	4
2	0	-2
2	1	-2
2	2	-2
2	3	6
3	0	0
3	1	0
3	2	0
3	3	0

Table A.1: Precoding table for quaternary CPM.

The latter component is Gaussian, while the coherent component, in terms of its complex envelope, is either a constant (Rayleigh model, Rice model) or is subjected to a log-normal transformation (Loo model). The log-normal transformation represents the effects of foliage attenuation, and is usually referred to as *shadowing*.

The sum of a constant-envelope signal and a Gaussian process has an envelope modeled by a Rician probability density function. In the absence of the constant-envelope component, the probability density function is of the Rayleigh type. The functional block diagram for the Rayleigh fading simulator is shown in Fig. A.2. The Gaussian noise source generates a sequence of white Gaussian noise samples. These samples pass trough a shaping filter, and modulate the in-phase and quadrature parts of a radio-frequency carrier. The theoretical model for the shaping filter is depicted in Fig. A.3, and its frequency response can be expressed in the form

$$H(f) = \begin{cases} A\left[1-(f/f_0)^2\right]^{-1/4} & |f| \le f_d \\ 0 & |f| > f_d \end{cases}$$

where $f_d = v/\lambda$ is the Doppler frequency spread corresponding to a vehicle speed v when the carrier wavelength is λ, and A is a gain constant. The probability density function of the fading sample is

$$f_\alpha(a) = 2ae^{-a^2}, \quad a \ge 0.$$

The phase of the Rayleigh sample has a uniform distribution between $-\pi$ and π.

The functional block diagram for the Rician fading simulator is shown in Fig. A.4. The upper arm is essentially the same as for the Rayleigh model simulator. The lower arm generates a Doppler-shifted signal component, which represents the direct path propagation. The probability density function for the Rician envelope is

$$f_\alpha(a) = 2a(1+K)e^{-K-a^2(1+K)} I_0\left(2a\sqrt{K(1+K)}\right), \quad a \ge 0,$$

where K is the ratio between the power in the direct path and the power in the multipath signal. The phase probability density function of the Rician fading samples is given by

$$f_\Theta(\theta) = \frac{e^{-K}}{2\pi} + \frac{1}{2\sqrt{\pi}}\sqrt{K}\cos\theta e^{-K\sin^2\theta}[2 - \mathrm{erfc}(\sqrt{K}\cos\theta)].$$

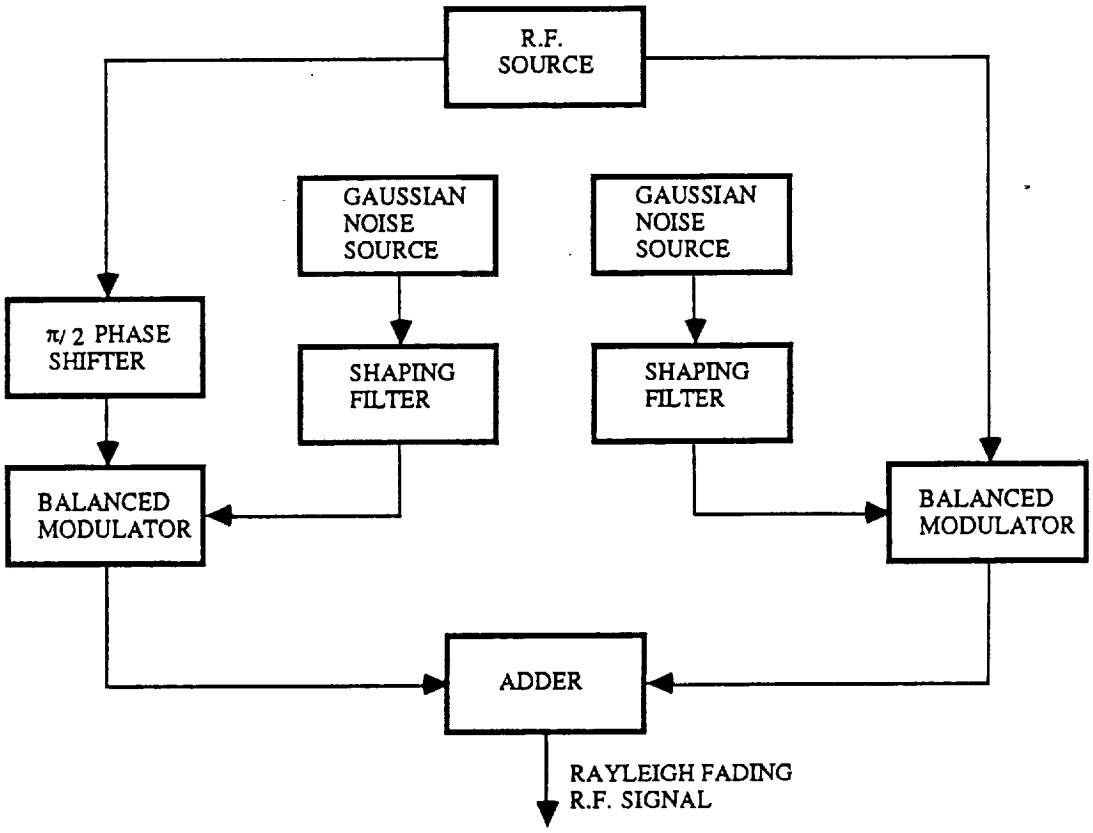

Figure A.2: Simulator for the Rayleigh model.

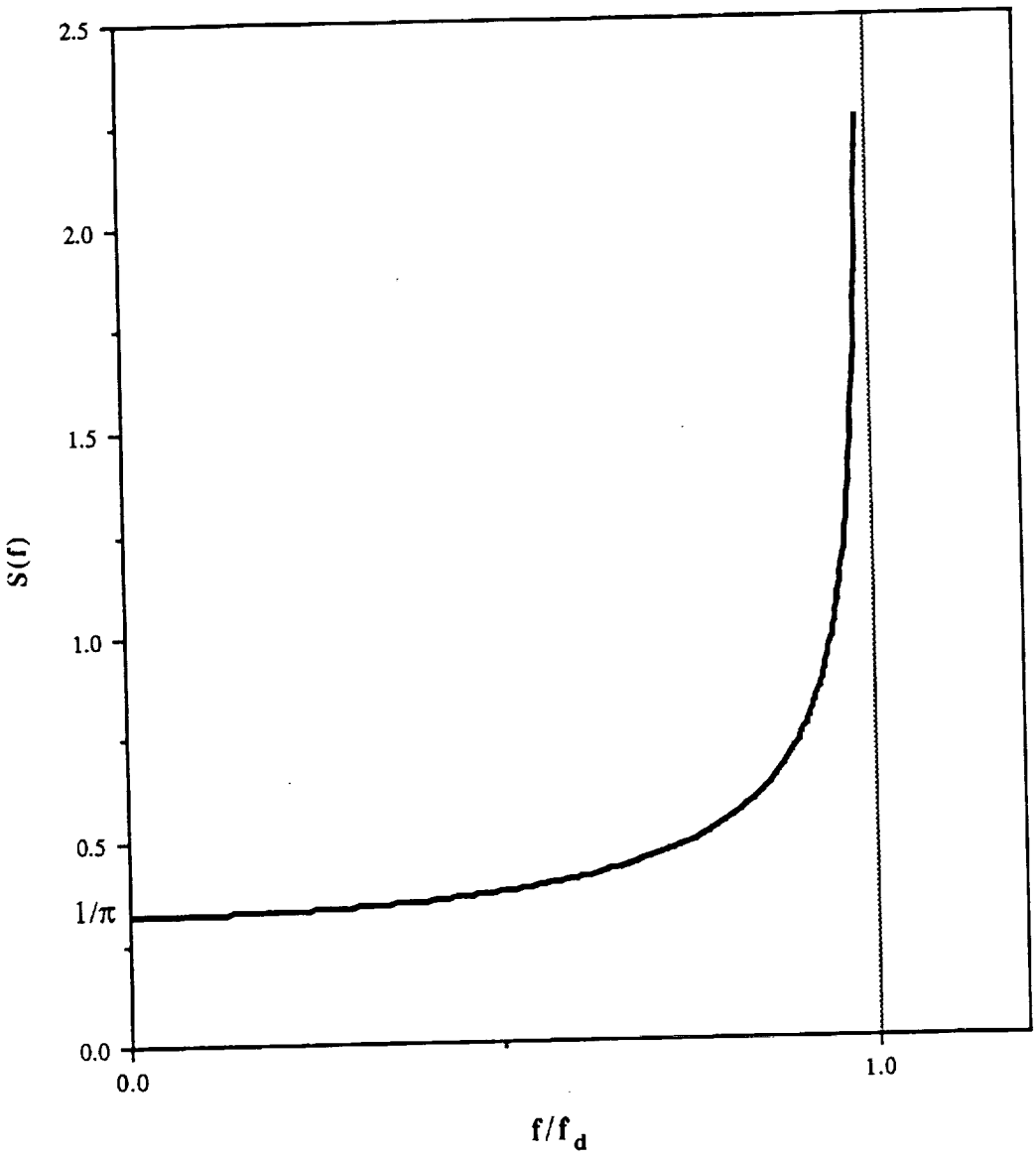

Figure A.3: Theoretical model for the shaping filter (Rayleigh model).

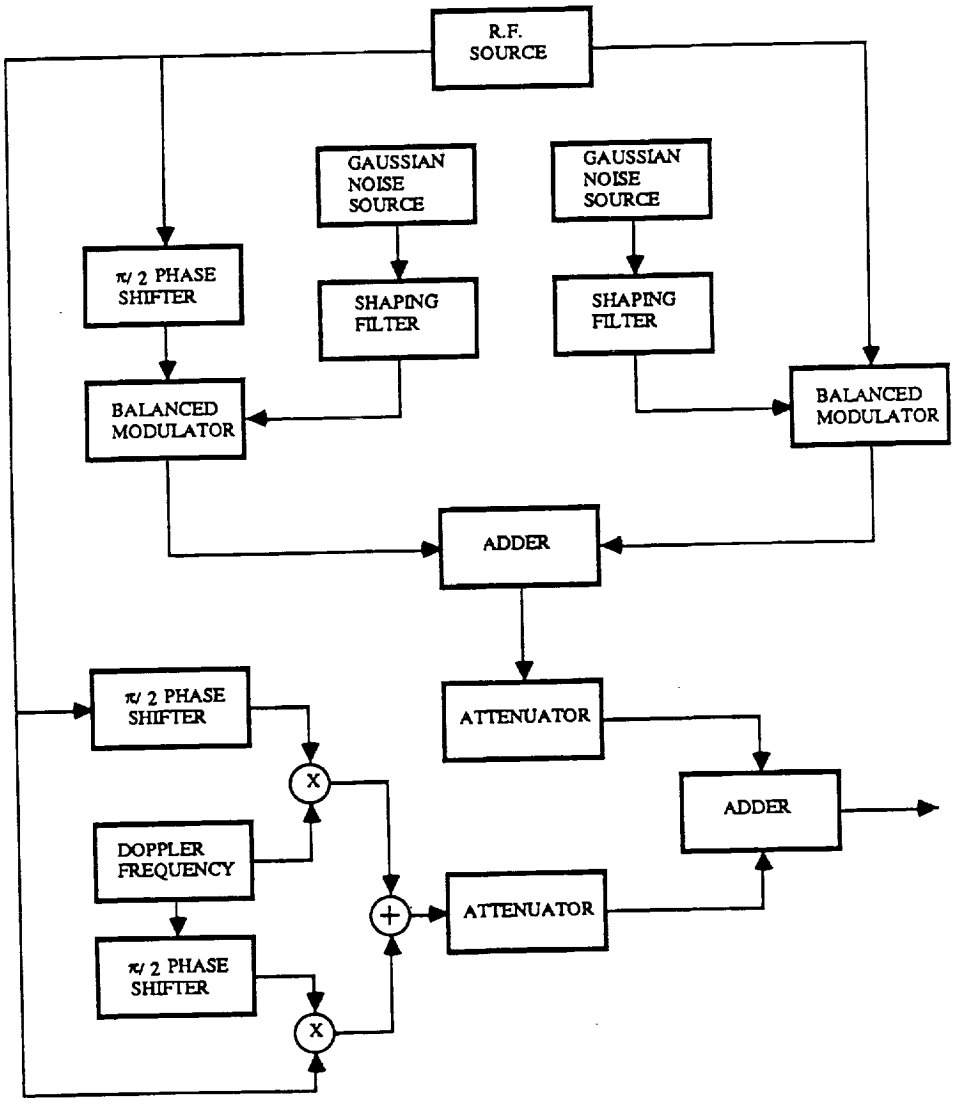

Figure A.4: Simulator for the Rice model.

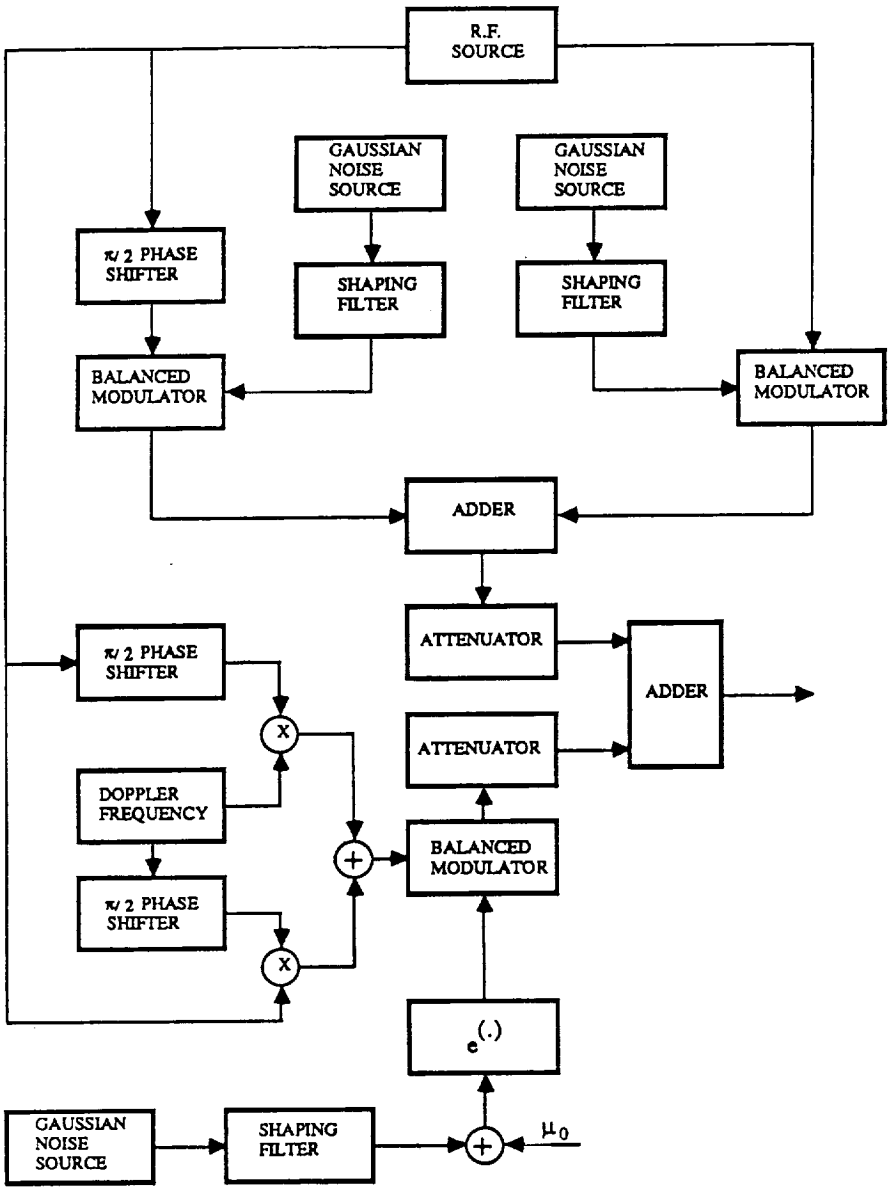

Figure A.5: Simulator for the Loo model.

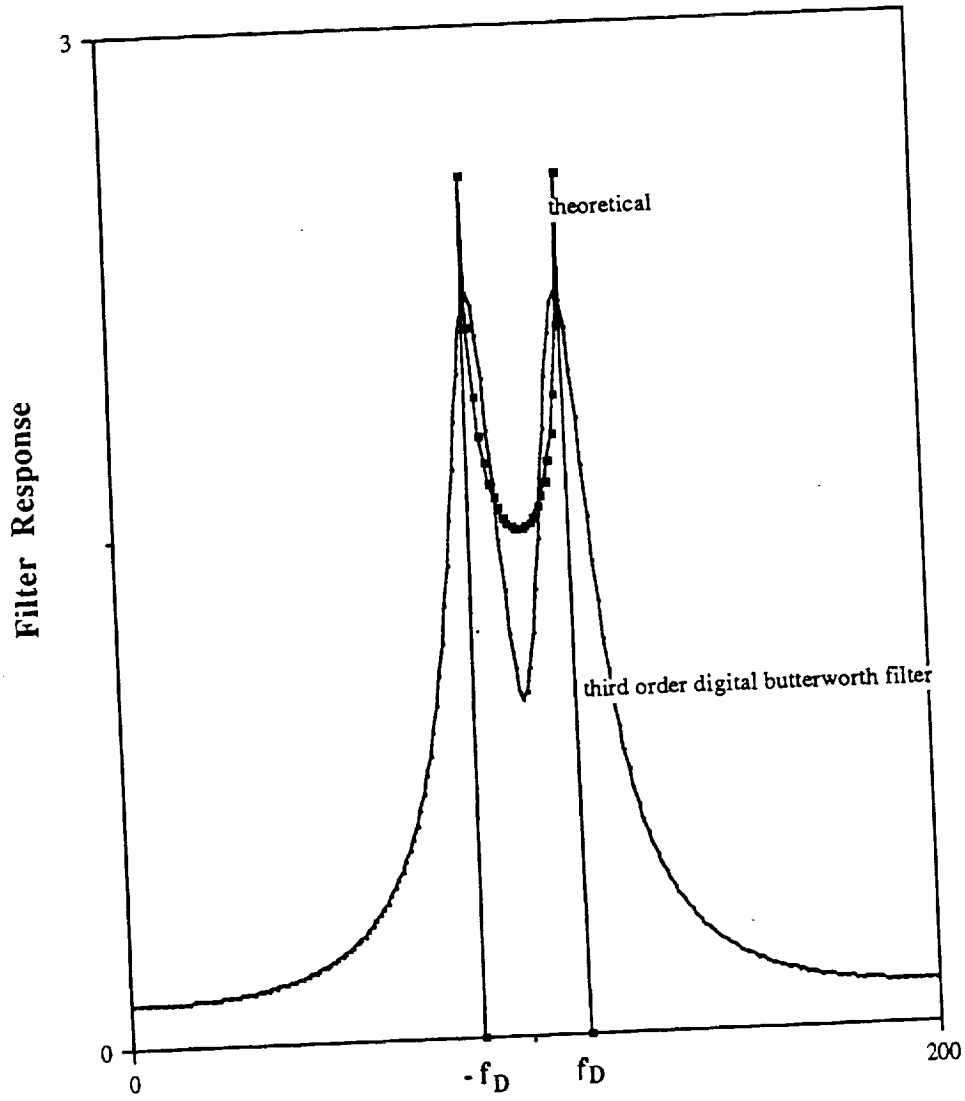

Figure A.6: Frequency response of the shaping filter.

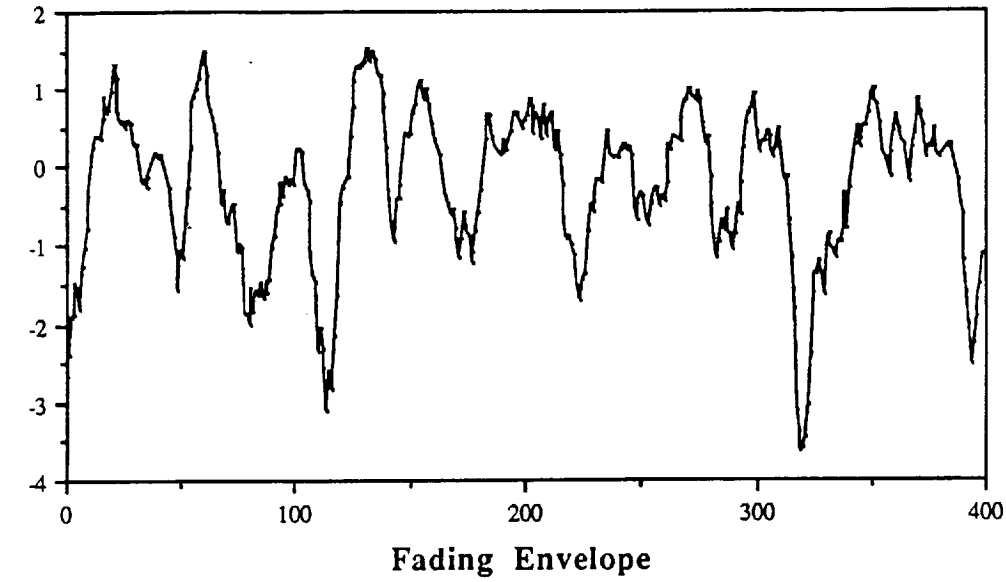

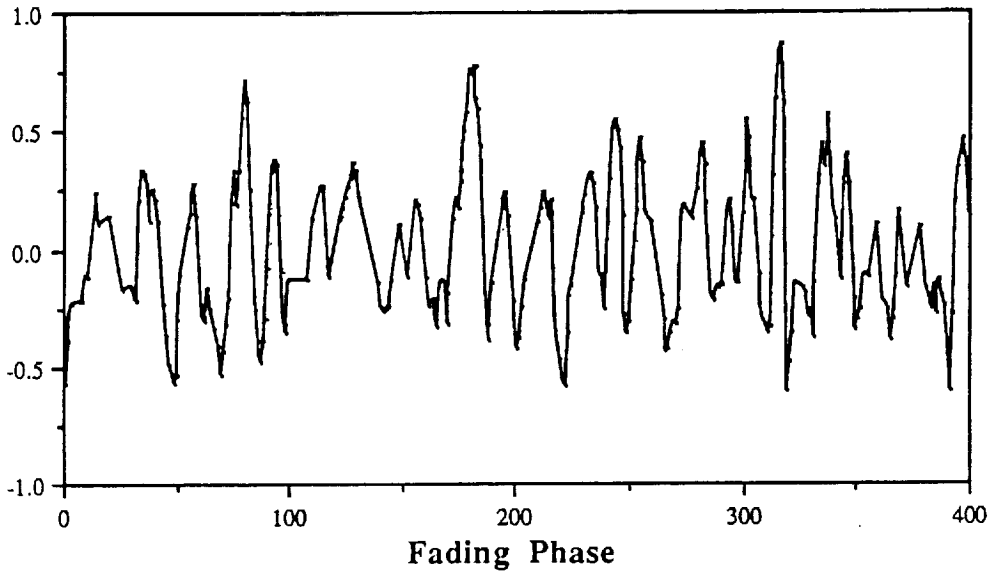

Figure A.7: Fading samples for vehicle speed 20 MPH.

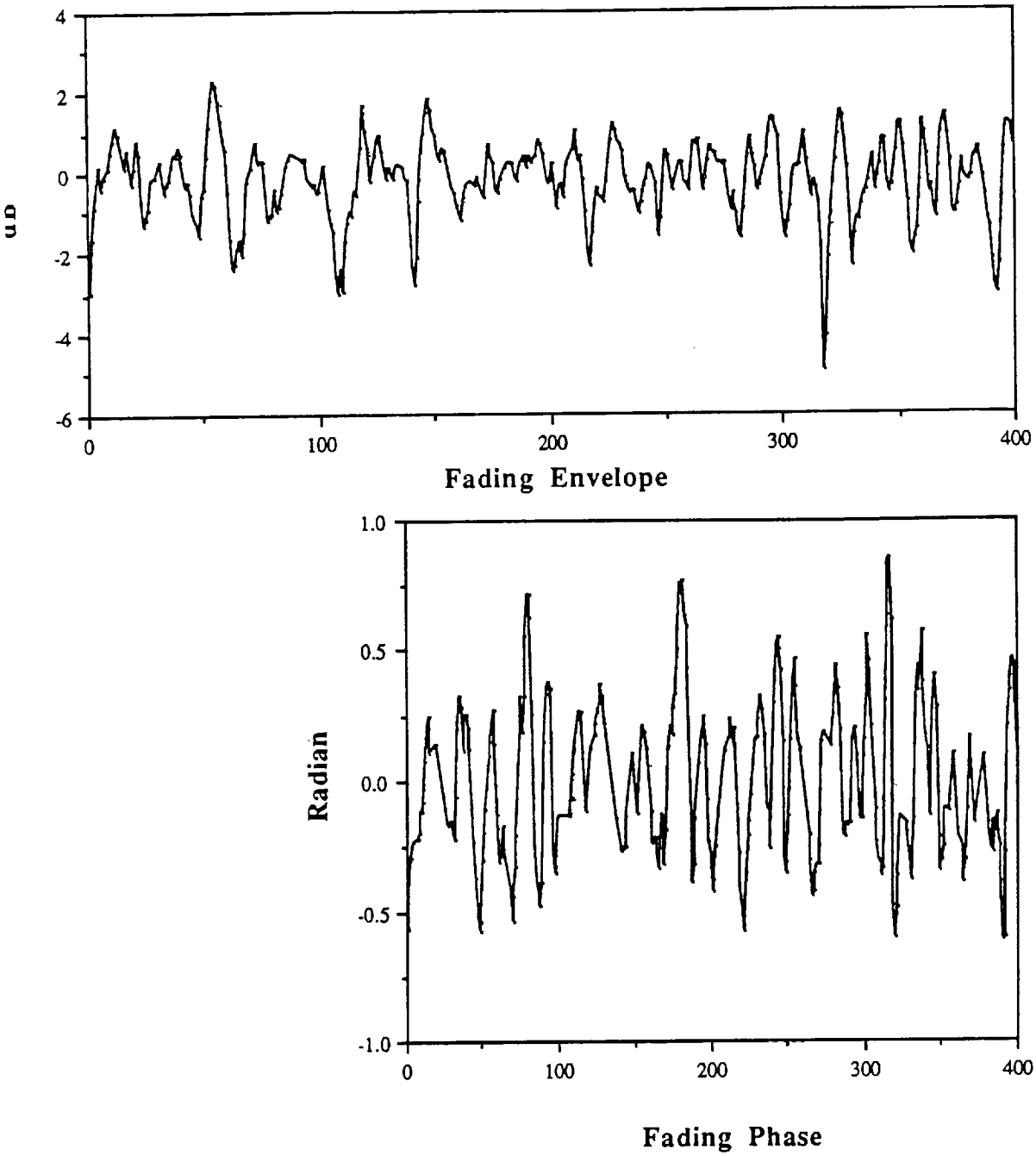

Figure A.8: Fading samples for vehicle speed 55 MPH.

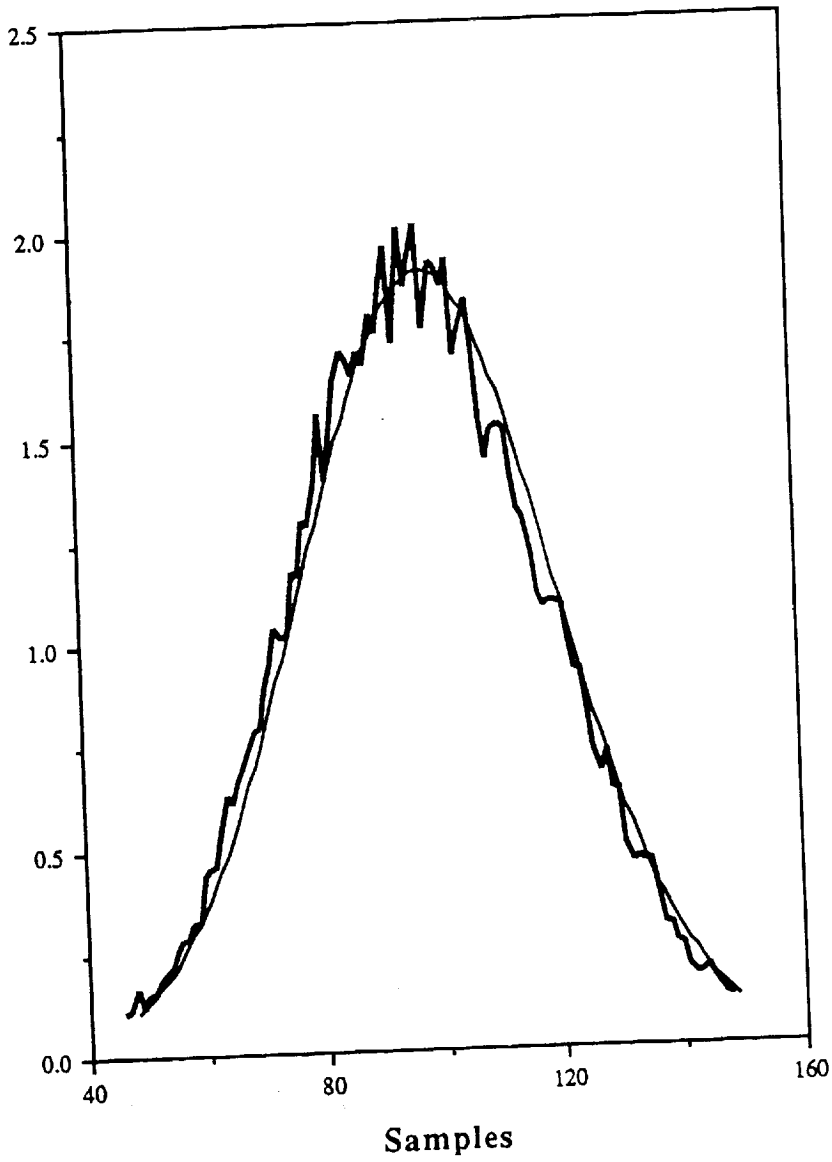

Figure A.9: Histogram of the envelope of Rician samples, $K = 10$.

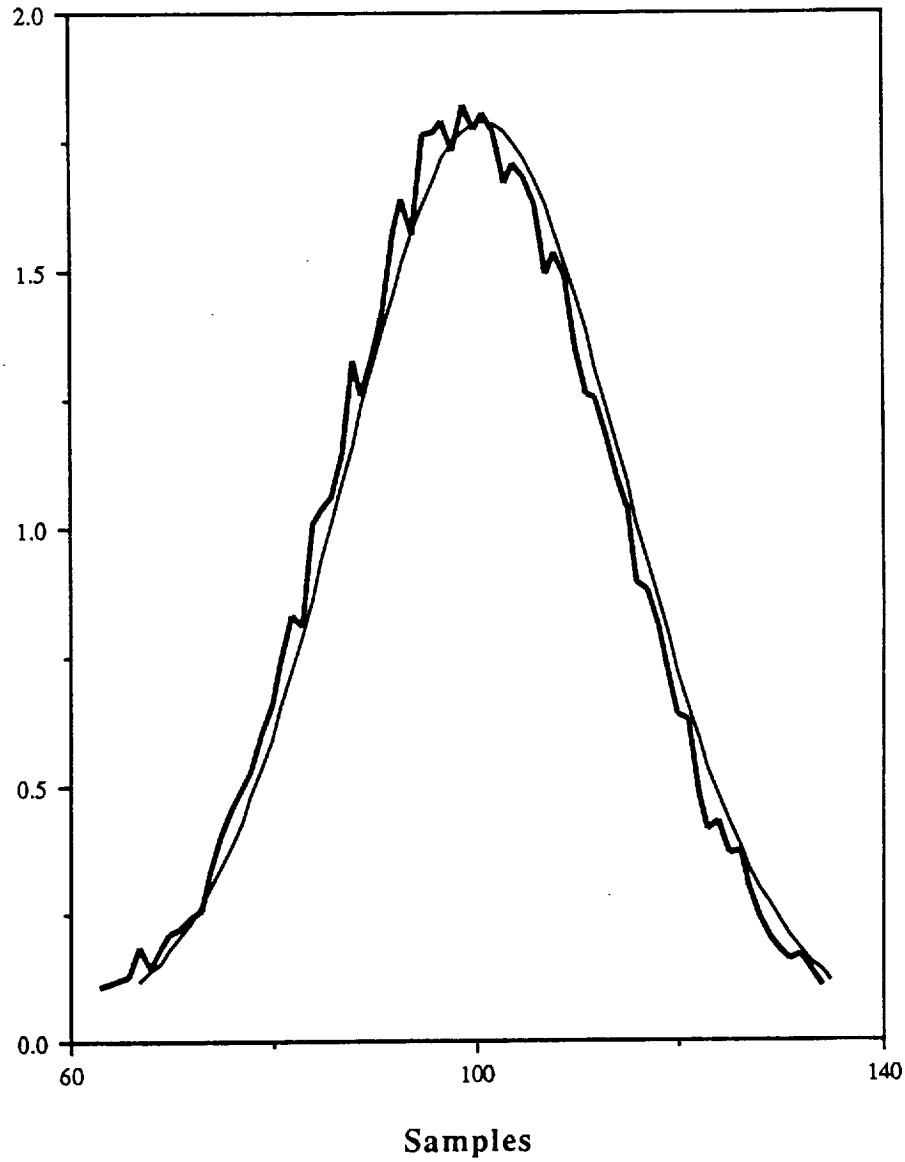

Figure A.10: Histogram of the phase of Rician samples, $K = 10$.

The block diagram of the shadowed Rician fading simulator is depicted in Fig. A.5. The simulator is similar to the Rice model, except for the lower arm signal path, which is modeled by a log-normal shadowing component. The probability density function of this shadowing component is

$$f_Y(y) = \frac{1}{\sqrt{2\pi}\sigma_0 y} \exp\left\{\frac{(\ln y - \mu_0)^2}{2\sigma_0^2}\right\}, \quad 0 \le y < \infty.$$

It is well known that a random process $y(t)$ whose probability density function is log-normal can be represented in the form

$$y(t) = \exp\{X(t)\},$$

where $X(t)$ is Gaussian, with mean μ_0 and variance σ_0^2. The bandwidth of the shaping filter for the lognormal component is about 0.01 narrower that that of the Rayleigh component.

Validation

The baseband equivalent representation of the faded samples is used in the computer simulations. The baseband equivalent signal samples can be obtained by forming the complex baseband signal. The shaping filter for the Rayleigh component is approximated by a third-order digital Butterworth filter with bandwidth f_d. The magnitude of the frequency response is depicted in Fig. A.6. The theoretical model for the frequency response of the third-order digital Butterworth filter has a peak at the frequency f_d. However, the out-of-band response of the Butterworth filter does not decrease sharply. This is due to the low filter order, and causes some higher-frequency noise components to pass through the filter.

The fading samples generated by using the third-order digital Butterworth filter are shown in Fig. A.7 and Fig. A.8 for a vehicle velocity of 20 MPH and 55 MPH, respectively. The carrier frequency is 1.5 GHz and the elevation angle is 90°. It can be seen that the fading samples for the lower speed vary much slower than those for higher speed. In both cases, as it can be observed, there is a high-frequency wiggle along the slower varying fading trajectory. This is due to the fact that the out-of-band attenuation of the third-order Butterworth filter is not large enough, so that the high-frequency noise component still passes through the filter and creates the wiggle. The high-frequency wiggle will produce some extra phase jitter in the differential detector, which makes the simulated system performance slightly worse than that obtained with the theoretical fading model.

To validate the fading simulator, the statistical frequency of a set of fading samples is plotted against the theoretical density function. Fig. A.9 shows one of these plots for the envelope of the samples in a Rician model with $K = 10$. Similarly, Fig. A.10 shows the phase of the fading samples. It can be seen that in both cases the histogram agrees very well with the theoretical probability density function.

A.1.2 Simulation of the receiver

In this section we describe in some detail the general structure of the receiver simulation subpackage.

In particular:

- The received signal may be a binary, quaternary, or octonary CPM signal.
- The front-end filter may have a Gaussian, LSRC, or RC response.
- The differential detector performs the function $x(t)\cdot x^*(t-T_s)$, where as usual T_s denotes the symbol interval and $*$ denotes complex conjugate.
- The post-detection filter may be Gaussian, LSRC, or RC.
- The "phase measurement" block performs the following operation:

$$\phi(t) = \tan^{-1} \frac{\mathbf{I}[y(t+\Delta)]}{\mathbf{R}[y(t+\Delta)]},$$

where, for $Q = 2M - 1$,

$$\Delta = \begin{cases} T_s/2 & \text{for full response,} \\ 0 & \text{for partial response,} \end{cases}$$

while for $Q = M$ we have

$$\Delta = \begin{cases} 0/2 & \text{for full response,} \\ T_s/2 & \text{for partial response,} \end{cases}$$

A.2 Eye patterns and their interpretation

In this section we first briefly describe the significance and the interpretation of the eye patterns of the signals obtained at the output of the differential

detector. Then we shall show a number of examples of eye patterns as derived by using our simulation package. The eye pattern, besides being helpful in qualitative interpretation of the channel performance, will help us in the selection of the detection time for each symbol interval.

Symbol precoding must be used not only in the case of partial-response CPM, but also for full-response scheme when the pulse is only approximately contained in a T_s-second interval (e.g., GMSK pulses with truncation length greater than or equal to 2). The eye diagram will be useful to verify this, and to validate the simulation results by verifying their consistency with the results expected from the analysis.

If we let the transmitted phase of a CPM signal be written in the form

$$\theta(t, \mathbf{a}) = 2\pi h \sum_{n=-\infty}^{\infty} a_n q(t - nT_s), \tag{A.1}$$

where $a_n \in \{0, \pm 1, \pm 3, \cdots, \pm(M-1)\}$, at the output of the differential detector, for any time t, we can get the phase difference between $\theta(t, \mathbf{a})$ and $\theta(t - T_s, \mathbf{a})$:

$$\Delta\theta(t, \mathbf{a}) = 2\pi h \sum_{n=-\infty}^{\infty} a_n q(t - nT_s) - 2\pi h \sum_{n=-\infty}^{\infty} a_n q(t - (n+1)T_s). \tag{A.2}$$

The eye diagram can be generated by slicing the signal $\Delta\theta$ in segments of duration NT_s seconds each, and superimposing the various slices in the interval $(0, NT_s)$.

Let us take, for illustration's sake, $N = 1$, and consider a partial-response CPM with pulse length L symbol intervals. Eq. (A.2) can be simplified by rewriting it in the form

$$\Delta\theta(t, \mathbf{a}) = 2\pi h \sum_{n=-k-L+1}^{k} (a_n - a_{n-1}) q(t - nT_s) + \pi h a_{k-L}, \tag{A.3}$$

where

$$kT_s \le t \le (k+1)T_s.$$

The above equation is the analytical description of the eye diagram in the interval $(kT_s, (k+1)T_s)$. If we consider a full-response CPM scheme, i.e., if we assume $L = 1$, (A.3) specializes to

$$\Delta\theta(t, \mathbf{a}) = 2\pi h(a_k - a_{k-1}) q(t - kT_s) + \pi h a_{k-1}, \quad kT_s \le t \le (k+1)T_s. \tag{A.4}$$

From the above equation, wa can observe that the eye diagram should reflect the shape of the $q(\cdot)$ function.

Example 1.

For a binary full-response CPFSK scheme, i.e.,

$$q(t) = \begin{cases} 0 & t \leq 0 \\ t/2T_s & 0 \leq t \leq T_s \\ 1/2 & t \geq T_s \end{cases},$$

we have

$$\Delta\theta(t, \mathbf{a}) = \pi h(a_k - a_{k-1})\frac{t - kT_s}{T_s} + \pi h a_{k-1}, \quad kT_s \leq t \leq (k+1)T_s. \quad \text{(A.5)}$$

The corresponding eye diagram is shown in Fig. A.11. □

Example 2.

Consider now a quaternary CPM scheme with $h = 0.25$, and a GMSK pulse with truncation length $L_T = 1$. We have for this case

$$\Delta\theta(t, \mathbf{a}) = 2\pi h(a_k - a_{k-1})q_{\text{GMSK}}(t - kT_s) + \pi h a_{k-1}, \quad kT_s \leq t \leq (k+1)T_s. \quad \text{(A.6)}$$

There are 4 possible initial states, i.e., $\{-3\pi, -\pi h, \pi h, 3\pi h\}$, and four transitions stemming from each state. For any given state, the slope of the transition, i.e., the coefficient of the $q(\cdot)$ function, will depend on the present state $a_{k-1}\pi h$ and on the input symbol a_k. For example, the transitions stemming from state $-3\pi h$ are

$$0, \quad 4\pi h q(t - kT_s), \quad ; 6\pi h q(t - kT_s), \quad ; 8\pi h q(t - kT_s).$$

The corresponding eye diagram is shown in Fig. A.12. □

Example 3.

Consider a partial-response binary CPM scheme with rectangular pulses, and $L = 2$. We have in particular

$$q(t) = \begin{cases} 0 & t \leq 0 \\ t/2LT_s & 0 \leq t \leq LT_s \\ 1/2 & t \geq LT_s \end{cases},$$

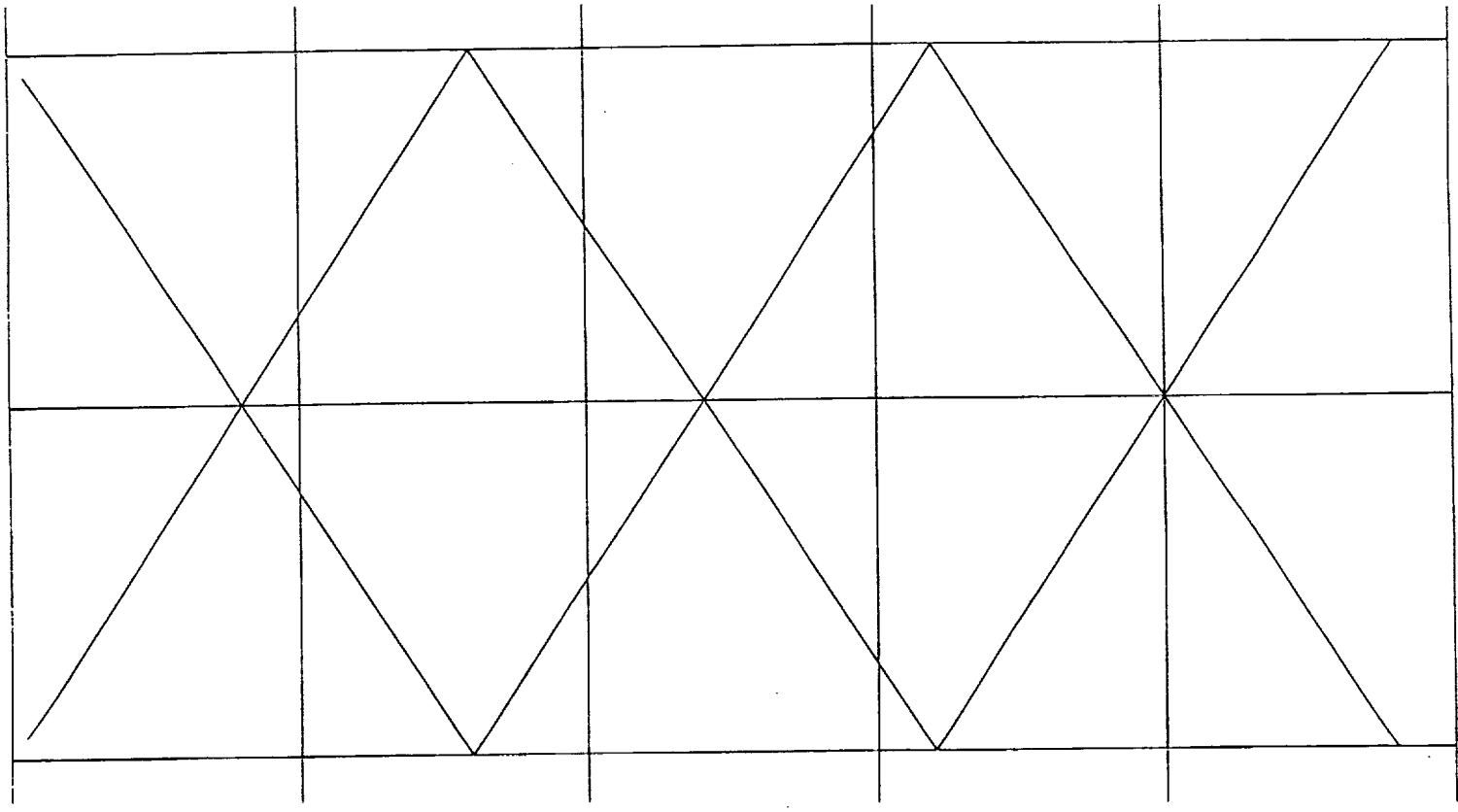

Figure A.11: Eye diagram of binary CPFSK.

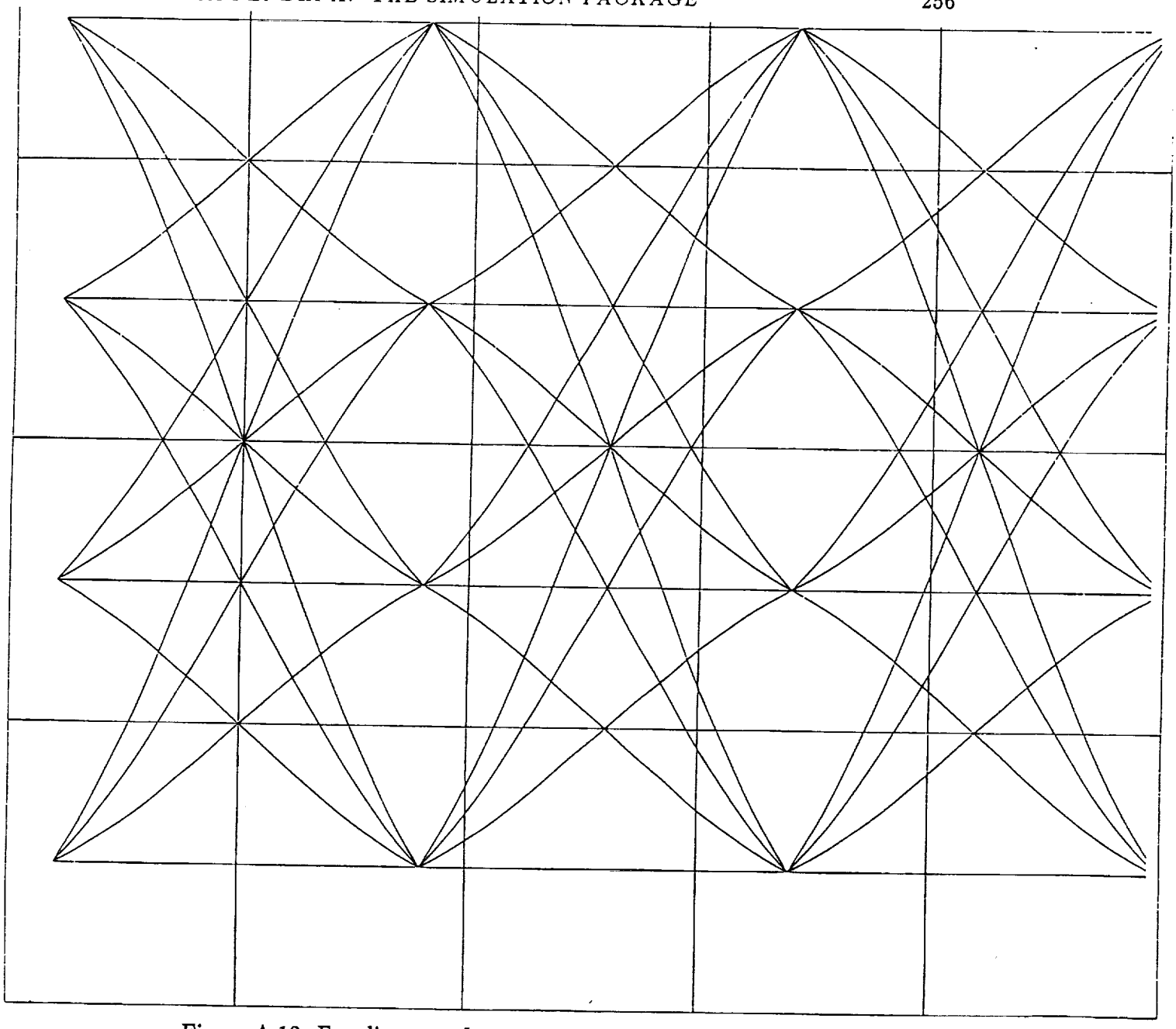

Figure A.12: Eye diagram of quaternary CPM with GMSK pulse, $h = 0.25$, $L_T = 1$.

so that

$$\begin{aligned}\Delta\theta(t,\mathbf{a}) &= 2\pi h(a_k - a_{k-1})\frac{t-kT}{4T_s} \\ &\quad +2\pi h(a_{k-1} - a_{k-2})\frac{t-kT}{4T_s} \\ &\quad +\pi h a_{k-2}.\end{aligned}$$

The corresponding eye diagram is shown in Fig. A.13. □

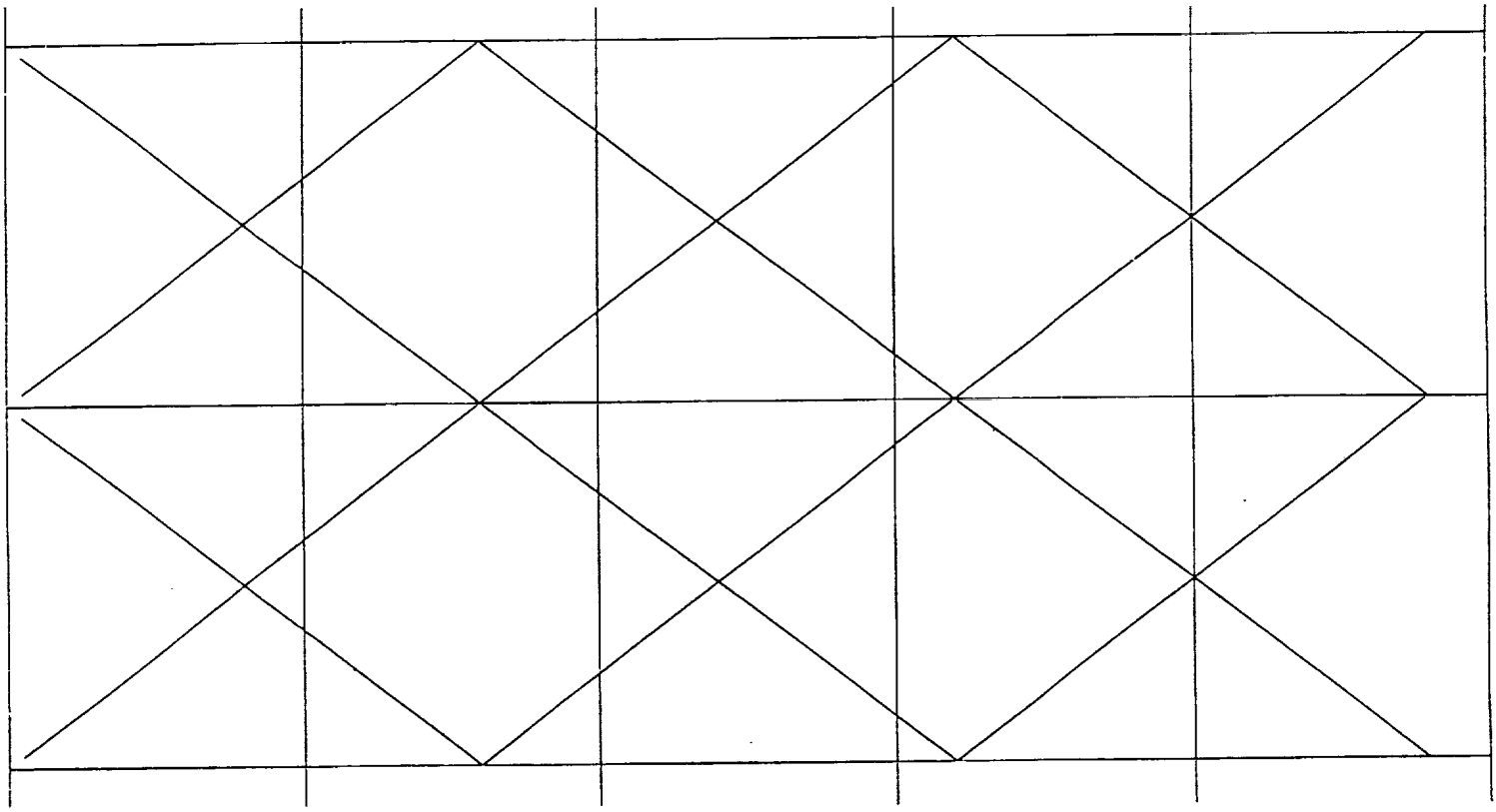

Figure A.13: Eye diagram of binary partial-response CPM with rectangular pulse.

Appendix B

Hardware Implementation

B.1 Introduction

This appendix describes the work done on the firmware implementation of the 4800 bps trellis coded CPM modem. The parameters associated with this hardware have been determined by the appropriate simulations and analysis. The overall functional block diagrams, for the full response and the partial response, are shown in Fig. B.1 and Fig. B.2 where the transmitter includes the following modules:

- Multiplexer.
- Trellis encoder.
- Interleaver.
- Precoder(not used in the full response due to performance degradation.)
- CPM modulator.
- D/A converter.
- Lowpass filter.
- IF frequency converter.

Accordingly, the receiver includes:

- Bandpass filters.

- Clock recovery.
- Differential detector.
- Deinterleaver.
- Trellis decoder.

The end-to-end system requires an extensive digital signal processing, mathematical calculations, and logical operations. The TMS320C25 DSP microprocessor (TMS) performs a major part of the mathematical operations. The supplemental digital and analog circuits will serve as peripheral hardware for frequency conversion, filtering, and interfacing.

B.2 Transmitter

The transmitter hardware interface diagram is shown in Fig. B.3. The TMS performs, at baseband, the trellis encoding, Interleaving, and CPM modulation. Additionally, the timing for all other circuits in the transmitter is coded on TMS. The resulting baseband signals I(t) and Q(t) signals are then upconverted to the desired IF level. The IF frequency is chosen to be 28.8 KHz. The transmitter circuits also needs synchronized timing signals that will include:

- A 4.8 KHz pulse for data source.
- A 2.4 KHz pulse for symbol rate.
- A 19.2 KHz pulse for sampling.

B.2.1 Baseband Processing

The data, at the rate of 4800 bps, may be provided by a codec or any terminal processor. The packetized data is fed to TMS in the form of 2 parallel bits each at the rate 2.4 Kbps. The data is encoded, in TMS, with a rate 2/3 trellis encoder, producing an aggregate rate of 7200 bps. Equivalently, the encoder output is generated at the rate of 2400 symbols per second (3 bits per symbol). The interleaver block is either (16 by 8) or (16 by 16). Implementation of both the trellis encoder and interleaver is done by TMS. The interleaved output symbols are input to the CPM modulator. The CPM signals are represented by 8 samples per symbol. Therefore the required sample rate is 19.2 KHz. This would mean that the

TMS must complete the entire entire operations, for each sample, within 1/19200 = 52 Micro seconds. A considerable speed is achieved by the use of various table look-ups representing all trigonometric operations as well as many transmitter functions. The computed I and Q digital data are sent through the appropriate data bus and loaded into two latches at the rate of 19.2 KHz. The D/A converter will transform the 12 bits digital I and Q components into the corresponding analog baseband signals.

The TMS software block diagram, for baseband processing, is illustrated in Fig. B.4.

B.2.2 IF Converter

The block diagram of the IF upconverter is shown in Fig. B.5. Here, the baseband components are upconverted to the IF band at the selected frequency of 28.8 KHz. The lowpass filters, multipliers, adders, phase shifters, and oscillator have all been implemented by analog circuits.

Two different types of lowpass filter are used for the IF conversion. The first is a fourth order linear phase lowpass filter for the analog I and Q. The bandwidth is set at 2.5 KHz. The second, on the other hand, is a fourth order chebychev. The transmitter circuit schematics are shown in Fig. B.6, Fig. B.7, Fig. B.8, and Fig. B.9.

B.3 Receiver

The receiver is considerably more complicated than the transmitter. A full digital receiver will be implemented in accordance with the basic block diagram shown in the Fig. B.10. Due to the substantial degree of computations involved in the transmitter-receiver operations, a single TMS will not be able to accommodate the maximum allowed processing time of 52 Microseconds per sample. There are eight sets of I and Q signal samples per symbol. The calculations have thus been split between four TMS microprocessor systems. The assignments are:

Systems one and two : perform the upconversions, downconversions , and the associated lowpass filtering operations.

System three : will do all the baseband processings.

System four: will perform the trellis decoding and deinterleaving.

B.3.1 IF Sampling

The 28.8 KHz IF signal is analog filtered for noise reduction and then applied to the input of the A/D converter. The filtered waveform is sampled at 115.2 KHz. The alignment of samples is achieved through a first order interpolation of in-phase samples. Here there are 8 groups of I and Q samples. The groups of the I, Q signals are separated by 52 Microseconds. The A/D output I and Q samples are separated by 8.681 Microseconds. This separation sets the upperbound on the converter speed. Therefore, a fairly high speed converter is required to meet the required timing . To retain the baseband component lowpass filtering is carried out by using TMS implemented appropriate FIR filters. Fig. B.10 illustrates the basic receiver architecture at the IF level.

The ground noise is expected to be larger than 1/256 of the input signal. Therefore, an 8 bit resolution associated with the A/D device should provide sufficient accuracy. The schematics of TMS systems one and two are shown in Fig. B.11 and Fig. B.12.

B.3.2 Baseband Operations

The baseband operations include filtering, clock recovery, and differential detection. These functions are implemented on the third TMS system. The block diagram of the differential detector is shown in Fig. B.13. Fig. B.14 and Fig. B.15 illustrate details of the third and fourth TMS systems.

B.3.3 Decoder and Deinterleaver

The fourth TMS system will perform operations of deinterleaving and Viterbi decoding. The schematics of this system is shown in The TMS is interrupted at the rate of 2.4 KHz. After the filtering, Doppler correction, and demodulation the data will be deinterleaved and decoded. Then the decoded symbols are loaded into the shift registers.

B.4 Status of the Hardware

1. The transmitter hardware has been completed and tested. The circuits include :
   - The TMS microprocessor system.
   - Peripheral circuits.

- IF upconversion circuits.

The TMS software for the transmitter is complete. It does not include the encoder. The eye diagrams corresponding the CPM signal with 1RC pulse, have been photographed and are shown in Fig. B.16 and Fig. B.17. The current system runs on a 2400 bps data rate. Thus transmitter hardware must be upgraded to accommodate the required 4800 bps data rate. This transmitter box, with operating instructions, has been delivered along with the final report.

2. As for the receiver, a total of four TMS microprocessor systems make up the receiver. The hardware for these systems have been completed. The components include:

   - The memory system.
   - Memory peripheral circuits.
   - System's timing,
   - A/D converter.
   - Interrupt circuits.
   - Handshaking logics for interfacing of the multiprocessor operations.

   Moreover, except the decoder, the software for the baseband receiver has been completed. In summary, additional time is required to complete the hardware implementation of the differential CPM system.

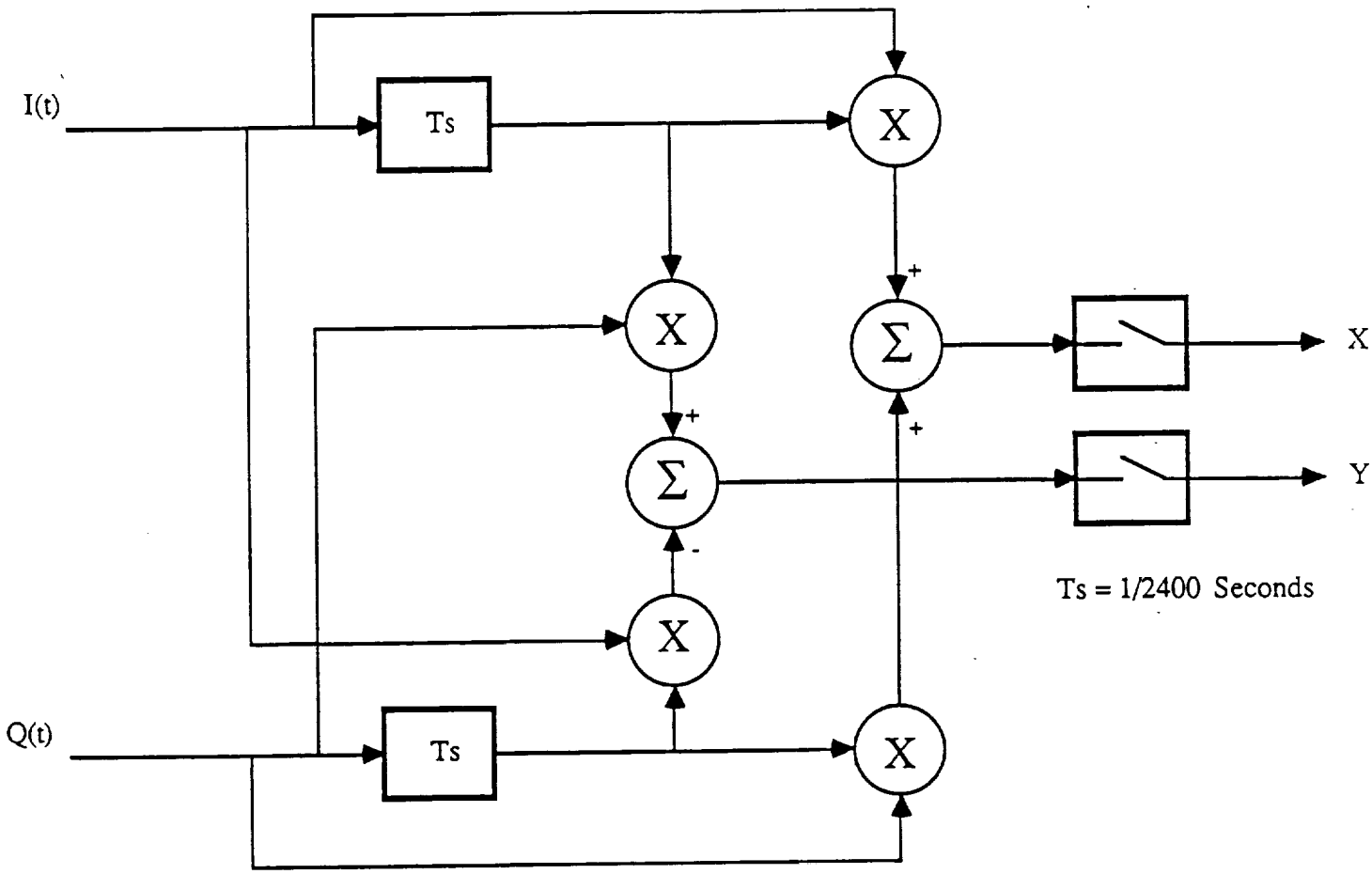

Differential detector

Figure B.1

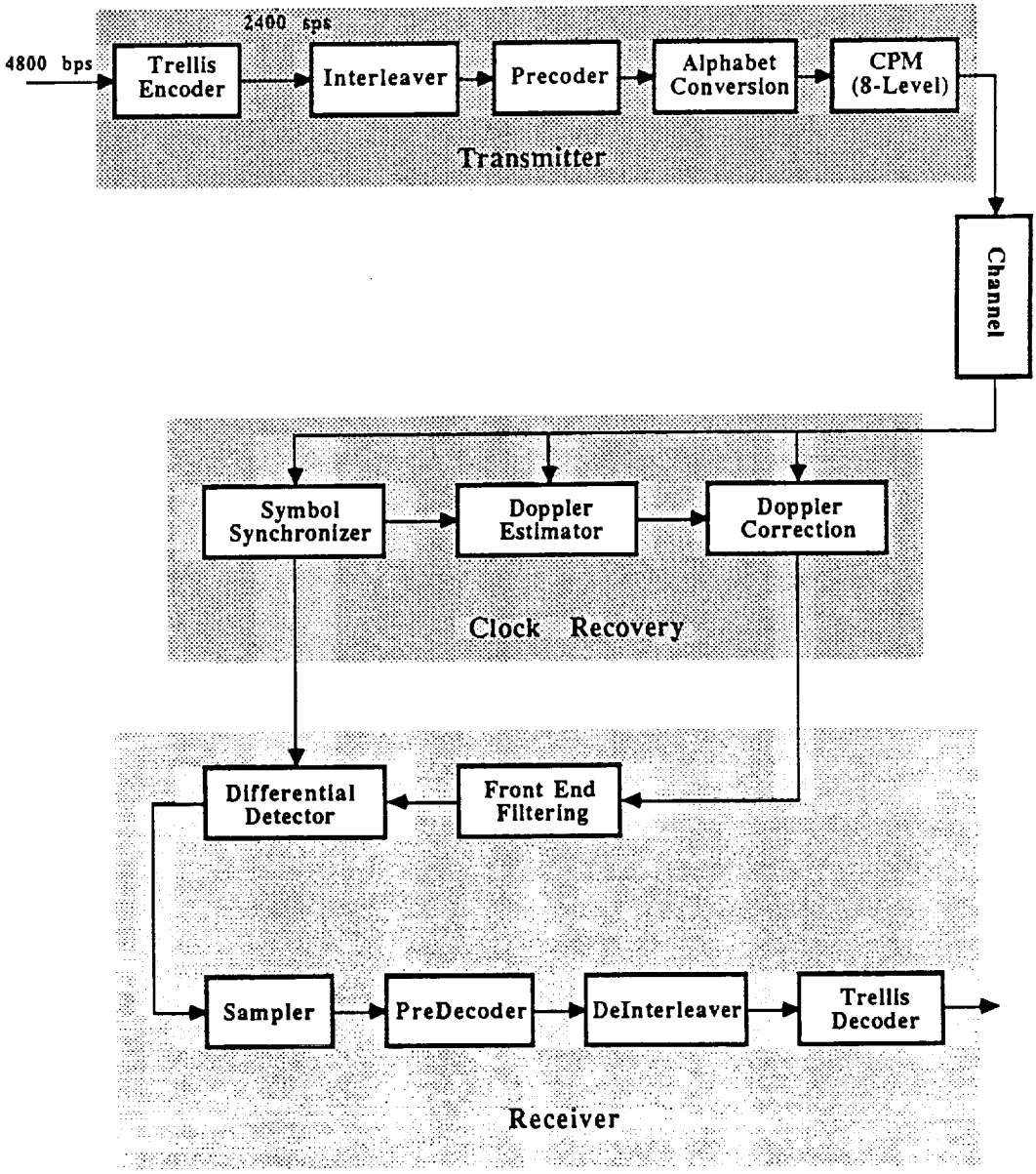

The Partial response system

Figure B.2

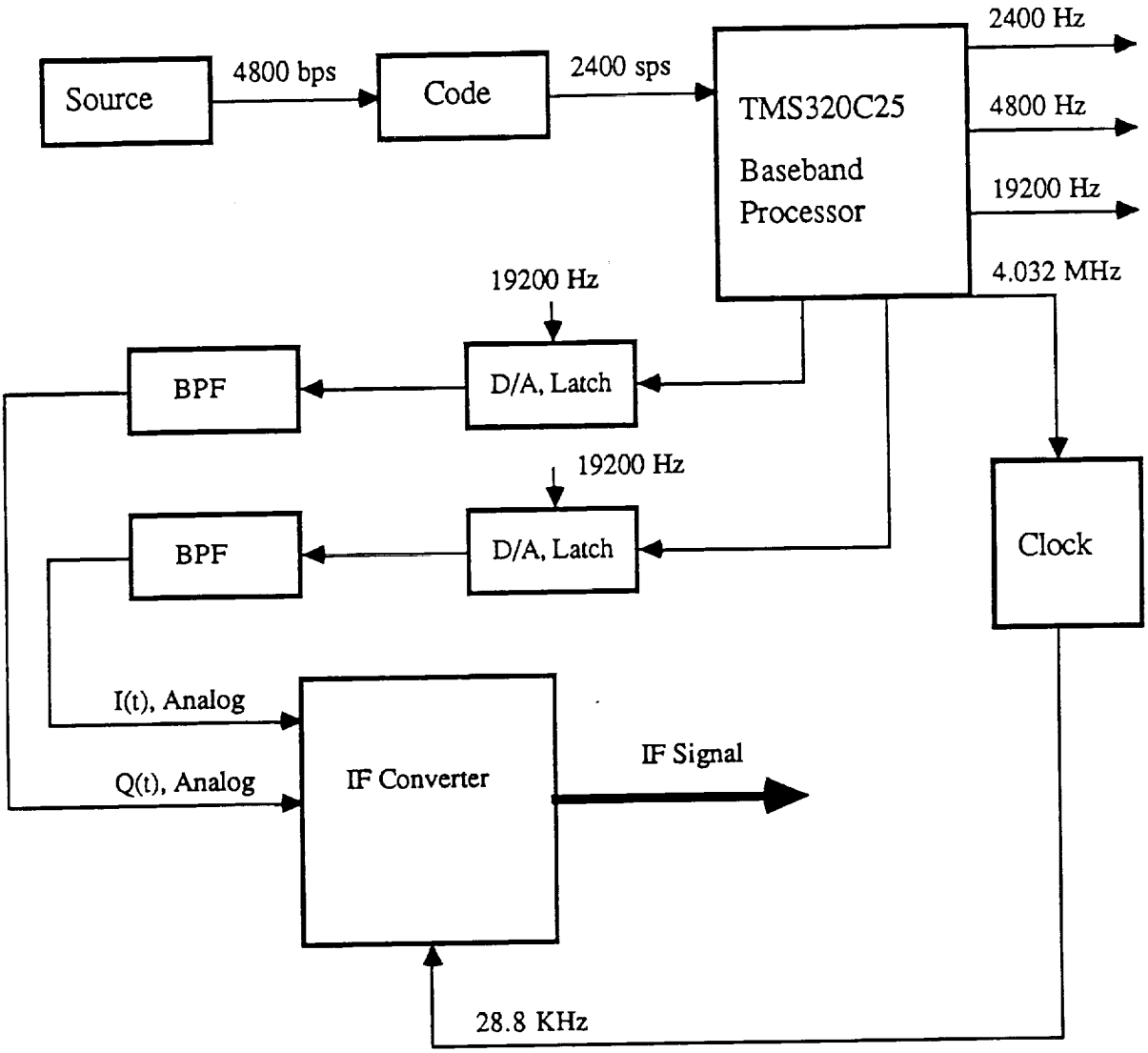

Transmitter block diagram

Figure B.3

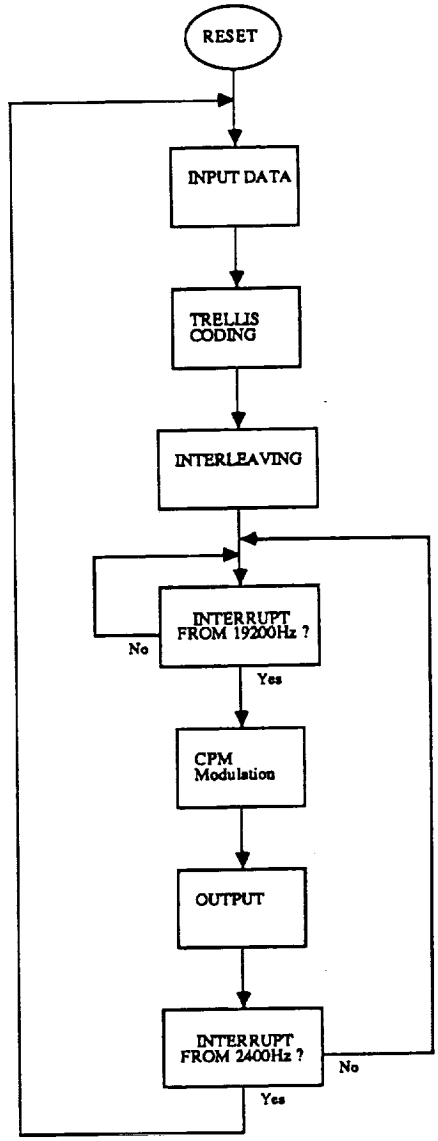

Flowchart for the baseband processor

Figure B.4

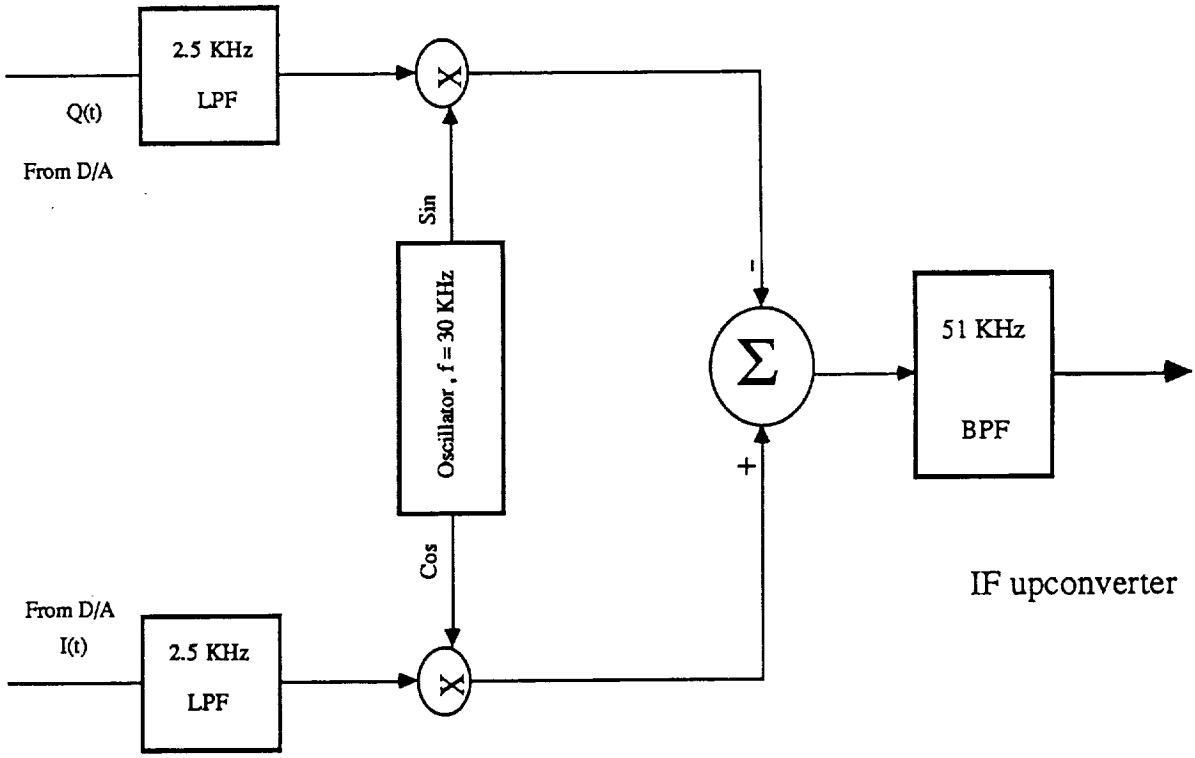
2.5 KHz
LPF
Q(t)
From D/A
X
Sin
Oscillator , f = 30 KHz
Cos
From D/A
I(t)
2.5 KHz
LPF
X
-
+
Σ
51 KHz
BPF
IF upconverter

Figure B.5

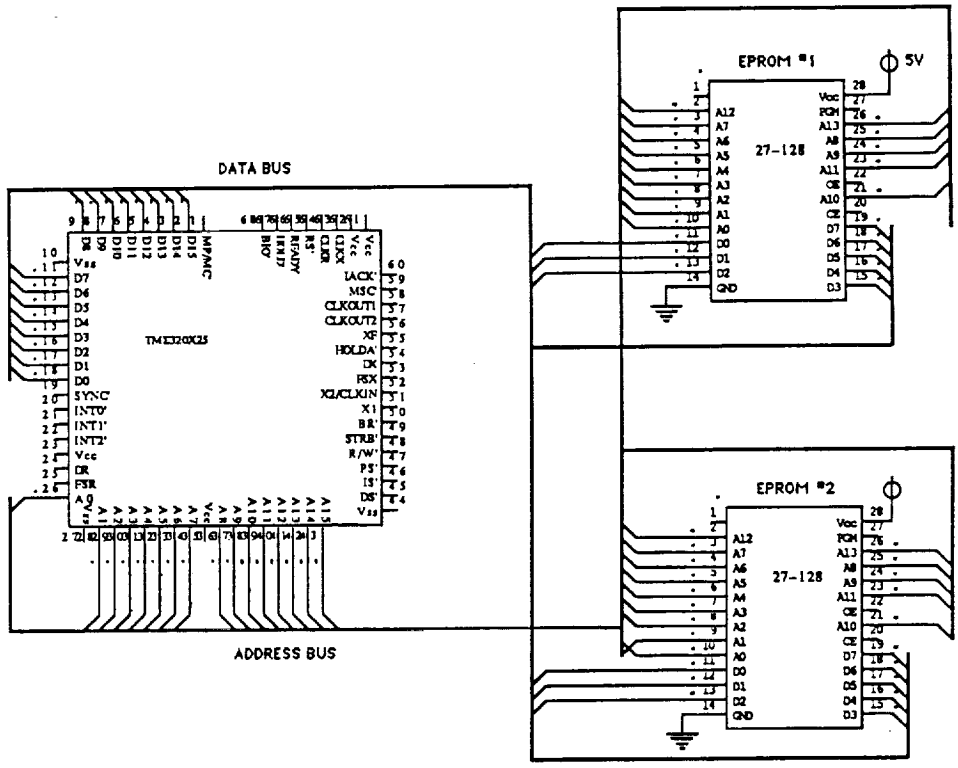

Transmitter board-first stage

Figure B.6

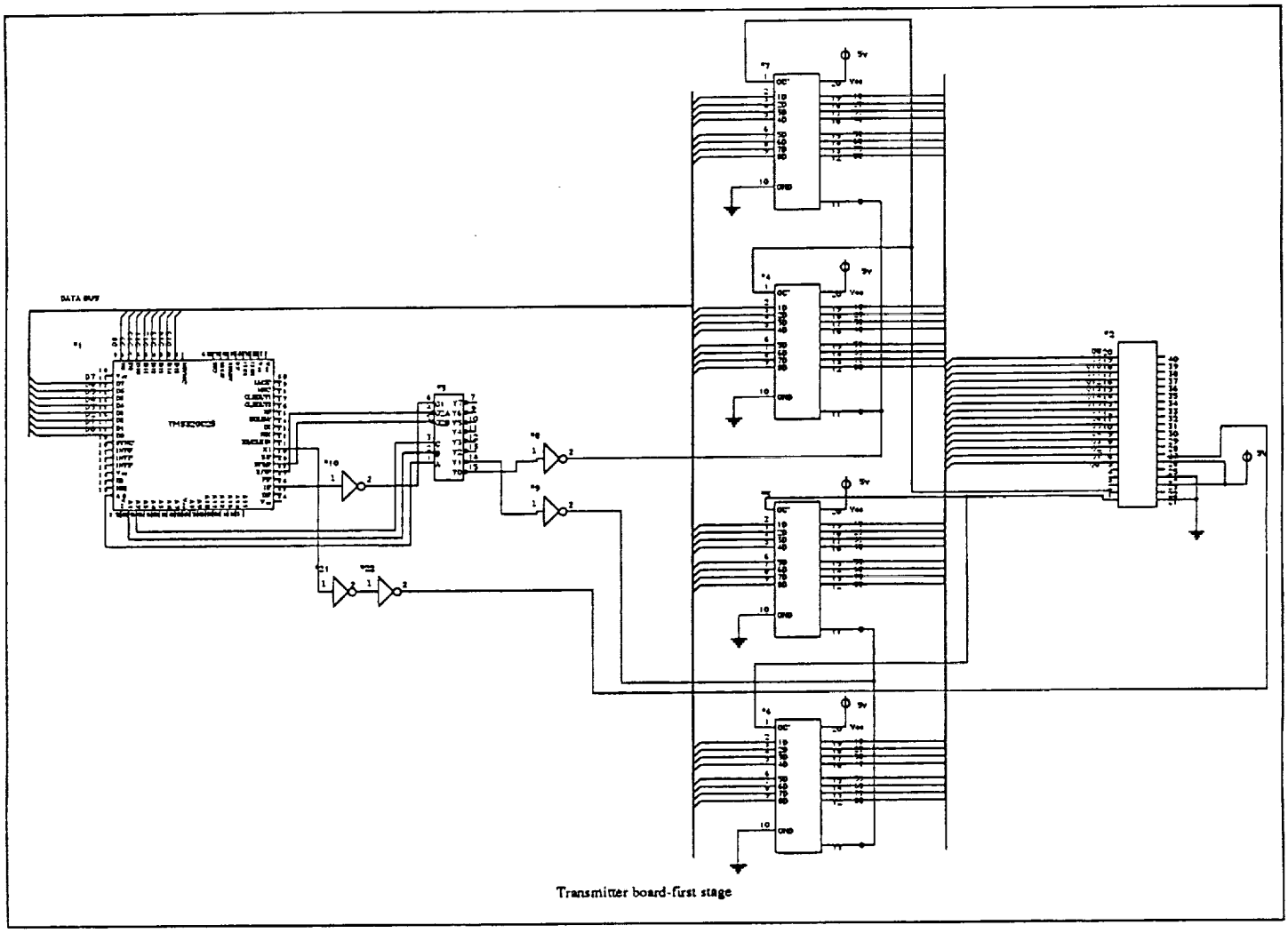

Figure B.7

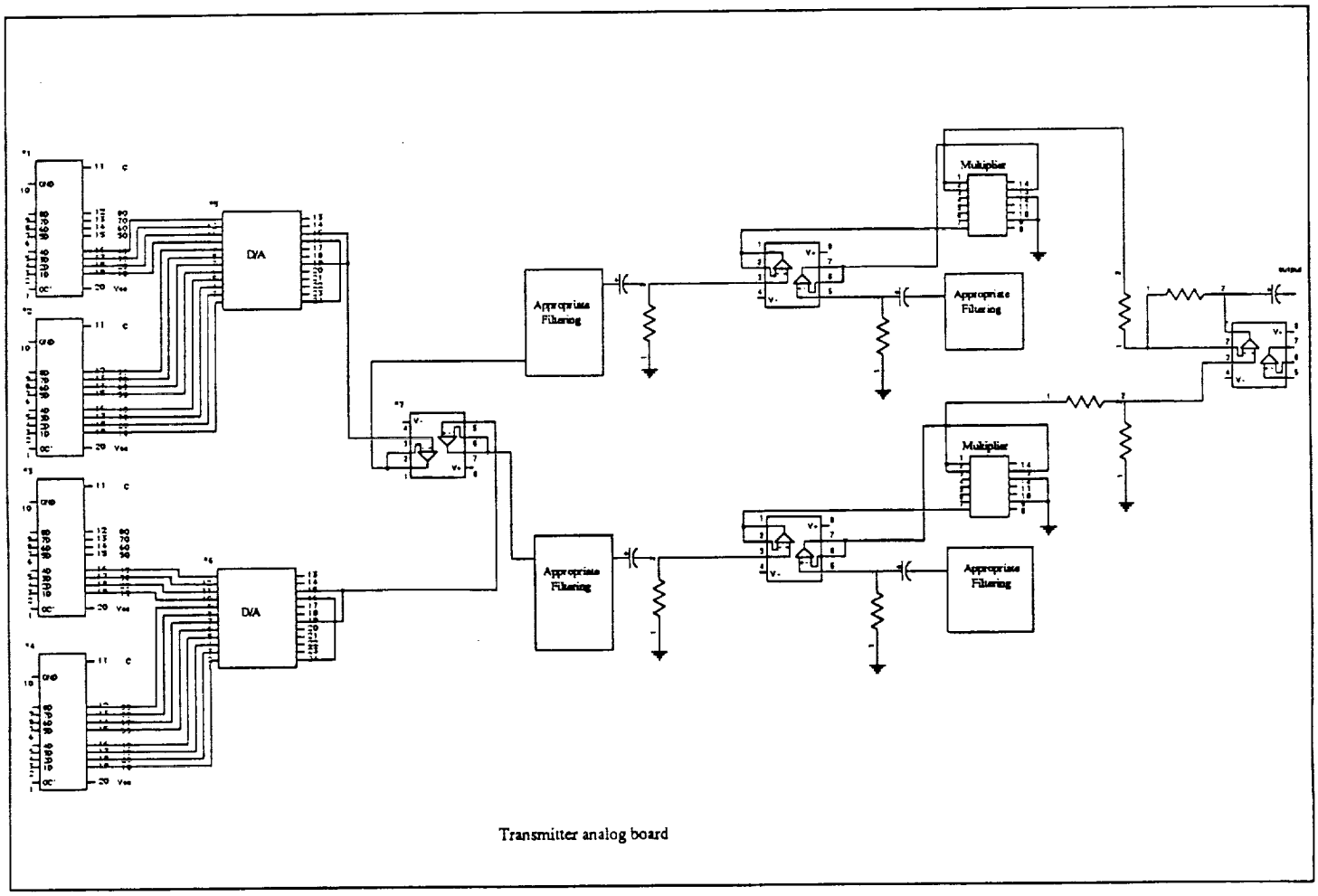
D/A
D/A
Appropriate Filtering
Appropriate Filtering
Appropriate Filtering
Appropriate Filtering
Multiplier
Multiplier
Transmitter analog board

Figure B.8

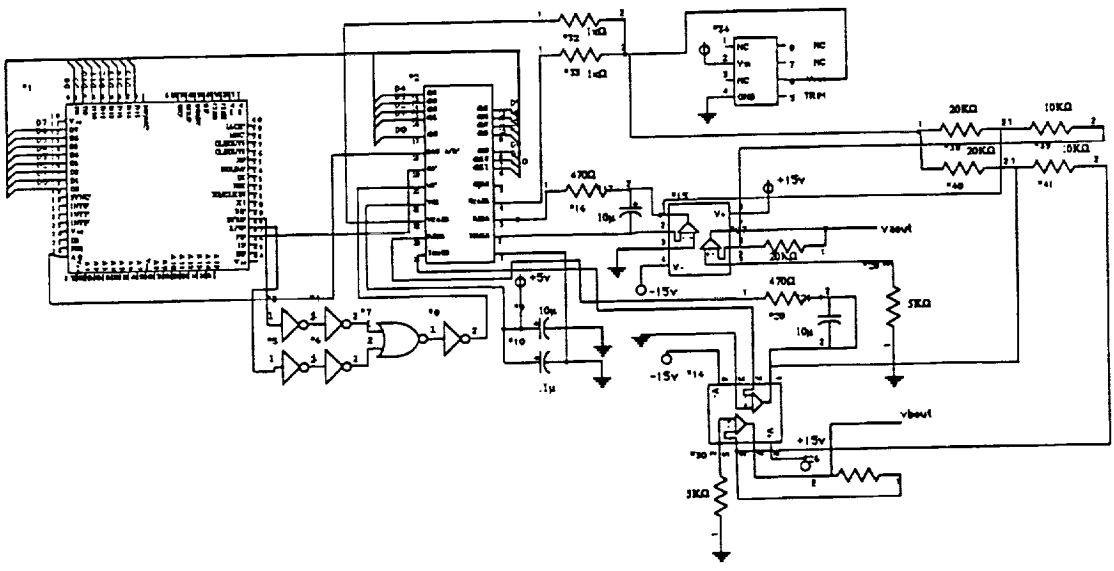

Transmitter board-second stage

Figure B.9

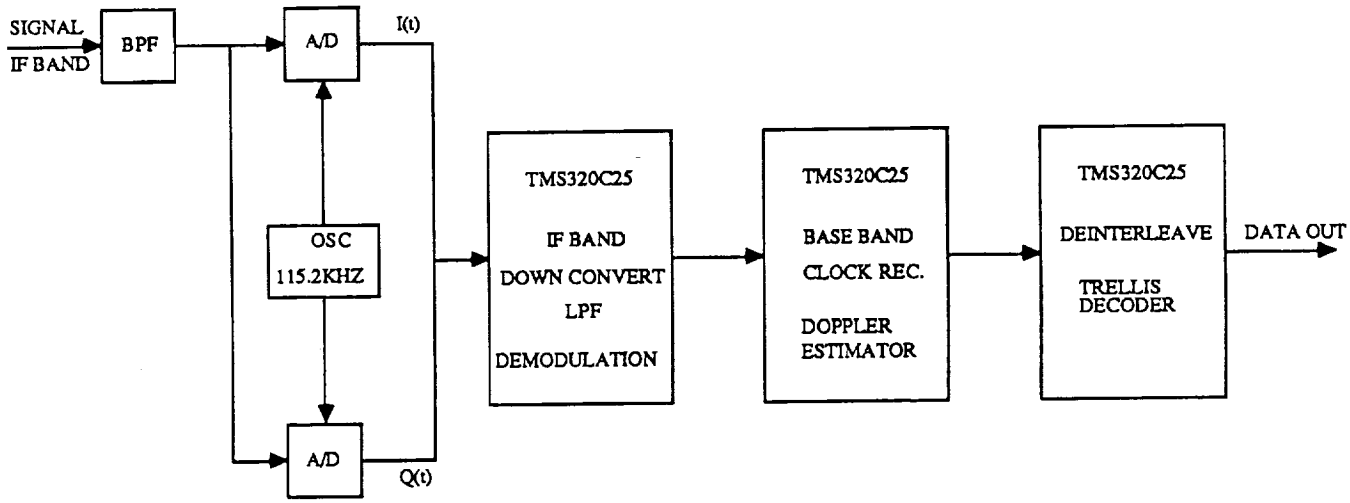

Receiver Architecture at IF band

Figure B.10

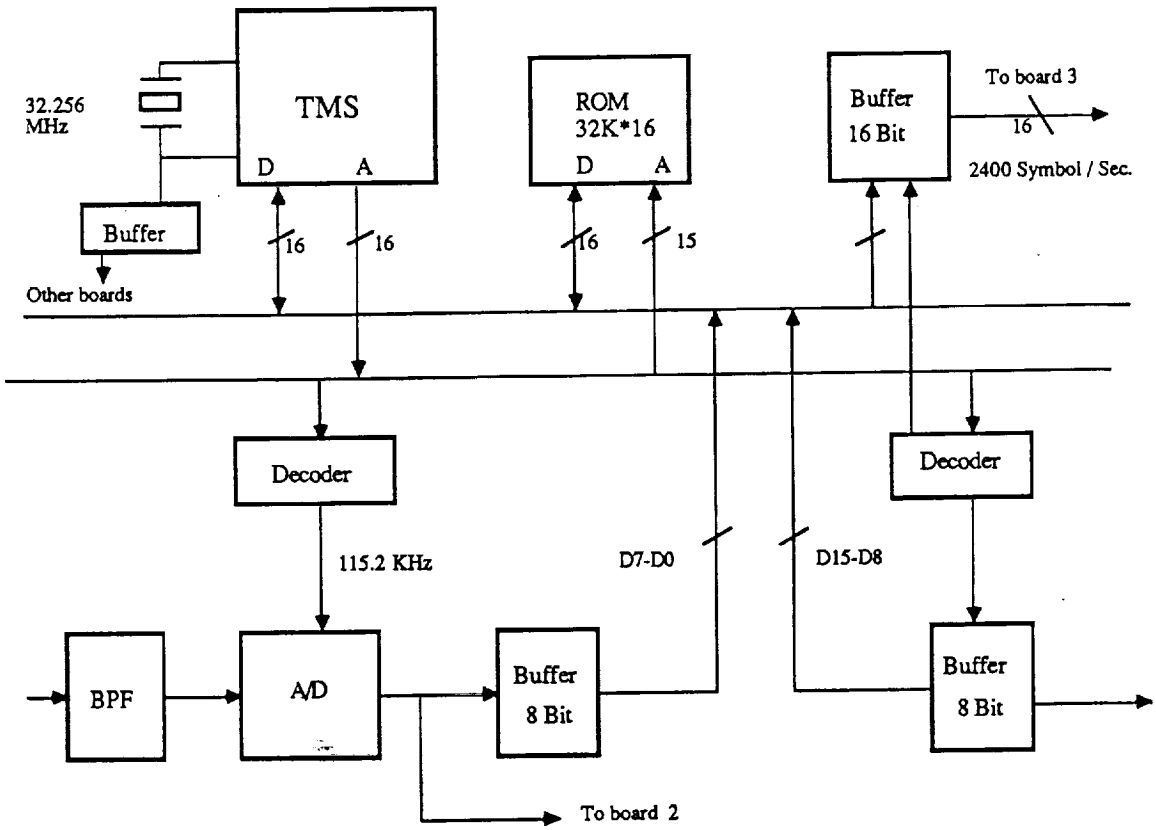

Board one : A/D, LPF, Detector (I component)

Figure B.11

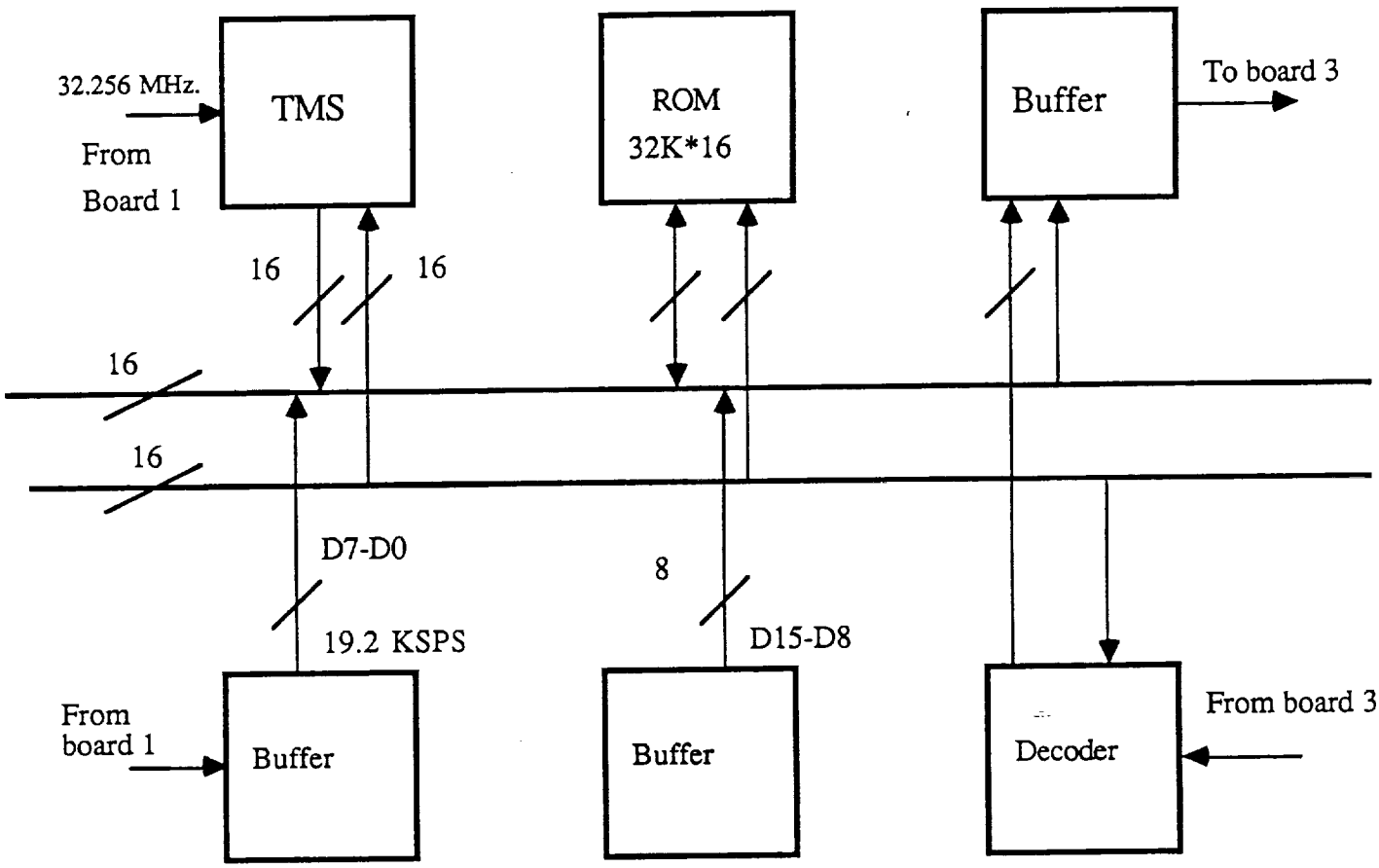

LPF and demodumation (Q component)

Figure B.12

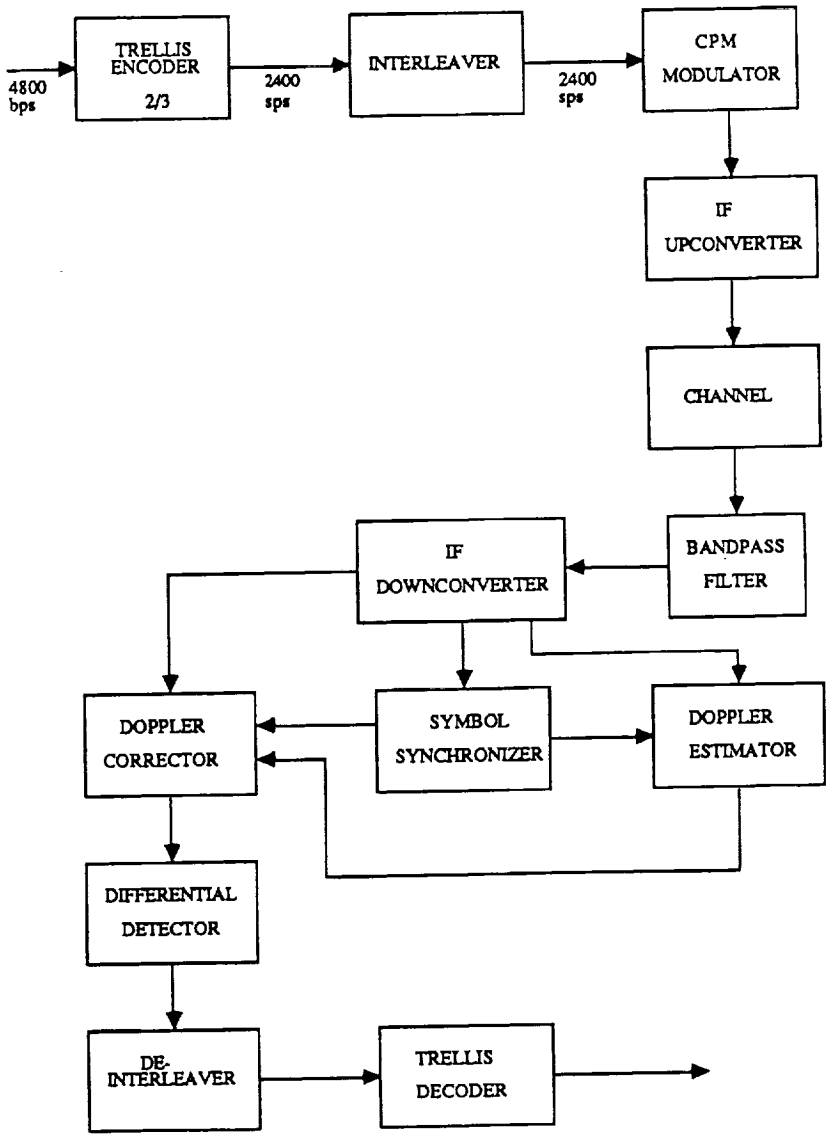

The full response system

Figure B.13

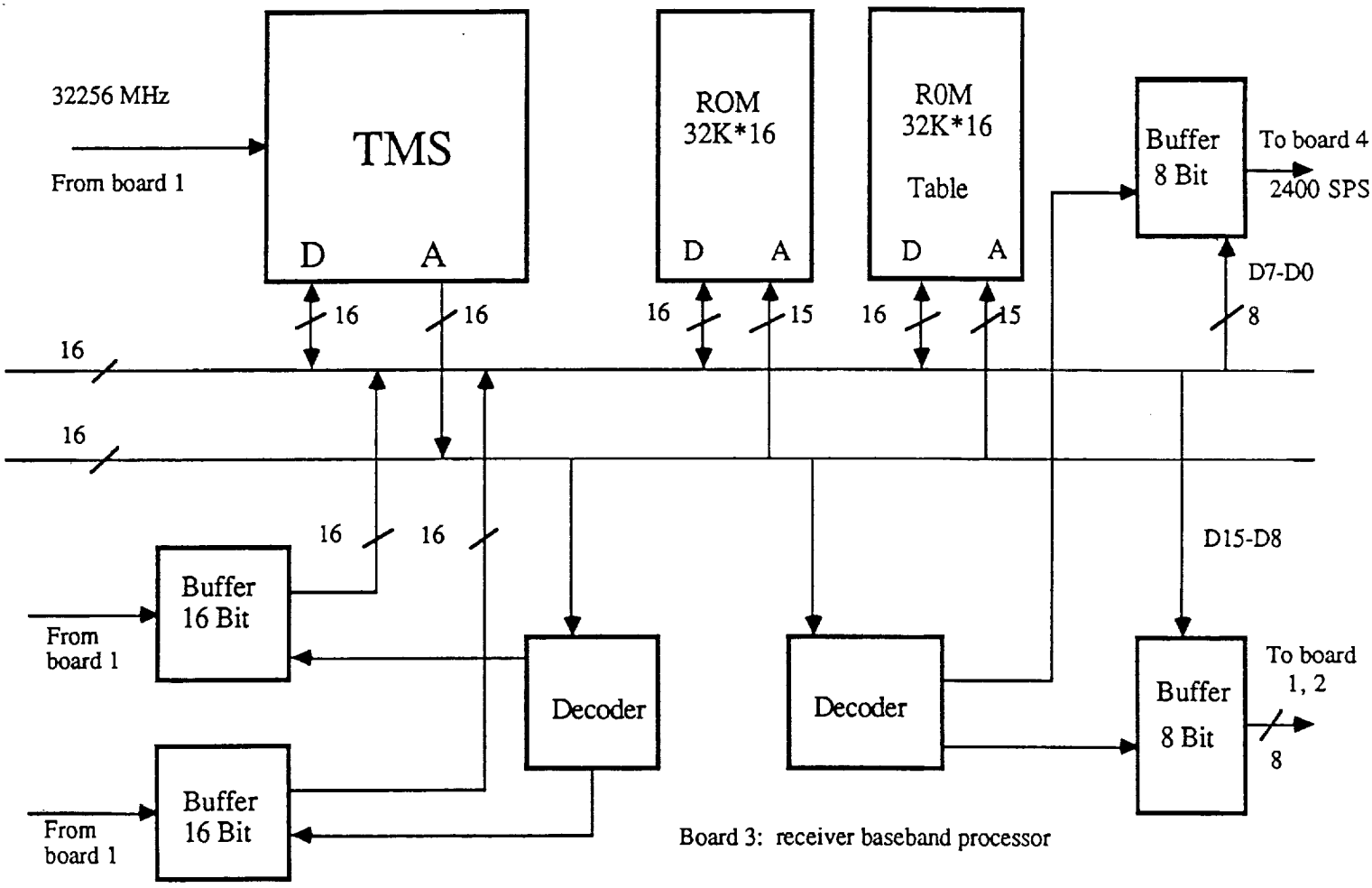

Board 3: receiver baseband processor

Figure B.14

C-4

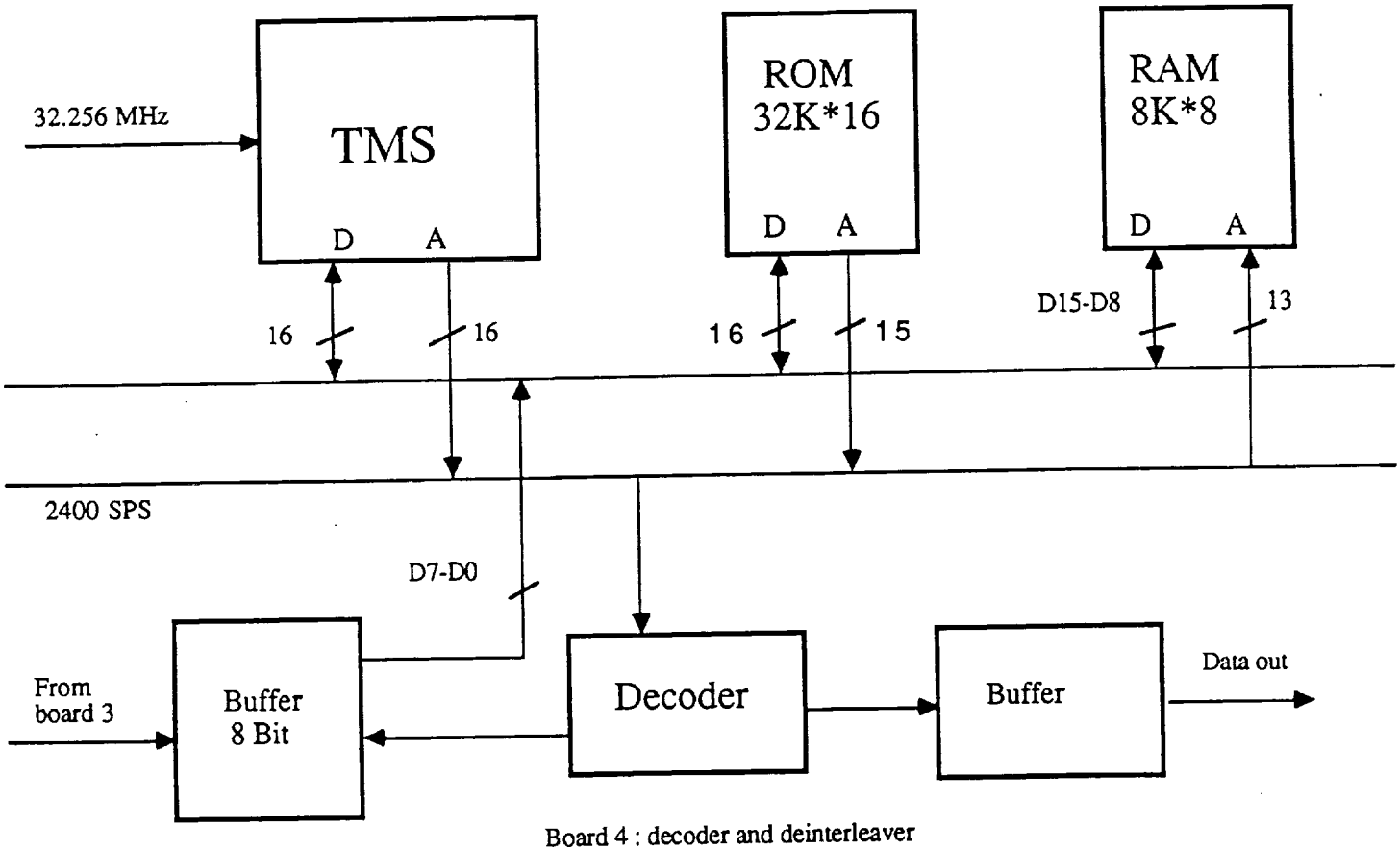

Board 4 : decoder and deinterleaver

Figure B.15

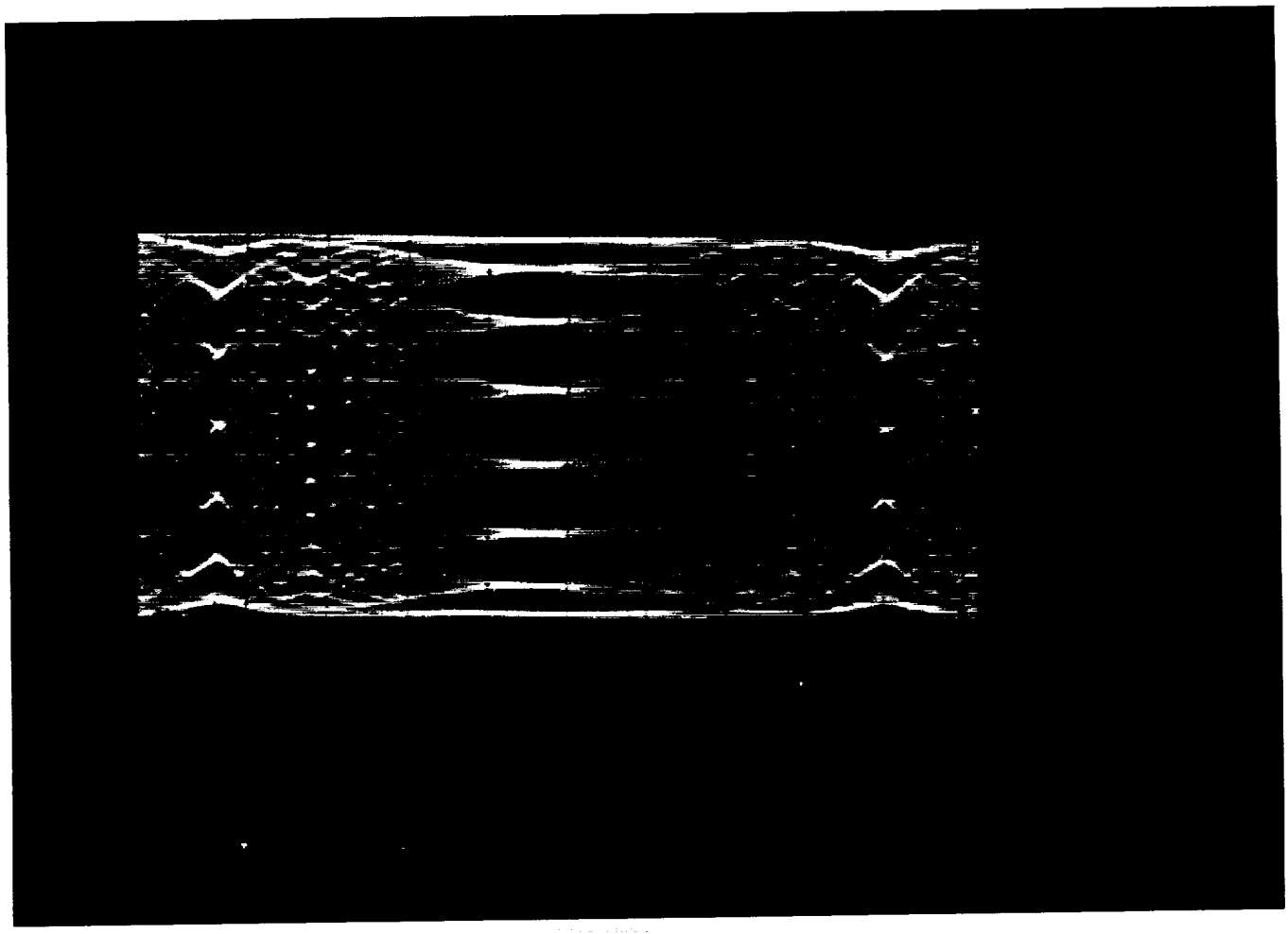

Figure B.16

Figure B.17

NASA
National Aeronautics and Space Administration

Report Documentation Page

1. Report No.	2. Government Accession No.	3. Recipient's Catalog No.
Final/ 9		

4. Title and Subtitle

Trellis Coding with Continuous Phase Modulation (CPM) for Satellite-Based Land mobile Communications

5. Report Date

September 1989

6. Performing Organization Code

7. Author(s)

F. Abrishamkar, E. Biglieri, M. Hagoo, Y. Jou, Y. Liu, J. Wang, Y. Yang, S. Wilson, L. Welch

8. Performing Organization Report No.

10. Work Unit No.

Final/9

9. Performing Organization Name and Address

TECHNOLOGY GROUP
1888 CENTURY PARK EAST , SUITE 10
LOS ANGELES, CA 90067

11. Contract or Grant No.

NAS7-1003

13. Type of Report and Period Covered

FINAL : 5/87 to 8/89

12. Sponsoring Agency Name and Address

14. Sponsoring Agency Code

16. Abstract

This volume of the final report summarizes the results of our studies on the satellite-based mobile communications project; it includes :

- A detailed analysis, design, and simulations of trellis coded, full/partial response CPM signals with/without interleaving over various Rician fading channels.
- Analysis and simulation of computational cutoff rates for coherent, noncoherent, and differential detection of CPM signals.
- Optimization of the complete transmission system.
- Analysis and simulation of power spectrum of the CPM signals.
- Design and development of a class of Doppler frequency shift estimators.
- Design and development of a symbol timing recovery circuit.
- Breadboard implementation of the transmission system.

Studies prove the suitability of the CPM system for mobile communications.

17. Key Words (Suggested by Author(s))	18. Distribution Statement
CPM, trellis codes, mobile; Doppler, synchronization, firmware Rician fading, cutoff rate, coherent, noncoherent, differential	Unlimited, Unclassified

19. Security Classif. (of this report)	20. Security Classif. (of this page)	21. No. of pages	22. Price
Unclassified			

NASA FORM 1626 OCT 86